Double parton scattering: parton correlations and their scale evolution

Dissertation
zur Erlangung des Doktorgrades
an der Fakultät für Mathematik, Informatik und Naturwissenschaften
Fachbereich Physik
der Universität Hamburg

vorgelegt von

Florian Fabry

Hamburg

2023

Abstract

Double parton scattering (DPS) describes a process in hadron-hadron scattering in which two partons are extracted from each initial hadron and then initiate hard scattering processes separated by a finite distance. After factorising the hadronic process, one obtains parton distributions functions that characterise the behaviour of partons inside the hadron at non-perturbative scales. A novel feature compared to ordinary single parton scattering (SPS) is that the two partons might be correlated in their quantum numbers. One example of such a quantum number is the colour charge under the strong force in quantum chromodynamics (QCD). This thesis focuses on the scale dependence of collinear distributions for partons correlated in their colour charge. Collinear double parton distributions (DPDs) depend on the collision energies of the partonic subprocesses and initial state rapidity. The evolution of DPDs under these variables is governed by the DGLAP and Collins-Soper (CS) equation, respectively. The corresponding coefficients, also called kernels, on which the equations depend can be calculated as a perturbation series in the strong coupling.

In the first part of the thesis, the next-to-leading order (NLO) contribution in perturbation theory to the DGLAP equation for correlated DPDs is computed. The calculation is performed for unpolarised and longitudinally polarised partons as well as transversely polarised quarks. Two independent methods with a large overlap in their produced results are combined to construct the full NLO kernels. The first method uses NLO calculations of the single parton DGLAP kernels which are already available in the literature and generalises them to correlated partons. The second one is based on the matching formula between collinear and transverse momentum dependent parton distributions. There, the results are derived from existing matrix elements of single partons with non-zero transverse momentum.

In the second part, an extension for an existing evolution library, CHILIPDF, is presented that is able to solve both the DGLAP and CS evolution equations for colour correlated DPDs. With this approach it is possible for the first time to assess the impact of colour correlated partons on DPS cross sections in a fully quantitative way. We study the effect of DGLAP evolution at different energies and interpartonic distances, the changes when taking NLO terms into account, and the contribution of correlated DPDs to the complete DPS cross-section.

Zusammenfassung

„Double parton scattering" (DPS) beschreibt einen Prozess mit zwei Hadronen im Anfangszustand, in dem zwei Partonen in endlicher Distanz aus jedem Hadron harte Streuprozesse initiieren. Faktorisiert man den hadronischen Prozess, so erhält man Partonverteilungsfunktionen, die das Verhalten der Partonen im Hadron bei nicht-perturbativen Skalen beschreiben. Anders als im „Single parton scattering" (SPS) können die beiden Partonen in ihren Quantenzahlen korreliert sein. Ein Beispiel für eine solche Quantenzahl ist die Farbladung der starken Wechselwirkung in der Quantenchromodynamik (QCD). Diese Arbeit stellt die Skalenabhängigkeit kollinearer Verteilungsfunktionen in den Fokus, die in der Farbladung korrelierte Partonen beschreiben. Kollineare Doppelpartonverteilungen (DPDs) hängen von der Kollisionsenergie der partonischen Subprozesse sowie der Rapidität des einlaufenden Zustandes ab. Die Evolution der DPDs unter diesen Variablen wird jeweils von der DGLAP und Collins-Soper (CS) Gleichung beschrieben. Die entsprechenden Koeffizienten, auch Kerne genannt, können als Störungsreihe in der starken Kopplung entwickelt werden.

Im ersten Teil der Arbeit wird der nächstführende (NLO) Term der DGLAP Kerne für korrelierte DPDs in der Stöhrungstheorie ausgerechnet. Die Rechnung erfolgt für unpolarisierte und longitudinal polarisierte Partonen sowie transversal polarisierte Quarks. Zwei unabhängige Methoden, die sich in den produzierten Ergebnissen stark überschneiden, werden kombiniert, um die kompletten NLO Kerne zu ermitteln. Die erste Methode benutzt NLO Rechnungen für die DGLAP Gleichung von SPS Verteilungen, die bereits in der Literatur verfügbar sind, und verallgemeinert sie zu korrelierten Partonen. Die zweite Methode basiert auf einer „Matching" Formel zwischen kollinearen Verteilungen und solchen, die vom partonischen Transversalimpuls abhängen. Dort werden die Ergebnisse aus existierenden Matrixelementen für einzelne Partonen mit nicht verschwindendem Transversalimpuls hergeleitet.

Im zweiten Teil wird eine Erweiterung einer schon existierenden Bibliothek für numerische Evolution, CHILIPDF, präsentiert, die fähig ist, die DGLAP und CS Gleichung für korrelierte DPDs zu lösen. Mit diesem Ansatz ist es zum ersten Mal möglich, den Beitrag farbkorrelierter Partonen im DPS Wirkungsquerschnitt auf einem vollständig quantitativen Weg abzuschätzen. Es werden die Effekte der DGLAP Evolution bei verschiedenen Skalen und interpartonischen Abständen, die Auswirkungen der NLO Terme und der Beitrag farbkorrelierter DPDs zum vollständigen DPS Wirkungsquerschnitt untersucht.

Contents

List of publications

This thesis is based on the author's contributions to the following publications:

* [1] M. Diehl, F. Fabry and A. Vladimirov, *Two-loop evolution kernels for colour dependent double parton distributions*, *JHEP* **2023** (2023) 67 [2212.11843].

* [2] M. Diehl, F. Fabry and P. Plößl, *Evolution of colour correlated double parton distributions: a quantitative study*, [2310.16432].

Chapter 1

Introduction

Particle physics today has reached a stage in which incredible precision meets an abundance of describable phenomena. The development of the Standard Model (SM) has played a crucial role in reaching this current state. As the main foundation for theoretical predictions, it describes three fundamental interactions of nature within the framework of quantum field theory. First, the electromagnetism was quantised under the name of quantum electrodynamics, which was later combined with the weak interaction into the electroweak theory. The strong force, which is responsible for the stability of atomic nuclei, is treated by the theory of quantum chromodynamics (QCD). All interactions are mediated by exchanges of gauge bosons with a certain coupling strength. In the case of QCD, these bosons are called gluons, and α_s stands for the strong coupling. Its most prominent feature is the asymptotic freedom, meaning that it decreases with growing distance/decreasing energy. This explains why the strong force is the predominant interaction at distances as small as the size of nuclei, compensating repulsory effects from the electromagnetic force and making it a stable particle, while at the same time being immeasurable in the macroscopic world. The charge under QCD as a non-abelian gauge theory has three manifestations which will be associated with red, green and blue. Particles that hold such a colour charge are called quarks.

The discovery of the Higgs-Boson by the ATLAS [3] and CMS [4] collaborations at the Large Hadron Collider (LHC) was the last missing puzzle piece for a now complete theory that is able to explain almost all modern measurements. The potential anomalies like the muon $g-2$ measurement [5,6] on the other hand are rare and not yet verified. Moreover, there are large incompletenesses including the absence of gravity, no explanation for the size of the asymmetry between matter and anti-matter, neutrino oscillations and masses, and missing dark matter candidates. On top of the discovery of the Higgs-particle, the hopes were high that such a dark matter particle would have been found at the LHC by direction detection, i.e. as a signal in the detectors. Since such a scenario has not occurred, the only option is to increase the precision both in measurements and SM calculations up to a point at which a discrepancy appears. Such an anomaly then needs to be explained by an extension beyond the SM (BSM).

Improving the accuracy of theory predictions for any LHC process necessarily involves

improving our understanding of the initial state particle, the proton. As a hadron, it consists of quarks and gluons, which are collectively known as partons and held together by the strong force. Although its Lagrangian is as simple as it is beautiful, describing a composite particle turns out to be quite challenging. It can be achieved by a method called "factorisation", first proposed by Collins, Soper, Sterman [7, 8], and Ellis, Curci, Furmanski, Petronzio [9, 10]. In this approach, low and high energetic parts of the process are separated and then connected via a convolutional product. For the high energy regions one can apply perturbation theory, i.e. expand quantities in the strong coupling α_s. At low energies on the other hand, α_s becomes too large to be used as an expansion parameter. Thus, quantities have to be extracted from measurements or calculated in a non-perturbative way. These parts of the process are described by so-called "parton distributions", which we abbreviate as TMD if they depend on the partonic transverse momentum, and PDF if the transverse momentum is already integrated such that partons can be viewed as collinear to the proton. In their orginal version, the factorisation proofs assumed the extraction of *one* parton from both protons which then initiate a scattering process at high energy scales. In the following, we will call this single parton scattering (SPS). A subclass of processes and kinematic configurations receives a sizeable contribution by double parton scattering (DPS), in which *two* partons out of each proton take part in two distinct partonic subprocesses.

After pioneering work in the 1980s, [11–15], DPS has received increasing attention in the last 25 years, both on the theoretical [16–33] and experimental side. Today, there is experimental evidence for DPS in the production for dijets + other products [34–36], multijets (+ other products) [37–42], one or more J/ψ (+ other products) [43–47], open charm + other products [48, 49], four leptons [50], same-sign WW [51, 52], and underlying event [53]. In addition, DPS is taken into account in BSM searches [54] and as a background of precision studies [55]. An overview of the whole field can be found in [56].

A rigorous treatment of hadronic processes in the frame work of QCD can again be achieved by the factorisation formalism. At the current time, the proof of factorisation in DPS [57–60] is on the same level as the one for SPS. This gives access to distribution functions describing the extraction of two partons from the proton as part of a complete DPS process. They will be called DTMDs if they depend on the partonic transverse momenta and DPDs if not. As the cross sections for DPS processes are comparatively small and DPDs depend on a variety of different variables, in contrast to SPS there are no experimental fits available for parton distributions in DPS. However, it is worth noting that there are alternative approaches in development to obtain non-perturbative information on DPDs: in these ongoing efforts, DPDs are extracted directly from QCD simulations on a discretised grid (lattice QCD) [61–63]. Besides being a crucial part of the factorisation formula, compared to SPS they also contain novel information about the inner structure of protons: as the two partons are separated by a finite distance, double parton distributions provide information about the spatial resolution of hadrons.

A qualitatively new feature is the correlation between both partons in potentially all their quantum numbers. In this thesis, we will investigate DPDs correlated in their

charge under QCD interactions, the colour quantum number. Although colour correlated DPDs were thought to be subleading compared to uncorrelated ones [19], recent studies [64] show that they might have a significant impact in certain kinematic regions. In the centre of this work will be the DGLAP evolution, which governs the behaviour of collinear parton distributions under the change of energy scales.

Based on publications by Dokshitzer, Gribov, Lipatov, Altarelli, and Parisi [65–67], the DGLAP equation is a differential equation in which the distributions are convolved with scale-dependent kernels. Parton distributions as a whole are non-perturbative objects, but these DGLAP kernels can be expanded perturbatively. parton correlations are not possible in SPS, which means that colour uncorrelated DPDs and PDFs share the same DGLAP kernels. While these DGLAP kernels are calculated up to N^3LO [68–70] and partial N^4LO [71–74], their colour correlated counterparts are only available at LO [26].

Colour correlated DPDs are a curiosity: their scale equation is governed by a DGLAP equation, but they also exhibit a rapidity dependence like TMDs, which is described by a Collins-Soper (CS) equation. We will enter unexplored territory by studying how distributions behave under *both* DGLAP and CS evolution combined. Existing phenomenological studies are only performed with LO DGLAP kernels [64], or DGLAP evolution is not even taken into account at all [75]. Furthermore, we aim to provide a numerical study over the whole kinematic range. The approach in [64, 75] is only applicable if both partons are in the same kinematic configuration.

The objective of this thesis is thus twofold: First, calculate the NLO DGLAP kernels for colour correlated DPDs, and then carry out a quantitative study[1] to assess the impact of DGLAP and CS evolution of DPDs both at LO and NLO.

Structure of the thesis.
The thesis is organised as follows:

In chapter 2, we start with an introduction into the field of double parton scattering. After that, double parton distributions are introduced with a special emphasis on the DGLAP equation. Also covered are a field theoretic definition, subtraction and renormalisation procedure and the CS equation.

The calculation of colour non-singlet DGLAP kernels at NLO is performed in chapter 3. Two methods are developed and used to compute overlapping parts of the kernels. The first one utilises existing results for single parton DGLAP evolution, while the second one is based on the matching formula between transverse momentum dependent and collinear distributions. The section is closed with a presentation of the complete results for colour correlated NLO DGLAP kernels in all parton polarisations.

Chapter 4 presents a numerical study for the solution of the combined DGLAP and CS evolution. It is described how the existing DGLAP evolution code CHILIPDF [76] for uncorrelated DPDs is expanded to cope with this new challenge. Due to the lack of experimental data DPDs need to be described by models. They are introduced

---

[1]It is amusing to note that more than 35 years ago in the concluding section of [13] this was introduced as an "particularly interesting" problem which "remain[s] to be investigated".

together with the non-perturbative ansätze for the CS kernel. After that, a variety of different plots is presented. We analyse how colour correlated DPDs change under CS and DGLAP evolution and what the effects of the newly calculated NLO kernels are in different kinematic settings. Furthermore, we will present the impact of colour correlated DPDs in cross sections for different processes and compare it with the colour uncorrelated case.

All figures were created with the help of either Jaxodraw [77] or Matplotlib [78]. Parts of the calculation were performed with FORM [79] and the ColorMath package [80].

Chapter 2

Theoretical description of double parton scattering

In this chapter, we give an introduction to the topic of DPS with a special emphasis on double parton distributions, their projection onto colour representations, and their scale evolution. In section 2.1, we start with a short summary of the factorisation proof and the DPS cross section. This is followed in section 2.2 by a detailed discourse on one of the main ingredients of this cross section, the double parton distributions, covering their field theoretic definition, evolution equations and most important characteristics. Then, in section 2.3, we give a detailed introduction to the DGLAP equation for colour correlated collinear DPDs. This chapter is closed by a recapitulation of the characteristic equations for double parton distributions in section 2.4.

There have been some comprehensive overviews [81, 82] and detailled reviews [26, 58] in the literature over the past years that serve as an orientation for the following sections. We assume the basic knowledge on the theory of QCD as can be found in every textbook on quantum field theory and the SM.

2.1 General properties

We first give an overview over the factorisation proof in section 2.1.1. Section 2.1.2 then introduces the final cross section in its factorised form including the double parton distributions.

Before diving into the details of the theory, let us first ask the question if all this additional work connected with DPS is even worth the effort. Or, in other words, is it not sufficient to describe a hadronic process with ordinary distributions and partonic cross sections for SPS? Of course, the answer is much more involved than just a simple Yes or No. On more formal grounds, power behaviour and different dependencies on coupling constants of SPS and DPS cross sections decide if it is important for a certain process to also consider the DPS contribution.

In general, it can be shown [81] that for collinear DPDs the DPS cross section is
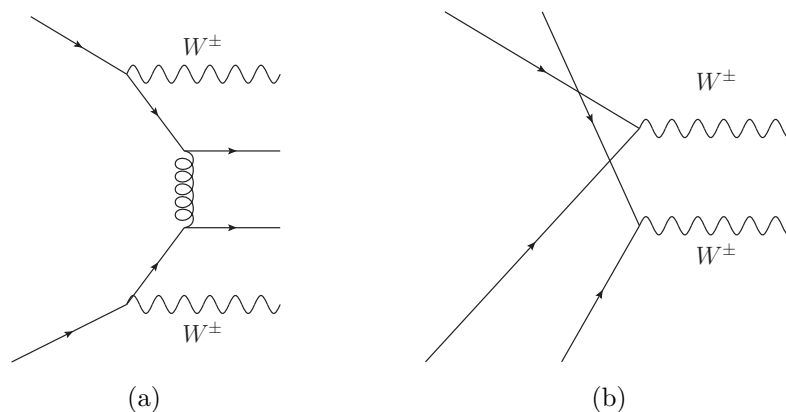
Figure 2.1: One of the lowest order partonic cross sections for same-sign W production in SPS (a), and the lowest order partonic cross section in DPS (b).

power suppressed,

$$\frac{\mathrm{d}\sigma_{\mathrm{DPS}}}{\mathrm{d}x_i \mathrm{d}\bar{x}_i} \bigg/ \frac{\mathrm{d}\sigma_{\mathrm{SPS}}}{\mathrm{d}x_i \mathrm{d}\bar{x}_i} \sim \frac{\Lambda^2}{Q^2}\,, \qquad (2.1)$$

but for DTMDs it is not,

$$\frac{\mathrm{d}\sigma_{\mathrm{DPS}}}{\mathrm{d}x_i \mathrm{d}\bar{x}_i d\boldsymbol{q}_i} \bigg/ \frac{\mathrm{d}\sigma_{\mathrm{SPS}}}{\mathrm{d}x_i \mathrm{d}\bar{x}_i d\boldsymbol{q}_i} \sim 1\,. \qquad (2.2)$$

Here, Λ is the Landau pole of QCD which serves as a generic non-perturbative scale. In factorisation theorems it is used as the order of magnitude of hadronic scales. Q is a characteristic hard scale of the process.

The relation (2.1) however does not strictly imply that DPS cross sections for collinear DPDs are always negligible. A very famous and deeply studied example is the production of two W-bosons with the same charge [51,52,83,84]. There, the hard process involving only the two partons from SPS is suppressed by coupling constants compared to the two hard scatterings of DPS, as shown in figure 2.1. Another example is the behaviour of double parton distributions at small x, where they are expected to grow proportional to squared single parton distributions and thus may compensate the Λ^2/Q^2 suppression.

2.1.1 Factorisation

Factorisation proofs for SPS were mainly developed in the 1980's. We base our framework on the approach developed in [7,8] and in an updated form in [85]. Due to the immense progress made in [57–60], DPS factorisation today is on the same level as for SPS. In this section, we give a rough summary of the current status of the DPS factorisation proof (with close analogies to the SPS case).

The main obstacle when describing the collision of two hadrons, i.e. bound states of the strong interaction, is the presence of both a perturbative high energy scale Q

and non-perturbative scale Λ of the order of the hadronic mass. Factorisation aims to solve this issue by describing a physical observable, like the cross section or a structure function, with an approximation that only takes contributions into account which are not power suppressed in Λ/Q.

These contributions inside a general Feynman graph, the so-called leading regions, can be found by power-counting, e.g. with the help of the Libby-Sterman analysis [86,87]. One finds that they are characterised by momenta being either hard, soft or collinear with respect to the proton's momentum. We give vectors in Minkovski space v^μ in terms of light-cone coordinates $v^\pm = (p^0 \pm p^3)/\sqrt{2}$ and the according transverse momentum $\boldsymbol{v}$,

$$v^\mu = (v^+, v^-, \boldsymbol{v}). \tag{2.3}$$

The rationale behind this along with important identities can be found in appendix B of [85]. Here and in the following we choose a frame where the protons move along the z-axis, thus

$$p^\mu = (p^+, 0, \boldsymbol{0}) \tag{2.4}$$

for a right-moving proton. The momentum of the left-moving proton has only a non-vanishing minus-component. In this notation, the momenta inside the leading regions are of order

$$
\begin{aligned}
\ell^\mu_{\text{hard}} &\propto (Q, Q, Q), \\
\ell^\mu_{\text{right-collinear}} &\propto (Q, \Lambda^2/Q, \Lambda), \\
\ell^\mu_{\text{left-collinear}} &\propto (\Lambda^2/Q, Q, \Lambda).
\end{aligned}
\tag{2.5}
$$

All components of soft momenta are either of order Λ or Λ^2/Q. Apparently, the collinear and soft factors lie in the non-perturbative region of QCD and thus can only be given in terms of matrix elements. In contrast, there is a perturbative expansion of the hard factor, often called the partonic cross section, as it describes the interactions of high-energy partons. Factorisation is then proven by showing that these regions decouple from each other. In order to do so, a variety of steps have to be made beforehand:

Kinematic approximations are applied to the momenta given above, mainly setting negligible components to zero. This greatly simplifies scalar products, which then can be approximated by the simple product of certain components. An especially important aspect is the Grammer-Yennie approximation [88], which allows for an insertion of a momentum between a product of region factors. For example, the expression of a gluon with momentum l flowing from a collinear factor C for a right- or left-moving proton into the hard factor H can be modified to

$$C_\mu(\tilde{l})\, H^\mu(l) \approx C_\mu(l)\, \frac{v_C^\mu}{l \cdot v_C + i\epsilon}\, \tilde{l}_\nu\, H^\nu(\tilde{l}). \tag{2.6}$$

The rationale behind v_C will be explained in section 2.2.2. $\tilde{l}$ is the hard approximation of l, where only the component of order Q is taken to be non-zero. The same kind of approximation is possible for the product of collinear and soft factors. In the form of

the right-hand side, Ward identities can be applied to absorb an arbitrary number of exchanged soft gluons flowing from the soft factor to the collinear factors and collinear gluons with an unphysical polarisation emerging from the collinear factors and entering the hard factor. In a gauge theory, both types of exchanges between leading regions are not power-suppressed. At all orders, this gives rise to Wilson lines (2.20) inside collinear and soft factor. This decoupling of soft and collinear gluons was derived in [60] for the case of DPS.

Soft gluons inside the Glauber region, whose momenta fulfil

$$\ell^\mu_{\text{Glauber}} \propto (\Lambda^2/Q, \Lambda^2/Q, \Lambda)\,, \tag{2.7}$$

spoil the Grammer-Yennie approximation for gluons between the soft and collinear factor. Here, the transverse contributions to a scalar product between hard and soft momenta are comparable to the collinear ones and therefore (2.6) is not justified anymore. To ensure that, nevertheless, factorisation is valid, one thus has to proof that Glauber gluons do not contribute to the soft factor at all orders in perturbation theory by showing that their contributions cancel in the sum over all graphs or by rooting the integration contour around this region in the complex plane. For double Drell-Yan scattering, this was done in [59]. Note that both for SPS and DPS it was possible to prove Glauber gluon cancellation only for colourless final states. Proofs for products with a non-trivial colour structure are still to be determined.

Subtractions of the hard and collinear factors are necessary to avoid double counting of soft and collinear momenta. Section 10.1 of [85] gives a detailed introduction into the subtraction procedure by Collins that builds on a recursive subtraction of smaller regions from larger ones. In general, two kinds of divergences appear: UV divergences which are handled by renormalisation factors that subtract energy regions in which partons are far off-shell, whereas rapidity divergences come from kinematical configurations with much larger rapidities than in the physical process. The latter ones are subtracted by combining the soft factor with the collinear ones. This leaves the hard and collinear factors, i.e. the partonic cross sections and the parton distributions functions, as the two building blocks of the complete hadronic cross section, which will be discussed in more detail in the next section. Renormalisation and subtraction are discussed in detail in section 2.2.2.

The double counting conflict between SPS and DPS on the level of hadronic cross sections is a novel feature of DPS factorisation. A solution to this problem is the Diehl-Gaunt-Schönwald scheme [57]. We will see its impact in the following section.

2.1.2 The DPS cross section

As for SPS, one of the main results of factorisation is the cross section of a DPS process in terms of the hard scattering cross sections $\hat{\sigma}_{ab}$ and the DPDs F_{ab}. The subscripts a and b are always reserved for (possibly polarised) parton flavours. We consider a proton-proton collision, where in the two hard processes (labelled by $i = 1, 2$) products with energies Q_i and transverse momenta $\boldsymbol{q}_i$ are produced. The final factorised cross section
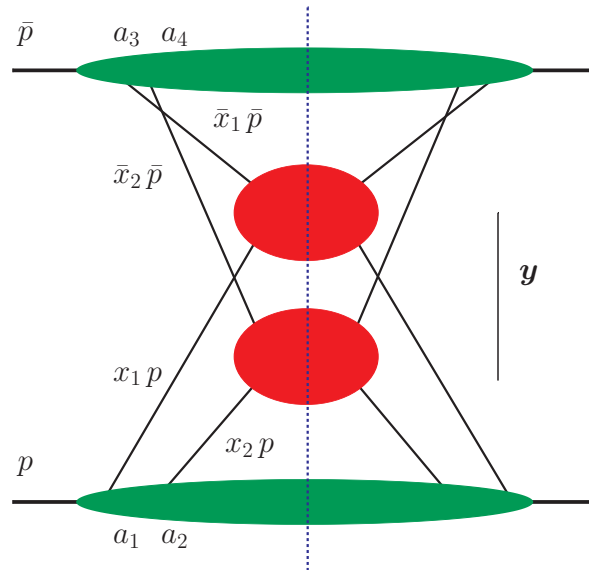
Figure 2.2: The factorised subtracted cross section for a double Drell-Yan process in a proton-proton collision with momenta p and $\bar{p}$. Green areas depict the parton distributions and the red ones the hard partonic cross sections. The dashed line is the final state cut. Parton flavours a_i are set equal on both sides as we ignore interference distributions. Kinematic variables like x_i and $\boldsymbol{y}$ also do not change in the complex conjugate amplitude. Further explanations can be found in the text.

separated into parton distributions and partonic cross sections is shown in figure 2.2. Translating it into an equation, we find

$$
\frac{\mathrm{d}\sigma_{\mathrm{DPS}}}{\mathrm{d}x_i \mathrm{d}\bar{x}_i d\boldsymbol{q}_i} = \frac{1}{C}\,\hat{\sigma}^{(1)}(Q_1,\mu_1)\,\hat{\sigma}^{(2)}(Q_2,\mu_2)\int\frac{\mathrm{d}^2\boldsymbol{z}_1}{2\pi^2}\frac{\mathrm{d}^2\boldsymbol{z}_1}{2\pi^2}\,e^{-i(\boldsymbol{q}_1\cdot\boldsymbol{z}_1+\boldsymbol{q}_2\cdot\boldsymbol{z}_2)}
$$
$$
\times \int \mathrm{d}^2\boldsymbol{y}\,\Phi(y_+\nu)\,\Phi(y_-\nu)\,F(x_i,\boldsymbol{z}_i,\boldsymbol{y},\mu_i,\zeta)\,F(\bar{x}_i,\boldsymbol{z}_i,\boldsymbol{y},\mu_i,\bar{\zeta}) \qquad (2.8)
$$

for DTMDs and

$$
\frac{\mathrm{d}\sigma_{\mathrm{DPS}}}{\mathrm{d}x_i \mathrm{d}\bar{x}_i} = \frac{1}{C}\int\limits_{x_1}^{1-x_2}\frac{\mathrm{d}x_1'}{x_1'}\int\limits_{x_2}^{1-x_1'}\frac{\mathrm{d}x_2'}{x_2'}\int\limits_{\bar{x}_1}^{1-\bar{x}_2}\frac{\mathrm{d}\bar{x}_1'}{\bar{x}_1'}\int\limits_{\bar{x}_2}^{1-\bar{x}_1'}\frac{\mathrm{d}\bar{x}_2'}{\bar{x}_2'}
$$
$$
\times\,\hat{\sigma}^{(1)}(x_1'\bar{x}_1's,\mu_1)\,\hat{\sigma}^{(2)}(x_2'\bar{x}_2's,\mu_2)
$$
$$
\times \int \mathrm{d}^2\boldsymbol{y}\,\Phi^2(y\nu)\,F(x_i',\boldsymbol{y},\mu_i,\zeta)\,F(\bar{x}_i',\boldsymbol{y},\mu_i,\bar{\zeta}) \qquad (2.9)
$$

for collinear DPDs. The formulae given above contain the following ingredients:

* The double parton distributions F, which will be properly introduced in section 2.2, depend on the momentum fractions x_i ($\bar{x}_i$), $i = 1, 2$, for partons in a proton moving to the right (left). They can be expressed in terms of the hard scale of the partonic processes Q_i, the centre-of-mass rapidities Y_i of the two partonic systems, and the centre-of-mass energy of the proton-proton collision s via

$$
x_i = \frac{Q_i}{\sqrt{s}}\,e^{Y_i}\,, \qquad\qquad \bar{x}_i = \frac{Q_i}{\sqrt{s}}\,e^{-Y_i}\,, \qquad\qquad (2.10)
$$

such that

$$
Q_i = \sqrt{x_i\,\bar{x}_i\,s}\,. \qquad\qquad (2.11)
$$

In (2.8), the DTMD F also depends on the respective Fourier conjugate to the transverse momentum $\boldsymbol{z}_i$, whereas in the collinear case DPDs contain an integration over these variables with additional divergences. Renormalisation (via dimensional regularisation) and rapidity subtraction introduce additional scales μ_i as well as ζ ($\bar{\zeta}$) for a right- (left-) moving proton. The RGE scales μ_i are typically chosen to be of order of Q_i to avoid large logarithms in $\hat{\sigma}^{(i)}$. Typical choices for the rapidity variable will be discussed at the end of section 4.1. A detailed introduction to renormalised and subtracted DPDs is given in section 2.2.2.

* Due to the factorisation theorem, the partonic cross sections $\hat{\sigma}^{(i)}$, $i = 1, 2$, contain only momenta of order Q_i. In the case of collinear factorisation, final state radiations enable momentum fractions x_i' and $\bar{x}_i'$ which are larger than the original ones. This explains the convolution integrals in the first line of (2.9). Again, renormalisation is needed to subtract ultraviolet diverging parts, hence the dependence on μ_i.

∗ A genuine feature of DPS compared to SPS is the interpartonic transverse distance $\boldsymbol{y}$ between the two scattering events. As it is not observable, the overall cross section contains an integration over $\boldsymbol{y}$. The single hard scattering event is agnostic about this scale, but the DPDs, describing both partons at once, depend on it. These integrals inside the cross section are called DPD luminosities:

$$\mathcal{L}(x_i, \bar{x}_i, \mu_i, \zeta, \bar{\zeta}) = \int \mathrm{d}^2\boldsymbol{y}\, \Phi^2(y\nu)\, F(x_i, \boldsymbol{y}, \mu_i, \zeta)\, F(\bar{x}_i, \boldsymbol{y}, \mu_i, \bar{\zeta})\,, \tag{2.12}$$

and analogously for the transverse momentum dependent DPDs.

∗ The function Φ is part of the Diehl-Gaunt-Schönwald framework [57], which solves the double counting problem between DPS and SPS. In a more practical sense, it serves as a regulator for $1/y^2$ divergences occurring in cross sections at small interpartonic distances. It must fulfil $\Phi \to 0$ if $y \to 0$ and $\Phi \to 1$ for $y \to \infty$. The DGS scheme also introduces subtraction terms for luminosities that take care of the double counting between SPS and DPS in the region of $y \sim 1/\nu$. They will be discussed in section 4.3.4.

∗ The combinatorial factor C is equal to 1, unless the to hard scattering processes are identical, where we have $C = 2$ instead.

In the expressions above we glossed over several indices to make the notation more compact. DPDs and hard cross sections carry two indices that indicate the flavours of the two partons: The overall cross section thus contains a sum over all possible parton flavour configurations. Strictly speaking, also interference distributions between different flavours are possible. But, as they cannot couple to gluon distributions, which are in many applications considered as the numerically most important ones, they are neglected in this and many other works.

In addition, every DPD has four open colour indices, which can be reduced to an irreducible representation pair R_1R_2 of two indices, respectively. More details are given in section 2.2.1. In the case of collinear DPDs, the same is true for the according hard cross section. Here, real radiations in the final state are possible, which leads to a non-trivial colour structure. For DTMDs, final state radiations would knock the transverse momenta out off the allowed kinematic region. Hence, the colour indices of the hard cross sections can only be in the singlet representation.

A common approach to simplify the complex expression for the cross sections above is given by the so-called "DPS pocket formula". Much of the complexity in DPS comes from the correlations between the two partons. Ignoring them, and also assuming that the $\boldsymbol{y}$-dependence in the DPDs factorises, leads to

$$F_{a_1 a_2}(x_1, x_2, \boldsymbol{y}) \approx f_{a_1}(x_1)\, f_{a_2}(x_2)\, G(\boldsymbol{y})\,, \tag{2.13}$$

where $f_{a_i}(x_i)$ is an ordinary PDF or TMD. In this approximation the integration over $\boldsymbol{y}$ in (2.8) and (2.9) can be carried out, leading to two factorised SPS cross sections:

$$\sigma_{\mathrm{DPS}} \approx \frac{1}{C}\, \frac{\sigma_{\mathrm{SPS}}^{(1)}\, \sigma_{\mathrm{SPS}}^{(2)}}{\sigma_{\mathrm{eff}}}\,, \tag{2.14}$$
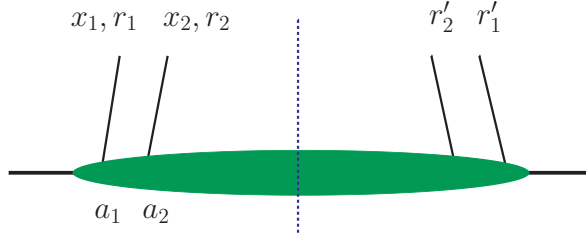
Figure 2.3: A DPD as a part of the full factorised cross section depicted in figure 2.2. Shown are the momentum fractions and flavours of the two partons as well as their colour indices in the amplitude and its complex conjugate on the right side of the final state cut.

with the effective cross section σ_{eff} as a normalisation factor. The procedure in experimental studies then is to extract σ_{eff} from measurements. However, this approximation becomes worse the more correlated the two partons become. Additionally, in certain regions of phase-space one crucial condition for DPS, $x_1 + x_2 < 1$, gets violated by the pocket formula. Hence, it is not surprising that these studies find different values for σ_{eff} depending on the considered process, ranging from 2 to 25 mb [34–53]. In other words, these discrepancies in σ_{eff} for different processes serve as a measure for parton correlations.

2.2 Double parton distributions

In the following, we first discuss the definition of collinear DPDs with a special focus on the colour degrees of freedom (section 2.2.1), and after that their subtraction and renormalisation procedure (section 2.2.2). After that, in section 2.2.3, a small discussion of DTMDs is added.

2.2.1 Definition

Operator definition. Figure 2.3 shows a DPD which emerges from the factorised cross section in figure 2.2 and eqs. (2.8) and (2.9). An unrenormalised and unsubtracted DTMD for (polarised or unpolarised) partons a_1 and a_2 in a right-moving proton is defined as

$$F_{B,\text{us},a_1 a_2}^{r_1 r_2}(x_i, \boldsymbol{z}_i, \boldsymbol{y}, v_L)$$
$$= 2p^+ (x_1 p^+)^{-n_1} (x_2 p^+)^{-n_2} \int dy^- \frac{dz_1^-}{2\pi} \frac{dz_2^-}{2\pi} e^{i(x_1 z_1^- + x_2 z_2^-)p^+}$$
$$\times \langle p| \mathcal{O}_{a_1}^{r_1}(y, z_1, v_L) \mathcal{O}_{a_2}^{r_2}(0, z_2, v_L) |p\rangle \,, \tag{2.15}$$

where $n_i = 0$ for (anti-)quarks and $n_i = 1$ for gluons. For its collinear counterpart we have

$$
\begin{aligned}
F_{B,\mathrm{us},a_1 a_2}^{r_1 r_2}&(x_i, \boldsymbol{y}, v_L) \\
&= 2p^+ (x_1 p^+)^{-n_1} (x_2 p^+)^{-n_2} \int \mathrm{d}y^- \frac{\mathrm{d}z_1^-}{2\pi} \frac{\mathrm{d}z_2^-}{2\pi} \, e^{i(x_1 z_1^- + x_2 z_2^-)p^+} \\
&\quad \times \langle p| \, \mathcal{O}_{a_1}^{r_1}(\boldsymbol{y}, z_1, v_L) \, \mathcal{O}_{a_2}^{r_2}(0, z_2, v_L) \, |p\rangle \Big|_{y^+ = z_1^+ = z_2^+ = 0, \; \boldsymbol{z}_1 = \boldsymbol{z}_2 = 0}.
\end{aligned}
\tag{2.16}
$$

Note that setting $\boldsymbol{z}_i$ to zero corresponds to an integral over $\boldsymbol{q}_i$ in Fourier space. The operators used in the matrix elements in (2.15) and (2.16) are

$$
\mathcal{O}_a^r(y, z, v_L) = \bar{q}_{s'}(y - \tfrac{1}{2}z) \, W_{s'r'}^\dagger (y - \tfrac{1}{2}z, v_L) \, \Gamma_a \, W_{rs}(y + \tfrac{1}{2}z, v_L) \, q_s(y + \tfrac{1}{2}z)
\tag{2.17}
$$

for a quark,

$$
\mathcal{O}_a^r(y, z, v_L) = -\bar{q}_s(y + \tfrac{1}{2}z) \, W_{sr}^\dagger (y + \tfrac{1}{2}z, v_L) \, \Gamma_a \, W_{r's}(y - \tfrac{1}{2}z, v_L) \, q_s(y - \tfrac{1}{2}z)
\tag{2.18}
$$

for an antiquark and

$$
\mathcal{O}_a^r(y, z, v_L) = \Pi_a^{jj'} \, G_{s'}^{+j'} (y - \tfrac{1}{2}z) \, W_{s'r'}^\dagger (y - \tfrac{1}{2}z, v_L) \, W_{rs}(y + \tfrac{1}{2}z, v_L) \, G_s^{+j}(y + \tfrac{1}{2}z)
\tag{2.19}
$$

for a gluon, all with arbitrary parton polarisation. Wilson lines are defined as

$$
W_{rs}(\xi, v) = \mathcal{P} \exp\left\{ -ig \, t_{rs}^b \int_0^\infty ds \, v \cdot A^b(\xi + sv) \right\},
\tag{2.20}
$$

where $\mathcal{P}$ denotes path-ordering of the gluon fields along the direction v. The generators of $SU(3)$, t^b, can be in the fundamental or adjoint representation, depending on the parton type. Γ_a ($\Pi_a^{jj'}$) is a spin projector for a quark (gluon):

$$
\Gamma_q = \frac{1}{2}\gamma^+, \qquad \Gamma_{\Delta q} = \frac{1}{2}\gamma^+\gamma^5, \qquad \Gamma_{\delta q}^i = \frac{1}{2}\sigma^{i+}\gamma^5,
\tag{2.21}
$$

and

$$
\Pi_g^{jj'} = \delta^{jj'}, \qquad \Pi_{\Delta g}^{jj'} = i\epsilon^{jj'}, \qquad \Pi_{\delta g}^{jj',ii'} = \tau^{jj',ii'}.
\tag{2.22}
$$

We write a bare index q and g for unpolarised partons. A longitudinally polarised parton is denoted with a leading Δ. The indices (i, i') are the spatial indices for a transversely polarised parton δq or δg. $\tau^{jj',ii'}$ is traceless and antisymmetric in (jj') and (ii'), which leaves two transverse dimensions. Antiquark projectors are identical to the ones for quarks, except for

$$
\Gamma_{\Delta\bar{q}} = -\Gamma_{\Delta q}.
\tag{2.23}
$$

Colour projectors. Every colour tensor that is an overall singlet can be projected onto irreducible representations in colour space in a particular way that will explained below. Among others, amplitudes, e.g. DPDs, meet this condition, as there is no net colour flow across the final state cut allowed.

We use the same conventions as in section 4.1 of [58]. They are based on early work on the correlation structure of DPS [13]. Note however that both publications are incomplete as certain projectors where overlooked completely. This was discussed in detail in the erratum I of [58].

One can project DPDs onto different sets of representations. In the "s-channel", the two indices on the left and right side of the final state cut are coupled to a product representation, respectively. In these representations, DPDs before renormalisation can be interpreted as probability densities [27]. Manifest decoupling in evolution equations (cf. section 2.2.2) can only be achieved in the "t-channel", where we couple an index with its complex conjugate partner on the right side of the cut. The relevant decompositions in the t-channel are [89]

$$3 \otimes \overline{3} = 1 \oplus 8 \tag{2.24}$$

for a quark-antiquark pair and

$$8 \otimes 8 = 1 \oplus A \oplus S \oplus 10 \oplus \overline{10} \oplus 27 \tag{2.25}$$

for a gluon-gluon pair. In the s-channel, we additionally have

$$3 \otimes 3 = \overline{3} \oplus 6 \,, \tag{2.26}$$

$$3 \otimes 8 = 3 \oplus \overline{6} \oplus 15 \,. \tag{2.27}$$

For pairs of partons, the irreducible representations are then be combined to pairs as well. From now on, arbitrary representations will be denoted by R. One can decompose an arbitrary colour tensor in t-channel representation space,

$$M^{\underline{r}\,\underline{s}} = \sum_{RR'} \frac{1}{m(R)} \left(P^{\underline{t}\,\underline{u}}_{\overline{R}\,\overline{R}'} M^{\underline{t}\,\underline{u}} \right) P^{\underline{r}\,\underline{s}}_{RR'} \,. \tag{2.28}$$

The multiplicity $m(R)$ gives the number of degrees of freedom of R and is defined in (B.17). The colour index pairs $\underline{r}$ and $\underline{s}$, fundamental or adjoint, are a combination of a parton and its complex conjugate in the squared amplitude, $\underline{r} = rr'$. We will use consecutive letters, sometimes with indices, in a similar way. The projectors[1] $P^{\underline{r}\,\underline{s}}_{R\overline{R}'}$ couple the representation pair $R\overline{R}'$ to an overall colour singlet. A necessary condition for this is that their respective multiplicities are equal, $m(R) = m(\overline{R}')$. The explicit expressions for all projectors as well as the most important identities are given in appendix B.1.

Notice that in the decompositions (2.24) to (2.27) the product of a representation with its charge conjugated counterpart produces the contribution of a singlet representation. A projection onto this representation corresponds to summing and averaging over

---

[1]As it is explained at the end of appendix B.1, not every tensor $P^{\underline{r}\,\underline{s}}_{R\overline{R}'}$ is a projector in a mathematical sense. For the sake of simplicity, we will nevertheless stick to this naming convention.

all colour indices, as can be read off eq. (B.1). Colour singlet DPDs thus describe partons which are uncorrelated in their colour degrees of freedom, while colour correlated DPDs are in colour non-singlet representations. Since parton distributions in SPS cannot be correlated in the parton colour, the characteristic equations described in section 2.2.2 for colour singlet DPDs and PDFs coincide.

The following manipulations are possible regardless of whether the DPD is unsubtracted and/or unrenormalised. Thus, we drop both labels in the following. Applying the colour expansion (2.28) to $F_{a_1a_2}^{r_1r_2}$, we can introduce representation dependent DPDs $^{R_1R_2}F_{a_1a_2}$ via

$$F_{a_1a_2}^{r_1r_2} = \sum_{R_1,R_2} \frac{1}{\epsilon(R_1)\,\epsilon(R)} \frac{1}{\mathcal{N}_{a_1}\mathcal{N}_{a_2}} \frac{1}{\sqrt{m(R_1)}} \, {}^{R_1R_2}F_{a_1a_2}\, P_{R_1R_2}^{r_1r_2}\,, \qquad (2.29)$$

where

$$\epsilon(R) = \begin{cases} i & \text{if } R = A \\ 1 & \text{otherwise} \end{cases} \qquad (2.30)$$

and

$$\mathcal{N}_a = \begin{cases} \sqrt{N^2-1} & \text{if } a \text{ is a gluon} \\ \sqrt{N} & \text{otherwise} \end{cases} \,. \qquad (2.31)$$

These prefactors ensure that $^{R_1R_2}F_{a_1a_2}$ is real-valued and $^{11}F_{a_1a_2}$ contains a sum over parton colours. From (2.29) one can deduce that

$$^{R_1R_2}F_{a_1a_2} = \epsilon(R_1)\,\epsilon(R_2)\,\mathcal{N}_{a_1}\mathcal{N}_{a_2}\,\frac{1}{\sqrt{m(R_1)}}\,P_{\overline{R_1}\,\overline{R_2}}^{r_1r_2}\,F_{a_1a_2}^{r_1r_2}\,. \qquad (2.32)$$

DPDs projected onto s-channel representations will be denoted by a trailing instead of a leading superscript, $F_{a_1a_2}^{R_1R_2}$. The matrices for linear transformations between s- and t-channel DPDs are given in appendix B.2.

Short distance matching. In the limit of small y, DPDs arise through perturbative splitting of SPS distributions,

$$^{R_1R_2}F_{a_1a_2}(x_i,\boldsymbol{y},\mu,\zeta) = \frac{1}{\pi y^2} \int\limits_{x_1+x_2}^{1} \frac{\mathrm{d}z}{z^2} \, {}^{R_1R_2}V_{a_1a_2,a_0}\left(\frac{x_1}{z},\frac{x_2}{z},y,\mu,\zeta\right) f_a(z,\mu)\,, \qquad (2.33)$$

where the matching kernels $^{R_1R_2}V$ can be calculated perturbatively. This formula holds for subtracted and renormalised DPDs that are discussed in section 2.2.2. Transverse momentum dependent distributions are connected in a similar way. [90] contains a NLO calculation for the colour singlet, while in [91] NLO matching coefficients are calculated in all non-singlet representations. A scheme for massive quarks is developed in [92].

2.2.2 Subtraction and Renormalisation

Subtraction. Wilson lines (2.20) in the DPD and the soft factor exhibit rapidity divergences in the limit of light-like directions v. In this section, we use the Collins regulator [85] to deal with these divergences, as it is one of the most intuitive ones. In section 3.2, also the δ regulator [93,94] will appear. It is worth noting that it was shown in [95] that both regulators are equivalent.

In the Collins scheme, the directions v_L (v_R) in Wilson lines appearing in right- (left-) moving proton are chosen to be space-like. The rapidities

$$Y_{L,R} = \frac{1}{2} \log \left| \frac{v_{L,R}^+}{v_{L,R}^-} \right| \tag{2.34}$$

serve as regulators in the limit of light-like directions of the Wilson lines, i.e. when $Y_L \to -\infty$ or $Y_R \to \infty$.

The fact that the soft factor is diagonal in representation space is a tremendous simplification compared to the transverse momentum dependent case, where the subtraction mechanism involves matrix multiplications and inversions [58]. Here, a simple division is sufficient to subtract the rapidity divergences in the DPD for a right-moving proton[2]:

$$^{R_1 R_2}F_{B,a_1 a_2}(x_i, \boldsymbol{y}, Y_C) = \lim_{Y_L \to -\infty} \frac{1}{\sqrt{^{R_1}S_B(2(Y_C - Y_L))}} {}^{R_1 R_2}F_{B,\text{us},a_1 a_2}(x_i, \boldsymbol{y}, Y_L). \tag{2.35}$$

R_1 and R_2 have the same multiplicity, thus $^{R_2}S = {}^{R_1}S$. For $R_1 = 1$, the soft factor is is unity and so $^{11}F_B$ coincides with $^{11}F_{B,\text{us}}$. Due to boost invariance, Y_C can enter $^R F_B$ only in a combination with a momentum, namely

$$\zeta = (p^+)^2 e^{-2Y_C} \tag{2.36}$$

for right-moving and

$$\bar{\zeta} = (\bar{p}^-)^2 e^{2Y_C} \tag{2.37}$$

for a left-moving proton. Their product evaluates to

$$\zeta \bar{\zeta} = 4(p^+ \bar{p}^-)^2 = s^2, \tag{2.38}$$

where $\sqrt{s}$ is the center of mass energy of the proton-proton process. Because $p^+ \propto e^{Y_p}$, where Y_p is the rapidity of the proton, ζ and $\bar{\zeta}$ depend on a rapidity difference and are therefore invariant under boosts along the collinear direction. The rapidity regulators Y_L and Y_R enter the unsubtracted DPDs in a similar way. Note that this definition is different from the predominant convention used for TMDs, where the ζ variable is defined with respect to partonic momenta instead. For DPDs, this would however lead to rescaling factors inside DPDs. With this choice, only the rapidity arguments of

---

[2] For this formula to hold, it is crucial that the soft factor can be decomposed into a left- and right-moving part. This is only an assumption, both in single and double parton factorisation.

partonic quantities need to be rescaled since they can only depend on partonic momenta $x_i p^+$.

The subtracted DPDs depend on ζ via a Collins-Soper (CS) equation,

$$\frac{\partial}{\partial \log \zeta} {}^{R_1 R_2} F_{B, a_1 a_2}(x_i, \boldsymbol{y}, \zeta) = \frac{1}{2} {}^{R_1} J_B(\boldsymbol{y}) {}^{R_1 R_2} F_{B, a_1 a_2}(x_i, \boldsymbol{y}, \zeta) \,. \tag{2.39}$$

The CS kernel ${}^R J_B$ is renormalised additively,

$$ {}^R J(\boldsymbol{y}, \mu_i) = {}^R J_B(\boldsymbol{y}) + {}^R \Lambda(\mu_1) + {}^R \Lambda(\mu_2), \tag{2.40}$$

where

$$\frac{\mathrm{d}}{\mathrm{d} \log \mu} {}^R \Lambda(\mu) = - {}^R \gamma_J(\mu) \tag{2.41}$$

and

$$\frac{\mathrm{d}}{\mathrm{d} \log \mu_i} {}^R J(y, \mu_1, \mu_2) = - {}^R \gamma_J(\mu_i) \,. \tag{2.42}$$

We expand ${}^R \gamma_J$ and every other anomalous dimension in the following way:

$$ {}^R \gamma_J(\mu) = \sum_{n=1}^{\infty} a_s^n(\mu) \, {}^R \gamma_J^{(n-1)} \,. \tag{2.43}$$

After renormalisation, the CS equation becomes

$$\frac{\partial}{\partial \log \zeta} {}^{R_1 R_2} F_{a_1 a_2}(x_i, \boldsymbol{y}, \mu_i, \zeta) = \frac{1}{2} {}^{R_1} J(\boldsymbol{y}, \mu_i) {}^{R_1 R_2} F_{a_1 a_2}(x_i, \boldsymbol{y}, \mu_i, \zeta) \,. \tag{2.44}$$

Renormalisation. By setting $\boldsymbol{z}_i = 0$, additional UV divergences arise in the collinear operators (2.17) to (2.19) between otherwise spatially separated Wilson lines. As a consequence, these objects need to be renormalised as a whole, leading to two renormalisation scales μ_1 and μ_2 inside a DPD. For the same reason, renormalisation factors depend on parton momenta and the renormalisation contains a Mellin convolution instead of an ordinary multiplication. Hence, we obtain

$$ {}^{R_1 R_2} F_{a_1 a_2}(x_i, \boldsymbol{y}, \mu_i, \zeta) = \sum_{\substack{b_1, b_2, \\ R', R''}} {}^{R_1 \overline{R}'} Z_{a_1 b_1}(x_1', \mu_1, x_1^2 \zeta) \underset{x_1}{\otimes} {}^{R_2 \overline{R}''} Z_{a_2 b_2}(x_2', \mu_2, x_2^2 \zeta) $$

$$ \underset{x_2}{\otimes} {}^{R' R''} F_{B, b_1 b_2}(x_i', \boldsymbol{y}, \zeta) \,, \tag{2.45}$$

using the definition

$$ A\big(x', s_A(x, x')\,\zeta\big) \underset{x}{\otimes} B\big(x', s_B(x, x')\,\zeta\big) = \int_x^1 \frac{dx'}{x'} A\big(x', s_A(x, x')\,\zeta\big) B\left(\frac{x}{x'}, s_B\left(x, \frac{x}{x'}\right)\zeta\right) $$

$$ \tag{2.46}$$

for the Mellin convolution. As defined in (2.36) the rapidity variable is defined with respect to protonic momenta, $\zeta \propto (p^+)^2$. Hence, in eq. (2.45) we need to rescale it by x_i^2 inside the renormalisation factors which are defined with respect to partonic quantities. In (2.46) the definition of the ordinary Mellin transform used in PDF and colour singlet DPD evolution is expanded to also include the treatment of the rapidity variable. With this convention the convolution is commutative,

$$A\big(x', s_A(x, x')\,\zeta\big) \underset{x}{\otimes} B\big(x', s_B(x, x')\,\zeta\big) = B\big(x', s_B(x, x')\,\zeta\big) \underset{x}{\otimes} A\big(x', s_A(x, x')\,\zeta\big), \quad (2.47)$$

and has the unity element

$$\delta(1 - x') \underset{x}{\otimes} B\big(x', s_B(x, x')\,\zeta\big) = B\big(x, s_B(x, x)\,\zeta\big). \quad (2.48)$$

However, the additional rapidity variable inhibits associativity:

$$\left[A(x'', x^2\zeta) \underset{x'}{\otimes} B(x'', x''^2 x^2\zeta/x'^2) \right] \underset{x}{\otimes} C(x', \zeta)$$
$$= A(x', x^2\zeta) \underset{x}{\otimes} \left[B(x'', x'^2\zeta) \underset{x'}{\otimes} C(x'', \zeta) \right]. \quad (2.49)$$

Generic DGLAP splitting kernels are implicitly defined by the scale evolution of renormalisation factors:

$$\frac{\mathrm{d}}{\mathrm{d}\log\mu}{}^{RR'}Z_{ab}(x, \mu, \zeta) = 2 \sum_{c,R''} {}^{R\overline{R}''}P_{ac}(x', \mu, \zeta) \underset{x}{\otimes} {}^{R''R'}Z_{cb}\big(x', \mu, x'^2\zeta/x^2\big), \quad (2.50)$$

where the rapidity scaling factor inside ${}^{RR'}Z$ can be derived by taking the RGE derivative on both sides of eq. (2.45) and then making use of (2.49). The factor of 2 on the right-hand side of (2.50) is purely conventional. We expand DGLAP kernels analogously to anomalous dimensions, see (2.43):

$$^{RR'}P_{ab}(x, \mu, \zeta) = \sum_{n=1}^{\infty} a_s^n(\mu)\, {}^{RR'}P_{ab}^{(n-1)}(x, \zeta/\mu^2), \quad (2.51)$$

Representation dependent DGLAP kernels are connected with their counterparts with open colour indices in an expansion as defined in eq. (2.28),

$$P_{ab}^{r\,s}(x, \mu, \zeta) = \sum_{RR'} \frac{\epsilon(R')\,\mathcal{N}_b}{\epsilon(R)\,\mathcal{N}_a}\, {}^{R_1 R'}P_{ab}(x, \mu, \zeta)\, P_{RR'}^{r\,s}, \quad (2.52)$$

and so

$$^{RR'}P_{ab}(x, \mu, \zeta) = \frac{\epsilon(R)\,\mathcal{N}_a}{\epsilon(R')\,\mathcal{N}_b} \frac{1}{m(R)} P_{\overline{R}_1\overline{R}'}^{r\,s}\, P_{ab}^{r\,s}(x, \mu, \zeta). \quad (2.53)$$

$\epsilon(R)$, $\mathcal{N}_a$ and $m(R)$ are defined in (2.30), (2.31), and (B.17), respectively. The DGLAP equation of a representation dependent DPD then is

$$\frac{\mathrm{d}}{\mathrm{d}\log\mu_1}{}^{R_1 R_2}F_{a_1 a_2}(x_i, \mu_i, \zeta) = 2 \sum_{b,R'} {}^{R_1 \overline{R}'}P_{a_1 b}(x_1', \mu_1, x_1^2\zeta) \underset{x_1}{\otimes} {}^{R'R_2}F_{ba_2}(x_1, x_2, \mu_i, \zeta). \quad (2.54)$$

Note the rapidity dependence of the DGLAP kernels. We will further examine this equation in section 2.3.

The mixed symmetric/anti-symmetric projectors are a product of the two colour tensor d^{abc} and f^{abc}, whereby the first one is symmetric and the second one anti-symmetric under charge conjugation. Hence,

$$^{SA}P_{gg} = {}^{AS}P_{gg} = 0 \,. \tag{2.55}$$

The behaviour under charge conjugation also directly yields

$$^{10\,\overline{10}}P_{gg} = {}^{\overline{10}\,10}P_{gg} \,. \tag{2.56}$$

Both relations hold to all orders and in all polarisations.

Sum rules   Taking the first and second Mellin moment of PDFs yields sum rules that these distributions have to fulfil,

$$\int_0^1 \mathrm{d}x f_{q_v}(x,\mu) = N_{q_v} \,, \tag{2.57}$$

$$\sum_a \int_0^1 \mathrm{d}x x f_a(x,\mu) = 1 \,. \tag{2.58}$$

N_{q_v} stands for the number of valence quarks of flavour q in the proton. These sum rules correspond to fully integrated PDF operators, eqs. (2.17) to (2.19), that resemble conserved currents of the QCD Lagrangian, namely flavour number and momentum conservation. Sum rules for colour singlet DPDs become more involved but follow the same rationale [96].

Taking the RGE derivative of both side of (2.57) and (2.58) yields the following identities for the DGLAP kernels:

$$\int_0^1 \mathrm{d}x \, {}^{11}P^-(x,\mu) = 0 \,, \tag{2.59}$$

$$\int_0^1 \mathrm{d}x \left({}^{11}P_{qq}(x,\mu) + {}^{11}P_{gq}(x) \right) = 0 \,, \tag{2.60}$$

$$\int_0^1 \mathrm{d}x \left({}^{11}P_{qg}(x,\mu) + {}^{11}P_{gg}(x) \right) = 0 \,, \tag{2.61}$$

where the linear combination P^- is defined in (2.93). Note that projecting a fully integrated PDF operator onto a specific colour representation does not lead to a conserved current. Thus, there is no equivalent to these sum rules in the colour non-singlet sector.

2.2.3 Transverse momentum dependent distributions

For the sake of completeness, we also give an overview over DTMDs, defined in eq. (2.15). Their CS evolution equation reads

$$\frac{\partial}{\partial \log \zeta}\, {}^{R_1 R_2}F_{a_1 a_2}(x_i, \boldsymbol{y}, \boldsymbol{z}_i, \mu_i, \zeta) = \frac{1}{2} \sum_{R_1', R_2'} {}^{R_1 R_2 \overline{R}_1' \overline{R}_2'}K_{a_1 a_2}(\boldsymbol{z}_i, \boldsymbol{y}, \mu_i)$$
$$\times\, {}^{R_1' R_2'}F_{a_1 a_2}(x_i, \boldsymbol{z}_i, \mu_i, \zeta)\,, \qquad (2.62)$$

where

$$\frac{\mathrm{d}}{\mathrm{d} \log \mu_1}\, {}^{R_1 R_2 R_1' R_2'}K_{a_1 a_2}(\boldsymbol{z}_i, \boldsymbol{y}, \mu_i) = -\, \delta_{R_1 \overline{R}_1'}\, \delta_{R_2 \overline{R}_2'}\, \gamma_{K,a_1}(\mu_1)\,, \qquad (2.63)$$

and equivalently for a_2. As in the collinear case, eq. (2.72), the ζ dependence inside the DTMDs can be made explicit by solving the CS equation, which gives rise to exponentiated Sudakov single and double logarithms.

The divergent part of the CS kernel $^{\cdots}K_{B,a_1 a_2}$ has no colour dependence since in DTMDs UV divergences only occur in operator products that are separated by a finite distance $\boldsymbol{z}_i$, cf. eq. (2.15). These products can be renormalised independently from one another such that their product colour representation is irrelevant. $^{\cdots}K_{a_1 a_2}$ thus shares the anomalous dimension $\gamma_{K,a}$ with its single parton TMD analogue K_a.

There is a fascinating connection between single and double parton distributions, namely the equality between gluon TMD and DPD octet soft factor [28]. As a relation on the level of Wilson lines it is a non-perturbative statement. Transferring it to the corresponding CS kernels yields

$$^{8}J(\boldsymbol{y}, \mu, \mu) = K_g(\boldsymbol{y}, \mu)\,. \qquad (2.64)$$

For the corresponding anomalous dimensions, this leads to

$$^{8}\gamma_J = \frac{1}{2}\gamma_{K,g}\,. \qquad (2.65)$$

The additional factor of $1/2$ on the right-hand side is due to the fact that ^{8}J depends on *two* RGE scales and K_g only on one.

The renormalisation of DTMDs is done in a multiplicative way,

$$\frac{\mathrm{d}}{\mathrm{d} \log \mu_1}\, {}^{R_1 R_2}F_{a_1 a_2}(x_i, \boldsymbol{y}, \boldsymbol{z}_i, \mu_i, \zeta) = \gamma_{F,a_1}(\mu_1, x_1^2 \zeta)\, {}^{R}F_{a_1 a_2}(x_i, \boldsymbol{y}, \boldsymbol{z}_i, \mu_i, \zeta)\,, \qquad (2.66)$$

where the cusp and non-cusp parts of the anomalous dimension are

$$\gamma_{F,a}(\mu, \zeta) = \gamma_a(\mu) - \frac{1}{2}\gamma_{K,a}(\mu) \log \frac{\zeta}{\mu^2}\,. \qquad (2.67)$$

Following the argument below eq. (2.46), the rapidity argument of $\gamma_{F,a}$ in (2.66) is rescaled with x_1^2. The anomalous dimension is colour independent and thus equal to the one for single parton TMDs.

DPDs and DTMDs are connected by a matching formula for small z,

$$
\begin{aligned}
{}^{R_1 R_2} F_{a_1 a_2}(x_1, & x_2, \boldsymbol{z}_1, \boldsymbol{z_2}, \boldsymbol{y}, \mu_i, \zeta) \\
&= \sum_{c,d,R_1',R_2'} {}^{R_1 \overline{R}_1'} C_{a_1 c}(x_1', \boldsymbol{z}, \mu_1, x_1^2 \zeta) \underset{x_1}{\otimes} {}^{R_2 \overline{R}_2'} C_{a_2 d}(x_2', \boldsymbol{z}, \mu_2, x_2^2 \zeta) \\
&\qquad \underset{x_2}{\otimes} {}^{R_1' R_2'} F_{cd}(x_1', x_2', \boldsymbol{y}, \mu_i, \zeta)\,,
\end{aligned}
\tag{2.68}
$$

which can be obtained from an operator product expansion. The colour singlet matching kernel $^{11}C_{ac}$ is identical to the one that connects single parton TMDs and PDFs, as it is the case for colour singlet kernels in PDF DGLAP evolution.

2.3 The colour non-singlet DGLAP equation

In section 2.2, we have introduced the definition, renormalisation and evolution of DPDs. Based on the erratum I of [58], we will develop an alternative prescription of DPDs to cope with their rapidity dependence in section 2.3.1. Then, in section 2.3.2, we introduce a basis that minimises mixing between different DPDs under DGLAP evolution. Section 2.3.3 describes how to change the number of active flavours when encountering threshold scales during evolution.

2.3.1 Treatment of rapidity dependence

Colour correlated DPDs evolve both with a CS equation (2.44) and a DGLAP equation (2.54), where both depends both on μ_i and ζ. Our goal in this section is to separate both dependencies by finding a representation in which, in contrast to (2.54), the DGLAP equation is rapidity independent.

By taking the $\log \zeta$ derivative of the DGLAP equation one can deduce the double logarithmic part of the splitting kernel which is governed by the anomalous dimension $^R\gamma_J$:

$$
\frac{\partial}{\partial \log \zeta} {}^{RR'} P_{ab}(x, \mu, \zeta) = -\frac{1}{4} \delta_{R_1 \overline{R}'} \, \delta_{ab} \, \delta(1-x) \, {}^R\gamma_J(\mu)\,.
\tag{2.69}
$$

This yields

$$
\begin{aligned}
{}^{RR'} P_{ab}(x, \mu, \zeta) &= {}^{RR'} \widehat{P}_{ab}(x) \\
&\qquad - \frac{1}{4} \delta_{R \overline{R}'} \, \delta_{ab} \, \delta(1-x) \, {}^R\gamma_J(\mu) \log \frac{\zeta}{\mu^2}\,,
\end{aligned}
\tag{2.70}
$$

with the starting condition

$$
{}^{RR'} \widehat{P}_{ab}(x) = {}^{RR'} P(x, \mu, \mu^2)\,.
\tag{2.71}
$$

Note that the rapidity dependence vanishes for colour singlet kernels since $^1\gamma_J = 0$. Eq. (2.70) can be seen as the equivalent of the decomposition into cusp and non-cusp anomalous dimension.

Following erratum I of [58], one can isolate the ζ dependence inside $^{R_1 R_2}F$,

$$^{R_1 R_2}F_{a_1 a_2}(x_i, \boldsymbol{y}, \mu_i, \zeta) = {}^{R_1}E(x_i, \mu_i, \zeta, \zeta_0)\, {}^{R_1 R_2}\widehat{F}_{a_1 a_2; \mu_{01}, \mu_{02}, \zeta_0}(x_i, \boldsymbol{y}, \mu_i)\,, \qquad (2.72)$$

where

$$^{R}E(x_i, \mu_i, \zeta, \zeta_0) = \exp\left\{ \frac{1}{2}\, {}^{R}J(\boldsymbol{y}, \mu_i) \log \frac{\zeta}{\zeta_0} - \sum_{i=0,1} \int_{\mu_{0i}}^{\mu_i} \frac{\mathrm{d}\mu}{\mu}\, {}^{R}\gamma_J(\mu) \log \frac{\sqrt{\zeta_0}}{\mu} \right\} \qquad (2.73)$$

are the resumed Sudakov logarithms. As ^{R}J contains logarithms in μ_i, we find both single and double logarithms inside the exponential. $^{R_1 R_2}\widehat{F}$ evolve like

$$\frac{\mathrm{d}}{\mathrm{d}\log\mu_1}\, {}^{R_1 R_2}\widehat{F}_{a_1 a_2; \mu_{01}, \mu_{02}, \zeta_0}(x_i, \boldsymbol{y}, \mu_i)$$
$$= 2 \sum_{b, R'} {}^{R_1 \overline{R}'}P_{a_1 b}(x_1', \mu_1, \mu_1^2) \underset{x_1}{\otimes} {}^{R' R_2}\widehat{F}_{b, a_2; \mu_{01}, \mu_{02}, \zeta_0}(x_1', x_2, \boldsymbol{y}, \mu_i)$$
$$- {}^{R_1}\gamma_J(\mu_1) \log x_1 \, {}^{R_1 R_2}\widehat{F}_{a_1 a_2; \mu_{01}, \mu_{02}, \zeta_0}(x_i, \boldsymbol{y}, \mu_i)\,, \qquad (2.74)$$

with the initial condition

$$^{R_1 R_2}\widehat{F}_{a_1 a_2; \mu_{01}, \mu_{02}, \zeta_0}(x_i, \boldsymbol{y}, \mu_i) = {}^{R_1 R_2}F_{a_1 a_2}(x_i, \boldsymbol{y}, \mu_0, \mu_0, \zeta_0)\,. \qquad (2.75)$$

With (2.74) we have found a DGLAP-like evolution equation that incorporates no rapidity dependence anymore. The additional term in the second line, which is absent in the colour singlet, leads to a qualitatively new behaviour which is discussed extensively in chapter 4.

2.3.2 Evolution basis

PDFs and DPDs mix under DGLAP evolution. For all active (anti-)quarks q_i ($\bar{q}_i$) and the gluon g we have

$$\frac{d}{d\log\mu_1}\, {}^{R_1 R_2}F_{a_1 a_2} = 2 \sum_{b, R'} {}^{R_1 \overline{R}'}P_{a_1 b} \underset{x_1}{\otimes} {}^{R' R_2}F_{b a_2}\,, \qquad (2.76)$$

where $a_1 = q_i, \bar{q}_i, g$, and b runs over all the active flavours. We will omit function arguments entirely in this section. All equations can be adapted for the evolution of the second parton a_2 in a straight-forward way.

Because QCD interactions do not depend on the electric charge, all DGLAP kernels are independent of the quark flavour q_i. This also allows us to apply the same decomposition to every pure quark kernel,

$$^{RR}P_{a_i b_j} = \delta_{ij}\, {}^{RR}P_{ab}^V + {}^{RR}P_{ab}^S\,, \qquad (2.77)$$

where $a, b = q$ or $\bar{q}$. Furthermore, we can use the behaviour under charge conjugation to reduce the number of independent kernels:

$$^{RR}P_{\bar{q}_i \bar{q}_j} = {}^{RR}P_{q_i q_j}\,, \qquad (2.78)$$

$$^{RR}P_{\bar{q}_i q_j} = {}^{RR}P_{q_i \bar{q}_j} \, , \tag{2.79}$$

$$^{RR'}P_{\bar{q}_i g} = \eta(R') \, {}^{RR'}P_{q_i g} \, , \tag{2.80}$$

$$^{RR'}P_{g\bar{q}_i} = \eta(R) \, {}^{RR'}P_{g q_i} \, , \tag{2.81}$$

where

$$\eta(R) = \epsilon^2(R) = \begin{cases} -1 & \text{if } R = A \\ 1 & \text{otherwise} \end{cases} \, . \tag{2.82}$$

This leaves

$$^{RR}P_{qq}^V \, , \qquad\qquad {}^{RR}P_{q\bar{q}}^V \, , \qquad\qquad {}^{RR}P_{qq}^S \, , \qquad\qquad {}^{RR}P_{q\bar{q}}^S \tag{2.83}$$

as the four independent pure quark kernels. The peculiarity for $R = A$ can be traced back to the fact that the structure constants f^{abc} contracted with gluon operators (i.e. gluon fields) are odd under charge conjugation, as it is shown in Appendix A of [91].

To minimise the number of coupled evolution equations, we change from the "parton basis"

$$\left({}^{R_1 R_2}F_{q_i a_2}, \, {}^{R_1 R_2}F_{\bar{q}_i a_2}, \, {}^{R_1 R_2}F_{g a_2} \right) \tag{2.84}$$

to the "evolution basis"

$$\left({}^{R_1 R_2}F_{\Sigma^\pm a_2}, \, {}^{R_1 R_2}F_{q_{ij}^\pm a_2}, \, {}^{R_1 R_2}F_{g a_2} \right) \, . \tag{2.85}$$

In the colour singlet sector, the corresponding linear combinations are well known [68, 69, 97]. Generalising them to arbitrary colour representations gives

$$^{R_1 R_2}F_{\Sigma^\pm a_2} = \sum_i {}^{R_1 R_2}F_{q_i^\pm a_2} = \sum_i \left({}^{R_1 R_2}F_{q_i a_2} \pm {}^{R_1 R_2}F_{\bar{q}_i a_2} \right) \, , \tag{2.86}$$

$$^{R_1 R_2}F_{q_{ij}^\pm a_2} = {}^{R_1 R_2}F_{q_i^\pm a_2} - {}^{R_1 R_2}F_{q_j^\pm a_2} \, . \tag{2.87}$$

The cross-talk between different distributions is then contained in the flavour singlet sector,

$$\frac{d}{d\log\mu_1} \begin{pmatrix} {}^{R_1 R_2}F_{\Sigma^+ a_2} \\ {}^{R_3 R_4}F_{g a_4} \end{pmatrix} = 2 \begin{pmatrix} {}^{R_1 R_1}P_{\Sigma^+\Sigma^+} & {}^{R_1 R_3}P_{\Sigma^+ g} \\ {}^{R_3 R_1}P_{g\Sigma^+} & {}^{R_3 R_3}P_{gg} \end{pmatrix} \underset{x_1}{\otimes} \begin{pmatrix} {}^{R_1 R_2}F_{\Sigma^+ a_2} \\ {}^{R_3 R_4}F_{g a_4} \end{pmatrix} \, ,$$
$$R_1 R_3 = 11, 8S \, , \tag{2.88}$$

$$\frac{d}{d\log\mu_1} \begin{pmatrix} {}^{8 R_2}F_{\Sigma^- a_2} \\ {}^{A R_4}F_{g a_4} \end{pmatrix} = 2 \begin{pmatrix} {}^{88}P_{\Sigma^-\Sigma^-} & {}^{8A}P_{\Sigma^- g} \\ {}^{A8}P_{g\Sigma^-} & {}^{AA}P_{gg} \end{pmatrix} \underset{x_1}{\otimes} \begin{pmatrix} {}^{8 R_2}F_{\Sigma^- a_2} \\ {}^{A R_4}F_{g a_4} \end{pmatrix} \, . \tag{2.89}$$

All the flavour non-singlet distributions evolve independently from one another,

$$\frac{d}{d\log\mu_1} {}^{11}F_{\Sigma^- a_2} = 2 \, {}^{11}P^- \underset{x_1}{\otimes} {}^{11}F_{\Sigma^- a_2} \, , \tag{2.90}$$

$$\frac{d}{d\log\mu_1} {}^{R_1 R_2}F_{q_{ij}^\pm a_2} = 2 \, {}^{R_1 R_1}P^\pm \underset{x_1}{\otimes} {}^{R_1 R_2}F_{q_{ij}^\pm a_2} \, , \quad R_1 = 1, 8 \, , \tag{2.91}$$

$$\frac{d}{d\log\mu_1} {}^{R_1 R_2}F_{gg} = 2 \, {}^{R_1 \bar{R}_1}P_{gg} \underset{x_1}{\otimes} {}^{R_1 R_2}F_{gg} \, , \quad R_1 R_2 = 10\overline{10}, \overline{10}10, 27 27 \, . \tag{2.92}$$

We have introduced the DGLAP kernels

$$^{RR}P^{\pm} = {}^{RR}P^V_{qq} \pm {}^{RR}P^V_{q\bar{q}}, \tag{2.93}$$

$$^{RR}P_{\Sigma^{\pm}\Sigma^{\pm}} = {}^{RR}P^{\pm} + n_f \left({}^{RR}P^S_{qq} \pm {}^{RR}P^S_{q\bar{q}} \right), \tag{2.94}$$

$$^{RR'}P_{\Sigma^{\pm}g} = 2 \, {}^{RR'}P_{q_i g}, \tag{2.95}$$

$$^{RR'}P_{g\Sigma^{\pm}} = {}^{RR'}P_{gq_i}. \tag{2.96}$$

There are no quarks in the higher-than-octet representations, hence the gluon evolves independently. The factor $\eta(A) = -1$ in eqs. (2.80) and (2.81) is the reason why the antisymmetric gluon distribution in the evolution equation (2.89) mixes with Σ^- instead of Σ^+.

The derivations above are possible regardless of whether the parton flavours are polarised or not. Longitudinally (transversely) polarised kernels are characterised by a Δ (δ) in front of the parton flavours, e.g. $P^V_{\Delta q \Delta q}$ ($P^V_{\delta q \delta q}$). Furthermore, we define

$$^{RR}P^{\pm}_{\Delta} = {}^{RR}P^V_{\Delta q \Delta q} \pm {}^{RR}P^V_{\Delta q \Delta \bar{q}}, \tag{2.97}$$

$$^{RR}P^{\pm}_{\delta} = {}^{RR}P^V_{\delta q \delta q} \pm {}^{RR}P^V_{\delta q \delta \bar{q}}. \tag{2.98}$$

2.3.3 Flavour matching

When evolving over a heavy quark threshold μ_Q, in the variable flavour number scheme [98,99] DPDs for the previous number of active flavours (n_{f1}, n_{f2}) need to be matched onto a set of DPDs in which one of the two flavour numbers is increased by one. This set includes DPDs with the heavy quark that decoupled before [100] and is considered as massless afterwards. Figure 2.4 shows how matching at flavour thresholds is embedded in a DGLAP evolution from initial to final scales. It was shown in appendix A of [97] that the final result is independent of the chosen path.

In the following, we restrict ourselves to contributions to the matching kernel only up to $\mathcal{O}(a_s)$, which is sufficient for NLO DGLAP evolution. At this order, the only kernels with non-trivial contributions are

$$^{RR'}A_{ab}(x, m_Q, \mu) = \delta(1-x) + a_s(\mu) \, {}^{RR'}A^{(1)}_{ab}(x, m_Q/\mu) + \mathcal{O}(a_s^2(\mu)),$$
$$ab = Qg, \ \bar{Q}g, \ gg, \tag{2.99}$$

whilst all other ones are simply

$$^{R\bar{R}}A_{aa}(x, m_Q, \mu) = \delta(1-x) + \mathcal{O}(a_s^2(\mu)), \tag{2.100}$$

$$^{RR'}A_{ab}(x, m_Q, \mu) = \mathcal{O}(a_s^2(\mu)), \ a \neq b. \tag{2.101}$$

The flavour Q with mass m_Q denotes the heavy quark that becomes light at the threshold. The coefficients $^{RR'}A^{(1)}_{Qg}$ and $^{RR'}A^{(1)}_{gg}$ can be found in eqs. (G.18) to (G.21), respectively. Flavour matching kernels behave similarly as DGLAP kernels under charge conjugation,

$$^{RR'}A_{\bar{Q}g} = {}^{RR'}A_{Qg}, \ RR' = 11, 8S, \tag{2.102}$$

$$^{8A}A_{\bar{Q}g} = - \, {}^{8A}A_{Qg}, \tag{2.103}$$
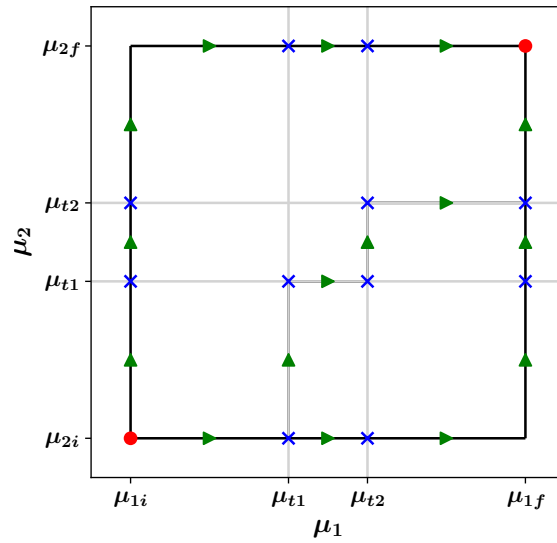
Figure 2.4: DGLAP evolution and flavour matching of a DPD from initial scales (μ_{1i}, μ_{2i}) to final scales (μ_{1f}, μ_{2f}) in the presence of two heavy quarks with matching scales μ_{Q1} and μ_{Q2}. Shown are three possible paths in the (μ_1, μ_2) plane. The arrows indicate DGLAP evolution and the crosses possible flavour matching, which is only performed in the corresponding flavour number if the path hits one of the grey lines at an angle of 90 degrees. After every matching procedure the respective flavour number is increased by one.

which was derived in section 2.3.2.

Adapting the matching formulae for PDFs [99] up to $\mathcal{O}(a_s)$, we find

$$
{}^{11}F_{Qa_2}^{(n_{f1}+1)}(\mu_Q) + {}^{11}F_{\bar{Q}a_2}^{(n_{f1}+1)}(\mu_Q) = 2\,a_s(\mu_Q)\,{}^{11}A_{Qg}^{(1)}(m_Q/\mu_Q) \underset{x_1}{\otimes} {}^{11}F_{ga_2}^{(n_{f1})}(\mu_Q)\,,
$$
(2.104)

$$
{}^{8R_2}F_{Qa_2}^{(n_{f1}+1)}(\mu_Q) + {}^{8R_2}F_{\bar{Q}a_2}^{(n_{f1}+1)}(\mu_Q) = 2\,a_s(\mu_Q)\,{}^{8S}A_{Qg}^{(1)}(m_Q/\mu_Q) \underset{x_1}{\otimes} {}^{SR_2}F_{ga_2}^{(n_{f1})}(\mu_Q)\,,
$$
(2.105)

$$
{}^{8R_2}F_{Qa_2}^{(n_{f1}+1)}(\mu_Q) - {}^{8R_2}F_{\bar{Q}a_2}^{(n_{f1}+1)}(\mu_Q) = 2\,a_s(\mu_Q)\,{}^{8A}A_{Qg}^{(1)}(m_Q/\mu_Q) \underset{x_1}{\otimes} {}^{AR_2}F_{ga_2}^{(n_{f1})}(\mu_Q)\,,
$$
(2.106)

$$
{}^{R_1R_2}F_{qa_2}^{(n_{f1}+1)}(\mu_Q) = {}^{R_1R_2}F_{qa_2}^{(n_{f1})}(\mu_Q)\,, \qquad R_1 = 1, 8\,,
$$
(2.107)

$$
{}^{R_1R_2}F_{ga_2}^{(n_{f1}+1)}(\mu_Q) = {}^{R_1R_2}F_{ga_2}^{(n_{f1})}(\mu_Q)
$$
$$
+ a_s(\mu_Q)\,{}^{R_1R_1}A_{gg}^{(1)}(m_Q/\mu_Q) \otimes {}^{R_1R_2}F_{ga_2}^{(n_{f1})}(\mu_Q)\,,
$$
$$
R_1 = S, A\,,
$$
(2.108)

$$
{}^{R_1\overline{R}_1}F_{gg}^{(n_{f1}+1)}(\mu_Q) = {}^{R_1\overline{R}_1}F_{gg}^{(n_{f1})}(\mu_Q)
$$
$$
+ a_s(\mu_Q)\,{}^{R_1R_1}A_{gg}^{(1)}(m_Q/\mu_Q) \otimes {}^{R_1\overline{R}_1}F_{gg}^{(n_{f1})}(\mu_Q)\,,
$$
$$
R_1 = 10, \overline{10}, 27\,.
$$
(2.109)

We omit all unnecessary functional arguments. "$\otimes$" denotes a usual Mellin transform and q stands for all active quarks. Their number is given in brackets as a superscript in every DPD. Parton a_2 is matched in the same way. With these matching equations in the parton basis the corresponding ones in the evolution basis can be derived easily. Identical equations hold for polarised partons.

2.4 Recapitulation of most important equations

Collinear double parton distributions are complex objects with a variety of different dependencies. Together with the lack of experimental data this makes a detailed description of these objects a challenging task. However, a few relations that were introduced in sections 2.2 and 2.3 guide our understanding of DPDs by determining their behaviour in some regions of parameter space. Before proceeding, let us quickly review them as a summary of this theoretical introduction:

* The *DGLAP equation* (2.54) is in the main focus of this work. Given a DPD at arbitrary initial RGE scales, it is able to predict the distribution at any other requested scales. For colour singlet DPDs, it has the same form as the DGLAP equation for PDFs. For colour non-singlet DPDs we have to deal with the additional rapidity dependence and calculate the higher order colour non-singlet DGLAP kernels.

∗ The *flavour matching equations* (2.104) to (2.109) allow us to vary between different numbers of active flavour while solving the DGLAP equation.

∗ The *CS equation* (2.44) governs the evolution of the rapidity variable ζ. In contrast to the DGLAP equation, it does not contain a Mellin convolution and can thus be solved analytically. A rapidity dependence cannot be found in PDFs and colour singlet DPDs, such that entangling it from the RGE scales (μ_1, μ_2) and their evolution is a novel challenge when dealing with colour non-singlet DPDs.

∗ The *matching equation at small y* (2.68) connects DPDs with PDFs. This is an important relation as it allows us to describe DPDs at least in some region of phase space by distributions that are fairly well understood, including an abundance of experimental data. This equation will be a major building block when constructing a model for DPDs at some initial scales in section 4.2.1.

  A note of caution is in order: In the literature, the term "splitting kernel" is often used when talking about DGLAP kernels. In this work, we will reserve this term exclusively for the kernels inside the matching relations at small y.

∗ Although it does not grant us more insights into the behaviour of collinear DPDs, the *matching equation at small b* (2.68) between DPDs and DTMDs is an important relation when describing transverse momentum dependent DPS. In this thesis, it also serves as a starting point for one of the two methods developed in chapter 3 with which the NLO DGLAP kernels are computed.

Chapter 3

Computation of NLO colour non-singlet DGLAP kernels

The following chapter is based on the author's contributions to [1].

In the computation of colour non-singlet DGLAP kernels, a natural starting point are the results for the well-known colour singlet DGLAP kernels used for PDFs. In section 3.1 it is worked out that the mere final expressions are not enough, but graph-by-graph results are needed to base a computation on the existing kernels. Fortunately, DGLAP kernels in such a form are indeed provided in the literature and utilised in this section. However, it will also become clear that this approach is not capable of producing the complete DGLAP kernels. Thus, in section 3.2, we pursue a different path, this time based on results for TMD matching kernels. In combination, both methods provide the full NLO DGLAP kernels for unpolarised and longitudinally polarised partons and transversely polarised quarks. They are presented in section 3.3.

3.1 First method: (re-)calculation of splitting graphs

In section 3.1.1, we will introduce a method to calculate colour singlet DGLAP kernels. Section 3.1.2 discusses the LO colour singlet results obtained from this method and explains how to obtain colour non-singlet kernels on this basis. Section 3.1.3 generalises the approach to NLO. This requires a recalculation of a special subset of splitting graphs, namely the ones that involve a gluon four-vertex, which is covered in section 3.1.4. In section 3.1.5, the DGLAP kernels for longitudinally polarised partons are shifted due to a renormalisation scheme change that restores helicity conservation in the colour singlet.

3.1.1 Calculation method

Structure. We will base our first method on the approach established in [9,10]. There, the *assumption* is made that some hadronic structure function F can be factorised into a partonic structure function F_p and a bare PDF f_B,

$$F = F_p \otimes f_B, \tag{3.1}$$

where "$\otimes$" is an ordinary Mellin convolution. We will drop unnecessary arguments, indices and sums over them in this section. It can be proven that the collinear singularities inside the partonic structure function can be further factorised,

$$F_p\left(\tfrac{1}{\epsilon}\right) = C_B \otimes \Gamma\left(\tfrac{1}{\epsilon}\right). \tag{3.2}$$

It is understood that dimensional regularisation in $D = 4 - 2\epsilon$ space-time dimensions is used for these collinear divergences. C_B is the "hard" structure function for some partonic process, whilst Γ is a process independent factor that isolates the collinear (or in that context called "mass") singularities. Absorbing it in the also process independent bare PDF yields

$$F = C_B \otimes \left(\Gamma \otimes f_B\right) = C_B \otimes f, \tag{3.3}$$

which is a factorisation formula free of unphysical infrared divergences. Γ subtracts these mass divergences inside f_B, and thus its single pole governs the scale evolution of the subtracted PDF,

$$\Gamma_{ab}(x, \tfrac{1}{\epsilon}) = \delta(1-x)\,\delta_{ab} + \sum_{n=1,i=1} \frac{1}{\epsilon^i}\,\Gamma_{ab}^{(n-1,i)}(x)$$

$$= \delta(1-x)\,\delta_{ab} - \frac{1}{\epsilon}\sum_{n=1}\frac{1}{n}\,a_s^n\,P_{ab}^{(n-1)}(x) + \mathcal{O}\left(\frac{1}{\epsilon^2}\right), \tag{3.4}$$

where we have restored flavour indices (ab). Hence, calculating $\Gamma_{ab}^{(1,1)}$ gives us direct access to the NLO DGLAP kernels. Γ can be derived from ladder graphs,

$$\Gamma_{ab}(x, \tfrac{1}{\epsilon}) = Z_j\left(\delta(1-x)\,\delta_{ij} + \left[\int \frac{d^D k}{(2\pi)^D}\, x\, \delta\left(x - \tfrac{k^+}{p^+}\right) U_a\, K\, \frac{1}{1 - \mathbb{P}K}\, L_b\right]_{-1}\right), \tag{3.5}$$

where

$$[\dots]_{-m} \tag{3.6}$$

extracts the mth pole in ϵ from the expression inside the brackets. The main task of the projector $\mathbb{P}$ is to extract collinear divergences of the graph it is applied on which yields a separation of the partonic structure function as described in (3.3). Its form is discussed e.g. in section 2.4 of [10]. K can be expanded in terms of two-particle irreducible ladder graphs K_0,

$$K = \frac{K_0}{1 - (1 - \mathbb{P})K_0} = K_0\left[1 + (1 - \mathbb{P})K_0 + (1 - \mathbb{P})\left(K_0(1 - \mathbb{P})K_0\right) + \dots\right]. \tag{3.7}$$

Notice that at higher perturbative orders, this expansion also spawns iterated lower order graphs with inserted projectors in between, e.g. through the last two terms on the right-hand side. The NLO topologies belonging to these terms are shown in figure 3.2 (h). Z_q (Z_g) subtracts divergences of the lower quark (gluon) propagator, and U_a (L_b) is the spin projector for the upper (lower) legs of the ladder graph.

To evaluate ladder graphs, the axial gauge (sometimes called light-cone gauge) is used. This gauge is characterised by setting the plus component of the gluon field A^μ to zero, which sets all Wilson lines to unity (cf. eq. (2.20)). Topologies like the ones shown in figures 3.1 and 3.2 thus contain only quark and gluon lines, but no Wilson lines. Furthermore, the principal value prescription is used to regulate divergences associated with the $1/\ell^+$ terms inside gluon propagators with some loop momentum ℓ. It is implemented by changing these terms to

$$\frac{1}{\ell^+} \to \frac{\ell^+}{(\ell^+)^2 + \delta^2 (p^+)^2} \,, \tag{3.8}$$

where p^+ is the incoming reference momentum of a splitting graph. In graph-by-graph results given in appendix G.6, it appears in the form of integrals

$$I_i = \int\limits_0^1 du \, \frac{u \ln^i(u)}{u^2 + \delta^2} \,, i = 0, 1 \,. \tag{3.9}$$

After summing over all graphs these contributions need to add up to zero, which will be a cross-check for our final results. Note however that this δ does *not* regulate rapidity divergences and thus may not be confused with the δ-regulator defined and used in [94,101,102]. In the method presented here, no rapidity regulator is used, as it is common in collinear factorisation of single parton processes. To the best of our knowledge there is no existing rapidity regulator that can be used in combination with the axial gauge.

Critique. Parallel to the method presented above, there is a different school of thought developed and explained in [7,8,85,103]. This approach has the advantage of being able to *prove* that a factorisation formula like (3.1) on the hadronic level exists. It thus can also provide an operator level definition of PDFs (and DPDs). In fact, the introduction in chapter 1 was mainly based on this concept as the same is true for the underlying literature [26,57,58,60,82]. An outline of a proof for hadronic factorisation based on this formalism is given in section 2.1.1.

The main difference to the "mass factorisation" scheme is that a concrete definition of bare PDFs in terms of operators is provided, similar to the one for DPDs given in section 2.2.1. The divergences of bare PDFs then come from UV-divergences inside the operators. The corresponding renormalisation factor Z has the same connection to the DGLAP kernels as Γ, see the RGE analysis in appendix E. Furthermore, it is argued in [104] that, although conceptually questionable, mass factorisation agrees with operator renormalisation when using dimensional regularisation. A scaleless integral over the whole range of $|k^2|$ vanishes in this case, yielding

$$\int\limits_0^\infty d|k^2| \ldots = 0 \Rightarrow \int\limits_0^{Q^2} d|k^2| \ldots = -\int\limits_{Q^2}^\infty d|k^2| \ldots \,. \tag{3.10}$$
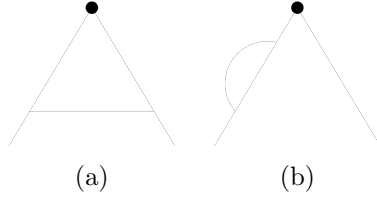
Figure 3.1: Topology for the real (a) and virtual (b) LO splitting graph.

Furthermore, a PDF operator insertion at the top of the ladder has the same effect as the projectors in (3.5). Extracting collinear poles in mass factorisation is hence equivalent to extracting UV poles in PDF operator renormalisation. Consequently, under these conditions the DGLAP kernels extracted from single poles of either Γ_{ab} or Z_{ab} agree in both approaches.

3.1.2 LO DGLAP kernels

Before focussing on NLO DGLAP kernels, let us first take a step back and calculate the LO kernels based on the colour singlet results, which was already done in [26]. One can classify the underlying splitting into two categories: Real and virtual graphs (figure 3.1), characterised by the presence or absence of real emissions over the final state cut. To reflect this also in the DGLAP kernel itself, we decompose it such that

$$
{}^{RR'}P_{ab}^{(n)}(x, \zeta/\mu^2) = {}^{RR'}\widetilde{P}_{ab}^{(n)}(x)
$$
$$
+ \frac{1}{2}\delta_{R\overline{R}'}\,\delta_{ab}\,\delta(1-x)\left[d_a^{(n)} + {}^Rc^{(n)} - \frac{1}{2}{}^R\gamma_J^{(n)}\ln\frac{\zeta}{\mu^2}\right],\ n = 0, 1\,. \tag{3.11}
$$

$\widetilde{P}$ contains all terms not proportional to $\delta(1-x)$, which are exclusively generated by real graphs. The coefficient $d_a^{(n)}$ consists of all terms proportional to $\delta(1-x)$ from the colour singlet kernel ${}^{11}P_{ab}$, whilst all the additional colour non-singlet terms are combined to ${}^Rc^{(n)}$. The last term proportional to ${}^R\gamma_J^{(n)}$ can be directly deduced from the rapidity derivative of the DGLAP kernel as given in (2.69). $\delta(1-x)$ terms can only appear if graphs conserve the flavour and parity of the incoming and outgoing partons, which explains the factors of $\delta_{R\overline{R}'}\,\delta_{ab}$ in front. The situation at LO is special in the sense that there is only one real graph per splitting channel. The only difference between calculating graphs in colour singlet and non-singlet representations is the different colour projector. Contracting these projectors with the open end of some ladder graph gives rise to a relative factor between different projected versions (with one notable exception, that first appears at NLO and is discussed in section 3.1.4). We obtain a colour factor

$$
c(RR') = \frac{\epsilon(R)}{\epsilon(R')}\frac{1}{m(R)}\,P_{RR'}^{\underline{r}\,\underline{s}}\,s^{\underline{r}\,\underline{s}} \tag{3.12}
$$

for some splitting graph with colour tensor structure $s^{\underline{r}\,\underline{s}}$. The prefactors on the right-hand side are inherited from the definition of colour projected splitting kernels (2.53).

In the presence of only one graph, $c(RR')$ becomes a global factor. For all open LO channels, we thus find

$$
{}^{88}\widetilde{P}_{qq}^{V(0)}(x) = c_{qq}(88)\,{}^{11}\widetilde{P}_{qq}^{V(0)}(x)\,, \tag{3.13}
$$

$$
{}^{8A}\widetilde{P}_{\Sigma^-g}^{(0)}(x) = c_{qg}(8A)\,{}^{11}\widetilde{P}_{\Sigma^+g}^{(0)}(x)\,, \qquad {}^{A8}\widetilde{P}_{g\Sigma^-}^{(0)}(x) = c_{gq}(A8)\,{}^{11}\widetilde{P}_{g\Sigma^+}^{(0)}(x)\,, \tag{3.14}
$$

$$
{}^{8S}\widetilde{P}_{\Sigma^+g}^{(0)}(x) = c_{qg}(8S)\,{}^{11}\widetilde{P}_{\Sigma^+g}^{(0)}(x)\,, \qquad {}^{S8}\widetilde{P}_{g\Sigma^+}^{(0)}(x) = c_{gq}(S8)\,{}^{11}\widetilde{P}_{g\Sigma^+}^{(0)}(x)\,, \tag{3.15}
$$

$$
{}^{R\overline{R}}\widetilde{P}_{gg}^{(0)}(x) = c_{gg}(R\overline{R})\,{}^{11}\widetilde{P}_{gg}^{(0)}(x)\,, \tag{3.16}
$$

where

$$
c_{qq}(88) = -\frac{1}{N^2 - 1}\,, \tag{3.17}
$$

$$
c_{qg}(8A) = c_{gq}(A8) = \sqrt{\frac{N^2}{2(N^2 - 1)}}\,, \tag{3.18}
$$

$$
c_{qg}(8S) = c_{gq}(S8) = \sqrt{\frac{N^2 - 4}{2(N^2 - 1)}}\,, \tag{3.19}
$$

$$
c_{gg}(AA) = c_{gg}(SS) = \frac{1}{2}\,, \tag{3.20}
$$

$$
c_{gg}(10\,\overline{10}) = 0\,, \tag{3.21}
$$

$$
c_{gg}(27\,27) = -\frac{1}{3}\,. \tag{3.22}
$$

The reader shall be reminded that ${}^{SA}\widetilde{P}_{gg}(x)$ and ${}^{AS}\widetilde{P}_{gg}(x)$ vanish to all orders and will be omitted here and in the following. In addition, at LO there are no quark-antiquark transition graphs and no pure singlet graphs, i.e.

$$
{}^{RR}P_{q\bar{q}}^{V(0)} = {}^{RR}P_{q\bar{q}}^{S(0)} = {}^{RR}P_{qq}^{S(0)} = 0\,. \tag{3.23}
$$

Since colour and spin projectors factorise, identical relations as (3.13) to (3.16) and (3.23) hold for polarised DGLAP kernels. This behaviour can be observed for every kernel that is generated by only one graph at some perturbative order. For more than one graph, this is no longer true as graphs have different x-dependencies for different polarisations. At LO, colour non-singlet kernels can thus be directly deduced from the colour singlet ones for all channels and polarisations. The explicit expressions are given in (G.1) to (G.9).

Virtual graphs consist only of internal loops which are always proportional to the identity operator in colour space. Upper and lower indices of one parton line are thus identical, and so a contraction with an arbitrary colour projector as in (3.12) reduces to

$$
\frac{1}{m(R)}\,P_{R\overline{R}}^{r\,\bar{s}}\,\delta^{rs}\,\delta^{r's'} = \frac{1}{m(R)}\,P_{R\overline{R}}^{r\,\bar{r}} = 1 \tag{3.24}
$$

due to the normalisation (B.17). Kinematically, the virtual graphs exclusively generate $\delta(1-x)$ terms. However, not all $\delta(1-x)$ terms are necessarily generated by virtual graphs: gluons coupling to Wilson lines also have $\delta(1-x)$ contributions. Even in the axial gauge, where Wilson lines are absent due to $A^+ = 0$, there is a potential source for $\delta(1-x)$ terms, namely remnants of the rapidity regulator. These rapidity dependent terms also are proportional to $\delta(1-x)$, see eq. (3.11). A method is of course only sensitive to those terms if such a rapidity regulator is used in the first place, which is naturally not the case in [10, 105]. There, the $\delta(1-x)$ terms are not even calculated but derived from momentum sum rules (2.60) and (2.61).

After having seen that colour projectors do not generate colour factors in virtual graphs, it has become obvious that we can combine colour singlet and non-singlet contributions in (3.11) additively, whilst the situation for real graphs is more involved. Furthermore, we have found a motivation for the decomposition into d_a and ^Rc, as the virtual graphs always give the same contribution regardless of the colour dimension. The explicit form of ^Rc and $^R\gamma_J$ on the other hand is shrouded as long as we do not introduce an explicit rapidity regulator. This will be the main motivation for the method that is applied in section 3.2. For now, let us explore how the x-dependent results generalise for colour non-singlet DGLAP kernels at NLO.

3.1.3 Calculation of NLO DGLAP kernels

In the following, we will derive a method that calculates the x-dependent parts of colour non-singlet DGLAP kernels from colour singlets results given in [10, 105–107].

At NLO, channels that are already open at LO receive contributions from a variety of different graphs. Their different topologies are displayed in figure 3.2. If one topology is assigned to two letters, there are two routing options of the external parton line leading to two different graphs. In some channels, the internal lines of the topologies (b) and (e) can be chosen to be quarks or gluons. In the tables of appendix G.6, the corresponding graph is labelled with a corresponding subscript, e.g. (b_q). The combined topology (h) is called "(h-i)" in [105] and contains the iterated LO topology shown in figure 3.1 (a), as explained in section 3.1.1. The inserted operator is a simple identity in colour space, hence both topologies produce the same colour factor in all channels and can be condensed into one for our purposes. Topologies (l,m,n) belong to the subclass of four-vertex topologies which only appear in (gg) graphs. They do not appear in [105] because its Feynman integrals vanish at an very early stage[1]. In section 3.1.4 we will, among others, explore if this is still the case if these graphs are projected onto colour non-singlet representations.

At NLO, all channels are open. This includes non-vanishing $^{RR'}P_{qq}^{S(1)}$, $^{RR'}P_{q\bar{q}}^{V(1)}$, and $^{RR'}P_{q\bar{q}}^{S(1)}$, which all did receive no contributions at LO, see (3.23). These new DGLAP kernels are generated by only one graph at NLO, such that they obey equivalent colour scaling laws as the LO kernels (3.13) to (3.16), but with different colour factors. These relations, along with all other results of this calculation, can be found in the appendices

---

[1]This was clarified by one of the authors of [105], W. Vogelsang, in private communication.
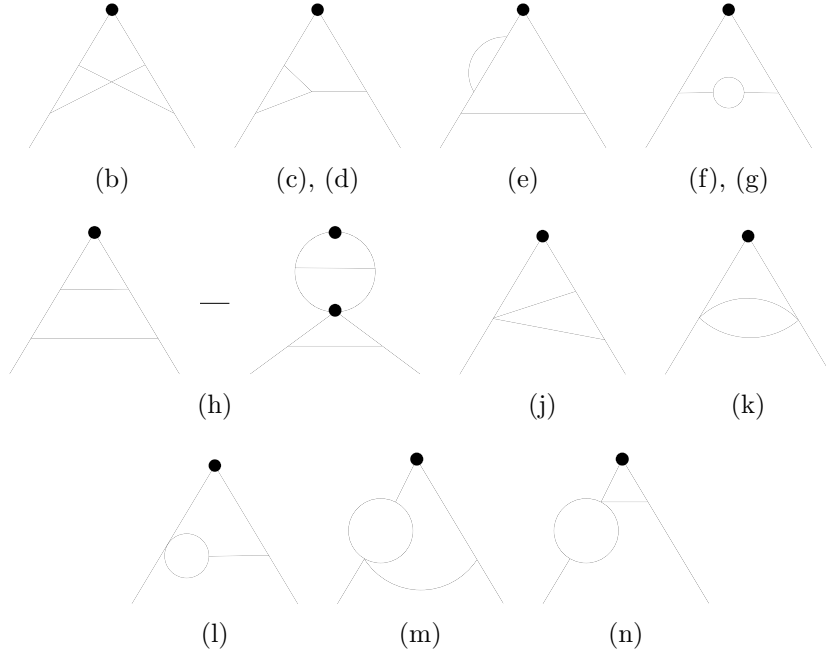
Figure 3.2: All topologies of NLO splitting graphs. The naming convention is taken from [105]. Complex conjugated graphs are not shown. Further explanations can be found in the text.

G.2, G.3 and G.4 for unpolarised, longitudinal and transverse kernels, respectively.

As explained in section 3.1.2, the contraction with colour projectors leads to a potentially different colour factor for every graph, but the x-dependent part remains unchanged. We can thus recycle the graph-by-graph results of [10,105–107] for PDF/colour singlet DGLAP kernels and recombine them with the colour factors that are calculated via (3.12). Both of these tables for every splitting channel can be found in appendix G.6. The contributions of real graphs for an arbitrary channel can then be obtained via the matrix product

$$^{RR'}\widetilde{P}^{(1)}(x) = \vec{v}(x) \cdot \underline{C} \cdot \vec{f}(RR'),\tag{3.25}$$

omitting the channel indices for the moment. Here, $\vec{f}(RR')$ is the column of a table of colour factors for every graph (e.g. table G.1), $\underline{C}$ are the coefficients for every x-term and graph (as given e.g. in table G.5), and $\vec{v}(x)$ are these x-terms written as a vector, i.e. the very first column of the table which $\underline{C}$ is based on. In the previous sentence, we gave the tables for the unpolarised (qq)-valence channel as an example. In this particular case, the first few entries of the ingredients on the right-hand side of (3.25), extracted

from the referenced tables, are

$$
\vec{v}_{qq,V}(x) = \begin{pmatrix} p_{qq}(x)\ln^2(x) \\ p_{qq}(x)\ln^2(1-x) \\ p_{qq}(x)\ln(x)\,\ln(1-x) \\ \vdots \end{pmatrix}, \qquad \underline{C}_{qq,V} = \begin{pmatrix} -1 & 1 & -1 & \dots \\ 0 & 0 & -2 & \dots \\ 0 & 2 & -6 & \dots \\ \vdots & \vdots & \vdots & \ddots \end{pmatrix},
$$

$$
\vec{f}_{qq,V}(11) = \begin{pmatrix} -\frac{N^2-1}{4N^2} \\ -\frac{N^2-1}{4N^2} \\ -\frac{N^2-1}{4} \\ \vdots \end{pmatrix}, \qquad \vec{f}_{qq,V}(88) = \begin{pmatrix} \frac{N^2+1}{4N^2} \\ \frac{1}{4N^2} \\ \frac{1}{4} \\ \vdots \end{pmatrix}. \tag{3.26}
$$

$p_{qq}(x)$ is defined in (G.10).

There is one family of exceptions to the master formula (3.25), namely all graphs that contain a gluon four-vertex. The Feynman rule for this vertex contains the sum of *three* colour tensors multiplied with different momentum tensors. Thus, every four-vertex inside a diagram a priori generates three graphs in colour space, each of them with a potentially different colour factor. The graphs correspond to topologies (j) to (n) of figure 3.2 and appear only in the (gg) channel. They have to be calculated again from scratch for every colour representation, which will be the topic of the next section.

3.1.4 NLO graphs with a gluon four-vertex

Unpolarised kernels Following section 3.1.1, the splitting kernels can be derived from

$$
\frac{1}{\epsilon}\,{}^{R\overline{R}}\Gamma^{(1,1)}_{gg,(y)}(x) = -\frac{1}{\epsilon}\,a_s^2\,{}^{R\overline{R}}\widetilde{P}^{(1)}_{gg,(y)}(x) = \left[\int\limits_0^{Q^2}\mathrm{d}|k^2|\int\mathrm{d}PS_{(y)}\frac{\mathcal{N}^{R\overline{R}}_{(y)}}{\mathcal{D}_{(y)}\,|k^2|^2}\right]_{-1}, \tag{3.27}
$$

where the subscript "(y)" labels the contribution of the corresponding graph to the complete contribution at NLO. Contributions of different graphs can be distinguished by different numerators $\mathcal{N}$ and denominators $\mathcal{D}$ that contain vertex factors and propagators. Note that projections onto different colour representations are also done inside the numerator. We insert a PDF operator Feynman rule instead of using the projectors of the mass factorisation approach in the original formula (3.5). The integral over $|k^2|$ is cancelled by a δ-distribution inside $\mathrm{d}PS_{(y)}$. The upper cut-off at some hard scale Q prevents the whole expression from vanishing as the integral would be scaleless otherwise. For the extraction of the collinear poles the exact size of the cut-off is irrelevant. As discussed in section 3.1.1, determining the UV pole by evaluating the integral in the limits $[Q^2,\infty)$ would lead to the same result.

As it was explained in section 3.1.3, there is no reason to assume that the numerators of four-vertex graphs are proportional to one another in different colour representations. Four-vertex graphs need to be recalculated by hand since the method discussed in section

3.1.3 cannot be applied on them. The explicit calculation is given in appendix C. We obtain the following final results for all four-vertex graphs (j) to (n) in figure 3.2:

$$^{R\overline{R}}\widetilde{P}^{(1)}_{gg,\,(\mathrm{j})}(x) = -\frac{1}{2}C^{R\overline{R}}_{(\mathrm{j})}\left(2(1+x)\ln(x) + 5(1-x)\right),\tag{3.28}$$

$$^{R\overline{R}}\widetilde{P}^{(1)}_{gg,\,(\mathrm{k})}(x) = \frac{1}{8}C^{R\overline{R}}_{(\mathrm{k})}\left(1-x\right),\tag{3.29}$$

$$^{R\overline{R}}\widetilde{P}^{(1)}_{gg,\,(\mathrm{l\text{-}n})}(x) = 0\,,\tag{3.30}$$

with

$$
\begin{aligned}
C^{11}_{(\mathrm{j})} &= 0\,, & C^{11}_{(\mathrm{k})} &= 9N^2\,, \\
C^{AA}_{(\mathrm{j})} = C^{SS}_{(\mathrm{j})} &= -\frac{1}{4}N^2\,, & C^{AA}_{(\mathrm{k})} = C^{SS}_{(\mathrm{k})} &= 3N^2\,, \\
C^{10\overline{10}}_{(\mathrm{j})} = C^{\overline{10}10}_{(\mathrm{j})} &= 0\,, & C^{10\overline{10}}_{(\mathrm{k})} = C^{\overline{10}10}_{(\mathrm{k})} &= 0\,, \\
C^{27\,27}_{(\mathrm{j})} &= 4\,, & C^{27\,27}_{(\mathrm{k})} &= -3\,.
\end{aligned}\tag{3.31}
$$

Remarkably, all different colour tensors inside (j) and (k) produce the same colour factors $C^{RR'}_{(\mathrm{j})}$ and $C^{RR'}_{(\mathrm{k})}$, which greatly simplifies the structure of the corresponding contributions (3.28) and (3.29). The sum of all four-vertex graphs then is

$$^{R\overline{R}}\widetilde{P}^{(1)}_{gg,\,4\text{-vertex}}(x) = \frac{1}{8}\left\{C^{R\overline{R}}_{(\mathrm{k})}(1-x) - 4\,C^{R\overline{R}}_{(\mathrm{j})}\Big(2(1+x)\ln(x) + 5(1-x)\Big)\right\},\tag{3.32}$$

which in the colour singlet agrees with table 4, terms (jk) of [105].

Longitudinal kernels For longitudinal kernels, we need to insert a projector onto longitudinal spin states

$$\mathcal{P}^{ii'jj'}_{\epsilon} = \frac{1}{2}\epsilon^{ii'}\epsilon^{jj'} = \frac{1}{2}\left(\bar{\delta}^{ij}\bar{\delta}^{i'j'} - \bar{\delta}^{ij'}\bar{\delta}^{i'j}\right)\tag{3.33}$$

instead of the sum and average over transverse spin states, $\delta^{ii'}\delta^{jj'}/(D-2)$. In this section, we will use (ii') and (jj') as transverse spatial indices of the lower and upper open parton legs of an arbitrary splitting graph. The expression (3.33) can be obtained from the product of the two projectors in eq. (9) of [106]. In the second step, we expressed the Levi-Civita tensors in terms of $\bar{\delta}$-tensors. They vanish if at least one of their indices becomes unphysical, i.e. larger than 2, as required in the HVBM scheme [108, 109] that is used in [106].

We use an alternative scheme in which we do not distinguish between physical and unphysical degrees of freedom and thus use ordinary δ-tensors inside the spin projector

$$\mathcal{P}^{ii'jj'}_{\delta} = c\left(\delta^{ij}\delta^{i'j'} - \delta^{ij'}\delta^{i'j}\right).\tag{3.34}$$

The normalisation constant c remains to be calculated, as this scheme is not covered in [106]. Since we are dealing with collinear distributions, the only possible form of the longitudinal gluon DGLAP kernel with open transverse indices is

$$
{}^{R\overline{R}}P_{\Delta g \Delta g}^{ii'jj'} \propto \left(\delta^{ij}\delta^{i'j'} - \delta^{ij'}\delta^{i'j} \right), \tag{3.35}
$$

as it needs to be antisymmetric under $j \leftrightarrow j'$. In the case of transverse momentum dependent distributions, dependencies on the partonic transverse momentum would have also been possible. Eq. (3.35) enables us to determine c since by definition both projectors, $\mathcal{P}_\epsilon$ and $\mathcal{P}_\delta$, need to have the same effect on the DGLAP kernel,

$$
\mathcal{P}_\epsilon^{ii'jj'}\,{}^{RR'}P_{\Delta g \Delta g}^{ii'jj'} = \mathcal{P}_\delta^{ii'jj'}\,{}^{RR'}P_{\Delta g \Delta g}^{ii'jj'}. \tag{3.36}
$$

Inserting (3.35) yields

$$
c = \frac{1}{(D-2)\,(D-3)}. \tag{3.37}
$$

The remaining part of the calculation is identical to the one for unpolarised kernels. The results have the same form as the unpolarised ones, eqs. (3.28) to (3.30):

$$
{}^{R\overline{R}}\widetilde{P}_{\Delta g \Delta g,\,(\mathrm{j})}^{(1)}(x) = -\frac{1}{2}C_{\Delta(\mathrm{j})}^{R\overline{R}}\left(2(1+x)\ln(x) + 5(1-x) \right) \tag{3.38}
$$

$$
{}^{R\overline{R}}\widetilde{P}_{\Delta g \Delta g,\,(\mathrm{k})}^{(1)}(x) = \frac{1}{8}C_{\Delta(\mathrm{k})}^{R\overline{R}}\left(1-x \right) \tag{3.39}
$$

$$
{}^{R\overline{R}}\widetilde{P}_{\Delta g \Delta g,(\mathrm{l\text{-}n})}^{(1)}(x) = 0\,, \tag{3.40}
$$

with

$$
\begin{aligned}
C_{\Delta(\mathrm{j})}^{11} &= -3N^2\,, & C_{\Delta(\mathrm{k})}^{11} &= 3N^2\,, \\
C_{\Delta(\mathrm{j})}^{AA} = C_{\Delta(\mathrm{j})}^{SS} &= -\frac{3}{4}N^2\,, & C_{\Delta(\mathrm{k})}^{AA} = C_{\Delta(\mathrm{k})}^{SS} &= 2N^2\,, \\
C_{\Delta(\mathrm{j})}^{10\overline{10}} = C_{\Delta(\mathrm{j})}^{\overline{10}10} &= 0\,, & C_{\Delta(\mathrm{k})}^{10\overline{10}} = C_{\Delta(\mathrm{k})}^{\overline{10}10} &= 0\,, \\
C_{\Delta(\mathrm{j})}^{27\,27} &= -3\,, & C_{\Delta(\mathrm{k})}^{27\,27} &= -17\,.
\end{aligned} \tag{3.41}
$$

The sum of all graphs again has the form

$$
{}^{R\overline{R}}\widetilde{P}_{\Delta g \Delta g,\,4\text{-vertex}}^{(1)}(x) = \frac{1}{8}\left\{ C_{\Delta(\mathrm{k})}^{R\overline{R}}(1-x) - 4\,C_{\Delta(\mathrm{j})}^{R\overline{R}}\left(2(1+x)\ln(x) + 5(1-x) \right) \right\}. \tag{3.42}
$$

For the colour singlet, we find agreement with table 4, terms (jk) of [106].

3.1.5 Scheme change for longitudinal kernels

Our calculation of longitudinal colour non-singlet DGLAP kernels is based on results from [106]. As already pointed out in section 3.1.4, the HVBM scheme [108, 109] is used there, in which space-time dimensions smaller and larger than 4 are treated in a different

way. In this context, we have seen that gluon spin projectors need to be handled with care. In fact, to calculate four-vertex graphs we have introduced a different scheme with a projector $\mathcal{P}_\delta$, mimicking the effect of the HVBM projector $\mathcal{P}_\epsilon$ and at the same time circumventing peculiarities coming from the special treatment of unphysical degrees of freedom.

In the quark sector, the HVBM scheme also causes an unwanted behaviour: Naively, one would expect helicity conservation in the colour singlet,

$$^{11}P_{\Delta q \Delta q}^{V(1)} = {}^{11}P_{qq}^{V(1)}. \tag{3.43}$$

In valence graphs, upper and lower quark lines are contained in the same trace. The two additional γ_5 matrices from the quark spin projector in (2.21) applied to incoming and outgoing quarks of the ladder graph can then be commuted with the remaining γ matrices inside the trace. Using $\gamma_5^2 = 1$ afterwards, we end up we with the same trace as in the unpolarised case. However, in the HVBM scheme, the γ_5 matrix does not commute with the other γ matrices in the unphysical space-time dimensions. The relation (3.43) does not hold for this scheme choice, which then also violates the conservation of the axial current [110].

For the colour singlet kernels, this motivates a scheme change that restores the equality (3.43) by multiplying with an additional renormalisation factor that subtracts the violating term at NLO, as discussed in [70, 106]. Note that this does not interfere with the different scheme we have introduced for four-vertex graphs in section 3.1.4, as we will later see that the (gg) channel is not affected by these changes. Effectively, such a change of the renormalisation scheme is a redefinition of the hard cross section and PDFs such that the physical conservation laws are reflected in the latter. All divergences are already subtracted in $\overline{\text{MS}}$, such that the renormalisation factor contains only finite terms.

Appendix D contains a calculation of the shifted DGLAP kernels, partially revisiting results from [106]. Here, we only give the results. The definitions for all kernels can be found in section 2.3.2.

* For the quark sector, we find that the $P^\pm$ kernels are shifted like

$$^{RR}P_{\Delta}^{\pm(0)}(x,\zeta) = {}^{RR}P_{\Delta,\overline{\text{MS}}}^{\pm(0)}(x,\zeta) \,, \tag{3.44}$$

and

$$^{RR}P_{\Delta}^{\pm(1)}(x,\zeta) = {}^{RR}P_{\Delta,\overline{\text{MS}}}^{\pm(1)}(x,\zeta) + \frac{1}{2}\left({}^{R}\gamma_J^{(0)}\ln(x) - \beta_0\right){}^{R}\widetilde{Z}^{(1)}(x)\,, R = 1, 8\,. \tag{3.45}$$

The kernels $^{RR}P_{\Delta q \Delta q}^V$ and $^{RR}P_{\Sigma^\pm \Sigma^\pm}$ are shifted in the same way, whilst $^{RR}P_{\Delta q \Delta \bar{q}}^V$, $^{RR}P_{\Delta q \Delta q}^S$, and $^{RR}P_{\Delta q \Delta \bar{q}}^S$ are not changed at all.

* For the mixed channels, we obtain

$$^{RR'}P_{\Delta \Sigma^\pm \Delta g}^{(0)}(x,\zeta) = {}^{RR'}P_{\Delta \Sigma^\pm \Delta g,\overline{\text{MS}}}^{(0)}(x,\zeta) \tag{3.46}$$

$$^{RR'}P^{(1)}_{\Delta\Sigma^\pm\Delta g}(x,\zeta) = {}^{RR'}P^{(1)}_{\Delta\Sigma^\pm\Delta g,\overline{\text{MS}}}(x,\zeta)$$
$$+ {}^{R}\widetilde{Z}^{(1)}(x',\zeta) \underset{x}{\otimes} {}^{RR'}P^{(0)}_{\Delta\Sigma^\pm\Delta g,\overline{\text{MS}}}(x',\zeta), \tag{3.47}$$

$$^{R'R}P^{(0)}_{\Delta g\Delta\Sigma^\pm}(x,\zeta) = {}^{R'R}P^{(0)}_{\Delta g\Delta\Sigma^\pm,\overline{\text{MS}}}(x,\zeta) \tag{3.48}$$

$$^{R'R}P^{(1)}_{\Delta g\Delta\Sigma^\pm}(x,\zeta) = {}^{R'R}P^{(1)}_{\Delta g\Delta\Sigma^\pm,\overline{\text{MS}}}(x,\zeta)$$
$$- {}^{R'R}P^{(0)}_{\Delta g\Delta\Sigma^\pm,\overline{\text{MS}}}(x',\zeta) \underset{x}{\otimes} {}^{R}\widetilde{Z}^{(1)}(x',\zeta), \tag{3.49}$$

where $RR' = 11, 8S$ for Σ^+ and $RR' = 8A$ for Σ^-.

∗ As already mentioned above, the gluon kernels remain untouched.

For the NLO term of $^{1}\widetilde{Z}$, we adopt the choice of [106],

$$^{1}\widetilde{Z}^{(1)}(x) = -4C_F(1-x). \tag{3.50}$$

This ensures that after the shift DGLAP evolution conserves helicity and the axial current. In the colour non-singlet, such conservation laws are absent, and so a scheme change is no longer motivated physically. However, it appears unnatural to us to perform the scheme change only for colour singlet and leave the colour octet untouched. A natural choice would rather be to scale the colour singlet expression with the colour factor $c_{qq}(88)$, just as it is the case for the LO DGLAP kernel (3.13):

$$^{8}\widetilde{Z}^{(1)}(x) = c_{qq}(88)\, {}^{1}\widetilde{Z}^{(1)}(x). \tag{3.51}$$

We will see how this affects the explicit DGLAP kernels in section 3.3, eqs. (3.101) and (3.102).

3.2 Second method: matching calculation with projected TMD matrix elements

In section 3.1, we have calculated the NLO colour non-singlet DGLAP kernels using existing results for PDF DGLAP kernels from the literature [10, 105–107]. This method was however limited by the absence of an rapidity regulator that probihited the computation of $\delta(1-x)$ dependent terms. In the afore mentioned publications, these terms were calculated using momentum sum rules that are no longer present in colour non-singlet representations.

We thus need to find a different approach to address this problem. Just as in section 3.1, we aim to reuse existing results from the literature to avoid a complete recalculation of the NLO splitting graphs. An obvious choice are TMD calculations, since these distributions also are rapidity dependent and therefore a suitable regulator is already implemented in the results. We use matrix elements of the transverse momentum dependent operator calculated in [94, 111] and connect them to their collinear counterparts

via the short distance matching equation. Expanding it to $\mathcal{O}(a_s^2)$ and the extracting the single pole in ϵ directly yields the full NLO DGLAP kernel, including the $\delta(1-x)$ terms.

In section 3.2.1, we first define the TMD and collinear matrix elements, their respective renormalisation and how they are connected through the matching equation. Then, in section 3.2.2, we expand this equation to extract the LO and NLO DGLAP kernels.

3.2.1 Definition of TMD and collinear matrix elements

We define

$$^{RR'}\widehat{\mathcal{M}}_{ab,B,\mathrm{us}}(x,\boldsymbol{z},\mu) = \frac{\epsilon(R)\,\mathcal{N}_a}{\epsilon(R')\,\mathcal{N}_b}\,\frac{1}{m(R)}\,P_{\overline{R'}R}^{\frac{r\,s}{R}}\,\langle b,p',r'|\,\mathcal{O}_{B,a}^s(x,\boldsymbol{z},\mu)\,|a,p,r\rangle \qquad (3.52)$$

as the unsubtracted TMD matrix elements for a small but finite transverse distance $\boldsymbol{z}$. The operator definitions can be found in eqs. (2.17) to (2.19). We project them onto partonic states characterised by the respective flavour, momentum, and colour representation to make the calculation fully perturbative. The subscript B indicates that bare couplings and fields are used inside the definition. The prefactors on the right-hand side are the same as for the definition of colour projected DGLAP kernels, eq. (2.53). Collinear matrix elements $^{RR'}\mathcal{M}_{ab,B,\mathrm{us}}(x,\mu)$ are defined equivalently,

$$^{RR'}\mathcal{M}_{ab,B,\mathrm{us}}(x,\mu) = \frac{\epsilon(R)\,\mathcal{N}_a}{\epsilon(R')\,\mathcal{N}_b}\,\frac{1}{m(R)}\,P_{\overline{R'}R}^{\frac{r\,s}{R}}\,\langle b,p',r'|\,\mathcal{O}_{B,a}^s(x,\boldsymbol{z}=\boldsymbol{0},\mu)\,|a,p,r\rangle\,. \qquad (3.53)$$

To calculate colour projected TMD matrix elements, one applies the colour factors from tables G.1 to G.4 to graph-wise results for the colour-singlet TMD matrix elements. Contrary to section 3.1 Feynman gauge is used, which introduces graphs containing Wilson lines.

Rapidity subtraction. In [94, 111], the δ regulator is used to cope with rapidity divergences. For a right moving proton, it is implemented as an exponential suppression in the argument of Wilson line exponentials[2]

$$\mathcal{P}\exp\left\{-ig\,t_{rs}^b\int\limits_0^\infty ds\,v\cdot A^b(\xi+sv)e^{\mp\delta^\pm s}\right\}. \qquad (3.54)$$

From now on we concentrate on δ^+ for right-moving protons. δ^- is implemented in the same way. Eikonal lines become

$$\frac{1}{(q_1^+ - i\delta^+)\,(q_2^+ - 2i\delta^+)\,\ldots\,(q_n^+ - ni\delta^+)}\,. \qquad (3.55)$$

In the bare subtracted matrix elements $^{RR'}\widehat{\mathcal{M}}_{B,ab}$ and $^{RR'}\mathcal{M}_{B,ab}$, the residual rapidity scale then is

$$\zeta = 2\,\frac{\delta^-}{\delta^+}\,(p^+)^2\,. \qquad (3.56)$$

---

[2]Note that in [94], a rescaling was applied to $\delta^\pm$. As mentioned in [91] this is not appropriate when partonic quantities are defined with respect to the partonic momentum xp^+, as it is done in this work.

Renormalisation. The remaining UV divergences inside $\mathcal{O}_a$ are dealt with by a convolutive renormalisation in the case of collinear matrix elements

$$^{RR'}\mathcal{M}_{ab}(x,\mu,\zeta) = Z_b^{-1}(\mu) \sum_{c,R''} {}^{R\overline{R}''}Z_{ac}(x',\mu,x^2\zeta) \underset{x}{\otimes} {}^{R''R'}\mathcal{M}_{B,cb}(x',\zeta)\,, \tag{3.57}$$

and a multiplicative one for the TMD matrix elements,

$$^{RR'}\widehat{\mathcal{M}}_{ab}(x,\boldsymbol{z},\mu,\zeta) = Z_b^{-1}(\mu)\,\widehat{Z}_a(\mu,x^2\zeta)\,{}^{RR'}\widehat{\mathcal{M}}_{ab,B}(x,\boldsymbol{z},\zeta)\,. \tag{3.58}$$

As discussed below (2.67), $\widehat{Z}$ is colour independent and identical to its single parton analogue. A renormalisation group analysis of both $^{RR'}Z_{ab}$ and $\widehat{Z}_a$ can be found in appendix E. The most important result is the connection to the DGLAP splitting kernels,

$$^{RR'}P_{ab}^{(n)} = -n\,{}^{RR'}Z_{ab}^{(n+1,1)}\,, \tag{3.59}$$

where the notation on the right-hand side is defined in (3.74).

The factor Z_b is used to renormalise parton fields,

$$q_{B,i} = \sqrt{Z_q}\,q_i\,, \qquad\qquad A_B^{a,\mu} = \sqrt{Z_g}\,A^{a,\mu}\,. \tag{3.60}$$

On this level, the colour singlet matrix elements are identical to their single parton counterparts. This is the reason why DGLAP and transverse momentum matching kernels are identical for single and double parton distributions.

The bare matrix element are calculated with respect to the unrenormalised strong coupling

$$a_{s,0} = \frac{\mu^{2\epsilon}}{S_\epsilon}\,Z_\alpha\,a_s\,, \tag{3.61}$$

where

$$S_\epsilon = \left(4\pi e^{-\gamma_E}\right)^\epsilon \tag{3.62}$$

and

$$Z_\alpha(\mu) = 1 + \sum_{n=1}^\infty a_s(\mu)\,Z_\alpha^{(n)}. \tag{3.63}$$

For our purposes, the first non-trivial value,

$$Z_\alpha^{(1)} = -\frac{1}{\epsilon}\frac{\beta_0}{2}\,, \tag{3.64}$$

is sufficient. Using (3.61), we can expand the bare matrix elements in terms of a_s,

$$^{RR'}\widehat{\mathcal{M}}_{B,ab}(x,\boldsymbol{z},\mu,\zeta) = \delta_{R\overline{R}'}\,\delta_{ab}\,\delta(1-x) + \sum_{n=1}^\infty \left(Z_\alpha(\mu)\,a_s(\mu)\right)^n {}^{RR'}\widehat{\mathcal{M}}_{B,ab}^{(n)}(x,\boldsymbol{z},\mu,\zeta)\,, \tag{3.65}$$

where the perturbative coefficients contain the factors of $(\mu^2/S_\epsilon)^n$ from (3.61).

The bare and unsubtracted collinear matrix element beyond the leading term contain no external scales except for the regulators $\delta^{\pm}$. However, they only appear in the integrals over plus- and minus-components and the $(D-2)$-dimensional transverse integrals remain scaleless and thus vanish. Therefore, there cannot be any graph-wise rapidity divergences inside the collinear unsubtracted matrix element. Consequently, the soft collinear matrix element also vanishes and the bare collinear matrix element simply is

$$^{RR'}\mathcal{M}_{B,ab}(x,\mu,\zeta) = \delta_{R\overline{R}'}\,\delta_{ab}\,\delta(1-x)\,. \tag{3.66}$$

Matching equation. Based on the matching equation between the complete DPDs and DTMDs for small z, we can relate subtracted and renormalised TMD matrix element $^{RR'}\widehat{\mathcal{M}}_{ab}$ to the collinear matrix elements:

$$^{RR'}\widehat{\mathcal{M}}_{ab}(x,\boldsymbol{z},\mu,\zeta) = \sum_{c,R''} {}^{R\overline{R}''}C_{ac}(x',\boldsymbol{z},\mu,x^2\zeta) \underset{x}{\otimes} {}^{R''R'}\mathcal{M}_{cb}(x',\mu,\zeta)\,. \tag{3.67}$$

This equation will be the backbone of the following analysis as it allows us to compute colour non-singlet DGLAP kernels for collinear operators with the help of already computed single poles of TMD matrix elements.

Perturbative expansions. The expanded renormalised matrix elements, matching coefficient and renormalisation factors read

$$^{RR'}\widehat{\mathcal{M}}_{ab}(x,\boldsymbol{z},\mu,\zeta) = \delta_{R\overline{R}'}\,\delta_{ab}\,\delta(1-x) + \sum_{n=1}^{\infty} a_s^n(\mu)\,{}^{RR'}\widehat{\mathcal{M}}_{ab}^{(n)}(x,\boldsymbol{z},\mu,\zeta)\,, \tag{3.68}$$

$$^{RR'}\mathcal{M}_{ab}(x,\mu,\zeta) = \delta_{R\overline{R}'}\,\delta_{ab}\,\delta(1-x) + \sum_{n=1}^{\infty} a_s^n(\mu)\,{}^{RR'}\mathcal{M}_{ab}^{(n)}(x,\zeta/\mu^2)\,, \tag{3.69}$$

$$^{RR'}C_{ab}(x,\boldsymbol{z},\mu,\zeta) = \delta_{R\overline{R}'}\,\delta_{ab}\,\delta(1-x) + \sum_{n=1}^{\infty} a_s^n(\mu)\,{}^{RR'}C_{ab}^{(n)}(x,\boldsymbol{z},\mu,\zeta)\,, \tag{3.70}$$

$$^{RR'}Z_{ab}(x,\mu,\zeta) = \delta_{ab}\,\delta_{R\overline{R}'}\,\delta(1-x) + \sum_{n=1}^{\infty} a_s^n(\mu)\,{}^{RR'}Z_{ab}^{(n)}(x,\zeta/\mu^2)\,, \tag{3.71}$$

$$\widehat{Z}_a(\mu,\zeta) = 1 + \sum_{n=1}^{\infty} a_s^n(\mu)\,\widehat{Z}_a^{(n)}(\zeta/\mu^2)\,, \tag{3.72}$$

$$Z_b(\mu) = 1 + \sum_{n=1}^{\infty} a_s^n(\mu)\,Z_b^{(n)}\,. \tag{3.73}$$

We can further expand the divergent part of a perturbative coefficient $A^{(n)}$ in a Laurent series,

$$A_{\text{divergent}}^{(n)} = \sum_{m=1}^{\infty} \frac{1}{\epsilon^m}\,A^{(n,m)}\,. \tag{3.74}$$

This is a short-hand notation for the bracket operator defined in (3.6),

$$A^{(n,m)} = \left[A^{(n)}\right]_{-m}.\tag{3.75}$$

Note that due to the additional factor of $1/S_\epsilon$ in (3.61) we use a $\overline{\text{MS}}$ scheme in which renormalisation factors consist only of pure poles.

The matching coefficient $^{RR'}C_{ab}$ contains no poles,

$$^{RR'}C_{ab}^{(n,m)} = 0 \,\, \forall m > 0\,,\tag{3.76}$$

as it relates two finite matrix elements. Re-expressing its $\mathcal{O}(a_s)$ contribution in terms of these matrix elements yields

$$^{RR'}C_{ab}^{(1)}(x',x^2\zeta) = \delta_{R\overline{R}'}\,\delta_{ab}\,\delta(1-x')\widehat{Z}_a^{(1)}(x^2\zeta)$$
$$- \,^{RR'}Z_{ab}^{(1)}(x',x^2\zeta) + \,^{RR'}\widehat{\mathcal{M}}_{B,ab}^{(1)}(x',x^2\zeta/x'^2)\,.\tag{3.77}$$

After expanding (3.57) and (3.58), we obtain renormalisation prescriptions for the $\mathcal{O}(a_s)$ and $\mathcal{O}(a_s^2)$ matrix elements:

$$^{RR'}\widehat{\mathcal{M}}_{ab}^{(1)}(x,\zeta) = \delta_{R\overline{R}'}\,\delta_{ab}\,\delta(1-x)\Big(\widehat{Z}_a^{(1)}(x^2\zeta) - Z_b^{(1)}\Big) + \,^{RR'}\widehat{\mathcal{M}}_{B,ab}^{(1)}(x,\zeta)\,,\tag{3.78}$$

$$^{RR'}\mathcal{M}_{ab}^{(1)}(x',\zeta) = -\,\delta_{R\overline{R}'}\,\delta_{ab}\,\delta(1-x')Z_b^{(1)} + \,^{RR'}Z_{ab}^{(1)}(x',x'^2\zeta)\,,\tag{3.79}$$

$$^{RR'}\widehat{\mathcal{M}}_{ab}^{(2)}(x,\zeta) = \delta_{R\overline{R}'}\,\delta_{ab}\,\delta(1-x)\Big[\big(Z_b^{(1)}\big)^2 - Z_b^{(2)} + \widehat{Z}_a^{(2)}(x^2\zeta) - Z_b^{(1)}\widehat{Z}_a^{(1)}(x^2\zeta)\Big]$$
$$+ \Big(\widehat{Z}_a^{(1)}(x^2\zeta) - Z_b^{(1)} + Z_\alpha^{(1)}\Big)\,^{RR'}\widehat{\mathcal{M}}_{B,ab}^{(1)}(x,\zeta)$$
$$+ \,^{RR'}\widehat{\mathcal{M}}_{B,ab}^{(2)}(x,\zeta)\,,\tag{3.80}$$

$$^{RR'}\mathcal{M}_{ab}^{(2)}(x',\zeta) = \delta_{R\overline{R}'}\,\delta_{ab}\,\delta(1-x')\Big[\big(Z_b^{(1)}\big)^2 - Z_b^{(2)}\Big] + \,^{RR'}Z_{ab}^{(2)}(x',x'^2\zeta)$$
$$- Z_b^{(1)}\,^{RR'}Z_{ab}^{(1)}(x',x'^2\zeta)\,.\tag{3.81}$$

3.2.2 Perturbative expansion of the matching equation

Inserting the perturbative expansion (3.68) to (3.73) into the matching equation (3.67), we obtain the following relations at $\mathcal{O}(a_s)$,

$$\delta_{R\overline{R}'}\,\delta_{ab}\,\delta(1-x)\Big(\widehat{Z}_a^{(1)}(x^2\zeta) - Z_b^{(1)}\Big) + \,^{RR'}\widehat{\mathcal{M}}_{B,ab}^{(1)}(x,\zeta)$$
$$= -\,\delta_{R\overline{R}'}\,\delta_{ab}\,\delta(1-x)Z_b^{(1)} + \,^{RR'}Z_{ab}^{(1)}(x,x^2\zeta) + \,^{RR'}C_{ab}^{(1)}(x,x^2\zeta)\,,\tag{3.82}$$

and $\mathcal{O}(a_s^2)$,

$$\delta_{R\overline{R}'}\,\delta_{ab}\,\delta(1-x)\Big[(Z_b^{(1)})^2 - Z_b^{(2)} + \widehat{Z}_a^{(2)}(x^2\zeta) - Z_b^{(1)}\widehat{Z}_a^{(1)}(x^2\zeta)\Big]$$

$$+ \Big(\widehat{Z}_a^{(1)}(x^2\zeta) - Z_b^{(1)} + Z_\alpha^{(1)}\Big)^{RR'}\widehat{\mathcal{M}}_{B,ab}^{(1)}(x,\zeta) + {}^{RR'}\widehat{\mathcal{M}}_{B,ab}^{(2)}(x,\zeta)$$

$$= \delta_{R\overline{R}'}\,\delta_{ab}\,\delta(1-x)\Big[(Z_b^{(1)})^2 - Z_b^{(2)}\Big] + {}^{RR'}Z_{ab}^{(2)}(x,x^2\zeta) - Z_b^{(1)\,RR'}Z_{ab}^{(1)}(x,x^2\zeta)$$

$$+ \sum_{c,R''} {}^{R\overline{R}''}C_{ac}^{(1)}(x',x^2\zeta) \underset{x}{\otimes} \Big\{-\delta_{R''\overline{R}'}\,\delta_{cb}\,\delta(1-x')Z_b^{(1)} + {}^{R''R'}Z_{cb}^{(1)}(x',x'^2\zeta)\Big\}$$

$$+ {}^{RR'}C_{ab}^{(2)}(x,x^2\zeta)\,. \tag{3.83}$$

Rearranging the terms and using (3.77) yields formulae for the poles of ${}^{RR'}Z_{ab}^{(n)}$:

$$^{RR'}Z_{ab}^{(1,m)}(x,x^2\zeta) = \Big[\delta_{R\overline{R}'}\,\delta_{ab}\,\delta(1-x)\widehat{Z}_a^{(1)}(x^2\zeta) + {}^{RR'}\widehat{\mathcal{M}}_{B,ab}^{(1)}(x,\zeta)\Big]_{-m} \tag{3.84}$$

$$^{RR'}Z_{ab}^{(2,m)}(x,x^2\zeta) = \Big[\delta_{R\overline{R}'}\,\delta_{ab}\,\delta(1-x)\widehat{Z}_a^{(2)}(x^2\zeta) - \widehat{Z}_a^{(1)}(x^2\zeta){}^{RR'}Z_{ab}^{(1)}(x,x^2\zeta)$$

$$+ \sum_{c,R''} {}^{R\overline{R}''}Z_{ac}^{(1)}(x',x^2\zeta) \underset{x}{\otimes} {}^{R''R'}Z_{cb}^{(1)}(x',x'^2\zeta)$$

$$+ \Big(\widehat{Z}_a^{(1)}(x^2\zeta) + Z_\alpha^{(1)}\Big)^{RR'}\widehat{\mathcal{M}}_{B,ab}^{(1)}(x,\zeta)$$

$$- \sum_{c,R''} {}^{R\overline{R}''}\widehat{\mathcal{M}}_{B,ac}^{(1)}(x',x^2\zeta/x'^2) \underset{x}{\otimes} {}^{R''R'}Z_{cb}^{(1)}(x',x'^2\zeta)$$

$$+ {}^{RR'}\widehat{\mathcal{M}}_{B,ab}^{(2)}(x,\zeta)\Big]_{-m}\,. \tag{3.85}$$

Be reminded that the coefficients ${}^{RR'}C_{ab}^{(n)}$ do not contain any poles. In the second and fourth line of (3.85), we find expressions containing convolutions of δ- and plus-distributions. In particular, the treatment of two convolved plus-distributions is non-trivial. All this is examined in detail in appendix F.

To evaluate eqs. (3.84) and (3.85), one needs the ϵ-poles of the LO and NLO coefficients of $\widetilde{Z}_a$ given in eqs. (E.37) to (E.42). For $m > 1$, one can compare the results of (3.84) and (3.85) to the expressions (E.27) to (E.32) obtained in appendix E from a renormalisation group analysis. This serves as a strong cross-check for the calculated TMD matrix elements and the implementation of the right-hand sides of (3.84) and (3.85). For $m = 1$, we can extract the LO and NLO DGLAP kernels using (3.59):

$$^{RR'}P_{ab}^{(0)}(x,x^2\zeta) = -\Big[\delta_{R\overline{R}'}\,\delta_{ab}\,\delta(1-x)\widehat{Z}_a^{(1)}(x^2\zeta) + {}^{RR'}\widehat{\mathcal{M}}_{B,ab}^{(1)}(x,\zeta)\Big]_{-1} \tag{3.86}$$

$$
\begin{aligned}
{}^{RR'}P_{ab}^{(1)}(x,x^2\zeta) = -2\Bigg[& \delta_{R\overline{R}'}\,\delta_{ab}\,\delta(1-x)\widehat{Z}_a^{(2)}(x^2\zeta) + \left(\widehat{Z}_a^{(1)}(x^2\zeta) + Z_\alpha^{(1)}\right){}^{RR'}\widehat{\mathcal{M}}_{B,ab}^{(1)}(x,\zeta) \\
& - \sum_{c,R''} {}^{R\overline{R}''}\widehat{\mathcal{M}}_{B,ac}^{(1)}\big(x',x^2\zeta/x'^2\big) \underset{x}{\otimes} {}^{R''R'}Z_{cb}^{(1)}\big(x',x'^2\zeta\big) \\
& + {}^{RR'}\widehat{\mathcal{M}}_{B,ab}^{(2)}(x,\zeta)\Bigg]_{-1}.
\end{aligned}
\tag{3.87}
$$

We could further simplify eqs. (3.84) and (3.85) by recalling that in our convention of $\overline{\text{MS}}$ the renormalisation factors consist of pure poles, such that a product of two of them can only contain terms proportional to $1/\epsilon^2$ or higher.

With the formulae (3.86) and (3.87) and the TMD matrix elements based on [94,111], we are able to obtain the full DGLAP splitting kernels for unpolarised partons and transverse quarks. The explicit expression are discussed in section 3.3. For longitudinal kernels, comparable results are not available in the literature. We thus calculate the longitudinal x-dependent terms only once with the method of section 3.1 and hence lack a cross-check that is present in unpolarised and transverse case. Also, there is no direct calculation of the longitudinal $\delta(1-x)$ terms at all. However, it is in fact not necessary to calculate these terms more than once as they are polarisation *independent*.

This can be seen by analysing the cases in which no plus-momentum is carried over the final state cut, i.e. in which $x = 1$. This happens either in virtual graphs when no parton crosses the cut at all, or when the radiated partons have vanishing plus-momentum. In the first case, there is no cross-talk between the two external parton lines and so the graphs yield the same result for every spin projector. In the last case, the exchanged partons are either gluons or a quark-antiquark pair from a gluon line. In both cases, the gluon lines on the left- and right-hand-side of the final state cut can be approximated by an eikonal line entering the operator. As these lines do not depend on the polarisation, we find that the graphs with real emissions also give the same contribution to the $\delta(1-x)$ terms in every polarisation. This argumentation is of course independent from the colour representation. Consequently, there was no recalculation of the $\delta(1 - x)$ terms of the polarised NLO DGLAP kernels for PDFs in [106, 111]. Calculating the $\delta(1 - x)$ terms in the unpolarised DGLAP kernels is therefore sufficient and agreement with the transversity quark terms nothing more than a cross-check.

Having discussed both methods for the calculation of colour non-singet NLO DGLAP kernels, we are finally in the position to reap the fruits of our work and discuss the combined results of the two calculations.

3.3 Results

In sections 3.1 and 3.2 we have presented two methods to calculate the colour non-singlet DGLAP kernels. Both have their limitations: While with the first one from section 3.1 we were only able to obtain the x-dependent parts, the second one presented in section 3.2 could not provide the longitudinal polarised kernels due to missing TMD matrix elements. However, combining both methods yields the complete kernels for unpolarised

and longitudinal partons and transverse quarks. Because the x-dependent terms can be calculated with both methods, we even have a strong cross-check for a large part of the unpolarised and transverse kernels at hand. In the following, we present the results merged together from the output of both methods. The explicit expressions of the x-dependent terms are moved to appendix G due to the large amount of long expressions.

We already introduced our convention for the DGLAP kernels in section 3.1.2. For better readability, we give here the decomposition formula (3.11) again:

$$
\begin{aligned}
{}^{RR'}P_{ab}^{(n)}(x, \zeta/\mu^2) = {}&{}^{RR'}\widetilde{P}_{ab}^{(n)}(x) \\
&+ \frac{1}{2}\delta_{R\overline{R'}}\,\delta_{ab}\,\delta(1-x)\left[d_a^{(n)} + {}^{R}c^{(n)} - \frac{1}{2}{}^{R}\gamma_J^{(n)}\ln\frac{\zeta}{\mu^2}\right], \; n = 0, 1\,.
\end{aligned}
$$

$$(3.88)$$

$\delta(1-x)$ **terms.** d_a is defined such that it contains precisely all $\delta(1-x)$-terms inside the colour singlet kernels. We have derived at the end of section 3.2.2 that

$$
d_q^{(n)} = d_{\Delta q}^{(n)} = d_{\delta q}^{(n)}\,, \qquad\qquad d_g^{(n)} = d_{\Delta g}^{(n)}\,. \tag{3.89}
$$

By definition, the additional terms ${}^{R}c^{(n)}$ vanish in the colour singlet,

$$
{}^{1}c^{(n)} = 0 \;\forall n\,. \tag{3.90}
$$

For higher representations, we find that their forms only depends on the multiplicity of R, i.e. there are only three distinct expressions

$$
{}^{8}c^{(n)} = {}^{A}c^{(n)} = {}^{S}c^{(n)}\,, \quad {}^{10}c^{(n)} = {}^{\overline{10}}c^{(n)}\,, \quad \text{and} \quad {}^{27}c^{(n)}\,. \tag{3.91}
$$

What remains are the ζ-dependent terms that are uniquely defined by the anomalous dimension ${}^{R}\gamma_J^{(n)}$ in the relation (2.70).

The exact form of $d_a^{(n)}$ can be e.g. extracted from [105], equations (67) and (68):

$$
d_q^{(0)} = 3C_F\,, \qquad\qquad d_g^{(0)} = \beta_0\,, \tag{3.92}
$$

and

$$
\begin{aligned}
d_q^{(1)} = C_F^2\left(\frac{3}{4} - \pi^2 + 12\zeta_3\right) + C_F C_A\left(\frac{17}{12} + \frac{11}{9}\pi^2 - 6\zeta_3\right) \\
- C_F n_f\left(\frac{1}{6} + \frac{2}{9}\pi^2\right)\,,
\end{aligned}
\tag{3.93}
$$

$$
d_g^{(1)} = C_A^2\left(\frac{16}{3} + 6\zeta_3\right) - \frac{4}{3}C_A n_f - C_F n_f\,. \tag{3.94}
$$

As there is only one Feynman graph with real emissions at LO, we have

$$
{}^{R}c^{(0)} = 0. \tag{3.95}
$$

In the colour octet, we find

$$^{8}\gamma_J^{(0)} = 2C_A \,, \tag{3.96}$$

$$^{8}c^{(1)} = C_A^2 \left(\frac{101}{27} - \frac{11}{72}\pi^2 - \frac{7}{2}\zeta_3 \right) + C_A n_f \left(-\frac{14}{27} + \frac{1}{36}\pi^2 \right) , \tag{3.97}$$

$$^{8}\gamma_J^{(1)} = C_A^2 \left(\frac{67}{9} - \frac{1}{3}\pi^2 \right) - \frac{10}{9}C_A n_f \,. \tag{3.98}$$

The non-perturbative relation between $^{8}\gamma_J$ and TMD Collins-Soper anomalous dimension (2.65) serves as a strong cross-check. For the higher representations, we find that both ^{R}c and $^{R}\gamma_J$ exhibit Casimir scaling up to NLO:

$$\frac{^{10}c^{(1)}}{^{8}c^{(1)}} = \frac{^{10}\gamma_J^{(0)}}{^{8}\gamma_J^{(0)}} = \frac{^{10}\gamma_J^{(1)}}{^{8}\gamma_J^{(1)}} = \frac{C_{10}}{C_A} = 2 \,, \tag{3.99}$$

$$\frac{^{27}c^{(1)}}{^{8}c^{(1)}} = \frac{^{27}\gamma_J^{(0)}}{^{8}\gamma_J^{(0)}} = \frac{^{27}\gamma_J^{(1)}}{^{8}\gamma_J^{(1)}} = \frac{C_{27}}{C_A} \overset{N=3}{=} \frac{8}{3} \,, \tag{3.100}$$

where C_{10} and C_{27} are the quadratic Casimir eigenvalues of their respective gluon representation, see eq. (A.2).

x-dependent terms. The results for $^{R_1 R_2}\widetilde{P}_{ab}$ can be found in appendix G, which also includes tables for colour factors and contributions of every individual graph. The interested reader is referred to that place for all explicit expressions. At this point, let us only mention the most striking features of the results:

In the quark singlet sector $^{11}\widetilde{P}_{qq}^S$ and $^{11}\widetilde{P}_{q\bar{q}}^S$ start to differ only at NNLO due to diagrams involving three gluons in the t-channel [68]. in the colour octet, this is already the case one order lower. The reason for that is that quark and antiquarks behave differently when contracted with a colour octet projector instead of a singlet one.

After the finite renormalisation scheme change discussed in section 3.1.5, we find that helicity is conserved also in the colour octet DGLAP evolution:

$$^{11}\widetilde{P}_{\Delta q \Delta q}^{V(1)}(x) = {}^{11}\widetilde{P}_{qq}^{V(1)}(x) \,, \tag{3.101}$$

$$^{88}\widetilde{P}_{\Delta q \Delta q}^{V(1)}(x) = {}^{88}\widetilde{P}_{qq}^{V(1)}(x). \tag{3.102}$$

This is a remarkable result because helicity conservation is physically absent in colour non-singlet representations. Hence, in contrast to the colour singlet, there is no obvious choice for the colour term $^{8}\widetilde{Z}$. In (3.51), we thus opted for making it proportional to the colour singlet with the canonical factor of $c_{qq}(88)$. Looking at the shift prescription for $^{88}\widetilde{P}_{qq}^{V(1)}(x)$, eq. (3.45), it is no way trivial to assume that this choice again restores helicity conservation on the level of DGLAP evolution.

The simple scaling between the symmetric and antisymmetric octet in quark-gluon mixing channels is conserved when going from LO to NLO:

$$\frac{^{8S}\widetilde{P}_{\Sigma+g}}{^{8A}\widetilde{P}_{\Sigma-g}} = \frac{c_{qg}(8S)}{c_{qg}(8A)} = \frac{^{S8}\widetilde{P}_{g\Sigma+}}{^{A8}\widetilde{P}_{g\Sigma-}} = \frac{c_{gq}(S8)}{c_{gq}(A8)} = \frac{\sqrt{N^2-4}}{N}, \tag{3.103}$$

and similarly for polarised kernels.

For $R = 10, \overline{10}$, we find

$$^{R\overline{R}}\widetilde{P}_{gg}^{(0)} = {}^{R\overline{R}}\widetilde{P}_{gg}^{(1)} = 0 \,. \tag{3.104}$$

Thus, the whole decuplet DGLAP kernels are proportional to $\delta(1 - x)$ and thus the solution of the DGLAP equation exponentiates. The μ_i dependence of decuplet DPDs hence has the same form as the one of transverse momentum dependent distributions (see eq. (2.66)). For $R_1 = 10, \overline{10}$ and up to $\mathcal{O}(a_s^2)$ we obtain

$$\frac{d}{d\log\mu_1} {}^{R_1 R_2}F_{ga_2}(x_i, \boldsymbol{y}, \mu_i, \zeta) = \frac{1}{2}\left[d_g + {}^{10}c - \frac{1}{2}{}^{10}\gamma_J \ln\frac{x_1^2\zeta}{\mu^2}\right] {}^{R_1 R_2}F_{ga_2}(x_i, \boldsymbol{y}, \mu_i, \zeta) \,, \tag{3.105}$$

and analogously for the second parton. The DGLAP evolution of decuplet distributions is thus governed exclusively by an x-dependent anomalous dimension. Using (E.39), we can simplify (3.87) for the colour decuplet to

$$\left[d_g^{(n)} + {}^{10}c^{(n)} - \frac{1}{2}{}^{10}\gamma_J^{(n)} \ln\frac{\zeta}{\mu^2}\right] = \gamma_{F,g}^{(n)}(\zeta/\mu^2) \,, \quad n = 0, 1 \,. \tag{3.106}$$

Eq. (E.4) allows us to decompose the right-hand side into the cusp and non-cusp anomalous dimension, which yields

$$d_g^{(0)} = \gamma_g^{(0)} \,, \qquad\qquad d_g^{(1)} + {}^{10}c^{(1)} = \gamma_g^{(1)} \,, \tag{3.107}$$

and

$$^{10}\gamma_J^{(n)} = \gamma_{K,g}^{(n)} \,, \quad n = 0, 1 \,. \tag{3.108}$$

Note that the last relation correctly reproduces the Casimir scaling factor (3.99) when compared to (2.65).

In the limits $x \to 1$ and $x \to 0$, the colour non-singlet kernels become proportional to the colour singlet ones for the same channel. For $x \to 1$, the proportionality factor is simply given by the LO colour factor $c_{ab}(RR')$, e.g.

$$^{R\overline{R}}\widetilde{P}_{gg}(x \to 1) \approx c_{gg}(R\overline{R})\,{}^{11}\widetilde{P}_{gg}(x \to 1) \,. \tag{3.109}$$

Furthermore, we find that in this limit the kernels become polarisation independent. Only channels that are already active at LO have a non-vanishing contribution.

For $x \to 0$, however, the factors become functions of N and n_f and there is no simple structure anymore. It is worth noting that in both limits all kernels have the same functional behaviour in x for all colour representations. The explicit expressions can be found in appendix G.5.

Chapter 4

Evolution of colour correlated DPDs

The following chapter is based on the author's contributions to [2].

In section 4.1, we explain the code structure of expanding the `C++` library ChiliPDF designed for the evolution of colour correlated DPDs. Before evolving DPDs, we first need to define all the non-perturbative input and relevant perturbative orders, which is done in section 4.2. This allows us to finally analyse the numerical output in section 4.3.

4.1 Code structure

The `C++` library developed to DGLAP evolve colour correlated DPDs is based on the framework of ChiliPDF [76] that already allows to evolve colour singlet DPDs [97]. In the following, we will first present the structure and main features of ChiliPDF and then explain the extensions that are necessary to also treat DPDs for colour non-singlet representations.

Colour singlet implementation. ChiliPDF is based on the Chebyshev interpolation [112] of PDFs, colour singlet DPDs and DGLAP kernels on a grid in x_1 and x_2 to solve the DGLAP equation. Compared to the interpolation with splines on an equidistant grid, which is used in existing evolution codes like the LHAPDF library [113], it needs less interpolation points to achieve comparable accuracies and is thus more runtime efficient. Furthermore, it avoids "Runge's phenomenom" [114] that describes the decreasing accuracy of interpolants when approaching the endpoints of an (equispaced) interpolation grid. After discretization, the DGLAP equation becomes a matrix multiplication,

$$\frac{\mathrm{d}}{\mathrm{d}\log\mu}\overline{F}_i(\mu) = \sum_{j=0}^{N}\sum_{n=0}^{n}\left(a_s(\mu)\right)^{n+1}\overline{P}_{ij}^{(n)}\,\overline{F}_j(\mu)\,, \tag{4.1}$$

where $\widetilde{F}_i(\mu) = x_i F(x_i, \mu)$ for some grid point x_i, and

$$\overline{P}_{ij}^{(n)} = \int\limits_{x_i}^{1} \frac{\mathrm{d}z}{z} \big(z P^{(n)}(z) \big) \, b_j \bigg(\log \frac{x_i}{z} \bigg). \qquad (4.2)$$

The kernel matrices are thus independent of the distribution F and can be computed once and for all for a given grid using the barycentric basis functions b_j, which are defined with respect to the points on the Chebyshev grid. Note that in the case of DPDs F depends on two x variables and thus becomes a matrix in (x_1, x_2) space. DGLAP evolution in one x variable does not depend on the other one such that DGLAP evolutions become matrix multiplications between $\overline{P}$ and $\overline{F}$.

The running coupling $\alpha_s(\mu)$ is obtained by solving its RGE (A.5) with the Runge-Kutta algorithm DOPRI8 [76, 115, 116] and a step size of 0.2. The same algorithm is used to solve the DGLAP equation itself, now with a step size of 0.22. To minimise mixing between different flavours, the evolution is done in the evolution basis, cf. section 2.3.2. One may encounter flavour thresholds while DGLAP evolving distributions to a high scale. If this is the case, they are first evolved to the matching scale, where the matching kernels are applied, cf. section 2.3.3. This procedure is repeated until the flavour numbers of the distribution correspond to the requested one. Note that the n_f values can be chosen independently from the μ_i scales, opposing to e.g. LHAPDF.

For PDF initialization, custom models can be given as an input or a PDF set from LHAPDF is called. For DPDs, there are no fitted models available due to the lack of necessary data. Thus, models based on custom functions need to given as an input to specify the DPD at the initial scales. Our ansatz for both the colour singlet and non-singlet DPDs is discussed in section 4.2.1.

The highest level classes are PDF and DPD callers that are initialised with a certain LHAPDF specifier (and some model for the initial conditions in the DPD case), all relevant perturbative orders, the initial conditions for α_s and grid information. One may then call the distribution at given $(n_{f1}, n_{f2}, x_1, x_2, \mu_1, \mu_2)$ (and, in the case of DPDs, y), which performs the DGLAP evolution as described above and finally interpolates in x_i (and y) if necessary. A variety of related calls to calculate e.g. integrals in y or Mellin moments, both relevant for the colour singlet sum rules discussed, are also provided. Finally, one can also calculate complete DPD luminosities as defined in (2.12).

Colour non-singlet implementation. To extend the framework to the colour non-singlet DGLAP evolution, we first need to establish additional degrees of freedom, namely the colour representations $(R_1 R_2)$ for calls of the new colour non-singlet DPD objects. The objects that store the discretized DPDs need to be expanded to be able to cope with all allowed colour-flavour combinations.

A colour correlated DPD evolved to from starting scales $\big((\mu_{01}, \mu_{02}), \zeta_0\big)$ to arbitrary

scales $\big((\mu_1, \mu_2), \zeta\big)$ has the form

$$
F(x_i, \boldsymbol{y}, \mu_i, \zeta) = \exp\left\{ \frac{1}{2} J(\boldsymbol{y}, \mu_i) \log \frac{\zeta}{\zeta_0} - \sum_{i=1,2} \int\limits_{\mu_{0i}}^{\mu_i} \frac{\mathrm{d}\mu}{\mu} \gamma_J(\mu) \log \frac{\sqrt{\zeta_0}}{\mu} \right\}
$$
$$
\times \int \left(\prod_{i=1,2} \mathrm{d}x_i' \, U(x_i', x_i, \mu_{0i}, \mu_i) \right) \widehat{F}_{\mu_{0i}, \zeta_0}(x_i', \boldsymbol{y}, \mu_{0i}) \,, \qquad (4.3)
$$

where $\widehat{F}$ is defined in (2.72). For better readability, we drop parton and colour labels here and in the following. The first line of (4.3) is the conversion from a F-DPD to a $\widehat{F}$-DPD with integrated CS evolution. The evolution operators U are obtained from a discretized version of the DGLAP equation (2.74) in the same manner as eq. (4.1). Hence, the integrals over x_i' are evaluated numerically via a matrix multiplication. All of these steps are implemented in a factorised form, using different classes and their interdependencies for every calculational step.

The Collins-Soper kernel ^{R}J is an entirely new object that has no equivalent in the colour singlet case. We define a new class that handles the initialization as explained in section 4.2.2 and its RGE running based on (4.41). The integrals of $^{R}\gamma_J$ appearing there and the transformation of "$\widehat{F}$-distributions" are solved by implementing the analytical results derived in [117] in a seperate class. Note that flavour matching kernels for the Collins-Soper kernel have non-vanishing contributions from heavy quark loops starting at $\mathcal{O}(a_s^2)$. Such effects are not implemented and exploring their impact is left to future work.

Compared to the colour singlet, the DGLAP equation for $\widehat{F}$, eq. (2.74), contains an additional term proportional to $\log(x)$ whose absolute size becomes large for small x. Colour non-singlet solutions thus exhibit a steeper form than colour singlet ones, which requires a finer Runge-Kutta step size. From the quadratic Casimir operators (A.2) one directly sees that

$$
^{27}\gamma_J > \,^{10}\gamma_J > \,^{8}\gamma_J > 0 \,, \qquad (4.4)
$$

such that the step size decreases for increasing colour dimension. We find that the step sizes $(0.15, 0.07, 0.02)$ for $R = 8, 10, 27$ satisfy closure tests for the created kernel matrices to a precision of order $\mathcal{O}(10^{-8})$ for a grid down to $x = 10^{-5}$. The relative runtime factor for the calculation of kernel matrices in the colour singlet is around 8.5 at LO and 6.5 at NLO. This is the part of the calculation in which runtime increases by far the most. However, in grids suited for interpolation the majority of overall runtime is needed for the *multiplication* of matrices, which remains unchanged when going from colour singlet to non-singlet DPDs.

Since we derived the DGLAP equation for "$\widehat{F}$-distributions", the transformation formula (2.72) back to the "F-distributions" needs to be applied in a higher level class that manages the convolution with the kernel matrices (4.2). The flavour matching needs to be extended to the colour non-singlet formulae (G.20) and (G.21), whilst α_s requires no change at all.

flavour number	colour singlet	colour non-singlet	ratio
n_f	$(2n_f)^2 + 4n_f + 1$ $= (2n_f + 1)^2$	$(2n_f)^2 + 8n_f + 7$ $= (2n_f + 1)^2 + 4n_f + 6$	$1 + \frac{2}{2n_f+1} + \frac{4}{(2n_f+1)^2}$
3	49	67	~ 1.37
4	81	103	~ 1.27
5	121	147	~ 1.21
6	169	199	~ 1.18

Table 4.1: Number of distributions for given n_f. In the fourth column, we give the relative number of colour non-singlet distributions compared to the colour singlet ones. In the first entry of the second and third column, we sum contributions from (qq), mixing terms and (gg) in that order.

For a lot of classes, code could be recycled by templatising the existing classes over a switch between types defined for colour singlet or non-singlet DPDs. Due to the absence of sum rules for the colour non-singlet sector, there are no special calling routines apart from a caller for the DPD itself. The runtime for a DGLAP and Collins-Soper evolution including flavour matching from $n_f = 4$ to $n_f = 5$ grows by a factor of around 1.8 compared to the colour singlet, both at LO and NLO. We find this to be a reasonable relative increase given the additional Collins-Soper evolution and more complex form of the DGLAP equation. Note that the increase in runtime is partly due to larger number of colour non-singlet distributions, as shown in table 4.1). This ratio between colour singlet and non-singlet marks the lower limit for optimisation efforts and lies between 1.2 and 1.3 for $n_f = 4, 5$.

We have designed a variety of different test cases to check every part of the code as much as possible. Besides regression tests for every class and numerical checks of all perturbative coefficients and their application, more advanced tests are also performed: We designed closure tests for the discretized DGLAP evolution operators $\underline{U}(\mu_0, \mu_1)$ that check

$$\underline{U}(\mu_0, \mu_1) \cdot \underline{U}(\mu_1, \mu_0) = \mathbb{1} \, . \tag{4.5}$$

Similar checks are performed for the CS evolution. These tests are also extended to DPD callers by checking if the output remains unchanged (up to some discretization and numerical errors) after forward and backward evolution.

We derived in eq. (3.105) that the evolution of gluon distributions in the decuplet representations contains no convolution in x. As we use the same formalism for every evolution channel we can test the whole the implementation by comparing the Runge-Kutta solution of this differential equation with the analytical one.

DGLAP evolution and flavour matching in the (μ_1, μ_2) plane allows for several options for the ordering of operations. Examples for such paths are shown in figure 2.4. Path independence of the results for the evolved DPD is a strong check for the consis-

tency of the whole code.

Treatment of rapidity.   At the level of DPD luminosities (2.12) only the product

$$\sqrt{\zeta\bar{\zeta}} = s = \frac{M_1 M_2}{\sqrt{x_1\,x_2\,\bar{x}_1\,\bar{x}_2}} \tag{4.6}$$

appears inside the Sudakov exponential (cf. eq. (2.38)). This is because

$$F(x_i, \boldsymbol{y}, \mu_i, \zeta)\,F(\bar{x}_i, \boldsymbol{y}, \mu_i, \bar{\zeta})$$

$$= \exp\left[{}^{R}J(\boldsymbol{y}, \mu_i)\,\log\frac{\sqrt{\zeta\bar{\zeta}}}{\zeta_0}\right] F(x_i, \boldsymbol{y}, \mu_i, \zeta_0)\,F(\bar{x}_i, \boldsymbol{y}, \mu_i, \zeta_0)\,, \tag{4.7}$$

where we assume that both DPDs are defined at some arbitrary reference scale ζ_0. Here, ζ, x_1, x_2 ($\bar{\zeta}$, $\bar{x}_1$, $\bar{x}_2$) are the rapidity scale and momentum fractions of the DPD describing the right- (left-) moving proton. R is equal to 8, 10 or 27 depending on the colour multiplicity which needs to be equal for both DPDs. M_i describe the invariant masses of the two hard processes. The values of μ_i are typically chosen to be of order of the hard scales Q_i such that large logarithms are avoided. Note that $M_i \geq Q_i$, where the limiting case of equality is fulfilled for an LO partonic cross section with no additional radiations.

Based on (4.6) one can argue that opposing to the case of μ_i there is no physically preferred values for ζ and $\bar{\zeta}$. Both values cannot be chosen independently from one another and ultimately each rapidity choice for one DPD needs to be compensated by the other one. The choice

$$\zeta = \frac{M_1 M_2}{x_1\,x_2}\,, \qquad\qquad \bar{\zeta} = \frac{M_1 M_2}{\bar{x}_1\,\bar{x}_2} \tag{4.8}$$

obviously fulfils (4.6). An additional Collins-Soper step

$$F(x_i, \boldsymbol{y}, \mu_i, \tfrac{M_1 M_2}{x_1 x_2})\,F(\bar{x}_i, \boldsymbol{y}, \mu_i, \tfrac{M_1 M_2}{\bar{x}_1 \bar{x}_2})$$

$$= \exp\left\{{}^{R}J(\boldsymbol{y}, \mu_i)\,\log\frac{M_1 M_2}{\mu_1\mu_2}\right\} F(x_i, \boldsymbol{y}, \mu_i, \tfrac{\mu_1\mu_2}{x_1 x_2})\,F(\bar{x}_i, \boldsymbol{y}, \mu_i, \tfrac{\mu_1\mu_2}{\bar{x}_1 \bar{x}_2}) \tag{4.9}$$

reveals that for $\mu_i \sim Q_i$ and sufficiently large y values of M_i away from the LO configuration are suppressed by a power law that goes with ${}^{R}J$.

We thus choose to store and call colour non-singlet DPDs not at a constant rapidity scale, but at

$$\zeta = \frac{\xi}{x_1 x_2}\,, \tag{4.10}$$

where ξ is independent from x_1 and x_2. Additional to the discussion above a practical reason is that DPDs become steeper in x_1 and x_2 for constant ζ. Thus, an interpolation needs denser grids and thus the matrix multiplications require more runtime in this case. Eq. (4.9) implies that a natural choice at given hard scales is

$$\xi = \mu_1\mu_2\,. \tag{4.11}$$

Note that $\widehat{F}$ in (2.72) needs to be defined with respect to a constant ζ_0. This can be realised with an additional CS step in (4.3),

$$F\big(x_i, \boldsymbol{y}, \mu_{0i}, \xi_0/(x_1 x_2)\big) = \exp\left\{ -J(\boldsymbol{y}, \mu_{0i}) \log\sqrt{x_1 x_2} \right\} \widehat{F}_{\mu_{0i}, \xi_0}(x_i, \boldsymbol{y}, \mu_{0i}). \qquad (4.12)$$

4.2 Models and ansätze

To evolve DPDs, we first need to describe them at some initial scales by an model (section 4.2.1). In section 4.2.2 we develop an ansatz for the Collins-Soper kernel ^{R}J and after that, in section 4.2.3, define configurations of orders for all perturbative objects.

4.2.1 DPD

Following [57, 118], we choose the decomposition

$$^{R_1 R_2}F_{a_1 a_2}(x_1, x_2, \boldsymbol{y}, \mu, \zeta) = {}^{R_1 R_2}F_{a_1 a_2, \text{int}}(x_1, x_2, \boldsymbol{y}, \mu, \zeta)$$
$$+ {}^{R_1 R_2}F_{a_1 a_2, \text{spl}}(x_1, x_2, \boldsymbol{y}, \mu, \zeta) \qquad (4.13)$$

as the model for the input DPDs. The first term represents the "intrinsic" part of the DPD, i.e. the part that stems from the wave function of the proton itself. Assuming that the partons a_1 and a_2 are uncorrelated, we can write it as a convolution of two impact parameter dependent PDFs with minor modifications,

$$^{R_1 R_2}F_{a_1 a_2, \text{int}}(x_1, x_2, \boldsymbol{y}, \mu, \zeta) = n(a_1 a_2)\, r(R_1 R_2) \int d^2 \boldsymbol{b}\, f(x_1, \boldsymbol{b} + \boldsymbol{y}, \mu)\, f(x_2, \boldsymbol{b}, \mu). \qquad (4.14)$$

$n(a_1 a_2)$ and $r(R_1 R_2)$ are defined further down below. In the following, we will call this part the product ansatz. If we describe the $\boldsymbol{b}$-dependence through a Gaussian distribution,

$$f_a(x, \boldsymbol{b}, \mu) = \frac{1}{4 h_a} \exp\left[-\frac{b^2}{4 h_a} \right] f(x, \mu), \qquad (4.15)$$

we arrive at the initial condition

$$^{R_1 R_2}F_{a_1 a_2, \text{int}}(x_1, x_2, \boldsymbol{y}, \mu_{y^*}, \zeta) = \frac{1}{4\pi h_{a_1 a_2}}\, n(a_1 a_2)\, r(R_1 R_2)\, \rho_{a_1 a_2}(x_1, x_2)$$
$$\times \exp\left[-\frac{y^2}{4 h_{a_1 a_2}} \right] f_{a_1}(x_1, \mu_{y^*}) f_{a_2}(x_2, \mu_{y^*}). \qquad (4.16)$$

The second term on the right-hand side of (4.13) is initialised as

$$^{R_1 R_2}F_{a_1 a_2, \text{spl}}(x_1, x_2, \boldsymbol{y}, \mu_{y^*}, \zeta) = n(a_1 a_2) \exp\left[-\frac{y^2}{4 h_{a_1 a_2}} \right]$$
$$\times {}^{R_1 R_2}F_{a_1 a_2, \text{spl}, \text{pt}}(x_1, x_2, \boldsymbol{y}, \mu_{y^*}, \zeta). \qquad (4.17)$$

It takes into account short distance "splitting" effects, where one parton a_0, coming from a PDF, splits into two. The last factor depends on the perturbative order at which the DPD matching formula (2.68) for small y is evaluated. The LO expression used in our numerical implementation reads [118]

$$^{R_1 R_2}F_{a_1 a_2, \text{spl,pt}}(x_1, x_2, \boldsymbol{y}, \mu_{y^*}, \zeta) = \frac{1}{\pi y^2} \frac{\alpha_s(\mu_{y^*})}{2\pi} \, ^{R_1 R_2}P_{a_1 a_2, a0}\left(\frac{x_1}{x_1 + x_2}\right) \frac{f_{a_0}(x_1 + x_2, \mu_{y^*})}{x_1 + x_2}. \tag{4.18}$$

For small y, it dominates the $^{R_1 R_2}F_{a_1 a_2}$ through its characteristic $1/y^2$ behaviour. In equations (4.16), (4.17) and (4.18) we have used the following building blocks:

* $f_a(x, \mu)$ is an ordinary PDF. Its parametrization at initial scales will be discussed in section 4.2.3.

* $\alpha_s(\mu)$ is the strong coupling. We choose to solve the β-equation (A.5) numerically using a Runge-Kutta algorithm. Its perturbative order will be discussed in section 4.2.3.

* The initial conditions are given at the starting scales

$$\mu_{y^*} = \frac{b_0}{y^*(y)}. \tag{4.19}$$

$b_0 \approx 1.123$ is defined in (A.7). Analogously to TMDs,

$$y^*(y) = \frac{y}{\left(1 + \frac{y^4}{y_{\max}^4}\right)^{\frac{1}{4}}}, \quad y_{\max} = \frac{b_0}{2} \, \text{GeV}^{-1}, \tag{4.20}$$

ensures that μ_{y^*} stays in the perturbative region for large y with a lower bound of $\mu_{y^*,\min} = 2\,\text{GeV}$. We adopt the convention for the functional form of y^* from [92]. For small y, μ_{y^*} behaves like the natural scale choice b_0/y which avoids large logarithms. The fourth power in the denominator ensures that this limiting behaviour is approached more rapidly than the commonly used second power.

* The factor

$$\rho_{a_1 a_2}(x_1, x_2) = \frac{(1 - x_1 - x_2)^2}{(1 - x_1)^2 (1 - x_2)^2} \tag{4.21}$$

leads to vanishing DPDs for $x_1 + x_2 > 1$, as required by phase space restrictions. Compared to a phase space factor that only consists of the numerator on the right-hand side, this form also satisfies the sum rules in the colour singlet sector reasonably well [25].

* "Number effects" are implemented via the factor

$$n(a_1 a_2) = \begin{cases} 0 & \text{if } (a_1, a_2) = (d^-, d^-) \\ \frac{1}{2} & \text{if } (a_1, a_2) = (u^-, u^-) \\ 1 & \text{else} \end{cases} \tag{4.22}$$

to make up for the fact that there are two valence up-quarks and only one valence down-quark inside the proton[1].

* $h_{a_1 a_2}$ is the Gaussian width in y. From (4.14) it is obvious that

$$h_{a_1 a_2} = h_{a_1} + h_{a_2} \,. \tag{4.23}$$

For the single partonic widths, we choose [57]

$$h_a = \begin{cases} 2.33 \,\mathrm{GeV}^{-2} & \text{if } a = g \\ 3.493 \,\mathrm{GeV}^{-2} & \text{otherwise} \end{cases} . \tag{4.24}$$

* The splitting kernels ${}^{R_1 R_2}P_{a_1 a_2, a_0}$ describe the matching for small y of DPD with parton flavours (a_1, a_2) onto a PDF of parton a_0. At LO, these kernels are proportional to the LO DGLAP kernels,

$$ {}^{R_1 R_2}P^{(0)}_{a_1 a_2, a_0} = c_{a_1 a_2, a_0}(R_1 R_2) \, {}^{R_1 R_2}P^{(0)}_{a_0 a_1} \,, \tag{4.25}$$

where the colour factors $c_{a_1 a_2, a_0}(R_1 R_2)$ are given in eq. (4.5) of [119] and $c_{a_1 a_2, a_0}(11) = 1$. Equivalent expressions exist for polarised quarks a_1 and a_2 with the initial quark a_0 staying unpolarised. The splitting kernels are calculated up to NLO in colour singlet [120] and non-singlet [119] representations. However, as there is no existing numerical implementation of the NLO kernels available, we use the LO form throughout.

* $r(R_1 R_2)$ incorporates the colour dependence of the model. We derive the values from two assumptions: First, we adopt the ansatz for colour singlet DPDs from [57, 118], i.e. we set

$$r(11) = 1 \tag{4.26}$$

for all parton flavours. Second, we saturate the positivity bounds[2] for s-channel DPDs introduced in section 2.2.1, using the transformation matrices given in appendix B.2. In other words, we set DPDs in only one s-channel representation to non-zero at $\mu_i = \mu_{y^*}$. Both sets of distributions, ${}^{R_1 R_2}\vec{F}_{a_1 a_2}$ and $\vec{F}^{R_1 R_2}_{a_1 a_2}$, are connected via linear transformation matrices:

$$ {}^{R_1 R_2}\vec{F}_{a_1 a_2} = K^{a_1 a_2}_{ts} \cdot \vec{F}^{R_1 R_2}_{a_1 a_2} \,. \tag{4.27}$$

All matrices $K^{a_1 a_2}_{ts}$ are given in appendix B.2. A saturated s-channel vector then has the form

$$\vec{F}^{R_1 R_2}_{a_1 a_2} \propto \vec{e}_j \,, \tag{4.28}$$

---

[1]Note that the definition above is only valid in a basis that contains the valence distributions $q^- = q - \bar{q}$ as basis elements.

[2]Note that these bounds were derived in [27] for unrenormalised DPDs. It was later shown in [89] that renormalised DPDs in fact violate these bounds. However, due to the lack of better guidance, we still take them as the starting point for our model.

where $\vec{e}_j$ is some unit vector that indicates the non-vanishing s-channel colour representation and can be chosen freely. For an arbitrary flavour pair $(a_1 a_2)$, this leads to

$$r(R_1 R_2) = \left(K_{ts}^{a_1 a_2}\right)_{ij} \Big/ \left(K_{ts}^{a_1 a_2}\right)_{1j} , \tag{4.29}$$

where i is the row index that corresponds to the representation pair $(R_1 R_2)$. Note that the mixing between different representations minimises when we take

$$\left(11, SS, AA, SA, AS, 10_{\mathrm{Re}}\,10_{\mathrm{Re}}, 10_{\mathrm{Im}}\,10_{\mathrm{Im}}, 27\,27\right) \tag{4.30}$$

for the t-channel and

$$\left(11, SS, AA, 10\,\overline{10}, \overline{10}\,10, 27\,27, \mathrm{Re}(SA), \mathrm{Im}(SA)\right) \tag{4.31}$$

for the s-channel as independent linear combinations. The new representations can be obtained from the old ones introduced in eq. (2.25) by

$$10_{\mathrm{Re}}\,10_{\mathrm{Re}} = \mathrm{Re}(10\,\overline{10}) = \frac{1}{2}\left(10\,\overline{10} + \overline{10}\,10\right) , \tag{4.32}$$

$$10_{\mathrm{Im}}\,10_{\mathrm{Im}} = \mathrm{Im}(10\,\overline{10}) = \frac{i}{2}\left(\overline{10}\,10 - 10\,\overline{10}\right) , \tag{4.33}$$

$$\mathrm{Re}(SA) = \frac{1}{2}\left(AS + SA\right) , \tag{4.34}$$

$$\mathrm{Im}(SA) = \frac{i}{2}\left(AS - SA\right) . \tag{4.35}$$

In all other colour representations, DPDs are real valued [58].

Due to lack of better guidance, our standard choice for j will be the representation with the same behaviour under charge conjugation as the one of the initiating parton flavour for an LO splitting into the flavour pair of interest, i.e.

$$(q\bar{q}) : (88),\ j = 2 ; \qquad\qquad (qg) : (3\bar{3}),\ j = 1 ; \tag{4.36}$$
$$(\bar{q}g) : (3\bar{3}),\ j = 1 ; \qquad\qquad (gg), \mathrm{P1} : (AA),\ j = 3 . \tag{4.37}$$

For pairs without an LO splitting graph, we choose

$$(qq) : (3\bar{3}),\ j = 1 ; \qquad\qquad (\bar{q}\bar{q}) : (3\bar{3}),\ j = 1 . \tag{4.38}$$

Note that for the flavour pairs in (4.36) and (4.37), the factors $r(R_1 R_2)$ correspond to the LO splitting kernel colour factors [91]. In particular, there is a vanishing decuplet contribution $r(10_{\mathrm{Re}}\,10_{\mathrm{Re}}\,10_{\mathrm{Im}}\,10_{\mathrm{Im}}) = r(10_{\mathrm{Im}}\,10_{\mathrm{Im}}\,10_{\mathrm{Re}}\,10_{\mathrm{Re}}) = 0$ in that constellation, which we called "P1". To also get an impression of decuplet distributions under evolution, in some occasions we set F_{gg}^{11} instead of F_{gg}^{AA} to non-zero,

$$(gg), \mathrm{P2} : (11),\ j = 1 . \tag{4.39}$$

Here, we find $r(10_{\mathrm{Re}}\,10_{\mathrm{Re}}) \neq 0$.

4.2.2 Collins-Soper kernel

Our ansatz for the Collins-Soper kernel (2.44) reads

$$
{}^R J(y, \mu_{y^*}, \mu_{y^*}) = {}^R J_{\text{pert}}\big(y^*(y), \mu_{y^*}, \mu_{y^*}\big) + {}^R \Delta J(y) \,. \tag{4.40}
$$

The conventions for the starting scale μ_{y^*} and y^*-prescription are given in equations (4.19) and (4.20), respectively. Note that the ansatz depends only on $|\boldsymbol{y}| = y$. ${}^R J$ at arbitrary scales (μ_1, μ_2) can obtained by solving its RGE (2.42),

$$
{}^R J(y, \mu_1, \mu_2) = {}^R J(y, \mu_{y^*}, \mu_{y^*}) - \sum_{i=1,2} \int_{\mu_{y^*}}^{\mu_i} \frac{\mathrm{d}\mu}{\mu} \, {}^R \gamma_J(\mu) \,. \tag{4.41}
$$

Let us have a closer look at the ansatz (4.40):

* The first term of (4.40) can be expanded in α_s,

$$
{}^R J_{\text{pert}}(y, \mu) = \sum_{n=1} \alpha_s^n(\mu) \, {}^R J_{\text{pert}}^{(n)}(y, \mu) \,. \tag{4.42}
$$

  Evaluating it at μ_{y^*} ensures that $\alpha_s(\mu_{y^*})$ stays perturbative for all values of y. The equality between ${}^8 J$ and the gluon TMD Collins-Soper kernel, eq. (2.64) gives us access to the colour octet coefficients of (4.42) up to $\mathcal{O}(\alpha_s^3)$ by using the results given in appendix D.2 of [94],

$$
{}^8 J_{\text{pert}}^{(n)}(y, \mu) = -2 C_A \sum_{k=0}^{n} d_{[94]}^{(n+1,k)} \log^k \frac{\mu^2 y^2}{b_0^2} \,. \tag{4.43}
$$

  Note that the logarithm on the right-hand side vanishes for the scale arguments in (4.40). For higher colour representations we assume Casimir scaling, i.e.

$$
{}^R J_{\text{pert}}(y, \mu) = \frac{C_R}{C_A} \, {}^8 J_{\text{pert}}(y, \mu), \ R = 10, 27 \,. \tag{4.44}
$$

* The second term of (4.40) reflects the non-perturbative behaviour of the Collins-Soper kernel at large y. Due to the lack of experimental or lattice data, we again need to fall back to the Collins-Soper kernels for TMDs. To the present day, there are fits [121–124] and lattice results [125–127] available only for the non-perturbative part of K_q. In lack of better options we thus assume Casimir scaling between the non-perturbative parts of K_g and K_q. This is motivated by the fact that their perturbative parts are connected via Casimir scaling up to $\mathcal{O}(\alpha_s^3)$ [94]. The connection to ${}^8 \Delta J$ is then made with the help of (2.64), while for higher colour representations we again assume Casimir scaling,

$$
{}^R \Delta J(y) = \frac{C_R}{C_A} \, {}^8 \Delta J(y), \ R = 10, 27 \,. \tag{4.45}
$$

Our choices for the non-perturbative parts are based on fits for $g(b)$ in

$$K_q(\boldsymbol{b}, \mu) = K_{q,\text{pert}}(b^*(b), \mu) + g(b) .\qquad(4.46)$$

Note that we cannot assign the non-perturbative part of some ansatz directly to our $^8\Delta J$ as K_q in a given decomposition (4.46) is evaluated at some $b^*(b)$, which may differ from our $y^*(b)$. To find the correct expression for the non-perturbative part in our ansatz (4.40) we equate both ansätze at the same scale μ_{y^*} and obtain

$$^8\Delta J(y) = {}^8J_{\text{pert}}\big(b^*(y), \mu_{y^*}\big) - {}^8J_{\text{pert}}\big(y^*(y), \mu_{y^*}\big) + \frac{C_A}{C_F}\, g(y)\qquad(4.47)$$

after making use of (2.64). Note that for reasons of simplicity, both perturbative quantities in (4.47) are expanded in α_s that is extracted from the PDF fit, not the fit of $g(b)$.

In the following, we list all the fits for $g(b)$ and $b^*(b)$ that we will use in the numerical studies:

SV19, [121]: $g(b) = -0.085 \cdot b\, b^*(b)$

$$b^*(b) = \frac{b}{\sqrt{1 + \frac{b^2}{1.93\,\text{GeV}^{-1}}}}\qquad(4.48)$$

HSV20C2, [122]: $g(b) = -0.064 \cdot b^2$

$$b^*(b) = \frac{b}{\sqrt{1 + \frac{b^2}{2.2\,\text{GeV}^{-1}}}}\qquad(4.49)$$

HSV20C6, [122]: $g(b) = -0.100 \cdot \big(b^*(b)\big)^2$

$$b^*(b) = \frac{b}{\sqrt{1 + \frac{b^2}{2.43\,\text{GeV}^{-1}}}}\qquad(4.50)$$

MAP22, [123]: $g(b) = -0.031 \cdot b^2$

$$b^*(b) = b_0\,\text{GeV}^{-1} \cdot \left(1 - \exp\big(-\tfrac{b^4}{(b_0\,\text{GeV}^{-1})^4}\big)\right)^{\frac{1}{4}}\qquad(4.51)$$

ART23, [124]: $g(b) = -\left(0.074 + 0.116 \cdot \log \frac{b^*(b)}{1.496\,\text{GeV}^{-1}}\right) b\, b^*(b)$

$$b^*(b) = \frac{b}{\sqrt{1 + \frac{b^2}{1.496\,\text{GeV}^{-1}}}}\qquad(4.52)$$

Figure 4.1 shows the shape of $^8J(y, 2\,\text{GeV})$ using these fits. For fixed μ, the large logarithms inside the perturbative part (4.43) drive the Collins-Soper kernel to positive values at small y. The behaviour at large y is determined by the functional forms of $^R\Delta J(y)$ given in eqs. (4.48) to (4.52).
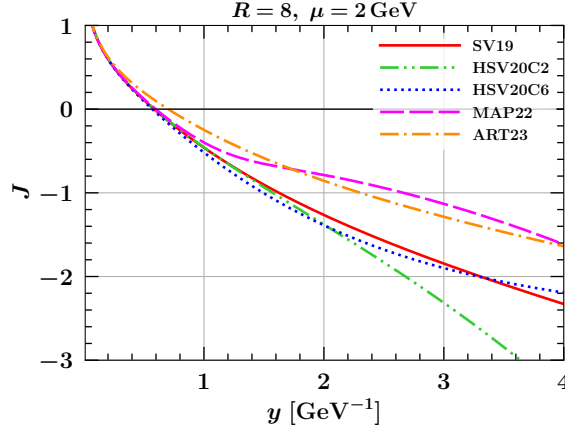
Figure 4.1: $^8J(y, 2\,\text{GeV})$ at NNLL for different fits of $g(y)$ specified in eqs. (4.48) to (4.52).

4.2.3 Perturbative orders

There is a variety of different perturbative ingredients appearing in the DPD ansatz (4.13) and its evolution equations. We will discuss their handling one-by-one in the list below. Table 4.2 summarises the different configurations of perturbative orders. In the following, we briefly present all perturbative quantities that appear in our ansätze and evolution equations.

* This work focuses on the effects of the DGLAP equation (2.74), especially the impact of the new NLO kernel calculated in chapter 3 compared to the already existing ones [26]. While solving the DGLAP equation, flavour matching may be necessary. The perturbative order of the corresponding matching kernels is chosen equal to the one for DGLAP kernels.

* By solving its RGE (A.5) with the expanded β-function we obtain the running coupling $\alpha_s(\mu)$. The perturbative order of $\beta(\alpha_s)$ matches the one of the DGLAP kernels to obtain a consistent solution of the DGLAP equation (2.74).

The β-function (A.5) itself appears in the RGE integrals inside the Sudakov factor (2.73) after a change of variables,

$$\int_{\mu_0}^{\mu_1} \frac{\mathrm{d}\mu}{\mu} \, ^R\gamma_J(\mu) = \int_{\alpha_s(\mu_0)}^{\alpha_s(\mu_1)} \frac{\mathrm{d}\alpha}{\beta(\alpha)} \, ^R\gamma_J(\alpha)\,, \tag{4.53}$$

$$\int_{\mu_0}^{\mu_1} \frac{\mathrm{d}\mu}{\mu} \, ^R\gamma_J(\mu) \log\frac{\mu}{\mu_0} = \int_{\alpha_s(\mu_0)}^{\alpha_s(\mu_1)} \frac{\mathrm{d}\alpha}{\beta(\alpha)} \, ^R\gamma_J(\alpha) \int_{\alpha_s(\mu_0)}^{\alpha} \frac{\mathrm{d}\alpha'}{\beta(\alpha')}\,. \tag{4.54}$$

	$\beta(\alpha_s)$	$\alpha_s(\mu)$	$^R\gamma_J$	J_{pert}	DGLAP	PDF fit
LL	LO	LO	LO	LO	LO	LO
NLL	NLO	LO	NLO	LO	LO	LO
NLL$'$	NLO	NLO	NLO	NLO	LO	NLO
NNLL	NNLO	NLO	NNLO	NLO	NLO	NLO

Table 4.2: Sets of perturbative orders used for the numerical studies. The convention is adapted to [128, 129].

Note that there is no need to solve these integrals numerically as closed analytical solutions are provided in [117]. In table 4.2, we distinguish between the perturbative order of the β-function inside (4.54) and $\alpha_s(\mu)$. Motivated by arguments derived in [128, 129], we choose the latter to agree with the perturbative order of the DGLAP kernels and the former to agree with the perturbative order of $^R\gamma_J$.

∗ The perturbative part of the Collins-Soper kernel can be extracted from [94], as explained below (4.42).

∗ The anomalous dimension $^R\gamma_J$ takes the role of a cusp anomalous dimension (2.42). The LO and NLO expressions can be found in eqs. (3.98) and (3.100), whilst we use $^8\gamma_J = \frac{1}{2}\gamma_{K,g}$ and assume Casimir scaling at NNLO. The NNLO expression of $\gamma_{K,g}$ can be found in [94].

The usual convention [128,129] is to count large logarithms as α_s^{-1} and thus expand the cusp anomalous dimension to one order higher in α_s than the perturbative part of the Collins-Soper kernel and the non-cups anomalous dimension. A primed logarithmic order such as NLL$'$ indicates that all ingredients are expanded to the same perturbative order. We deviate from this rule at LL, where both γ_J and the DGLAP kernels are taken at $\mathcal{O}(\alpha_s)$.

∗ In the splitting ansatz (4.17), short distance splitting kernels occur. As explained in section 4.2.1, the LO kernels are chosen for every configuration due to the lack of an implementation at NLO.

∗ Both parts of our model (4.13) use PDFs as main ingredients. We work with the latest parametrisations of the MSHT working group, MSHT20 [130]. For the NLO fit, the parameters for $\alpha_s(M_Z) = 0.118$ are chosen. For reasons of consistency, the perturbative order of the fit corresponds to the one for $\alpha_s(\mu)$ and the DGLAP kernels.

4.3   Quantitative studies

After introducing the underlying code, models and ansätze, we are in the position to present and discuss the effects of combined DGLAP and CS evolution of colour non-singlet DPDs. The results of chapter 3 enable us to extend this analysis not only to LL, but full NLL′ accuracy.

Typical DPS events as introduced in chapter 1 include heavy flavour and jet production as well as double Drell-Yan processes. Therefore, we choose to evolve the DPDs to the typical scales of $10\,\mathrm{GeV}$ for low-p_T jets, and $80\,\mathrm{GeV}$ for high-p_T jets and double Drell-Yan production.

For central events with vanishing final state rapidities, the formulae (2.10) yield x-values of around 7×10^{-4} and 6×10^{-3}, if we assume the centre-of-mass energy of the LHC, $\sqrt{s} = 14\,\mathrm{TeV}$. To cover a wide kinematical region of $|Y_i| \lesssim 4$, we need to take DPD values of up to $x_i \sim \mathcal{O}(10^{-5})$ into account.

Hence, we use the grids

$$(10^{-5}, 5 \times 10^{-3}, 0.5, 1)_{[16,16,24]} \qquad \text{(colour singlet)} \qquad (4.55)$$

and

$$(10^{-5}, 3 \times 10^{-4}, 10^{-2}, 0.5, 1)_{[16,16,24,24]} \qquad \text{(colour non-singlet)} \qquad (4.56)$$

to discretize the DPDs in x_i. For y, we use the grids

$$(10^{-2}, b_0/m_b)_{[16]} \,;\, (b_0/m_b, b_0/m_c, 5, \infty)_{[16,12,12]} \qquad (4.57)$$

for both colour singlet and non-singlet. The brackets contain the end-points of the subgrids, while the subscript contains the corresponding number of subgrid points. The grid notation together with the settings for colour singlet DPDs is taken from [97]. A comprehensive discussion on different grid transformations is given in the same place. The main reason for larger grids for colour non-singlet DPDs is the additional steepness introduced by the CS Sudakov factor, which makes the DPDs harder to approximate numerically.

The x-grids are not chosen equispaced in x_i itself, but in

$$u(x) = \log x \,. \qquad (4.58)$$

For y, we use a composite grid made out of two independent subgrids. The first one for small y uses an inverse power law transformation

$$u(y) = -y^{-0.2} \,, \qquad (4.59)$$

and the second one a Gaussian transformation

$$u(y) = -\exp\left(-(m^2 y^2 + my)/4\right), \; m = \sqrt{\frac{1}{4h_{gg}}}\,\mathrm{GeV}\,, \qquad (4.60)$$

as the DPD models become steeper in the large y region. In addition, DPDs on the small-y grid are initialized with $(n_{f1}, n_{f2}) = (5, 5)$ active flavours, while on the large-y grid $(n_{f1}, n_{f2}) = (4, 4)$ is chosen due to $\mu_{y^*} \lesssim m_b$.

Unless stated otherwise, our choice for the interpartonic distance will be the intermediate value of

$$y = 0.5 \, \text{GeV}^{-1} \,, \tag{4.61}$$

at which

$$\mu_{y^*} \approx 2.54 \, \text{GeV} \,. \tag{4.62}$$

Our standard choice for the parametrisation of the non-perturbative part of the Collins-Soper kernel is "SV19" [121], see (4.48).

We structure our analysis as follows: First, in section 4.3.1, we split the DGLAP equation into Sudakov factor and pure Mellin convolution to understand the effect of different parts of the DGLAP and CS kernels. In section 4.3.2, we analyse the effects of LL evolution on the x- and y-dependence for different flavour combinations and polarisations. After getting an impression of the overall effects of colour non-singlet evolution, we present the impact of NLL$'$ and NNLL evolution in section 4.3.3. In a phenomenological context, the most important quantities are the DPD luminosities, which are shown and discussed for different processes in section 4.3.4 and appendix H.

4.3.1 Separating Sudakov factor and Mellin convolution

Defining $\widetilde{F}$. To separate the effects of different ingredients in the colour non-singlet DGLAP evolution, we define a second alternative prescription for DPDs,

$$
{}^{R_1 R_2}\widetilde{F}_{a_1 a_2; \mu_{01}, \mu_{02}, \xi_0}(x_1, x_2, y, \mu_1, \mu_2)
$$
$$
= \exp\left\{ \sum_{i=1,2} \int_{\mu_{0i}}^{\mu_i} \frac{\mathrm{d}\mu}{\mu} \, {}^{R_i}\gamma_J(\mu) \log x_i - {}^R J(y, \mu_{01}, \mu_{02}) \log \sqrt{x_1 x_2} \right\}
$$
$$
\times \, {}^{R_1 R_2}\widehat{F}_{a_1 a_2; \mu_{01}, \mu_{02}, \xi_0}(x_1, x_2, y, \mu_1, \mu_2) \,, \tag{4.63}
$$

with a DGLAP equation

$$
\frac{\mathrm{d}}{\mathrm{d}\log\mu_1} \, {}^{R_1 R_2}\widetilde{F}_{a_1 a_2; \mu_{01}, \mu_{02}, \xi_0}(x_1, x_2, y, \mu_1, \mu_2)
$$
$$
= 2 \sum_{b, R'} {}^{R_1 \overline{R}'}\widehat{P}_{a_1 b}\left(x_1', \mu_1\right) \underset{x_1}{\otimes} \, {}^{R_1 R_2}\widetilde{F}_{a_1 a_2; \mu_{01}, \mu_{02}, \xi_0}(x_1', x_2, y, \mu_1, \mu_2) \,. \tag{4.64}
$$

Compared to the DGLAP equation of $\widehat{F}$ (2.74), this evolution equation looks even more like the colour singlet one as there is no additional term proportional to ${}^R\gamma_J \log x_1$

anymore. However, we pay the price of modified, effective DGLAP kernels

$$
{}^{RR'}\widehat{P}_{ab}(x,\mu) = \exp\left\{\left[\int\limits_{\mu_{01}}^{\mu_1}\frac{\mathrm{d}\mu}{\mu}\,{}^{R}\gamma_J(\mu) - \frac{1}{2}{}^{R}J(y,\mu_{01},\mu_{02})\right]\log x\right\}{}^{R\overline{R}'}P_{a_1b}(x,\mu,\mu^2)\,,\quad (4.65)
$$

which would make this prescription cumbersome to implement in CHILIPDF.

Inserting the decomposition (3.11) into (4.65) yields

$$
\begin{aligned}
{}^{RR'}\widehat{P}^{(n)}_{ab}(x,\mu) &= \exp\left\{\left[\int\limits_{\mu_{01}}^{\mu_1}\frac{\mathrm{d}\mu}{\mu}\,{}^{R}\gamma_J(\mu) - \frac{1}{2}{}^{R}J(y,\mu_{01},\mu_{02})\right]\log x\right\}{}^{R_1\overline{R}'}\widetilde{P}^{(n)}_{a_1b}(x,\mu) \\
&\quad + \frac{1}{2}\delta_{R\overline{R}'}\,\delta_{ab}\,\delta(1-x)\left[d^{(n)}_a + {}^{R}c^{(n)}\right],\; n = 0,1\,.
\end{aligned}\quad (4.66)
$$

We have thus found a way to strictly separate Mellin convolution and multiplication with Sudakov factors. Evolving colour non singlet DPDs can thus be decomposed into a multiplication with the combined Sudakov exponential

$$
\begin{aligned}
{}^{R_1R_2}&S_{a_1,a_2;\mu_{01},\mu_{02},\xi_0}(x_1,x_2,\mu_1,\mu_2,\xi) \\
&= \exp\left\{\int\limits_{\mu_{01}}^{\mu_1}\frac{\mathrm{d}\mu}{\mu}\left({}^{R_1}\gamma_J(\mu)\,\log\frac{\mu}{\sqrt{x_1\xi/x_2}} + d_{a_1}(\mu) + {}^{R_1}c(\mu)\right)\right. \\
&\qquad + \int\limits_{\mu_{02}}^{\mu_2}\frac{\mathrm{d}\mu}{\mu}\left({}^{R_2}\gamma_J(\mu)\,\log\frac{\mu}{\sqrt{x_2\xi/x_1}} + d_{a_2}(\mu) + {}^{R_2}c(\mu)\right) \\
&\qquad \left. + \frac{1}{2}{}^{R}J(y,\mu_{01},\mu_{02})\,\log\frac{\xi}{\xi_0}\right\},
\end{aligned}\quad (4.67)
$$

where

$$
d_{a_1}(\mu) = \sum_{n=1} d^{(n)}_{a_1} a^n_s(\mu)\,,\quad (4.68)
$$

$$
{}^{R}c(\mu) = \sum_{n=1}{}^{R}c^{(n)} a^n_s(\mu)\,,\quad (4.69)
$$

followed by a Mellin convolution with the first term on the right hand side of (4.66).

Effect of Sudakov exponentials in DGLAP evolution. In practice, the discussion above enables us to assess the relative impact of cusp anomalous dimensions and the multiplicative parts of the non-cusp ones and compare it to the one of full DGLAP evolution including the terms inside ${}^{RR'}\widetilde{P}_{ab}$. Figure 4.2 shows the difference between effective and usual DGLAP kernels at the example of ${}^{R\overline{R}}\widetilde{P}^{(0)}_{gg}$ for $\mu = 10\,\mathrm{GeV}$ and $\mu = M_Z$. We set $\mu_0 = \mu_{01} = \mu_{02}$ to the minimal possible value $\mu_{y^*,\mathrm{min}}$, which is $2\,\mathrm{GeV}$ for our choice
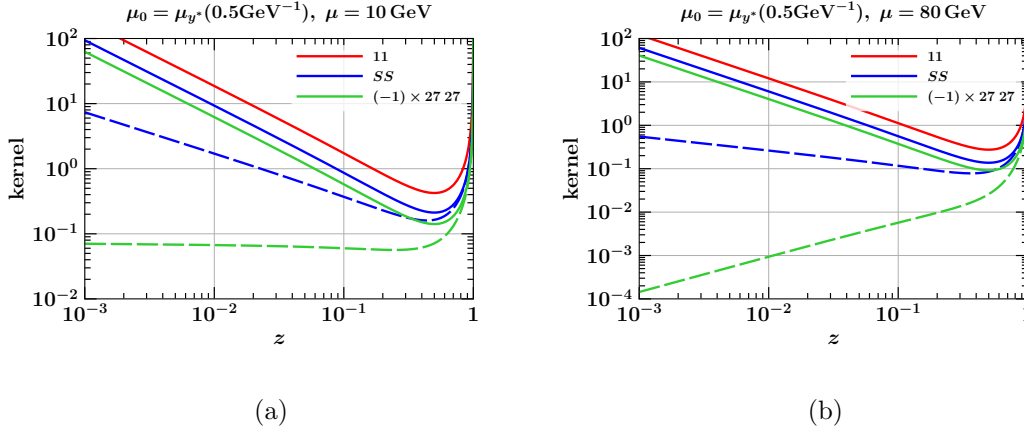
Figure 4.2: The x-dependent parts of the LO gg DGLAP kernel at (a) $\mu = 10\,\mathrm{GeV}$ and (b) $\mu = 80\,\mathrm{GeV}$. The effective kernels with the suppressing prefactor given in the first line of (4.66) are shown as dashed curves.

of $y^*(y)$, eq. (4.20). The LO colour factors, eqs. (3.17) to (3.22), manifest themselves as constant shifts between the different colour representations in the logarithmic plot. To get a better impression of relative sizes, we also show the colour singlet here and in the following.

The prefactor in (4.66) is 1 at $x' = 1$ and falls off for $x' \to 0$. In figure 4.2, it manifests itself as a powerlaw, which can be seen nicely at small x'. Inside the Mellin convolution (4.64), this leads to a suppression of DPD values far away from $x_1/x' = x_1$. This suppression grows stronger for higher colour multiplicities and larger scales μ due to the increasing values of $^R\gamma_J$ and RGE integrals in the exponential. Other DGLAP kernels receive changes of the same kind.

Next, let us investigate how this suppression affects the DGLAP evolution. Figures 4.3 and 4.4 show the combined DGLAP and CS evolution at LL for different final scales (μ_1, μ_2) separated into two steps, first only with the multiplied Sudakov factor (4.67), and then the complete DGLAP evolution. Here and in the following, the rapidity scale is determined by the RGE scales using our convention $\xi = \mu_1 \mu_2$. Note that no flavour matching is performed to avoid a more complex structure of the Sudakov exponential.

For equal scales $\mu_1 = \mu_2 = \mu_f$ and $\mu_{01} = \mu_{02} = \mu_0$ the Sudakov factor becomes x-independent and simplifies to

$$
^{R_1 R_2}S_{a_1 a_2; \mu_0, \mu_0, \xi_0}(x_1, x_2, \mu_f, \mu_f, \xi) = \exp\left\{ 2 \int_{\mu_0}^{\mu_f} \frac{\mathrm{d}\mu}{\mu} \left(^{R_1}\gamma_J(\mu) \log\frac{\mu}{\sqrt{\xi}} + d_{a_1}(\mu) + {}^{R_1}c(\mu) \right) \right.
$$
$$
\left. + \frac{1}{2}{}^R J(y, \mu_0, \mu_0) \log\frac{\xi}{\xi_0} \right\} \tag{4.70}
$$

Be remined that R_1 and R_2 have the same multiplicities and the integrand of the RGE

integrals is negative for our choice of $\xi = \mu_1 \mu_2 = \mu_f^2$. Thus, $^{R_1 R_2}S$ causes a suppression of DPDs constant in x_i at the starting scale over multiple degrees of freedom. This suppression becomes stronger for growing colour representations and final scales due to larger values of $^R\gamma_J$ and $-^R J$.

For (gg) in figure 4.3, the additional impact of the effective DGLAP kernels in turn is of order $\mathcal{O}(1)$ and thus relatively weak. As the small-x tail of the effective DGLAP kernels is suppressed, the large x region and the subtraction terms of the plus-distributions as defined in (A.8) become increasingly important. For the *two octets*, the shift becomes negative for larger μ. This is due to the negative subtraction terms of the plus distribution inside the splitting kernel, since $c_{gg}(AA) = c_{gg}(SS) > 0$. Symmetric and antisymmetric octet differ slightly after the complete DGLAP evolution, which is due to the mixing with different flavour singlet distributions according to the evolution equations (2.88) and (2.89). For reasons of better visibility, only the symmetric octet is shown. The effective DGLAP evolution does not change the *decuplet* as the x-dependent terms of its DGLAP kernel are zero (see eq. (2.56)). It is thus not shown in the plots. The *27-multiplet* is enhanced after full DGLAP evolution, which is mainly because of the positive subtraction terms of the plus-distribution due to $c_{gg}(27\,27) < 0$. In addition, there is only a mere change in shape which can be traced back to the large suppression in the effective DGLAP kernel as shown in figure 4.2.

The effective DGLAP evolution $(u\bar{u})$ in figure 4.4 has a considerably larger effect. It leads to changes in sign at small and large x_1 and enhances colour non-singlet DPDs at large x_1 by several orders of magnitudes. This leads to comparable sizes of colour singlet and non-singlet in that region for $\mu_i = 10\,\text{GeV}$. At larger μ_i, the Sudakov suppression tends to dominate more and more again. Note however that we find this behaviour of the DGLAP evolution to be a rather special case: For most other kinematical configurations and flavour combinations, the multiplication with $^{R_1 R_2}S$ serves as a reasonable estimate for the order of magnitude of the fully evolved DPD, as we have seen in figure 4.3. Some deviations from this rule can be observed in the pure quark sector.

Subfigures 4.3 (c) and 4.4 (c) show DPDs evolved to asymmetric scales $(\mu_1, \mu_2) = (10\,\text{GeV}, M_Z)$. In this case, the Sudakov factor (4.70) is multiplied with an additional factor of

$$\left(\frac{x_1}{x_2}\right)^{\int_{\mu_1}^{\mu_2} \frac{\mathrm{d}\mu}{\mu} {}^R\gamma_J(\mu)/2}. \tag{4.71}$$

This introduces a power law which suppresses the region $x_1 < x_2$ and enhances the DPD at $x_1 > x_2$. For (gg), this change in shape dominates the DPDs over the whole range of x_1 and leads to colour non-singlet DPDs having the same order of magnitude as colour singlet ones at large x_1.
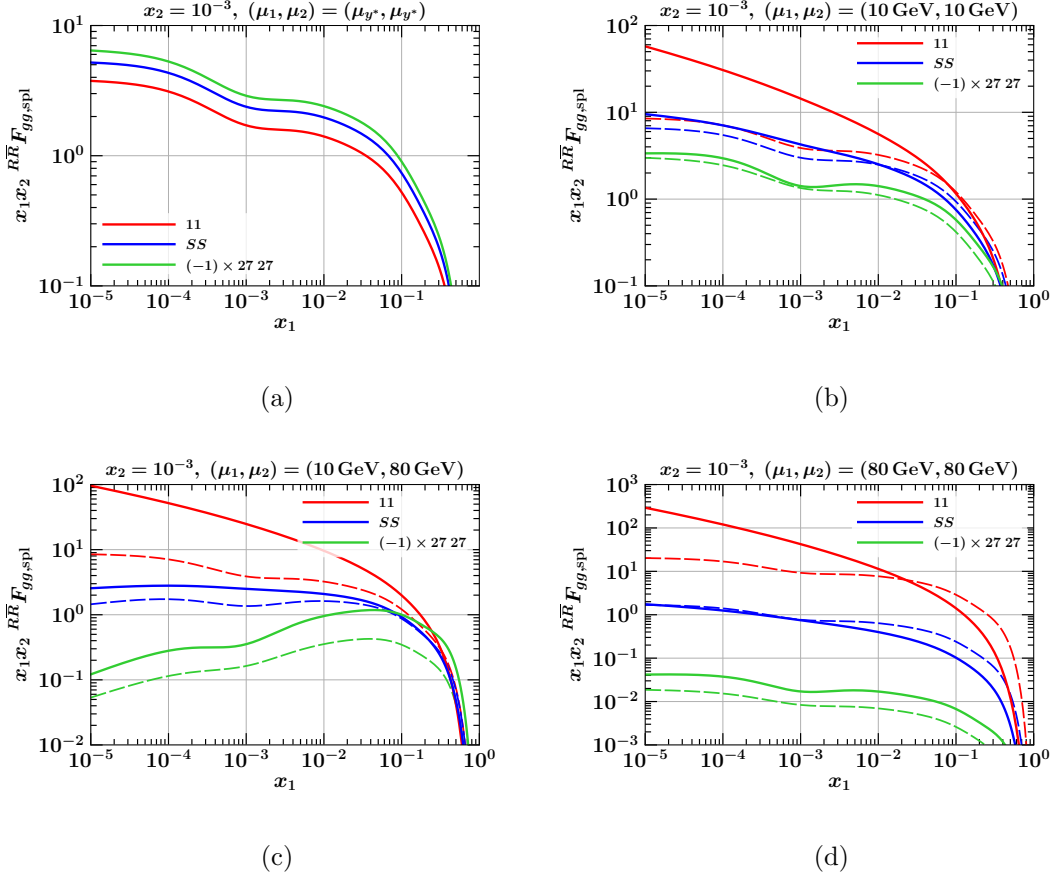
Figure 4.3: Multiplication with the Sudakov exponential (4.67) (dashed) vs. complete DGLAP and CS evolution (solid) of $^{R\overline{R}}F_{gg,\mathrm{spl}}$ at LL. Figure (a) shows the starting conditions at $\mu_i = \mu_{y^*}$, (b) - (d) contain different final scales including asymmetric ones in (c).
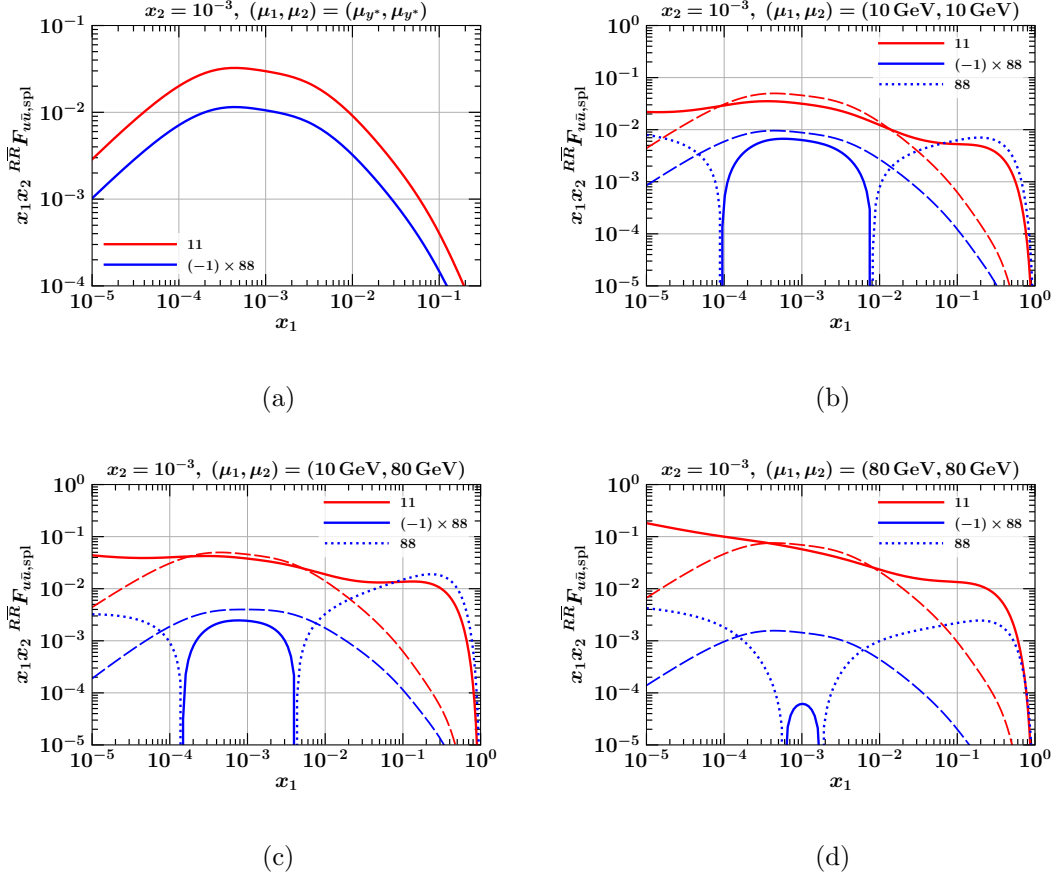
Figure 4.4: Multiplication with the Sudakov exponential (4.67) (dashed) vs. complete DGLAP and CS evolution (solid) of $^{RR}F_{u\bar{u},\mathrm{spl}}$ at LL. Figure (a) shows the starting conditions at $\mu_i = \mu_{y^*}$, (b) - (d) contain different final scales including asymmetric ones in (c).

4.3.2 DGLAP evolution at LL

In this section, we aim to get a comprehensive understanding of the behaviour of colour non-singlet DPDs under evolution at LL. In order to achieve this, we will successively vary different parameters and function arguments, namely the momentum fraction x_2, the DPD ansatz, parton flavours, polarisation, and the interpartonic distance y. DPDs are always plotted against x_1 while x_2 and y are held fix. An exception to this rule is figure 4.10, where they are plotted against y with fixed values for x_i. Our standard choice is to show the DPDs both at μ_{y^*} and at the final scale to better visualize effects from evolution. Most of the times DPDs will be evolved to $10\,\mathrm{GeV}$, as at this comparatively small scale the Sudakov suppression only has a rather mild effect.

In general, colour singlet distributions become more and more enhanced at larger final scales, especially in the small-x region. Colour non-singlet DPDs on the other hand are suppressed by the Sudakov factor (4.67), which becomes smaller at larger scales. As already observed in the previous section, DPDs usually become comparable in size in the large-x region for not too large final scales.

DPDs for three settings $x_2 = x_1$, 10^{-3}, and 0.3 are shown in figure 4.5. We see that the choice for x_2 has a significant impact on the sign changes of the $(u\bar{u})$ DPD. For large x_2, the absolut size decreases, while there the colour octet DPD is of the same order of magnitude as the colour singlet one on a x_1 range.

Figure 4.6 shows the behaviour of the product ansätze P1, P2 (as defined in eqs. (4.37) and (4.39)) and the splitting ansatz under evolution. Although numerical values differ in the evolved distributions, the hierarchy after evolution between colour representations is identical in every case. This can be traced back to the dominating influence of the Sudakov exponential, which does not depend on the ansatz. Hence, if evolved to higher scales, the decuplet would become larger than the 27-multiplet distribution. Notice that the sign of the latter distribution changes between P1 and P2, which shows a how unconstrained the available intrinsic ansätze are due to the lack of information on DPDs at the initial scale.

The behaviour of mixed quark-gluon flavour DPDs can be found in figure 4.7. The two octet distributions are now distinguishable due to their different splitting kernels. Their qualitative behaviour under evolution however is comparable to the (gg) DPDs, as they are still dominated by the contributions of the gluon distributions under evolution. That they mix with different distributions, Σ^+ and Σ^-, evidently has only a minor impact. The evolved DPDs exhibit a similar behaviour as the other flavour combinations in the two regions of small and large x_1.

In figure 4.8, we show additional flavour combinations that are not generated with small-y splitting at LO and thus vanish at $\mu_i = \mu_{y^*}$: there is no LO splitting graph that creates a $(u\bar{d})$ pair, and at $y = 0.5\,\mathrm{GeV}^{-1}$ only 4 flavours are active so that b flavours are prohibited in splitting graphs. Both DPDs are thus generated only during DGLAP evolution in the mixing with other distributions. Nevertheless, their shape does not show any particular peculiarities compared to other flavour combinations.

The evolution of polarised DPDs for different flavour combinations is shown in figure 4.9. As stated below (4.25), the incoming quarks in the small-y splitting kernels for every

polarisation are unpolarised. Hence, the MSHT20 set is used also used for polarised splitting DPDs. We see that polarised evolution behaves very similar to the unpolarised one. It is worth noting that colour singlet and non-singlet distributions tend to be closer together, as the colour singlet DGLAP evolution does not enhance the distributions at small x as strongly as it does in the unpolarised case. Both observations extend to the evolution of linear gluons and transverse quarks.

Figure 4.10 illustrates the y-dependence of (gg) DPDs for different ansätze. Note that for these plots we need to use a more dense y-grid

$$(10^{-2}, b_0/m_b)_{[16]} \, ; \, (b_0/m_b, b_0/m_c, 2, 5, \infty)_{[16,16,16,12]} \tag{4.72}$$

to avoid interpolation artefacts in the region $y \gtrsim 1 \, \mathrm{GeV}^{-1}$. DPDs evolved with the five different fits for the CS-kernel presented in eqs. (4.48) to (4.52) are shown as bands between minimum and maximum of all five evolved DPDs. At μ_{y^*}, the two product ansätze P1 and P2 are dominated by a Gaussian fall-off as given in (4.16), and the splitting ansatz exhibits the characteristic $1/y^2$ behaviour, see eq. (4.17). While the DGLAP evolution of colour singlet DPDs is y-independent, CS evolution of colour non-singlet DPDs introduces an additional y-dependence through the exponentiated CS-kernel given in figure 4.1. This suppresses the DPDs at large y, which both grows stronger for larger scales and colour dimension. At $y \lesssim 0.1 \, \mathrm{GeV}^{-1}$, the evolved colour non-singlet DPDs stay larger than their colour singlet counterparts. For y approaching b_0/ν, the lower boundary of the luminosity integrals, the CS kernel is close to zero and μ_{y^*} close to the final scales. Therefore, CS evolution has a weak effect and the DGLAP evolution path is small, such that the initial DPD is only merely changed. At $y \gtrsim 1 \, \mathrm{GeV}^{-1}$ colour singlet DPDs start to exceed the non-singlet ones by many orders of magnitude. The threshold between these two regions moves further to the right for larger x_i, which can be also seen in figure 4.5.
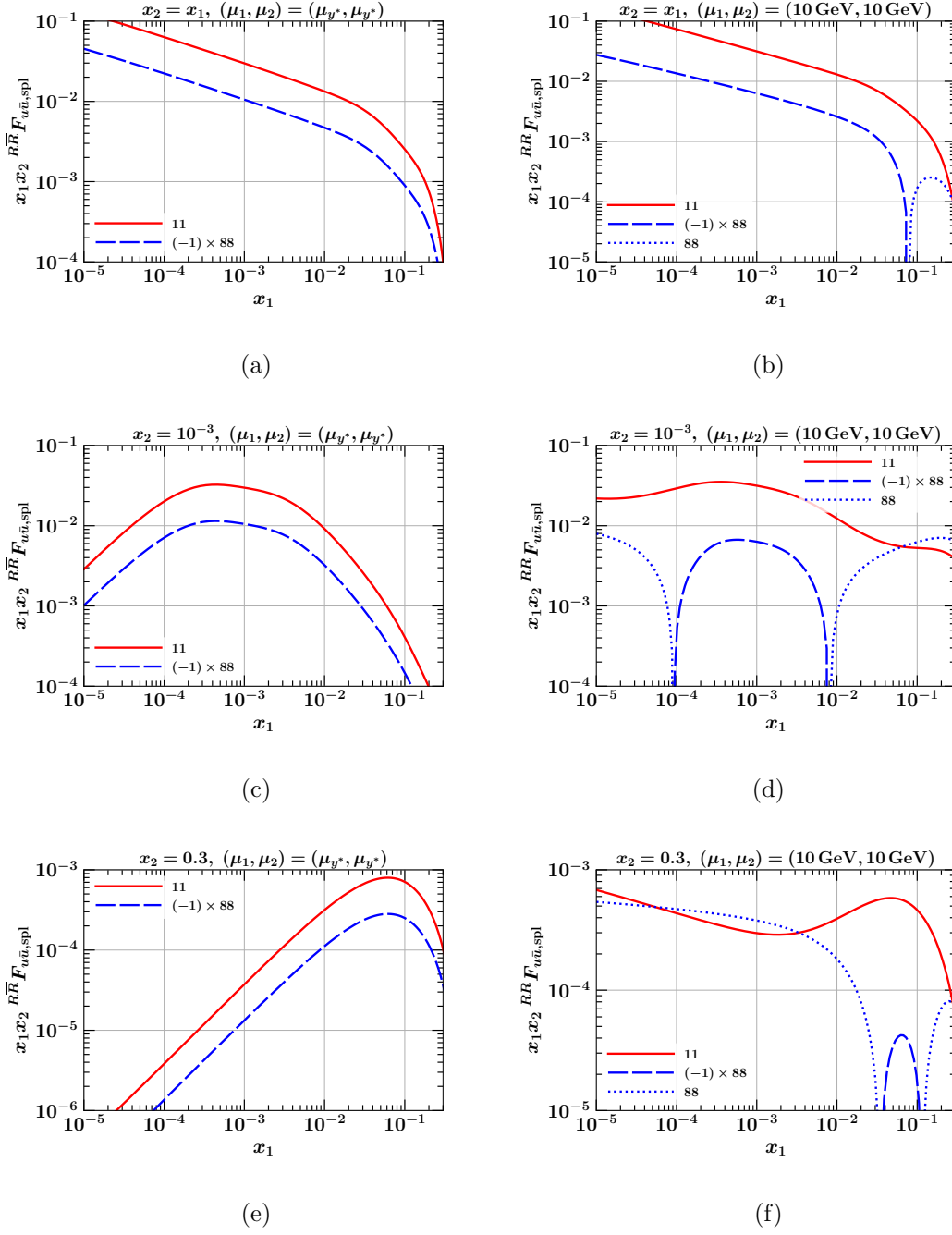
Figure 4.5: Behaviour of $^{RR}F_{gg,\text{int}}$ under LL evolution for different settings of x_2. (a), (c), and (e) show the starting conditions at $\mu_i = \mu_{y^*}$ for $x_2 = x_1$, 10^{-3}, and 0.3, respectively. (b), (d) and (f) contain the corresponding DPDs evolved to $\mu_i = 10\,\text{GeV}$.
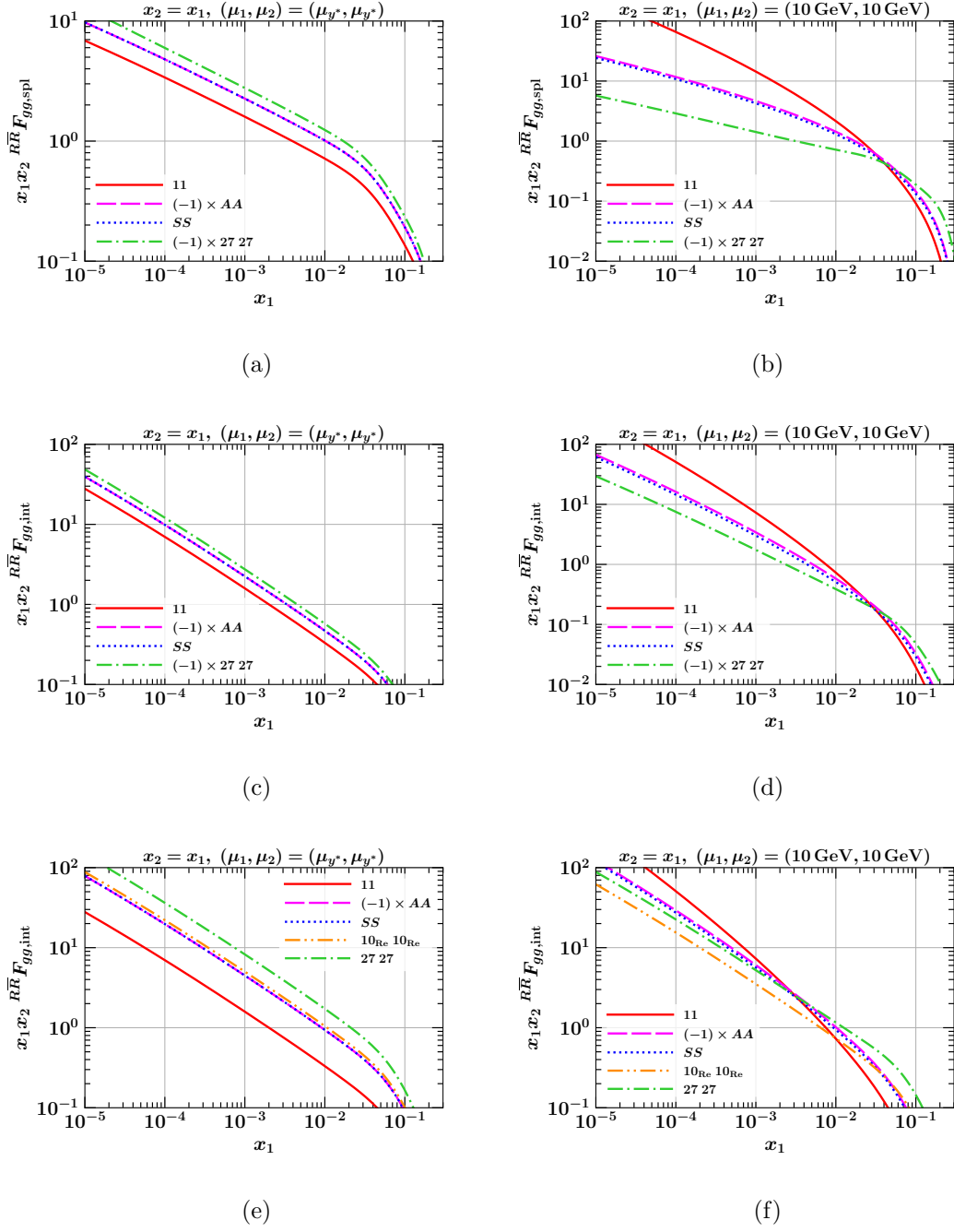
Figure 4.6: Behaviour of different ansätze for $^{RR}F_{gg}$ under LL evolution. (a), (c) and (e) show the starting conditions at $\mu_i = \mu_{y^*}$ for the splitting ansatz and the product ansätze P1 and P2, respectively. (b), (d) and (f) contain the corresponding DPDs evolved to $\mu_i = 10\,\text{GeV}$.
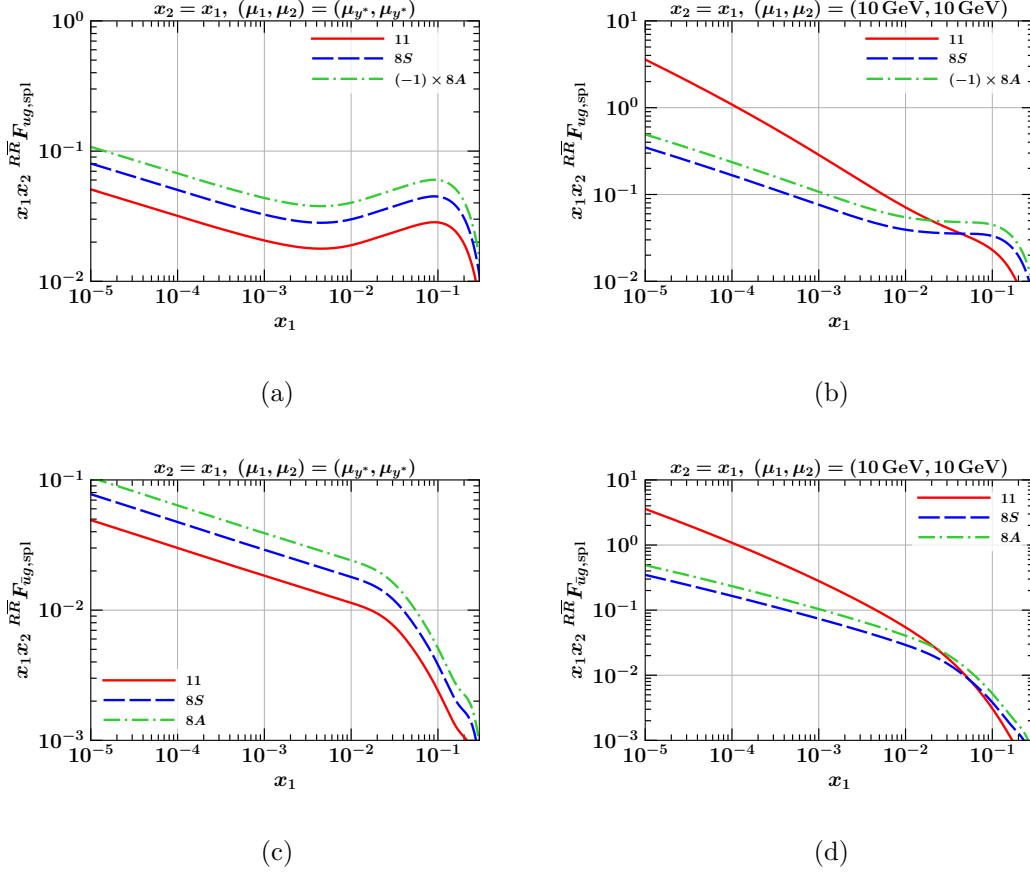
Figure 4.7: LL evolution of $^{R_1 R_2} F_{ab,\mathrm{spl}}$, $(ab) = (ug)$ and $(\bar{u}g)$. They are shown in (a) and (c) at $\mu_i = \mu_{y^*}$, and in (b) and (d) at $\mu_i = 10\,\mathrm{GeV}$.
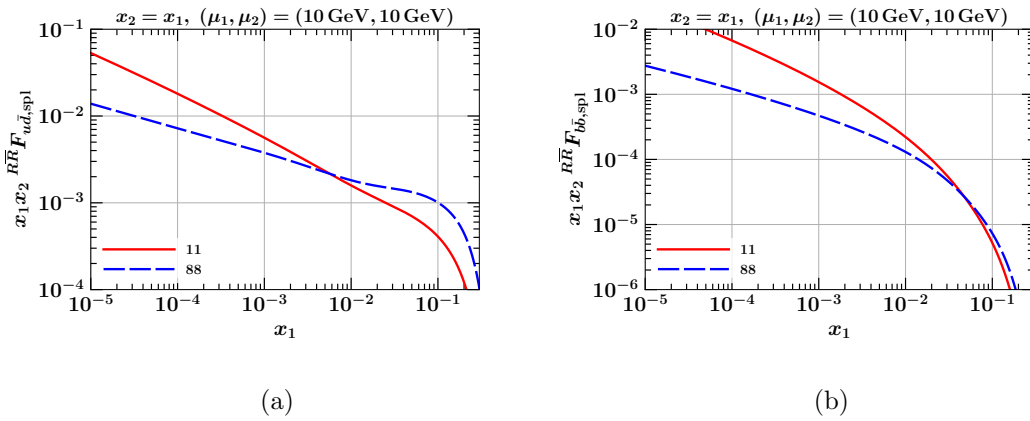
Figure 4.8: The DPDs $^{RR} F_{a_1 a_2,\mathrm{spl}}$, $(a_1 a_2) = (u\bar{d})$ and $(b\bar{b})$, LL evolved to $\mu_i = 10\,\mathrm{GeV}$.
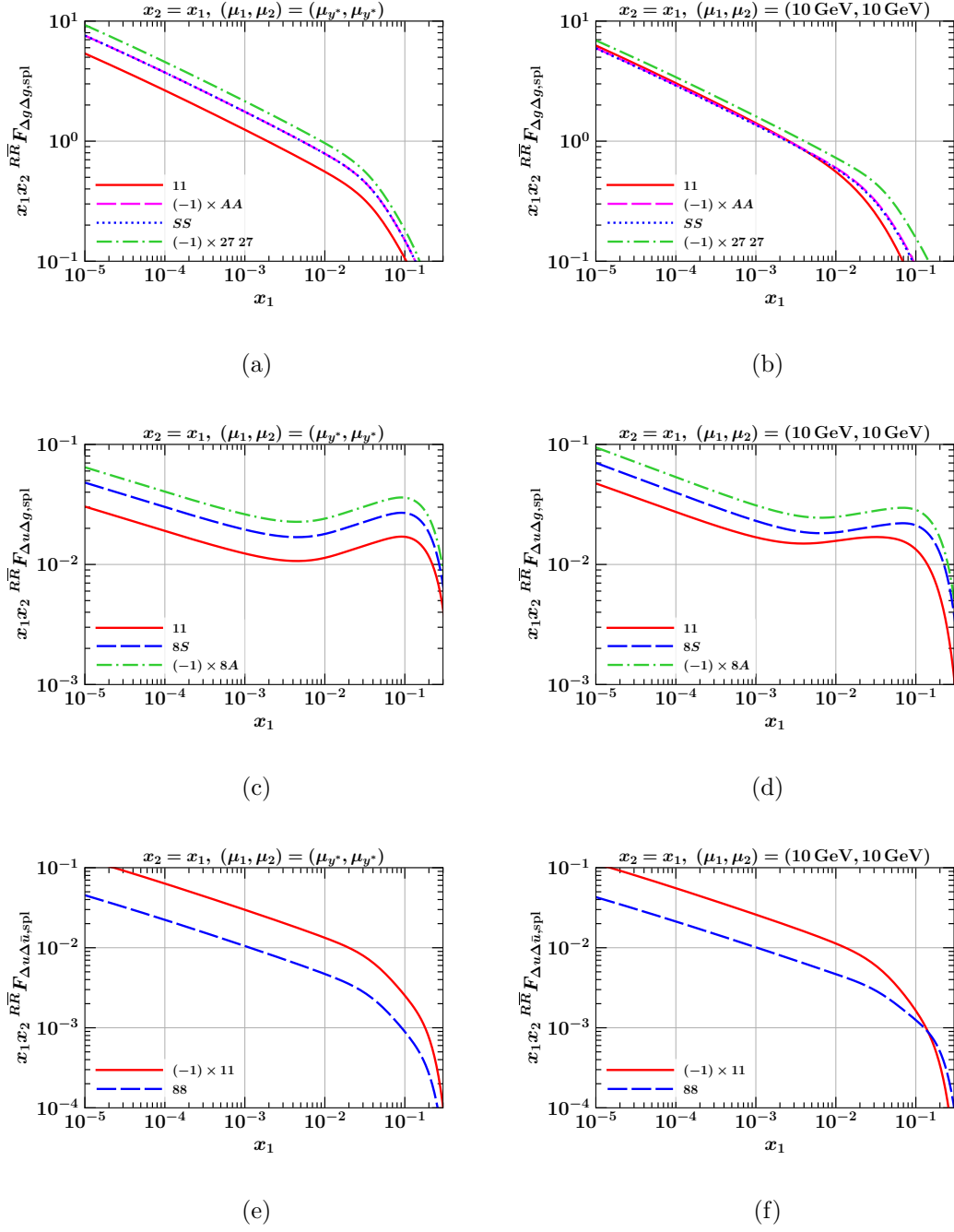
Figure 4.9: LL Evolution of longitudinal DPDs $^{R_1 R_2}F_{\Delta a_1 \Delta a_2,\text{spl}}$. (a), (c) and (e) show the starting conditions at $\mu_i = \mu_{y^*}$ for $(a_1 a_2) = (gg)$, (ug), and $(u\bar{u})$, respectively. (b), (d) and (f) contain the corresponding DPDs evolved to $\mu_i = 10\,\text{GeV}$.
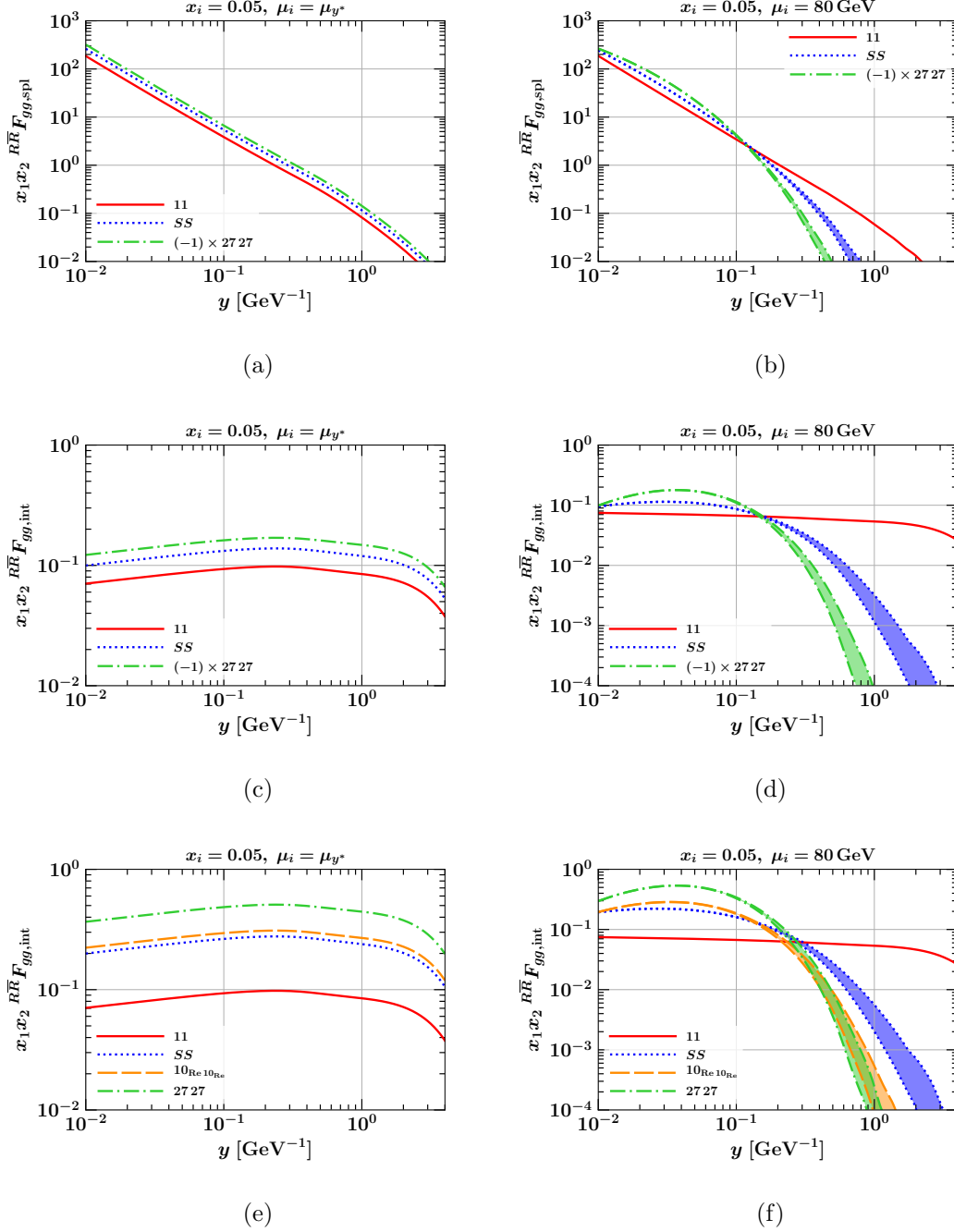
Figure 4.10: y dependence of ${}^{R_1 R_2}F_{gg}$ for different ansätze. (a), (c) and (e) show the starting conditions at $\mu_i = \mu_{y^*}$ for the splitting ansatz and the product ansätze P1 and P2, respectively. (b), (d) and (f) contain the corresponding DPDs evolved to $\mu_i = 80\,\mathrm{GeV}$. Bands show the area between minimum and maximum of DPDs evolved witht the non-perturbative ansätze for ${}^R\Delta J$ given in eqs. (4.48) to (4.52)

79

4.3.3   Impact of NLL′ and NNLL evolution

In this section we will examine the effect of the NLO DGLAP kernels that were calculated in chapter 3. Note that at NLL′ the initial conditions change compared to LL as we now make use of the PDF fit at NLO accuracy from the MSHT20 set. To be sensitive to the impact of NLL′ *evolution* only, we introduce the double ratio

$$^{R_1 R_2}\rho_{\mathrm{NLL}'}(\mu_1, \mu_2) = \frac{^{R_1 R_2}r_{\mathrm{NLL}'}(\mu_1, \mu_2)}{^{R_1 R_2}r_{\mathrm{NLL}'}(\mu_{y^*}, \mu_{y^*})} . \tag{4.73}$$

The single ratios $r_{...}$ are defined as follows:

$$^{R_1 R_2}r_{\mathrm{NLL}'}(\mu_1, \mu_2) = \frac{^{R_1 R_2}F_{\mathrm{NLL}'}(\mu_1, \mu_2)}{^{R_1 R_2}F_{\mathrm{LL}}(\mu_1, \mu_2)} , \tag{4.74}$$

where we omit most function arguments and indices for the moment and indicate the evolution order in the subscript. An equivalent ratio can be defined one order higher:

$$^{R_1 R_2}\rho_{\mathrm{NNLL}}(\mu_1, \mu_2) = \frac{^{R_1 R_2}r_{\mathrm{NNLL}}(\mu_1, \mu_2)}{^{R_1 R_2}r_{\mathrm{NNLL}}(\mu_{y^*}, \mu_{y^*})} , \tag{4.75}$$

with

$$^{R_1 R_2}r_{\mathrm{NNLL}}(\mu_1, \mu_2) = \frac{^{R_1 R_2}F_{\mathrm{NNLL}}(\mu_1, \mu_2)}{^{R_1 R_2}F_{\mathrm{NLL}'}(\mu_1, \mu_2)} . \tag{4.76}$$

Note that $^{R_1 R_2}r_{...}(\mu_{y^*}, \mu_{y^*})$ is in fact representation independent, because the only difference between the ansätze for DPDs in different colour representations are the colour factors, which cancel in the ratio. In addition, in the LO splitting ansatz it is identical for flavour combinations that originate from the same initiating parton, which is u for (ug) and g for any other combination. The ratios at initial scales are shown in figure 4.11, while the double ratios can be found in figure 4.12.

These plots contain the double ratio $\rho_{\mathrm{NLL}'}$ for different flavour combinations and polarisations. The divergence in subfigure (c) is an artefact of the sign change in $^{88}F_{u\bar{u},\mathrm{spl}}$, see figure 4.5 (b). Overall, colour non-singlet corrections tend to be of the same order of magnitude as the colour singlet ones. In some cases, they are on percent level, e.g. for $(\delta u \delta \bar{u})$, but most of the times $\rho_{\mathrm{NLL}'}$ is of order $\mathcal{O}(0.1)$ to $\mathcal{O}(1)$. And although the order of magnitude between different colour representations is comparable, the shapes differ considerably and cannot be deduced from the colour singlet ratios. Not even the sign of the correction needs to remain the same. For larger scales, the colour non-singlet double ratios are more and more dominated by the Sudakov factor (4.67), which leads to a flattened out shape for equal scales.

These findings justify the efforts we have made in chapter 3. In precision studies, NLO corrections can evidently have a crucial impact on the evolved DPDs. At least at not too large scales, they cannot be deduced from the Sudakov exponential alone, which makes the DGLAP kernels expanded to NLO an essential ingredient of a precise colour non-singlet evolution code.

To assess the impact of NNLL evolution, we show the double ratio ρ_{NNLL} for (gg) in figure 4.13 at $10\,\text{GeV}$ and $80\,\text{GeV}$. The PDF used to create the ansatz at initial scales does not change, thus we trivially have

$$r_{\text{NNLL}}(\mu_{y^*}, \mu_{y^*}) = 1 \,. \tag{4.77}$$

The same is true for the colour singlet distributions at all scales as the DGLAP kernels remain unchanged.

Further expanding ${}^R\gamma_J$ to NNLO does not only lead to a change in the Sudakov factor (4.67), but also in the DGLAP equation (4.64). Hence, ρ_{NNLL} is not constant in x_i. For $R = 27$, where the anomalous dimension is largest, it even incorporates a sign change. The double ratio is significantly smaller than $\rho_{\text{NLL}'}$. We thus see the typical behaviour of a perturbative series, in which the contributions of higher order terms become less and less important.
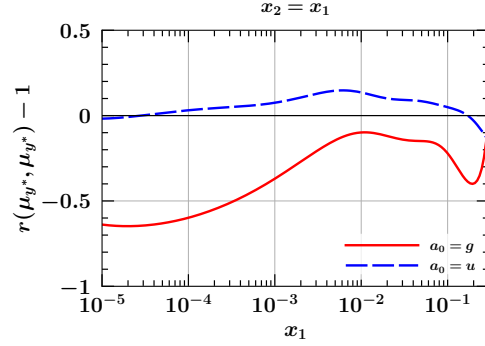
Figure 4.11: The initial ratios $r_{\text{NLL}'}(\mu_{y^*}, \mu_{y^*})$ for the two initiating parton types g and q.
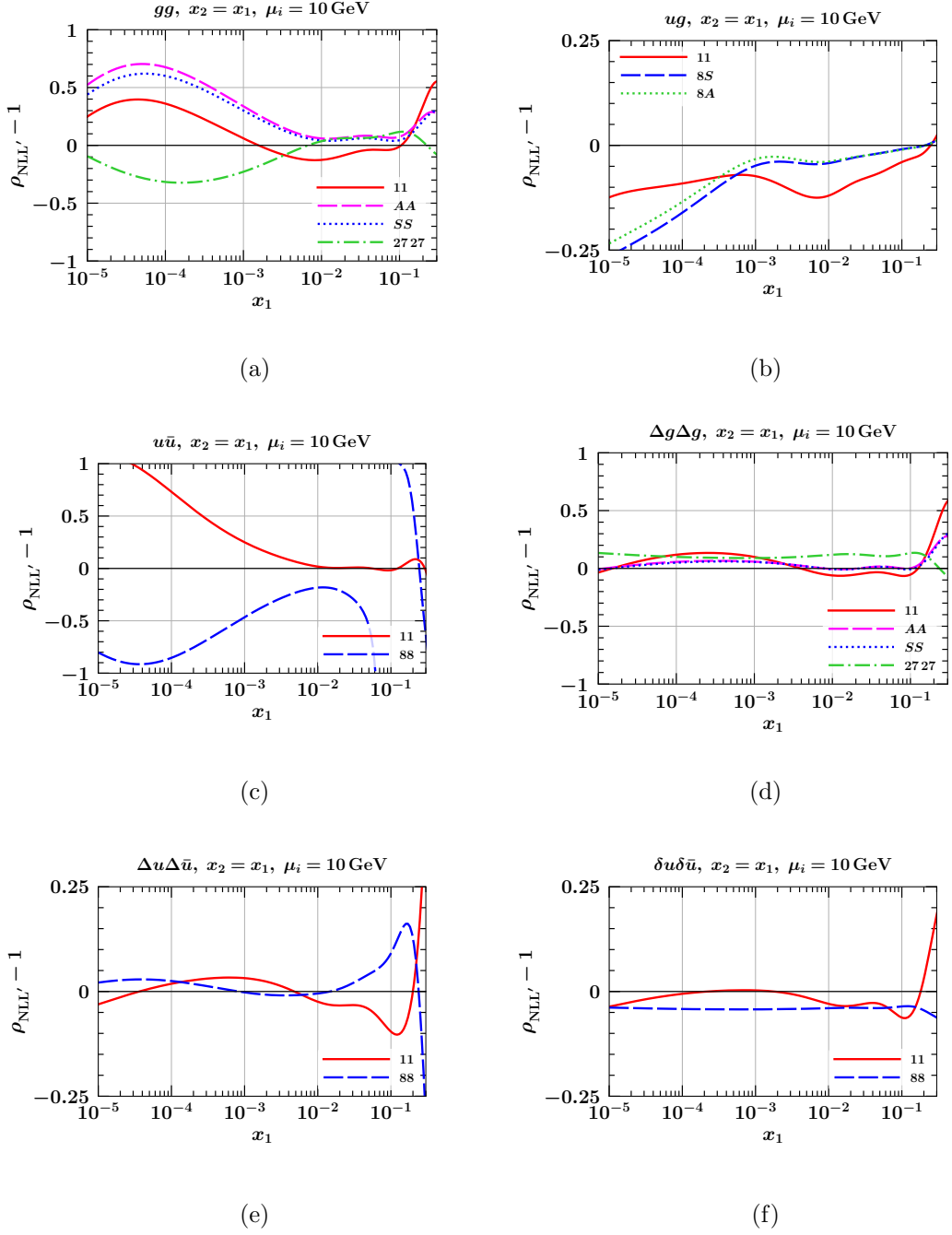
Figure 4.12: Double ratio of NLL evolved DPDs $^{R_1 R_2} F_{ab,\mathrm{spl}}$ for different flavour combinations and polarisations.

(a)   (b)
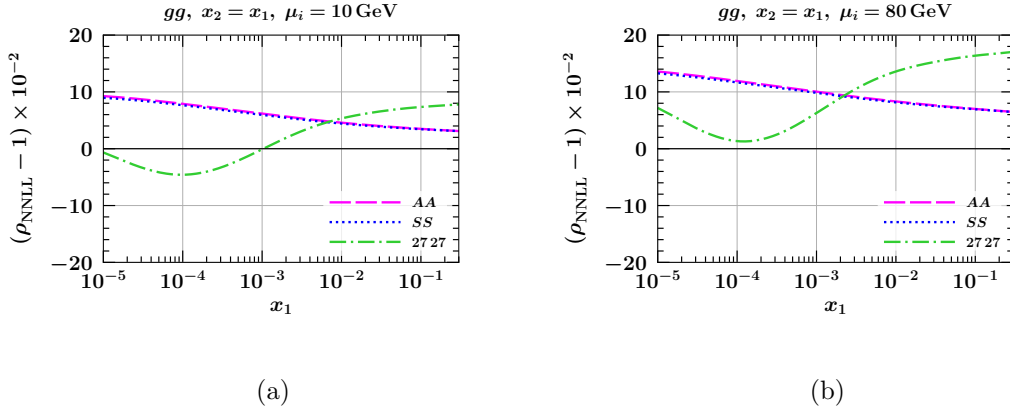
Figure 4.13: Double ratio for NNLL evolved DPDs $^{R_1R_2}F_{gg,\text{spl}}$ for $\mu_i = 10\,\text{GeV}$ (a) and $\mu_i = 80\,\text{GeV}$ (b).

4.3.4 DPD luminosities

To obtain an reasonable estimate of the influence of DPDs on a complete hadronic cross section we compute their luminosities as introduced in (2.12). We choose the regulator function Φ to be a hard cut-off,

$$\Phi(y\nu) = \Theta(y\nu - b_0)\,, \tag{4.78}$$

where b_0 is defined in (A.7), and the cut-off scale is

$$\nu = \min(Q_1, Q_2) \tag{4.79}$$

in accordance with [57], section 6. Based on our model ansatz (4.13) as a sum of an intrinsic and a splitting DPD, a generic luminosity is a sum of four building blocks:

$$
\begin{aligned}
\mathcal{L}(x_i, \bar{x}_i, Q_i, \sqrt{s}) &= 2\pi \int\limits_{b_0/\nu}^{\infty} \mathrm{d}y\, y\, F(x_i, y, Q_i, \zeta)\, F(\bar{x}_i, y, Q_i, \bar{\zeta}) \\
&= 2\pi \int\limits_{b_0/\nu}^{\infty} \mathrm{d}y\, y\, \bigg(F_{\text{int}}(x_i, y, Q_i, \zeta)\, F_{\text{int}}(\bar{x}_i, y, Q_i, \bar{\zeta}) \\
&\quad + F_{\text{spl}}(x_i, y, Q_i, \zeta)\, F_{\text{spl}}(\bar{x}_i, y, Q_i, \bar{\zeta}) + F_{\text{int}}(x_i, y, Q_i, \zeta)\, F_{\text{spl}}(\bar{x}_i, y, Q_i, \bar{\zeta}) \\
&\quad + F_{\text{spl}}(x_i, y, Q_i, \zeta)\, F_{\text{int}}(\bar{x}_i, y, Q_i, \bar{\zeta}) \bigg) \\
&= \mathcal{L}_{2\text{v}2}(x_i, \bar{x}_i, Q_i, \sqrt{s}) + \mathcal{L}_{1\text{v}1}(x_i, \bar{x}_i, Q_i, \sqrt{s}) \\
&\quad + \mathcal{L}_{2\text{v}1}(x_i, \bar{x}_i, Q_i, \sqrt{s}) + \mathcal{L}_{1\text{v}2}(x_i, \bar{x}_i, Q_i, \sqrt{s})\,.
\end{aligned} \tag{4.80}
$$

The naming convention in the last two lines is adapted from [22] and refers to the number of initiating partons in the two involved ansätze. We made use of fact that the integrand contains no angular dependencies, i.e. $d^2\boldsymbol{y} = 2\pi dy\, y$, and inserted our choice for Φ, eq. (4.78). Be reminded that luminosities can only depend on the centre-of-mass energy $\sqrt{s}$ as given in eq. (4.6) and that we choose

$$\mu_i = Q_i \,. \tag{4.81}$$

In (4.80), we have omitted indices for better readability. Luminosities and DPD products have to be dressed in the following way:

$$\mathcal{L}_{...} \to {}^{R_1 R_2 R_3 R_4} \mathcal{L}_{a_1 a_2 b_1 b_2, \,...} \,, \tag{4.82}$$

$$F_{...}(\dots)\, F_{...}(\dots) \to {}^{R_1 R_2} F_{a_1 a_2, \,...}(\dots)\, {}^{R_3 R_4} F_{b_1 b_2, \,...}(\dots)\,. \tag{4.83}$$

To avoid double counting between SPS and DPS inside luminosities, the DGS scheme [57] defines subtraction terms for luminosities. The overall cross section therefore includes a third term,

$$\sigma_{\text{SPS}} - \sigma_{\text{1v1,pt}} + \sigma_{\text{1v1}} \,. \tag{4.84}$$

In σ_{SPS}, the splitting graphs are considered as part of the hard cross section which are initiated by PDFs. σ_{1v1} is derived from $\mathcal{L}_{\text{1v1}}$ using eq. (2.9). $\sigma_{\text{1v1,pt}}$ mediates between the SPS and DPS cross section by subtracting results from regions of the phase space that are taken into account twice. "pt" stands for fixed order pertubation theory, which will be explained in the next paragraph. As the second and third term of (4.84) differ only in the used distributions, we will condense them into

$$\mathcal{L}_{\text{1v1}} - \mathcal{L}_{\text{1v1,sub}} \tag{4.85}$$

on the level of luminosities. There are equivalent prescriptions for $\mathcal{L}_{\text{1v2}}$ and $\mathcal{L}_{\text{2v1}}$, which are beyond the scope of this work.

For equal scales $Q_1 = Q_2 = Q$, the subtraction term has the form

$$\mathcal{L}_{\text{1v1,sub}} = 2\pi \int\limits_{b_0/\nu}^{\infty} dy\, y\, F_{\text{spl,pt}}(x_i, \dots, Q, Q, Q^2 \,|\, Q, Q^2)\, F_{\text{spl,pt}}(\bar{x}_i, \dots, Q, Q, Q^2 \,|\, Q, Q^2)\,, \tag{4.86}$$

where $F_{\text{spl,pt}}$ is defined in eq. (4.18). The notation $F(\dots, Q_1, Q_2, \xi | \mu_0, \xi_0)$ stands for a DPD that is initialized at (μ_0, μ_0, ξ_0) and evolved to (Q_1, Q_2, ξ) (for colour singlet DPDs, the rapidity argument can of course be ignored). In the subtraction term DPDs are thus initialized at the final scale Q, using only fixed order pertubation theory and no resummation of large logarithms through DGLAP evolution. Therefore, at the lower integral limit $y = b_0/\nu = b_0/Q$ they coincide with the DPDs initialised at μ_{y^*}. For larger y, the two DPDs deviate more and more due to the growing evolution path. Hence, the subtracted luminosity receives less contributions from the region close to the cut-off, which is also taken into account in σ_{SPS}. Note that for our choices of scales the DPDs in (4.86) are always initialised at $n_f = 5$.
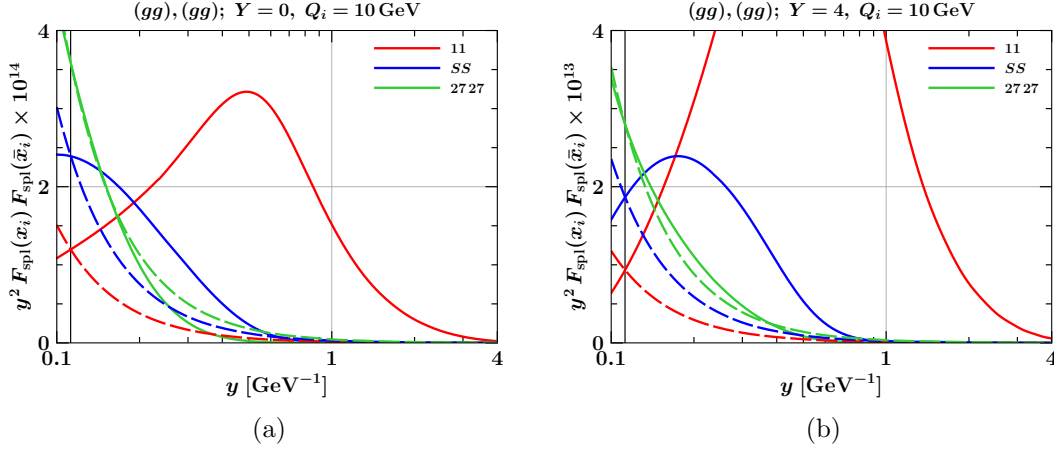
Figure 4.14: Integrands of $\mathcal{L}_{1\mathrm{v}1}$ (solid) and $\mathcal{L}_{1\mathrm{v}1,\mathrm{sub}}$ (dashed) for $(gg), (gg)$ at $Q_i = 10\,\mathrm{GeV}$ at $Y = 0$ (a) and $Y = 4$ (b). The vertical lines marks the lower integral limit $y = b_0/\nu$.

In figure 4.14, we show the integrands for $\mathcal{L}_{1\mathrm{v}1}$ and $\mathcal{L}_{1\mathrm{v}1,\mathrm{sub}}$ at two different final state rapidities Y_i. In this section, we will fix the momentum fraction x_i and $\bar{x}_i$ through these rapidities using the formulae (2.10). Furthermore, we work with the kinematical configuration

$$Y_1 = -Y_2 = Y \tag{4.87}$$

throughout. The axes in figure 4.14 are chosen such that the area under the curves is proportional to the corresponding luminosity, allowing for an estimate of the contribution of different regions in y. While for $R = 1, S,$ and A intermediate y values have a sizeable impact, distributions for $R = 27$ are so steep that in that case only small y values dictate the size of the integral. This may even drive the luminosity to negative values, cf. figure 4.14 (a) for $Y = 0$. However, this does not lead to an overall negative cross section, as σ_{SPS} also needs to be taken into account.

For unequal scales $Q_1 \neq Q_2$, the situation becomes more involved. As there is no obvious initial scale anymore, the DGS scheme [57], section 6.3, suggests using a profile function $p(u, \mu_1, \mu_2)$ that smoothly interpolates between μ_1 at small u and μ_2 at large u. Expanding this formalism to colour non-singlet representations, DPDs inside the subtraction term (4.86) are now initialised and evaluated at

$$F_{\mathrm{spl,pt}}\big(\ldots, p(y\nu; Q_1, \mu_h),\, p(y\nu; Q_2, \mu_h),\, Q_1 Q_2 \,|\, p(y\nu; \nu, \mu_h),\, p^2(y\nu; \nu, Q_1 Q_2) \big). \tag{4.88}$$

This choice ensures that at large y initial and final DPD coincide such that neither a DGLAP nor a CS evolution is possible. In addition, it is evaluated at the same final rapidity as the DPDs inside $\mathcal{L}_{1\mathrm{v}1}$, which is fixed by the product $\sqrt{x_1 x_2 \bar{x}_1 \bar{x}_2}\, s$ according to (2.11). Hence, in this region the subtraction term still contains only fixed order pertubation theory. Following [128, 131], a comprehensive quantitative analysis would in this case also contain a variation of the theory parameters inside the profile function

that determine how rapidly the function approaches μ_1 and μ_2. This is beyond the scope of this work, which is why the luminosities for mixed scales in figures 4.16, H.2, and H.3 do not contain the subtracted 1v1 luminosity.

Figures 4.15, 4.16, and 4.17 show luminosities for $(gg), (gg)$ with $Y \in [-4, 4]$ at $(Q_1, Q_2) = (10\,\text{GeV}, 10\,\text{GeV})$, $(80\,\text{GeV}, 10\,\text{GeV})$, and $(80\,\text{GeV}, 80\,\text{GeV})$, respectively. Luminosities for more flavour combinations can be found in appendix H. All luminosities are obtained with DPD evolution at LL accuracy, matching the current order of available partonic cross sections [23]. They correspond to the following final states:

$$
\begin{aligned}
(g, g), (g, g) &: \text{4-jet}, & (u, g), (\bar{d}, g) &: W^+ + \text{dijet}, \\
(b, g), (g, b) &: \text{two } b\text{-jets}, & (u, \bar{d}), (\bar{d}, u) &: W^+ W^+, \\
(u\bar{u}), (\bar{d}, d) &: W^+ W^-, & (c, \bar{b}), (\bar{s}, c) + (c, \bar{s}), (\bar{b}, c) &: W^+ W^+.
\end{aligned}
$$

We take into account two channels in the last line due to indistinguishable final states. This is not the case for the remaining channels: for example, $(\bar{d}, g), (u, g)$ leads to a different polarisation of the produced W-boson as the weak interaction is not invariant under parity.

Even after subtraction, the 1v1 luminosities tend to be the largest ones for almost all flavour and colour combinations. If not, then they are of the same order of magnitude as $\mathcal{L}_{2v2}$. As $\mathcal{L}_{1v1}$ is the part of the overall luminosity that suffers the least from ambiguities when defining the corresponding ansatz F_{split}, this fact leads to an increased model independence of our results.

In addition, the colour singlet and non-singlet luminosities are closest together in the 1v1 channel. Before subtraction, they are even larger than the colour singlet distributions for some combinations. Subtracted 1v1 luminosities in different colour representations are never further apart than a factor of 10, often it is only a factor of 5 to 1. In these graphs, the bands from the different ansätze for ΔJ are the smallest, even barely visible at all. This can be explained with the steepest fall-off of the product of two splitting DPDs in y compared to one or two product DPDs.

Luminosities for some combinations of unequal flavours in appendix H are quite asymmetric around $Y = 0$, with sometimes more than two orders of magnitude difference between them at $Y = \pm 4$. For luminosities involving the product ansatz, this can be explained with the behaviour of PDFs for different flavours. At small x, evolved quark and antiquark flavours are driven by the gluon PDF, thus both families roughly have the same size: $f_g > f_q \sim f_{\bar{q}}$. At large x however, we have $f_q > f_g > f_{\bar{q}}$ for valence quarks. When going from $Y > 0$ to $-Y$, we effectively switch the values of x_1 $(\bar{x}_1)$ and x_2 $(\bar{x}_2)$. Hence, values of product DPDs for flavour combinations like $(q, \bar{q})$, (q, g), and $(\bar{q}, g)$ strongly depend on whether the first or second flavour is evaluated at large x. As explained above, the large asymmetries cannot be observed for non-valence flavours.

$\mathcal{L}_{1v1}$ on the other hand does not contain such an asymmetry in the initial conditions of the respective DPDs. In figure H.4 (a) for example the integrand at initial scales, as derived from (4.17), is completely symmetric in Y due to $P_{qg}^{(0)} = P_{\bar{q}g}^{(0)}$. Hence, the asymmetry at final scales is generated exclusively by the different behaviour of the flavours u and $\bar{d}$ under evolution.

This quantitative study underlines the importance of colour correlations in double parton scattering. Although colour correlated DPDs are suppressed by a Sudakov factor, their luminosities have a sizeable contribution to the DPS cross section, in most of the cases with the same order of magnitude than the colour singlet ones. Simply neglecting them a priori after referring to this Sudakov suppression is therefore not an option in calculations of full cross sections. The NLO calculations in chapter 3 may thus add a valuable ingredient to corresponding phenomenological studies in the future.
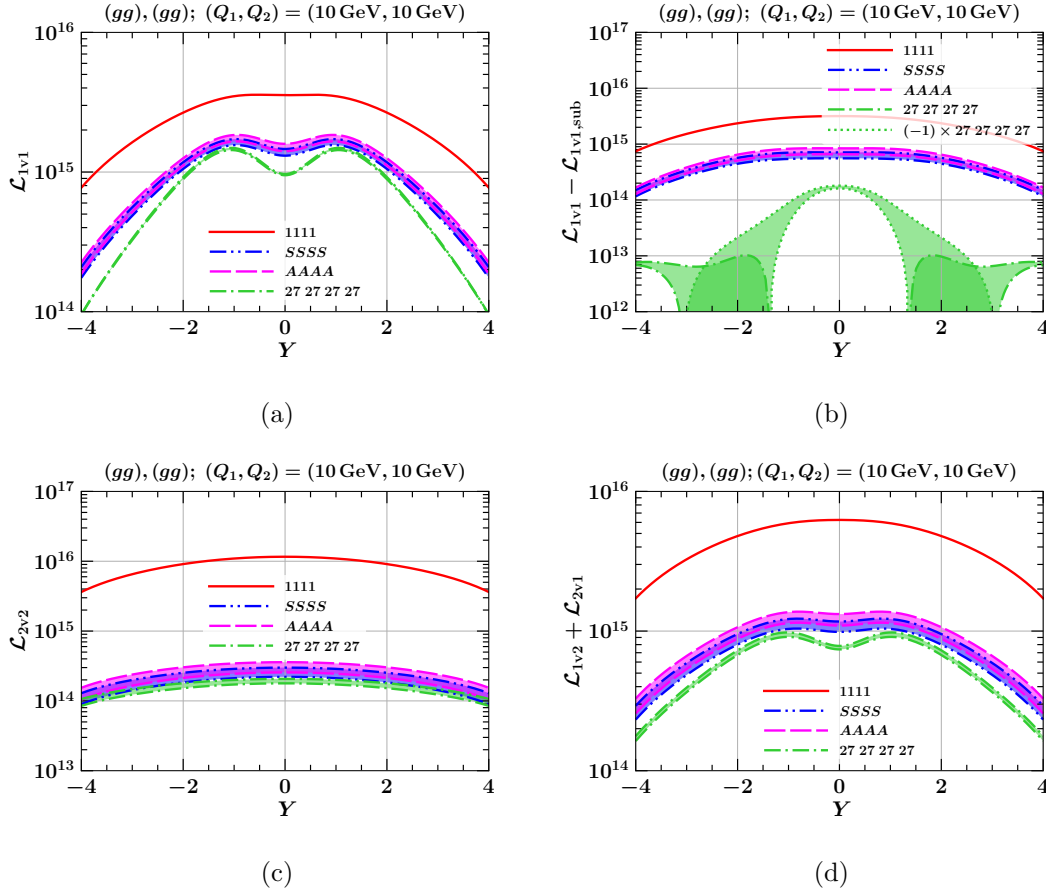
Figure 4.15: Luminosities for $(gg),(gg)$ at $(Q_1, Q_2) = (10\,\mathrm{GeV}, 10\,\mathrm{GeV})$ in all colour representations. The bands span the area between minimum and maximum of luminosities calculated with the five ansätze for ${}^R\Delta J$ given in eqs. (4.48) to (4.52).

(a)

(b)

(c)
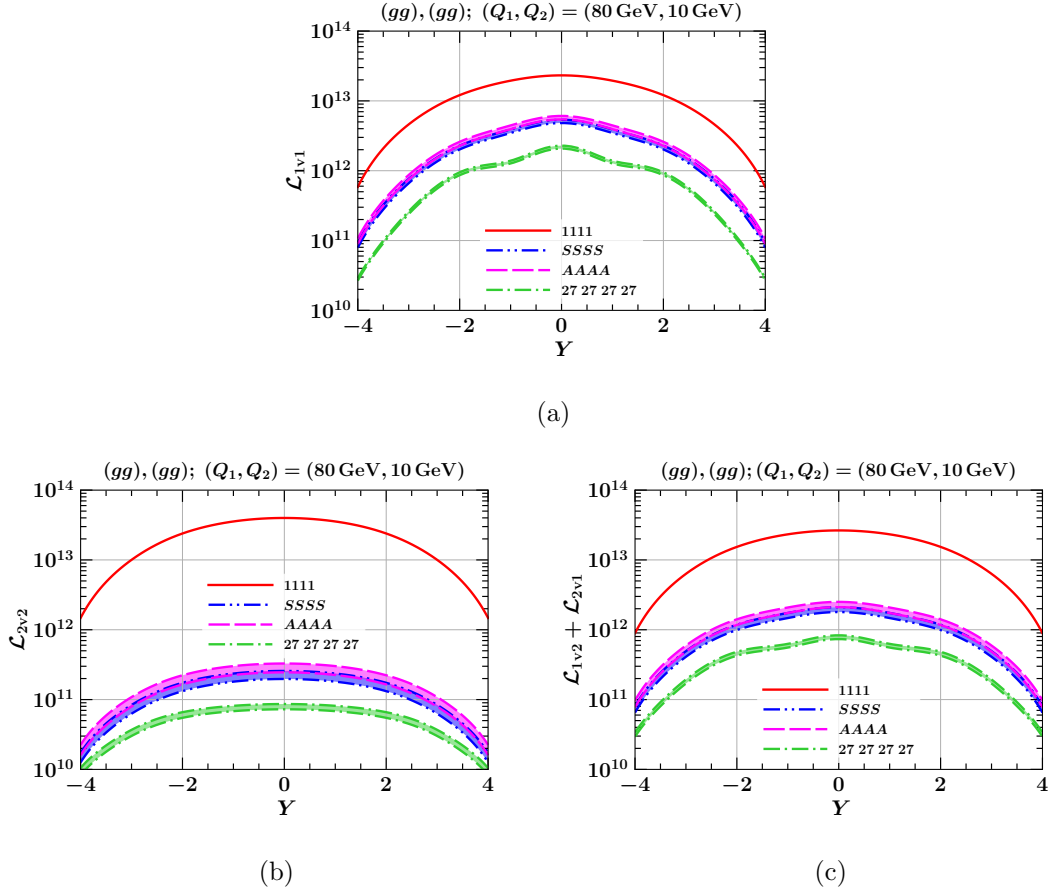
Figure 4.16: Luminosities for $(gg), (gg)$ at $(Q_1, Q_2) = (80\,\text{GeV}, 10\,\text{GeV})$ in all colour representations. The bands span the area between minimum and maximum of luminosities calculated with the five ansätze for $^R\Delta J$ given in eqs. (4.48) to (4.52).
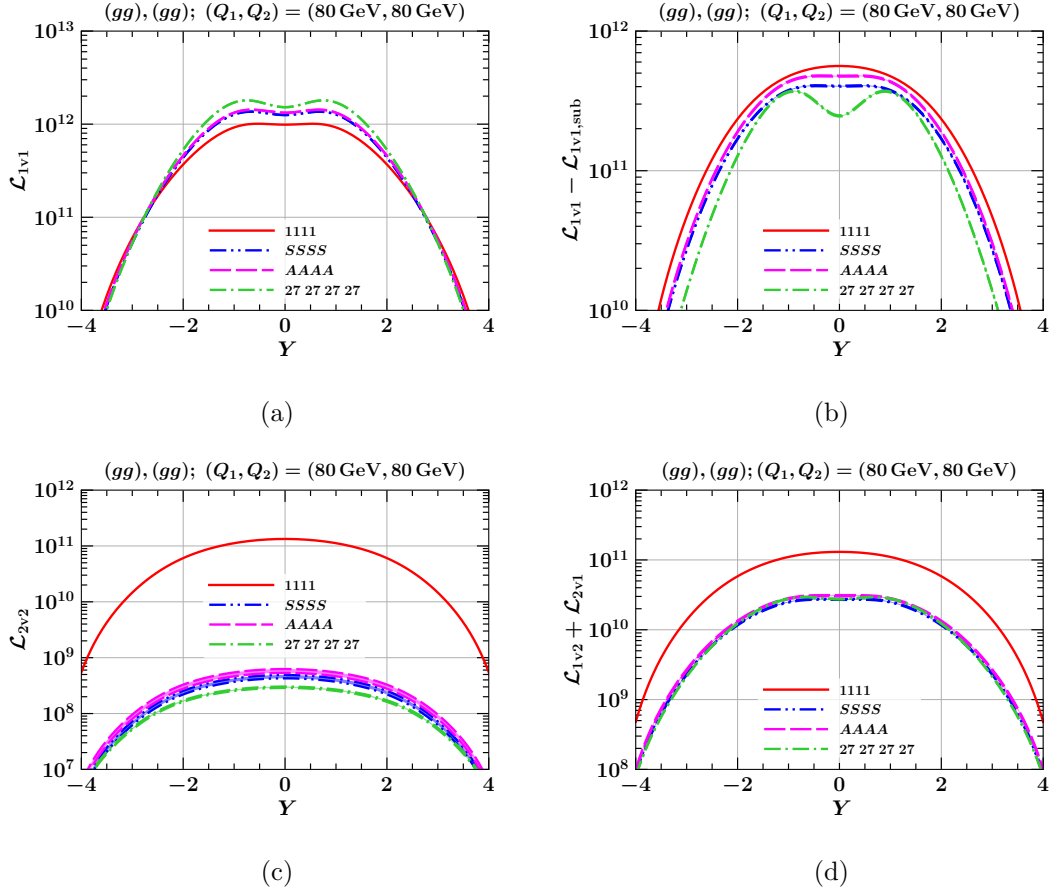
Figure 4.17: Luminosities for $(gg), (gg)$ at $(Q_1, Q_2) = (80\,\text{GeV}, 80\,\text{GeV})$ in all colour representations. The bands span the area between minimum and maximum of luminosities calculated with the five ansätze for $^R\Delta J$ given in eqs. (4.48) to (4.52).

Chapter 5

Conclusions

Over the last decades, the field of double parton scattering has made significant progress towards a fully phenomenological description of DPS processes. Their contribution has been measured in a variety of final states, while at the same time formalisms for factorised cross sections, interplay with single parton scattering, and even prescriptions for lattice QCD are in development. Despite all these impressive achievements, the description of DPS still suffers from a large gap between theory and experiment. On the one hand, experimentalists are far from being able to provide (precise) enough data for parton distributions, on the other hand, theorists are struggling to provide predictions with a more sophisticated ansatz than the DPS pocket formula (2.14). The aim of this thesis was to bring theory closer to phenomenological predictions that take into account the full wealth of interpartonic correlations inside the proton, focusing on their colour charge under QCD. Assessing the behaviour of colour-correlated DPDs is a key step towards the calculation of a full cross section as given in eq. (2.9).

In chapter 3 we computed the NLO contributions to the colour non-singlet DGLAP kernels for unpolarised and longitudinally polarised partons and transversely polarised quarks. Two methods were used: The first one used existing results of PDF DGLAP kernels to compute all x-dependent parts. A key feature of colour non-singlet DPDs is their rapidity dependence, which is absent in colour singlet distributions and propagates to the DGLAP kernels for colour correlated partons. A computation of these parts must therefore be sensitive to rapidity divergences, as it is the case in transverse momentum dependent factorisation. Therefore, in the second computation, we extracted the complete unpolarised and transverse kernels from colour projected TMD matrix elements via the small-z matching relation to collinear matrix elements. In combination, both methods yielded the NLO DGLAP kernels for all polarisations. Large parts of the results were calculated twice, which served as a strong cross-check. In contrast to the LO contributions, the x-dependent terms exhibit a complex structure and could not be trivially derived from the colour singlet kernels. This is due to the abundance of different NLO splitting graphs, each with its own behaviour under projection onto colour representations. We found remarkable simplicity in the $\delta(1-x)$ terms of the kernels: the cusp anomalous dimension $^R\gamma_J$ exhibits Casimir scaling both at LO and NLO. After

subtracting the contribution of the colour singlet kernel from the non-cusp part, the remaining terms also scale with the quadratic Casimir of the adjoint representation.

Chapter 4 then brought these results to life. We presented an extension to the DGLAP evolution library CHILIPDF that is capable of evolving colour-correlated DPDs. This was not only limited to the inclusion of the new DGLAP kernels, but also included a disentanglement of the DGLAP and CS equation. With the implementation of colour-correlated flavour matching relations and small-y splitting onto PDFs, the code is on the same level as the existing one for colour uncorrelated DPDs. After specifying the DPD models, the non-perturbative ansätze for the CS kernel, and the configurations of perturbative orders, we could thus perform a comprehensive quantitative study on the effects of scale evolution on DPDs in each colour representation.

First, we quantified the impact of different parts of DGLAP and CS kernels on DPDs. It became clear that in many cases a Sudakov factor that includes the double logarithmic terms and CS evolution serves as a good estimate for the order of magnitude after evolution. However, DGLAP evolution could still lead to severe changes in shape, with even sign changes being possible. The CS evolution also led to a change in the y-shape which drastically suppressed DPDs at large y. The NLO corrections to the evolution kernels typically were of the same order of magnitude both in the colour singlet and non-singlet case, underlining the importance of our calculations in chapter 3 for future precision studies.

Colour correlated DPD luminosities were mostly found to be smaller than their uncorrelated counterparts. In particular, the ansatz-dependent luminosity $\mathcal{L}_{2v2}$ tends to be orders of magnitude smaller in the colour correlated case. However, for the (subtracted) luminosity $\mathcal{L}_{1v1}$, which is fully dictated by perturbation theory, all colour representations are usually of the same order of magnitude. In most cases, this contribution is also the largest overall, showing that a priori colour non-singlet contributions cannot be neglected at the level of luminosities.

Altogether we strongly believe that we have made some valuable steps towards a more profound theoretical description of double parton scattering. A defining feature of DPS is the correlation between the two partons involved. For the first time, we have described colour correlated partons in DPS in a fully quantitative approach for all possible kinematical configurations.

As a next step, a numerical calculation of collinear DPS cross sections would be very revealing. CHILIPDF is now able to provide not only colour averaged, but also colour correlated DPDs at NLO accuracy. To match this improvement in the description of DPDs, the colour correlated partonic cross sections have to be improved to NLO. In addition, there are ongoing efforts to incorporate DPS in a Monte-Carlo framework of parton showers, dShower [32]. Furthermore, collinear DPDs dictate the behaviour of DTMDs at small z_i through the matching relation (2.68) and thus also play an important role in transverse momentum dependent DPS cross sections.

Appendix A

Conventions

Transverse momenta are denoted by a symbol in bold font, e.g. $\boldsymbol{y}$. Its counterpart in non-bold font denotes the Euclidian length of the vector, e.g.

$$y = |\boldsymbol{y}| = \sqrt{y_1^2 + y_2^2}\,. \tag{A.1}$$

If not stated otherwise, we use the Einstein notation, i.e. an implicit summation over any kind of index that appears twice in an expression. Exceptions of this rule are representation indices and parton flavours.

We define

$$C_A = N\,, \qquad C_F = \frac{N^2 - 1}{2N}\,, \qquad C_{10} = 2N\,, \qquad C_{27} \overset{N=3}{=} 8 \tag{A.2}$$

for the colour group $\mathrm{SU}(N)$. The last two Casimir eigenvalues can be found in eq. (A.25) of [132]. C_{27} is always taken at $N = 3$ for the same reason as below eq. (B.10). We set

$$T_F = \frac{1}{2} \tag{A.3}$$

in the whole work such that this normalisation constant does not appear explicitly.

We always expand perturbative quanitities in

$$a_s(\mu) = \frac{\alpha_s(\mu)}{2\pi}\,. \tag{A.4}$$

For its RGE equation we use the convention

$$\frac{\mathrm{d}}{\mathrm{d}\log\mu}a_s(\mu) = \frac{\beta\big(a_s(\mu)\big)}{\pi} = -a_s\sum_{n=1}\beta_{n-1}\,a_s^{n+1}(\mu)\,, \tag{A.5}$$

where

$$\beta_0 = \frac{11}{3}C_A - \frac{2}{3}n_f\,. \tag{A.6}$$

In chapter 4 we encounter the constant

$$b_0 = 2e^{-\gamma_E} \approx 1.1229189671 \,, \tag{A.7}$$

where $\gamma_E \approx 0.5772156649$ is the Euler-Mascheroni constant.

The plus-distribution of some function $f(x)$ is defined with the help of a smooth test function $t(x)$, $x \in [0,1]$:

$$\int\limits_x^1 \mathrm{d}x' \left[f(x') \right]_+ t(x') = \int\limits_x^1 \mathrm{d}x' \, f(x') \left(t(x') - t(1) \right) - t(1) \int\limits_0^x \mathrm{d}x' \, f(x') \,. \tag{A.8}$$

The prescription defines a functional that maps an arbitrary test function to a real number.

Appendix B

Colour matrices

B.1 Colour projectors

For two quark flavours, we have

$$P_{11}^{\underline{i}\,\underline{j}} = \frac{1}{N}\delta_{ii'}\delta_{jj'} \tag{B.1}$$

$$P_{88}^{\underline{i}\,\underline{j}} = 2t_{ii'}^a t_{jj'}^a, \tag{B.2}$$

and for two gluons

$$P_{11}^{\underline{a}\,\underline{b}} = \frac{1}{N^2-1}\delta^{aa'}\delta^{bb'} \tag{B.3}$$

$$P_{AA}^{\underline{a}\,\underline{b}} = \frac{1}{N}f^{aa'c}f^{bb'c} \tag{B.4}$$

$$P_{SS}^{\underline{a}\,\underline{b}} = \frac{N}{N^2-4}d^{aa'c}d^{bb'c} \tag{B.5}$$

$$P_{AS}^{\underline{a}\,\underline{b}} = \frac{1}{\sqrt{N^2-4}}f^{aa'c}d^{bb'c} \tag{B.6}$$

$$P_{SA}^{\underline{a}\,\underline{b}} = \frac{1}{\sqrt{N^2-4}}d^{aa'c}f^{bb'c} \tag{B.7}$$

$$P_{10\,\overline{10}}^{\underline{a}\,\underline{b}} = \frac{1}{4}\left(\delta^{ab}\delta^{a'b'} - \delta^{ab'}\delta^{a'b}\right) - \frac{1}{2}P_{AA}^{\underline{a}\,\underline{b}} - \frac{i}{4}\left(d^{abc}f^{a'b'c} + f^{abc}d^{a'b'c}\right) \tag{B.8}$$

$$P_{\overline{10}\,10}^{\underline{a}\,\underline{b}} = \frac{1}{4}\left(\delta^{ab}\delta^{a'b'} - \delta^{ab'}\delta^{a'b}\right) - \frac{1}{2}P_{AA}^{\underline{a}\,\underline{b}} + \frac{i}{4}\left(d^{abc}f^{a'b'c} + f^{abc}d^{a'b'c}\right) \tag{B.9}$$

$$P_{27\,27}^{\underline{a}\,\underline{b}} = \frac{1}{2}\left(\delta^{ab}\delta^{a'b'} + \delta^{ab'}\delta^{a'b}\right) - P_{SS}^{\underline{a}\,\underline{b}} - P_{11}^{\underline{a}\,\underline{b}}. \tag{B.10}$$

For $N > 3$, there is an additional irreducible representation which is absent in the decomposition (2.25). Hence, to avoid an impression of generality where there is none, in the case of $R = 27$ all expressions are given with N set to 3.

A note of caution: Whenever we contract two fundamental index pairs, a triplet index like i always has to be contracted with an antitriplet one like i' to ensure the right

behaviour under gauge transformations. This becomes particularly important when we deal with projected quark-antiquark splitting kernels.

For the mixed cases, $q \to g$ and $g \to q$, the projectors are

$$P_{11}^{i\,a} = \frac{1}{\sqrt{N(N^2 - 1)}} \delta_{ii'} \delta^{aa'} \,, \tag{B.11}$$

$$P_{8A}^{i\,a} = P_{A8}^{a\,i} = \sqrt{\frac{2}{N}} t_{ii'}^c f^{aa'c} \,, \tag{B.12}$$

$$P_{8S}^{i\,a} = P_{S8}^{a\,i} = \sqrt{\frac{2N}{N^2 - 4}} t_{ii'}^c d^{aa'c} \,. \tag{B.13}$$

Thus,

$$P_{R\overline{R}'}^{r\,s} = P_{\overline{R}'R}^{s\,r} \tag{B.14}$$

holds for all projectors. In this convention, the projectors also fulfil

$$P_{R_1 R_2}^{r\,s} P_{R_3 R_4}^{s\,t} = \delta_{R_2 \overline{R}_3} P_{R_1 R_4}^{r\,t} \tag{B.15}$$

and

$$P_{R_1 R_2}^{r\,s} P_{R_3 R_4}^{r\,s} = \delta_{R_1 \overline{R}_3} \delta_{R_2 \overline{R}_4} m(R) \,, \tag{B.16}$$

where

$$m(R) = P_{R\overline{R}}^{r\,r} \tag{B.17}$$

is the multiplicity of the representation R. Its explicit values are

$$m(1) = 1 \,, \tag{B.18}$$

$$m(8) = m(A) = m(S) = N^2 - 1 \stackrel{N=3}{=} 8 \,, \tag{B.19}$$

$$m(10) = m(\overline{10}) = \frac{(N^2 - 1)(N^2 - 4)}{4} \stackrel{N=3}{=} 10 \,, \tag{B.20}$$

$$m(27) = 27 \,. \tag{B.21}$$

Note that there is an ambiguity in our naming convention. We call colour tensors $P_{R\overline{R}'}^{r\,s}$ "projectors", although technically speaking this term is wrong for the cases $R\overline{R}' = AS$ and SA. These are the only two representation pairs that do not fulfil $\overline{R}' = \overline{R}$. As DGLAP kernels vanish for these combinations because of their behaviour under charge conjugation, these cases can be ignored anyway.

B.2 Transformation matrices between s- and t-channel

In the following, we list all matrices $K_{ts}^{a_1 a_2}$ introduced in eq. (4.27). They can be obtained by inverting the matrices $\mathbf{M}_{a_1 a_2}$ given in [27, 89][1], i.e.

$$K_{st}^{a_1 a_2} = \mathbf{M}_{a_1 a_2} \,. \tag{B.22}$$

---

[1]We thank one of the authors of [89], Peter Plößl, for providing us with the missing matrix $\mathbf{M}_{gg}$.

We find

$$K_{ts}^{qq} = K_{ts}^{\bar{q}\bar{q}} = 3 \begin{pmatrix} 1 & 2 \\ -\sqrt{2} & \sqrt{2} \end{pmatrix}, \tag{B.23}$$

$$K_{ts}^{q\bar{q}} = K_{ts}^{\bar{q}q} = \begin{pmatrix} 1 & 8 \\ 2\sqrt{2} & -2\sqrt{2} \end{pmatrix}, \tag{B.24}$$

$$K_{ts}^{qg} = K_{ts}^{gq} = 3 \begin{pmatrix} 1 & 2 & 5 \\ \sqrt{\frac{5}{2}} & -\sqrt{10} & \sqrt{\frac{5}{2}} \\ -\frac{3}{\sqrt{2}} & -\sqrt{2} & \frac{5}{\sqrt{2}} \end{pmatrix}, \tag{B.25}$$

$$K_{ts}^{\bar{q}g} = K_{ts}^{g\bar{q}} = 3 \begin{pmatrix} 1 & 2 & 5 \\ \sqrt{\frac{5}{2}} & -\sqrt{10} & \sqrt{\frac{5}{2}} \\ \frac{3}{\sqrt{2}} & \sqrt{2} & -\frac{5}{\sqrt{2}} \end{pmatrix}, \tag{B.26}$$

$$K_{ts}^{gg} = \begin{pmatrix} 1 & 8 & 8 & 10 & 10 & 27 & 0 & 0 \\ 2\sqrt{2} & -\frac{24\sqrt{2}}{5} & 8\sqrt{2} & -8\sqrt{2} & -8\sqrt{2} & \frac{54\sqrt{2}}{5} & 0 & 0 \\ -2\sqrt{2} & -8\sqrt{2} & -8\sqrt{2} & 0 & 0 & 18\sqrt{2} & 0 & 0 \\ 0 & 0 & 0 & 4\sqrt{10} & -4\sqrt{10} & 0 & 0 & 16\sqrt{2} \\ 0 & 0 & 0 & 4\sqrt{10} & -4\sqrt{10} & 0 & 0 & -16\sqrt{2} \\ \sqrt{10} & -16\sqrt{\frac{2}{5}} & 0 & 2\sqrt{10} & 2\sqrt{10} & -9\sqrt{\frac{2}{5}} & 0 & 0 \\ 0 & 0 & 0 & 0 & 0 & 0 & 16\sqrt{2} & 0 \\ 3\sqrt{3} & \frac{24\sqrt{3}}{5} & -8\sqrt{3} & -2\sqrt{3} & -2\sqrt{3} & \frac{21\sqrt{3}}{5} & 0 & 0 \end{pmatrix}. \tag{B.27}$$

The ordering of representations in rows and columns is the same as the one in eqs. (4.30) and (4.31) for gluons and in eq. (2.24) for quarks.

Appendix C

Contribution of all four-vertex graphs to the gluon DGLAP kernel

In this appendix, we calculate the results provided in section 3.1.4 by using methods explained in appendix B of [10]. The starting point is the master formula (3.27), which we recite here for the sake of readability:

$$
-\frac{1}{\epsilon} a_s^2 \, ^{R\overline{R}}\widetilde{P}_{gg,(\mathrm{y})}^{(1)}(x) = \left[\int\limits_0^{Q^2} \mathrm{d}|k^2| \int \mathrm{d}PS_{(\mathrm{y})} \frac{{}^{R\overline{R}}\mathcal{N}_{(\mathrm{y})}}{\mathcal{D}_{(\mathrm{y})} \, |k^2|^2} \right]_{-1}. \tag{C.1}
$$

As explained in section 3.1.4, the key step to isolate the mass singularities of every graph is to cut-off the upper limit of the $|k^2|$ integration at Q^2. This additional integration is compensated inside the phase-space integration measure $\mathrm{d}PS_{(\mathrm{y})}$ by a δ-distribution fixing $|k^2|$ through momentum conservation,

$$
\delta\big(|k^2| + \Sigma^2\big). \tag{C.2}
$$

Here, Σ is the sum of p and all momenta going over the final state cut. The main computational challenge will be to find suitable integration variables such that Σ^2 and/or all the internal propagators contain no scalar products between different momenta anymore. Under these conditions one is able to integrate out the δ-distribution and perform angular integrations in the easiest way possible.

Graph (j)

Graph (k)

Graph (l)
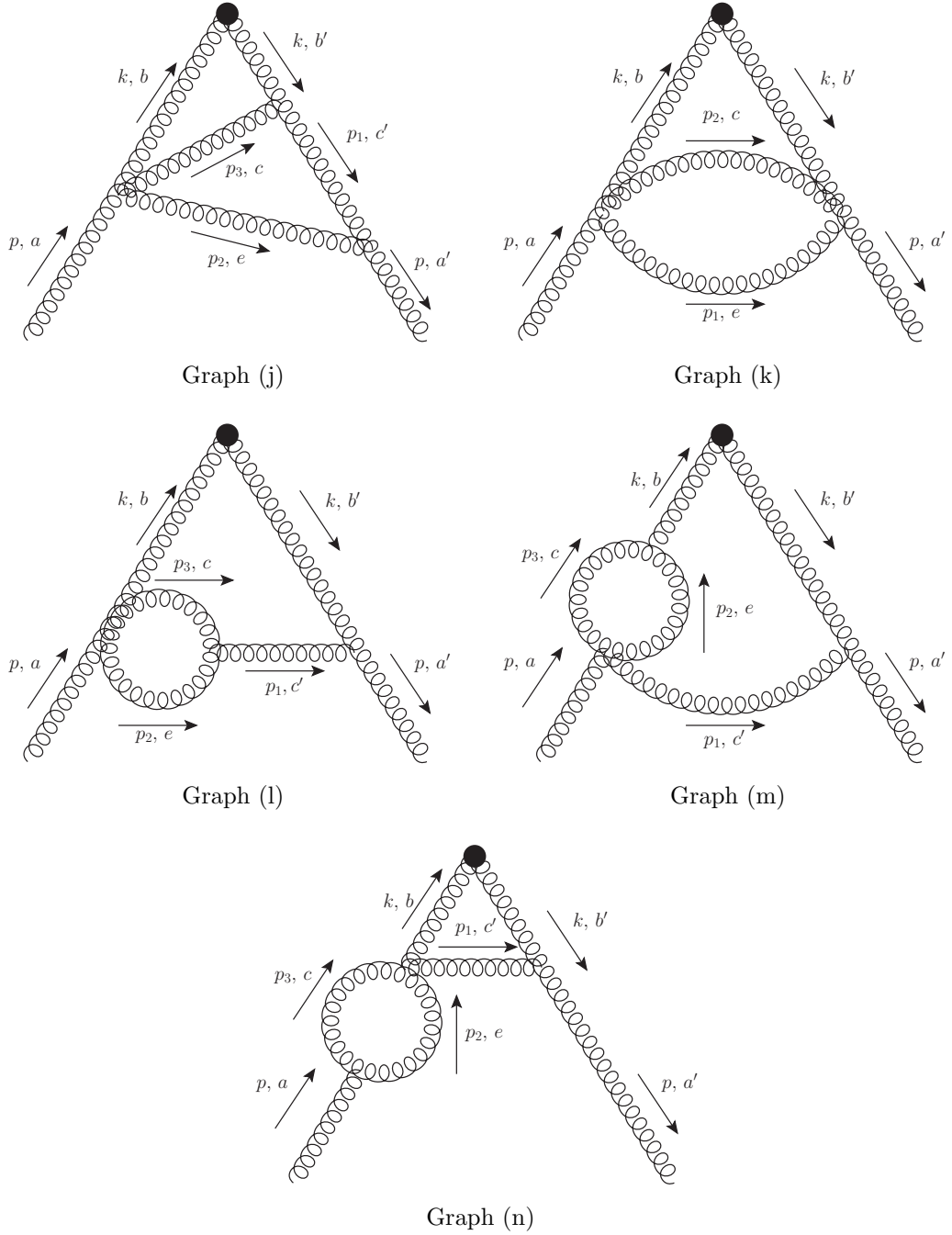
Graph (m)

Graph (n)

Figure C.1: All NLO splitting graphs involving a four-gluon vertex. All internal and external momenta with corresponding colour indices are shown. The Lorentz indices can be deduced from the $d_{\mu\nu}(\dots)$ factors inside the numerators in eqs. (C.4) to (C.7).

C.1   Feynman graphs

Figure C.1 shows all Feynman graphs with at least one four-gluon vertex. From these diagrams, we derive the following numerators and denominators:

$$
\mathcal{N}_{(\mathrm{j})}^{\underline{a\,b}} = S^{\mu\nu\rho\sigma}\, d_{\sigma\sigma'}(k)\, d_{\gamma\gamma'}(p_1)\, d_{\beta\beta'}(p_2)\, d_{\alpha\alpha'}(p_3)
$$
$$
\times\, V_{4,\,bcea}^{\nu'\alpha'\beta'\mu}\, V_{3,\,cb'c'}^{\alpha\sigma'\gamma'}(p_3,\,k,\,-p_1)\, V_{3,\,ec'a'}^{\beta\gamma\rho}(p_2,p_1,-p) \tag{C.3}
$$

$$
\mathcal{N}_{(\mathrm{k})}^{\underline{a\,b}} = S^{\mu\nu\rho\sigma}\, d_{\sigma\sigma'}(k)\, d_{\beta\beta'}(p_1)\, d_{\alpha\alpha'}(p_2)\, V_{4,\,bcea}^{\nu'\alpha'\beta'\mu}\, V_{4,\,cb'a'e}^{\alpha,\sigma',\rho,\beta} \tag{C.4}
$$

$$
\mathcal{N}_{(\mathrm{l})}^{\underline{a\,b}} = S^{\mu\nu\rho\sigma}\, d_{\nu\nu'}(k)\, d_{\sigma\sigma'}(k)\, d_{\gamma\gamma'}(p_1)\, d_{\beta'\beta}(p_2)\, d_{\alpha\alpha'}(p_3)
$$
$$
\times\, V_{4,\,bcea}^{\nu'\alpha'\beta'\mu}\, V_{3,\,cc'e}^{\alpha\gamma'\beta}(p_3,\,-p_1,p_2)\, V_{3,\,c'b'a'}^{\gamma\sigma'\rho}(p_1,k,-p) \tag{C.5}
$$

$$
\mathcal{N}_{(\mathrm{m})}^{\underline{a\,b}} = S^{\mu\nu\rho\sigma}\, d_{\nu\nu'}(k)\, d_{\sigma\sigma'}(k)\, d_{\gamma'\gamma}(p_1)\, d_{\beta\beta'}(p_2)\, d_{\alpha\alpha'}(p_3)
$$
$$
\times\, V_{4,\,cec'a}^{\alpha\beta\gamma'\mu}\, V_{3,\,cbe}^{\alpha'\nu'\beta'}(p_3,\,-k,\,-p_2)\, V_{3,\,c'b'a'}^{\gamma\sigma'\rho}(p_1,k,-p) \tag{C.6}
$$

$$
\mathcal{N}_{(\mathrm{n})}^{\underline{a\,b}} = S^{\mu\nu\rho\sigma}\, d_{\nu\nu'}(k)\, d_{\sigma\sigma'}(k)\, d_{\gamma'\gamma}(p_1)\, d_{\beta\beta'}(p_2)\, d_{\alpha\alpha'}(p_3)
$$
$$
\times\, V_{4,\,bc'ec}^{\nu'\gamma'\beta'\alpha'}\, V_{3,\,cea}^{\alpha\beta\mu}(-p_3,\,-p_2,p)\, V_{3,\,c'b'a'}^{p_1,\gamma\sigma'\rho}(p_1,k,-p)\,, \tag{C.7}
$$

and

$$
\mathcal{D}_{(\mathrm{j})} = \mathcal{D}_{(\mathrm{l}),\mathrm{le}} = p_1^2 + i\varepsilon \tag{C.8}
$$
$$
\mathcal{D}_{(\mathrm{k})} = 1 \tag{C.9}
$$
$$
\mathcal{D}_{(\mathrm{l}),\mathrm{ri}} = \mathcal{D}_{(\mathrm{m})} = \mathcal{D}_{(\mathrm{n})} = (p_2^2 + i\varepsilon)\,(p_3^2 + i\varepsilon)\,. \tag{C.10}
$$

We have used the Feynman rules from appendix D of [58] and

$$
-\,i\,g^2\, V_{4,\,abcd}^{\mu\nu\rho\sigma} \tag{C.11}
$$

for the four-gluon vertex. The factors

$$
V_{3,\,abc}^{\mu\nu\rho}(p,q,r) = f^{abc}\big((p-q)^\rho g^{\mu\nu} + (q-r)^\mu g^{\nu\rho} + (r-p)^\nu g^{\rho\mu}\big) \tag{C.12}
$$
$$
V_{4,\,abcd}^{\mu\nu\rho\sigma} = f^{e'ab}\, f^{e'cd}\big(g^{\mu\rho}g^{\nu\sigma} - g^{\mu\sigma}g^{\nu\rho}\big)
$$
$$
+ f^{e'ac}\, f^{e'bd}\big(g^{\mu\nu}g^{\rho\sigma} - g^{\mu\sigma}g^{\nu\rho}\big)
$$
$$
+ f^{e'ad}\, f^{e'bc}\big(g^{\mu\nu}g^{\rho\sigma} - g^{\mu\rho}g\nu\sigma\big) \tag{C.13}
$$

describe the colour, Lorentz, and momentum dependencies of the three- and four-gluon vertex, respectively.

The final state cut can be applied to graph (l) in two different ways: Either through p_2 and p_3 (**le**ft cut), or through p_1 (**ri**ght cut). This has no effect on the numerator, as both a cut gluon line and a gluon propagator contain the sum over physical polarisations, but propagators receive an additional denominator proportional to the momentum squared, cf. eq. (C.15). On the other hand, gluons going over the final state cut are on the mass shell, which needs to be taken into account in the respective phase-space integrals.

For every gluon line, there is a contribution of

$$d_{\mu\nu}(q) = -g_{\mu\nu} + \frac{q^\mu n^\nu + n^\mu q^\nu}{q^+} \,, \tag{C.14}$$

where $q \cdot n = q^+$, see eq. (C.26). The Lorentz indices are ordered in the direction of q. For the propagators $D_{\mu\nu}(q)$, we use the $i\varepsilon$ prescription for proper time ordering,

$$D_{\mu\nu}(q) = \frac{i}{q^2 + i\varepsilon} \, d_{\mu\nu}(q)\,. \tag{C.15}$$

We summarize the spin projector and the collinear operator contribution into

$$S_{\mu\nu\rho\sigma} = g^4 \mu^{4\epsilon} \frac{k^+}{p^+} \frac{1}{D-2} \, g_{T\,\mu\rho}\, g_{T\,\nu\sigma}\,, \tag{C.16}$$

with the transverse metric

$$g_T^{\mu\nu} = g^{\mu\nu} - n^\mu \bar{n}^\nu - \bar{n}^\mu n^\nu \tag{C.17}$$

that projects a Lorentz index on a transverse one. The vectors n and $\bar{n}$ are defined in (C.26) and (C.25), respectively. The Feynman rule for the collinear operator insertion can be derived after transforming the operator definition (2.19) to momentum space and expand to $\mathcal{O}(g)$. We find the correspondence

$$G_a^{+j}(q)W_{ab}(q) \stackrel{\cong}{=} (-i)\, k^+ g_\nu^j\,. \tag{C.18}$$

Together with the global factor $1/(k^+ p^+)$ from the DPD definition (2.16) and combined with the sum over transverse degrees of freedom for unpolarised outgoing gluons, both contributions (left and right from the final state cut) combine to

$$\frac{1}{k^+ p^+} \, k^+ g_\nu^j \, k^+ g_\sigma^{j'} \, \delta_{jj'} = \frac{k^+}{p^+} \, g_{T\nu\sigma}\,. \tag{C.19}$$

Summing and averaging the incoming gluons over transverse polarisations gives an additional factor of $g_{T\,\mu\rho}/(D-2)$, which together with the coupling vertex factors form the tensor $S_{\mu\nu\rho\sigma}$ defined in (C.16).

The longitudinal numerators can be obtained from the unpolarised ones by exchanging $S_{\mu\nu\rho\sigma}$ for

$$S_{\Delta,\mu\nu\rho\sigma} = g^4 \mu^{4\epsilon} \frac{k^+}{p^+} \frac{1}{(D-2)(D-3)} \big(g_{T\,\mu\nu}\, g_{T\,\rho\sigma} - g_{T\,\mu\sigma}\, g_{T\,\rho\nu}\big)\,, \tag{C.20}$$

using the projector $\mathcal{P}_\delta$ defined in (3.34) instead of the sums and averaging factor. The denominators remain unchanged.

To obtain DGLAP kernels for different colour representations, we compute the colour projected version of the numerator via

$$^{R\overline{R}}\mathcal{N}_{(\mathrm{y})} = \frac{1}{m(R)} P^{a\,b}_{R\overline{R}} \, \mathcal{N}^{a\,b}_{(\mathrm{y})} \,. \tag{C.21}$$

The normalisation comes from the definition of a colour projected DGLAP kernel, eq. (2.53). The remaining prefactors there reduce to a factor of

$$\frac{\epsilon(R)\,\mathcal{N}_g}{\epsilon(\overline{R})\,\mathcal{N}_g} = 1 \tag{C.22}$$

in the (gg) channel.

C.2 Calculation

We decompose the momenta as follows:

$$k^\mu = x\,p^\mu + k^-\,n^\mu + t_k^\mu \tag{C.23}$$

$$p_i^\mu = z_i\,p^\mu + p_i^-\,n^\mu + t_i^\mu \,, \tag{C.24}$$

with

$$p^\mu = p^+\bar{n}^\mu = (p^+, 0, \mathbf{0}) \tag{C.25}$$

$$n^\mu = (0, 1, \mathbf{0}) \tag{C.26}$$

$$t^\mu = (0, 0, \boldsymbol{t}) \,. \tag{C.27}$$

We use light-cone coordinates for a four-vector (v^0, v^1, v^2, v^3) with the convention

$$v^\mu = \left(v^+ = \frac{v^0 + v^3}{\sqrt{2}}, \, v^- = \frac{v^0 - v^3}{\sqrt{2}}, \, \boldsymbol{v} = (v^1, v^2)\right) \,. \tag{C.28}$$

The differential reads

$$\mathrm{d}^D v = \mathrm{d}v^+\,\mathrm{d}v^-\,\mathrm{d}^{D-2}\boldsymbol{v} \,. \tag{C.29}$$

In the following computation, we order the graphs by increasing complexity of their denominator. For every graph, we first simplify the phase-space integrals as much as possible before performing the non-trivial integrations involving $\mathcal{N}$ and $\mathcal{D}$. Unless stated otherwise, we take p_1 and p_2 as the independent momenta.

Graph (k). The phase-space integral is

$$
\int dPS_{(k)} = \int \frac{d^D p_1\, d^D p_2\, d^D k}{(2\pi)^{3D}} \delta(x - k^+)\, \delta\big(|k^2| + (p - p_1 - p_2)^2\big)
$$

$$
\times (2\pi)\delta^+(p_1^2)\,(2\pi)\delta^+(p_2^2)\,(2\pi)^D \delta^{(D)}(p - k - p_2 - p_3)
$$

$$
= \frac{1}{4(2\pi)^{2D-2}} \int \frac{dz_1}{z_1} \frac{dz_2}{z_2}\, d^{D-2}\boldsymbol{t}_1\, d^{D-2}\boldsymbol{t}_2
$$

$$
\times \delta\big(|k^2| - a_1\, \boldsymbol{t}_1^2 - a_2\, \boldsymbol{t}_2^2 - 2\, \boldsymbol{t}_1 \cdot \boldsymbol{t}_2\big)\, \delta(1 - x - z_2 - z_3)\,, \tag{C.30}
$$

where

$$
a_1 = \frac{1 - z_2}{z_1}\,, \qquad\qquad a_2 = \frac{1 - z_1}{z_2}\,. \tag{C.31}
$$

To simplify the structure of the δ-distribution, we introduce

$$
\boldsymbol{t}_1' = \boldsymbol{t}_1 + \frac{1}{a_1}\boldsymbol{t}_2\,, \tag{C.32}
$$

which turns the δ-distribution fixing $|k^2|$ into

$$
\frac{1}{a_1}\delta\Big((\boldsymbol{t}_1')^2 + \frac{1}{a_1}\Big(a_2 - \frac{1}{a_1}\Big)\boldsymbol{t}_2^2 - \frac{1}{a_1}|k^2|\Big)\,, \tag{C.33}
$$

allowing us to evaluate the integration over $(\boldsymbol{t}_1')^2$. Furthermore, this condition sets the upper border of the $\boldsymbol{t}_2^2$ integration to

$$
t_m^2 = \frac{|k^2|}{a_2 - \frac{1}{a_1}} = \frac{z_2(1 - z_2)}{x}|k^2|\,. \tag{C.34}
$$

Because the integrand $\mathcal{N}_{(k)}/\mathcal{D}_{(k)}$ does not depend on any angular variable, the angular integrations can be performed already at this point and we obtain

$$
\int d^{D-2}\boldsymbol{t}_i = \frac{1}{2}\,\Omega_{D-2} \int d\boldsymbol{t}_i^2\,(\boldsymbol{t}_i^2)^{\frac{D}{2}-2}\,, \tag{C.35}
$$

with

$$
\Omega_{D-2} = \frac{2\pi^{\frac{D}{2}-1}}{\Gamma(\frac{D}{2} - 1)}\,. \tag{C.36}
$$

What is left is

$$
\int dPS_{(k)}^{(2)} = \frac{1}{16(2\pi)^{2D-2}}(\Omega_{D-2})^2 a_1^{3-D} \int \frac{dz_1}{z_1} \frac{dz_2}{z_2}\, \delta(1 - x - z_1 - z_2)
$$

$$
\times \int\limits_0^{t_m^2} d\boldsymbol{t}_2^2 \Big[\Big(|k^2| - \frac{x}{z_2(1 - z_2)}\boldsymbol{t}_2^2\Big)\boldsymbol{t}_2^2\Big]^{\frac{D}{2}-2}\,. \tag{C.37}
$$

The last integral is obviously not divergent for $\epsilon \to 0$. After extracting a factor of $|k^2|^{D-3}$ and substituting $(\tilde{t}_2)^2 = t_2^2/|k^2|$, we can thus expand the remaining integral around $\epsilon = 0$ and keep only the leading term:

$$a_1^{3-D} \int_0^{t_m^2} \mathrm{d}t_2^2 \left[\left(|k^2| - \frac{x}{z_2(1-z_2)} t_2^2 \right) t_2^2 \right]^{\frac{D}{2}-2}$$

$$= |k^2|^{D-3} \left(\frac{z_1}{1-z_2} \right)^{D-3} \int_0^{\frac{z_2(1-z_2)}{x}} \mathrm{d}(\tilde{t}_2)^2$$

$$\times \left[\frac{z_1^2}{(1-z_2)^2} \left(1 - \frac{x}{z_2(1-z_2)} (\tilde{t}_2)^2 \right) (\tilde{t}_2)^2 \right]^{\frac{D}{2}-2}$$

$$= \frac{z_1 z_2}{x} |k^2|^{D-3}. \tag{C.38}$$

Contracting the Lorentz and colour structure of the numerator and projecting it onto colour representations yields

$$^{R\overline{R}}\mathcal{N}_{(\mathrm{k})} = C_{(\mathrm{k})}^{R\overline{R}} g^4 \mu^{4\epsilon} (D-3) x. \tag{C.39}$$

The colour factors $C_{(\mathrm{k})}^{R\overline{R}}$ are given in (3.31). The integrations over plus momenta are thus trivial and give

$$\int \mathrm{d}PS_{(\mathrm{k})} \, ^{R\overline{R}}\mathcal{N}_{(\mathrm{k})} = \frac{1}{4} \left(\frac{(4\pi)^\epsilon g^2 \mu^{2\epsilon}}{8\pi^2 \Gamma(1-\epsilon)} \right)^2 (1-2\epsilon) |k^2|^{1-2\epsilon} C_{(\mathrm{k})}^{R\overline{R}} (1-x) \tag{C.40}$$

after setting $D = 4 - 2\epsilon$. Be reminded that $\mathcal{D}_{(\mathrm{k})} = 1$. The last integral thus evaluates to

$$\int_0^{Q^2} \frac{\mathrm{d}|k^2|}{|k^2|} \left(\frac{\mu^2}{|k^2|} \right)^{2\epsilon} = -\frac{1}{2\epsilon} \mu^{4\epsilon} \left(\frac{1}{(Q^2)^{2\epsilon}} - 0^{-2\epsilon} \right) = -\frac{1}{2\epsilon} \left(\frac{\mu^2}{Q^2} \right)^{2\epsilon} \tag{C.41}$$

since $\epsilon < 0$, as required for IR divergences. The final expression therefore is

$$\left[\int_0^{Q^2} \mathrm{d}|k^2| \frac{1}{2} \int \mathrm{d}PS_{(\mathrm{k})} \frac{^{R\overline{R}}\mathcal{N}_{(\mathrm{k})}}{\mathcal{D}_{(\mathrm{k})} |k^2|^2} \right]_{-1} = -\frac{1}{\epsilon} \frac{1}{2} a_s^2 \frac{1}{8} C_{(\mathrm{k})}^{R\overline{R}} (1-x), \tag{C.42}$$

and thus

$$^{R\overline{R}}P_{gg,(\mathrm{k})}(x) = \frac{1}{8} C_{(\mathrm{k})}^{R\overline{R}} (1-x). \tag{C.43}$$

Notice the additional factor of $1/2$ on the left-hand side of eq. (C.42). This is the symmetry factor of graph (k), which can be derived e.g. by the general formula given in [133] or simply by counting the number of Wick contractions.

For longitudinally polarised gluons, the numerator becomes

$$
{}^{R\overline{R}}\mathcal{N}_{\Delta(\mathrm{k})} = \frac{C_{\Delta(\mathrm{k})}^{R\overline{R}}}{C_{(\mathrm{k})}^{R\overline{R}}} \, {}^{R\overline{R}}\mathcal{N}_{(\mathrm{k})} \tag{C.44}
$$

after applying the momentum conservation relations and contracting Lorentz and colour tensors . The $C_{\Delta(\mathrm{k})}^{R\overline{R}}$ factors are given in (3.41). The final result is

$$
{}^{R\overline{R}}\widetilde{P}_{\Delta g \Delta g,(\mathrm{k})}(x) = \frac{1}{8} C_{\Delta(\mathrm{k})}^{R\overline{R}} \, (1-x) \,. \tag{C.45}
$$

Graph (j). We choose p_2 and p_3 as independent momenta. The phase-space integral then simplifies to

$$
\begin{aligned}
\int \mathrm{d}PS_{(\mathrm{j})} &= \int \frac{\mathrm{d}^D p_1 \, \mathrm{d}^D p_2 \, \mathrm{d}^D p_3 \, \mathrm{d}^D k}{(2\pi)^{3D}} \delta(x - k^+) \, \delta\big(|k^2| + (p_1 - p_3)^2\big) \\
&\quad \times (2\pi)\delta^+(p_2^2) \, (2\pi)\delta^+(p_3^2) \\
&\quad \times (2\pi)^D \delta^{(D)}(p - k - p_2 - p_3) \, (2\pi)^D \delta^{(D)}(p_1 - k - p_3) \\
&= \frac{1}{4(2\pi)^{2D-2}} \int \frac{\mathrm{d}z_2}{z_2} \frac{\mathrm{d}z_3}{z_3} \, \mathrm{d}^{D-2}\boldsymbol{t}_2 \, \mathrm{d}^{D-2}\boldsymbol{t}_3 \\
&\quad \times \delta\Big(|k^2| - a_2 \, \boldsymbol{t}_2^2 - a_3 \, \boldsymbol{t}_3^2 - 2 \, \boldsymbol{t}_2 \cdot \boldsymbol{t}_3\Big) \,.
\end{aligned} \tag{C.46}
$$

In the same manner as in the calculation of graph (k), we define

$$
a_2 = \frac{1-z_3}{z_2} \qquad a_3 = \frac{1-z_2}{z_3} \,, \tag{C.47}
$$

and substitute

$$
\boldsymbol{t}_3' = \boldsymbol{t}_3 + \frac{1}{a_3} \, \boldsymbol{t}_2 \,. \tag{C.48}
$$

After momentum conservation, the denominator becomes

$$
\mathcal{D}_{(\mathrm{j})} = p_1^2 + i\varepsilon = -\frac{1}{z_2}\boldsymbol{t}_2^2 + i\varepsilon \,, \tag{C.49}
$$

whilst the numerator $\mathcal{N}_{(\mathrm{j})}$ depends on a linear combination of $\boldsymbol{t}_2^2$ and $\boldsymbol{t}_2 \cdot \boldsymbol{t}_3$. We find that

$$
\int \mathrm{d}^{D-2}\boldsymbol{t}_2 \mathrm{d}^{D-2}\boldsymbol{t}_3' \, \frac{\boldsymbol{t}_2 \cdot \boldsymbol{t}_3'}{\boldsymbol{t}_2^2 + i\varepsilon} \frac{1}{a_3} \delta\big(\boldsymbol{t}_3^2 + \tfrac{1}{a_3}\tfrac{x}{z_2(1-z_2)}\boldsymbol{t}_2^2 - \tfrac{1}{a_3}|k^2|\big) = 0 \tag{C.50}
$$

after performing one of the angular integrations. This is because

$$
\int\limits_0^{2\pi} \mathrm{d}\varphi_2 \, \boldsymbol{t}_2 \cdot \boldsymbol{t}_3' \propto \int\limits_0^{2\pi} \mathrm{d}\varphi_2 \, \cos(\varphi_2 - \varphi_3) = 0 \,, \tag{C.51}
$$

where φ_2 (φ_3) is the angular variable of $\boldsymbol{t}_2$ ($\boldsymbol{t}'_3$). We could set $\epsilon = 0$ due to the absence of singularities.

For the second transverse integral, we reuse the result from graph (k), eq. (C.38):

$$
\int \mathrm{d}^{D-2}\boldsymbol{t}_2 \mathrm{d}^{D-2}\boldsymbol{t}'_3 \, \frac{\boldsymbol{t}_2^2}{\boldsymbol{t}_2^2 + i\varepsilon} \frac{1}{a_3} \delta\big(\boldsymbol{t}_3^2 + \tfrac{1}{a_3} \tfrac{x}{z_2(1-z_2)} \boldsymbol{t}_2^2 - \tfrac{1}{a_3}|k^2|\big)
$$
$$
= (\Omega_{D-2})^2 \frac{z_2 z_3}{x} |k^2|^{D-3} . \tag{C.52}
$$

After contracting Lorentz and colour tensors in the numerator, we can perform the z_2 integration:

$$
2 \int \mathrm{d}PS^{(2)} \frac{{}^{R\overline{R}}\mathcal{N}_{(\mathrm{j})}}{\mathcal{D}_{(\mathrm{j})}} = -\frac{1}{2} \left(\frac{(4\pi)^\epsilon g^2 \mu^{2\epsilon}}{8\pi^2 \Gamma(1-\epsilon)} \right)^2 (1 - 2\epsilon) \, |k^2|^{1-2\epsilon}
$$
$$
\times C_{(\mathrm{j})}^{R\overline{R}} \int\limits_0^{1-x} \mathrm{d}z_2 \, \frac{(2x + z_2 - 1)(z_2 + 1)}{(z_2 - 1)^2}
$$
$$
= -\frac{1}{2} \left(\frac{(4\pi)^\epsilon g^2 \mu^{2\epsilon}}{8\pi^2 \Gamma(1-\epsilon)} \right)^2 (1 - 2\epsilon)
$$
$$
\times C_{(\mathrm{j})}^{R\overline{R}} \left(2(1+x) \ln(x) + 5(1-x) \right) |k^2|^{1-2\epsilon} . \tag{C.53}
$$

The additional global factor of 2 takes into account the complex conjugate of graph (j), while its symmetry factor is 1. The factors $C_{(\mathrm{j})}^{R\overline{R}}$ can be found in (3.31). The integral over $|k^2|$ is solved as the one for graph (k) in eq. (C.41), which yields

$$
{}^{R\overline{R}}P_{gg,(\mathrm{j})}(x) = -\frac{1}{2} C_{(\mathrm{j})}^{RR'} \left(2(1+x) \ln(x) + 5(1-x) \right) \tag{C.54}
$$

as the final result.

For the longitudinal kernels, after applying the momentum conservation relations and contracting Lorentz and colour tensors we find

$$
{}^{R\overline{R}}\mathcal{N}_{\Delta(\mathrm{j})}^{RR'} = \frac{C_{\Delta(\mathrm{j})}^{R\overline{R}}}{C_{(\mathrm{j})}^{R\overline{R}}} \, {}^{R\overline{R}}\mathcal{N}_{\Delta(\mathrm{j})} \tag{C.55}
$$

and thus

$$
{}^{R\overline{R}}\widetilde{P}_{\Delta g \Delta g,(\mathrm{j})}(x) = -\frac{1}{2} C_{\Delta(\mathrm{j})}^{RR'} \left(2(1+x) \ln(x) + 5(1-x) \right) . \tag{C.56}
$$

The colour factors $C_{\Delta(\mathrm{j})}^{R\overline{R}}$ can be found in (3.41).

Graph (l) - left cut. With k and p_2 as the independent momenta, the phase space becomes

$$
\int \mathrm{d}PS_{(\mathrm{l}),\mathrm{ri}} = \int \frac{\mathrm{d}^D p_1 \, \mathrm{d}^D p_2 \, \mathrm{d}^D p_3 \, \mathrm{d}^D k}{(2\pi)^{3D}} \delta(x - k^+)
$$
$$
\times \delta\big(|k^2| + (p - p_1)^2\big) (2\pi)\delta^+(p_2^2) (2\pi)\delta^+(p_3^2)
$$
$$
\times (2\pi)^D \delta^{(D)}(p_1 - p + k) (2\pi)^D \delta^{(D)}(p_3 - p_1 + p_2)
$$

$$= \frac{1}{(2\pi)^{2D-2}} \int \frac{dz_2}{2z_2} d^{D-2}\boldsymbol{t}_2 dk^- d^{D-2}\boldsymbol{t}_k$$
$$\times \delta^+\left((p-p_2-k)^2\right) \delta\left(|k^2| + (p-p_2-p_3)^2\right), \tag{C.57}$$

and

$$k = p - p_1 \tag{C.58}$$
$$p_3 = p_1 - p_2. \tag{C.59}$$

Substituting

$$\boldsymbol{t}_2' = \boldsymbol{t}_2 - \frac{z_2}{z_1}\boldsymbol{t}_k, \tag{C.60}$$

the argument of the last δ-distribution of (C.57) simplifies:

$$\int \mathrm{d}PS_{(\mathrm{l}),\mathrm{ri}} = \frac{1}{(2\pi)^{2D-2}} \int \frac{\mathrm{d}z_2}{2z_2} \mathrm{d}^{D-2}\boldsymbol{t}_2' \mathrm{d}k^- \mathrm{d}^{D-2}\boldsymbol{t}_k$$
$$\times \delta^+\left(f\left(|k^2|, k^-, \boldsymbol{t}_2', \boldsymbol{t}_k\right)\right) \delta\left(g\left(|k^2|, (\boldsymbol{t}_2')^2\right), \boldsymbol{t}_k^2\right), \tag{C.61}$$

where

$$f\left(|k^2|, k^-, \boldsymbol{t}_2', \boldsymbol{t}_k\right) = |k^2| - \frac{1-x}{z_2}\left(\boldsymbol{t}_2' + \tfrac{1-x}{z_2}\boldsymbol{t}_k\right)^2$$
$$- 2(1+z_2)\, p^+ k^- - 2\left(\boldsymbol{t}_2' - \tfrac{1-x}{z_2}\boldsymbol{t}_k\right) \cdot \boldsymbol{t}_k \tag{C.62}$$
$$g\left(|k^2|, \boldsymbol{t}_k^2, (\boldsymbol{t}_2')^2\right) = |k^2| - \frac{x^2-x}{z_2(z_2+1-x)}(\boldsymbol{t}_2')^2 - \frac{1}{1-x}\boldsymbol{t}_k^2. \tag{C.63}$$

The δ-distribution containing $f(\dots)$ can be used to fix k^-. With this new set of variables, we find that p_1^2 inside the propagator contains no scalar products between $\boldsymbol{t}_k$ and $\boldsymbol{t}_2'$. For the numerator, we find

$$^{R\overline{R}}\mathcal{N}_{(\mathrm{l})} \propto \boldsymbol{t}_k \cdot \boldsymbol{t}_2'. \tag{C.64}$$

This enables us to use (C.50) for the angular integrations, and therefore this graph does not contribute:

$$^{R\overline{R}}\widetilde{P}_{gg,(\mathrm{l}),\mathrm{le}}(x) = 0. \tag{C.65}$$

Graph (l) - right cut. The phase-space integral simplifies to

$$\int \mathrm{d}PS_{(\mathrm{l}),\mathrm{ri}} = \int \frac{\mathrm{d}^D p_1\, \mathrm{d}^D p_2\, \mathrm{d}^D p_3\, \mathrm{d}^D k}{(2\pi)^{3D}} \delta(x-k^+)\, \delta\left(|k^2| + (p-p_1)^2\right) (2\pi)\delta^+(p_1^2)$$
$$\times (2\pi)^D \delta^{(D)}(k-p+p_1)\,(2\pi)^D \delta^{(D)}(p_3-p_1+p_2)$$
$$= \frac{1-x}{(2\pi)^{D-1}} \int \mathrm{d}^{D-2}\boldsymbol{t}_1\, \mathrm{d}^D p_2\, \delta\left(\boldsymbol{t}_1^2 - (1-x)|k^2|\right), \tag{C.66}$$

with

$$k = p - p_1 \tag{C.67}$$

$$p_3 = p_1 - p_2 \,. \tag{C.68}$$

This graph is a loop correction to the three-gluon vertex inside the LO graph, hence this is the first time we encounter more than one propagator. We choose to eliminate one of the two propagators by using Cauchy's theorem for the integration of the minus component. This sets p_2 on-shell,

$$p_2^- = \frac{\boldsymbol{t}_2^2}{2 z_2 p^+} \,. \tag{C.69}$$

Looking at (C.66), this leaves the non-trivial integrations over z_2, $\boldsymbol{t_2}$ and the angular components of $\boldsymbol{t}_1$. We could use (C.50) again for the angular integrations if the denominator, i.e. p_3^2, would not contain any scalar products of the two transverse integration momenta. This is not the case for our currrent choice $\boldsymbol{t}_1$ and $\boldsymbol{t}_2$, motivating a shift of the latter (shifting $\boldsymbol{t}_1$ would make the remaining δ-distribution in (C.66) non-trivial again). Introducing

$$\boldsymbol{t}_2' = \boldsymbol{t}_2 - \frac{z_2}{z_1}\, \boldsymbol{t}_1 \tag{C.70}$$

solves this problem. With this new set of variables the numerator has the form

$${}^{R\overline{R}}\mathcal{N}_{(\mathrm{n})} \propto \boldsymbol{t}_1 \cdot \boldsymbol{t}_2' \,. \tag{C.71}$$

Making use of (C.50), the whole expression vanishes after angular integrations and we find

$${}^{R\overline{R}}\widetilde{P}_{gg,(\mathrm{l}),\mathrm{ri}}(x) = 0 \,. \tag{C.72}$$

Graph (m). Just as the right cut of graph (l), graph (m) belongs to the subgroup of vertex corrections to the LO graph. Thus, its phase-space integral is identical to (C.66), only with a different momentum conservation relation for p_3,

$$p_3 = p - p_1 - p_2 \,. \tag{C.73}$$

Again, we can make use of Cauchy's theorem to eliminate the p_2 propagator and put it on-shell. p_3 can be made a function of only squared transverse momenta with the transformation

$$\boldsymbol{t}_2 = \boldsymbol{t}_2' - \frac{z_2}{1 - z_1}\, \boldsymbol{t}_1 \,. \tag{C.74}$$

In this new set of variables, the numerator fulfils

$${}^{R\overline{R}}\mathcal{N}_{(\mathrm{m})} \propto \boldsymbol{t}_1 \cdot \boldsymbol{t}_2' \,, \tag{C.75}$$

and so after angular integrations (cf. (C.50)) the complete Feynman integral vanishes:

$${}^{R\overline{R}}\widetilde{P}_{gg,(\mathrm{n})}(x) = 0 \,. \tag{C.76}$$

Graph (n). Also being a vertex correction to the LO graph, the computation of graph (n) is identical to the one of graph (l) and (m). The momentum conservation

$$p_3 = p - p_2 \tag{C.77}$$

however makes this graph the easiest to compute, as the p_3 propagator is proportional to $\boldsymbol{t}_2^2$ without any change of integration variables. Also, the numerator behaves like

$$^{R\overline{R}}\mathcal{N}_{(n)} \propto \boldsymbol{t}_1 \cdot \boldsymbol{t}_2 \tag{C.78}$$

right from the start. After angular integrations (cf. (C.50)), we thus immediately find that

$$^{R\overline{R}}\widetilde{P}_{gg,(m)}(x) = 0 \,. \tag{C.79}$$

Appendix D

Finite shift of longitudinal DGLAP kernels

In this appendix, we will calculate the effect that a finite change of the renormalisation scheme has on the longitudinal DGLAP kernels. For a detailed discussion of the prerequisites, see section 3.1.5.

Operators. To preserve invariance under charge conjugation, we apply the same renormalisation factor to both the quark- and antiquark-operator:

$$^{R}\mathcal{O}_{\Delta q_i} = {}^{R}\widetilde{Z} \otimes {}^{R}\mathcal{O}_{\Delta q_i, \overline{\mathrm{MS}}}\,, \tag{D.1}$$

$$^{R}\mathcal{O}_{\Delta \bar{q}_i} = {}^{R}\widetilde{Z} \otimes {}^{R}\mathcal{O}_{\Delta \bar{q}_i, \overline{\mathrm{MS}}}\,, \tag{D.2}$$

where

$$^{R}\widetilde{Z}(a_s, x) = \delta(1-x) + \sum_{n=1}^{\infty} a_s^n \, {}^{R}\widetilde{Z}^{(n)}(x)\,. \tag{D.3}$$

We use a subscript for operators that were renormalised via $\overline{\mathrm{MS}}$. Operators without this subscript are viewed as final in the sense that they have received the scheme change. We adopt this convention for other quantities further down below. As already discussed in section 3.1.5, the corresponding renormalisation factor $\widetilde{Z}$ is finite and therefore does not include any poles in ϵ.

The quark flavour combinations for DPDs in the evolution basis were defined in section 2.3.2. The same linear combinations on the operator level trivially inherit this shift:

$$^{R}\mathcal{O}_{\Delta q_{ij}^{\pm}} = {}^{R}\widetilde{Z} \otimes {}^{R}\mathcal{O}_{\Delta q_{ij}^{\pm}, \overline{\mathrm{MS}}}\,, \tag{D.4}$$

$$^{R}\mathcal{O}_{\Delta \Sigma^{\pm}} = {}^{R}\widetilde{Z} \otimes {}^{R}\mathcal{O}_{\Delta \Sigma^{\pm}, \overline{\mathrm{MS}}}\,. \tag{D.5}$$

Since the gluon operators stays untouched, the flavour singlet sector is renormalised as follows:

$$\begin{pmatrix} {}^{R_1}\mathcal{O}_{\Delta \Sigma^+} \\ {}^{R_2}\mathcal{O}_{\Delta g} \end{pmatrix} = \begin{pmatrix} {}^{R_1}\widetilde{Z} & 0 \\ 0 & \delta(1-x) \end{pmatrix} \otimes \begin{pmatrix} {}^{R_1}\mathcal{O}_{\Delta \Sigma^+} \\ {}^{R_2}\mathcal{O}_{\Delta g} \end{pmatrix}_{\overline{\mathrm{MS}}}\,, \quad R_1 R_2 = 11, 8S\,, \tag{D.6}$$

and

$$\begin{pmatrix} {}^{8}\mathcal{O}_{\Delta\Sigma^{-}} \\ {}^{A}\mathcal{O}_{\Delta g} \end{pmatrix} = \begin{pmatrix} {}^{8}\widetilde{Z} & 0 \\ 0 & \delta(1-x) \end{pmatrix} \otimes \begin{pmatrix} {}^{8}\mathcal{O}_{\Delta\Sigma^{-}} \\ {}^{A}\mathcal{O}_{\Delta g} \end{pmatrix}_{\overline{\mathrm{MS}}} . \tag{D.7}$$

DGLAP kernels - flavour non-singlet. The flavour non-singlet DPDs are affected by the scheme change as follows:

$$ {}^{R_1 R_2}F_{(\Delta q_i^{\pm} - \Delta q_k^{\pm})a_2} = {}^{R_1}\widetilde{Z} \underset{x_1}{\otimes} {}^{R_1 R_2}F_{(\Delta q_i^{\pm} - \Delta q_k^{\pm})a_2}^{\overline{\mathrm{MS}}} , \tag{D.8}$$

and equivalently for the second parton. To see the effect on the DGLAP kernels, we take the μ_1 derivative,

$$ 2\, {}^{R_1 R_1}P_{\Delta}^{\pm} \underset{x_1}{\otimes} \left[{}^{R_1}\widetilde{Z} \underset{x_1'}{\otimes} {}^{R_1 R_2}F_{(\Delta q_i^{\pm} - \Delta q_k^{\pm})a_2}^{\overline{\mathrm{MS}}} \right] = \left(\frac{d}{d\ln\mu_1} {}^{R_1}\widetilde{Z} \right) \underset{x_1}{\otimes} {}^{R_1 R_2}F_{(\Delta q_i^{\pm} - \Delta q_k^{\pm})a_2}^{\overline{\mathrm{MS}}} $$

$$ + 2\, {}^{R_1}\widetilde{Z} \underset{x_1}{\otimes} \left[{}^{R_1 R_1}P_{\Delta,\overline{\mathrm{MS}}}^{\pm} \underset{x_1'}{\otimes} {}^{R_1 R_2}F_{(\Delta q_i^{\pm} - \Delta q_k^{\pm})a_2}^{\overline{\mathrm{MS}}} \right] . \tag{D.9}$$

When changing the order of convolutions above, we need to pay particular attention to the rapidity arguments due to the law of associativity for the Mellin convolution (2.49). Applying that to both sides of the equation, we obtain

$$ {}^{RR}P_{\Delta}^{\pm}(x',\zeta) \underset{x}{\otimes} {}^{R}\widetilde{Z}(x') = \frac{1}{2} \frac{d}{d\ln\mu} {}^{R}\widetilde{Z}(x) + {}^{R}\widetilde{Z}(x') \underset{x}{\otimes} {}^{RR}P_{\Delta,\overline{\mathrm{MS}}}^{\pm}(x', x'^2\zeta/x^2) . \tag{D.10}$$

Expanding all quantities to NLO yields

$$ {}^{RR}P_{\Delta}^{\pm(0)}(x,\zeta) = {}^{RR}P_{\Delta,\overline{\mathrm{MS}}}^{\pm(0)}(x,\zeta) \tag{D.11}$$

and

$$ {}^{RR}P_{\Delta}^{\pm(1)}(x,\zeta) = {}^{RR}P_{\Delta,\overline{\mathrm{MS}}}^{\pm(1)}(x,\zeta) + \frac{1}{2} \left({}^{R}\gamma_J^{(0)} \ln(x) - \beta_0 \right) {}^{R}\widetilde{Z}^{(1)}(x) . \tag{D.12}$$

To derive the second relation, we made use of

$$ {}^{RR}P_{\Delta,\overline{\mathrm{MS}}}^{\pm}(x', x'^2\zeta/x^2) - {}^{RR}P_{\Delta,\overline{\mathrm{MS}}}^{\pm}(x',\zeta) = \frac{1}{2}\delta(1-x') {}^{R}\gamma_J \ln(x) , \tag{D.13}$$

obtained from the ζ-dependence of DGLAP kernels, (2.70), and the definition of ${}^{RR}P_{\Delta}^{\pm(1)}$, (2.97). Inverting this definition reveals that

$$ {}^{RR}P_{\Delta q \Delta q}^{V} = \left({}^{RR}P_{\Delta}^{+} + {}^{RR}P_{\Delta}^{-} \right) \Big/ 2 \tag{D.14}$$

is shifted in the same way, whereas

$$ {}^{RR}P_{\Delta q \Delta \bar{q}}^{V} = \left({}^{RR}P_{\Delta}^{+} - {}^{RR}P_{\Delta}^{-} \right) \Big/ 2 \tag{D.15}$$

remains unchanged.

DGLAP kernels - flavour singlet. The derivation of the shift of the flavour singlet sector follows the same steps. The equivalent to (D.10) is

$$\begin{pmatrix} {}^{RR}P_{\Delta\Sigma^+\Delta\Sigma^+} & {}^{RR'}P_{\Delta\Sigma^+\Delta g} \\ {}^{R'R}P_{\Delta g\Delta\Sigma^+} & {}^{R'R'}P_{\Delta g\Delta g} \end{pmatrix} \underset{x}{\otimes} \begin{pmatrix} {}^{R}\widetilde{Z}(x') & 0 \\ 0 & \delta(1-x') \end{pmatrix} = \frac{1}{2}\begin{pmatrix} d{}^{R}\widetilde{Z}(x)/(d\ln\mu) & 0 \\ 0 & 0 \end{pmatrix}$$

$$+ \begin{pmatrix} {}^{R}\widetilde{Z}(x') & 0 \\ 0 & \delta(1-x') \end{pmatrix} \underset{x}{\otimes} \begin{pmatrix} {}^{RR}P_{\Delta\Sigma^+\Delta\Sigma^+,\overline{\text{MS}}} & {}^{RR'}P_{\Delta\Sigma^+\Delta g,\overline{\text{MS}}} \\ {}^{R'R}P_{\Delta g\Delta\Sigma^+,\overline{\text{MS}}} & {}^{R'R'}P_{\Delta g\Delta g,\overline{\text{MS}}} \end{pmatrix}, \ RR' = 11, 8S, \tag{D.16}$$

where the upper left component has the same form as (D.10). There is an identical version (derived from (D.7) instead of (D.6)) for $RR' = 8A$ when changing Σ^+ to Σ^-. This implies that the DGLAP kernels

$$ {}^{RR}P^{(1)}_{\Delta\Sigma^+\Delta\Sigma^+}, \qquad\qquad\qquad {}^{RR}P^{(1)}_{\Delta\Sigma^-\Delta\Sigma^-}, \ R = 1, 8, \tag{D.17}$$

obey the same transformations as in (D.11) and (D.12). We could include ${}^{11}P_{\Delta\Sigma^-\Delta\Sigma^-}$ because the corresponding evolution equation (2.90) is flavour non-singlet like. Hence, the complete shift of the (qq) flavour singlet kernels is governed by the valence kernels. It follows from (2.94) that the pure singlet kernels ${}^{RR}P^S_{\Delta q\Delta q}$ and ${}^{RR}P^S_{\Delta q\Delta\bar{q}}$ are changed neither at LO nor at NLO.

Note that (qg) and (gq) channels do not receive additional contributions from (D.13) as they do not depend on ζ. Calculating their shift thus simplifies and from (D.16) we obtain

$$ {}^{RR'}P^{(0)}_{\Delta\Sigma^\pm\Delta g} = {}^{RR'}P^{(0)}_{\Delta\Sigma^\pm\Delta g,\overline{\text{MS}}}, \tag{D.18}$$

$$ {}^{RR'}P^{(1)}_{\Delta\Sigma^\pm\Delta g} = {}^{RR'}P^{(1)}_{\Delta\Sigma^\pm\Delta g,\overline{\text{MS}}} + {}^{R}\widetilde{Z}^{(1)} \otimes {}^{RR'}P^{(0)}_{\Delta\Sigma^\pm\Delta g,\overline{\text{MS}}}, \tag{D.19}$$

$$ {}^{R'R}P^{(0)}_{\Delta g\Delta\Sigma^\pm} = {}^{R'R}P^{(0)}_{\Delta g\Delta\Sigma^\pm,\overline{\text{MS}}}, \tag{D.20}$$

$$ {}^{R'R}P^{(1)}_{\Delta g\Delta\Sigma^\pm} = {}^{R'R}P^{(1)}_{\Delta g\Delta\Sigma^\pm,\overline{\text{MS}}} - {}^{R'R}P^{(0)}_{\Delta g\Delta\Sigma^\pm,\overline{\text{MS}}} \otimes {}^{R}\widetilde{Z}^{(1)}, \tag{D.21}$$

where $RR' = 11, 8S$ for Σ^+ and $RR' = 8A$ for Σ^-. From the lower left component of (D.16) we can further on deduce that there is no shift of the (gg) channel to all orders,

$$ {}^{R\overline{R}}P_{\Delta g\Delta g} = {}^{R\overline{R}}P_{\Delta g\Delta g,\overline{\text{MS}}}. \tag{D.22}$$

Appendix E

RGE analysis of renormalisation factors

We want to express the TMD renormalisation factor $\widetilde{Z}_{ab}$ and its collinear counterpart $^{RR'}Z_{ab}$ in terms of their corresponding anomalous dimensions/DGLAP kernels using their respective renormalisation group equation. They were already given in eqs. (2.50) and (2.66) and repeated here for better readability:

$$\frac{\mathrm{d}}{\mathrm{d}\log\mu}{}^{RR'}Z_{ab}(x,\mu,\zeta) = 2\sum_{c,R''} {}^{R\overline{R}''}P_{ac}(x',\mu,\zeta) \underset{x}{\otimes} {}^{R''R'}Z_{cb}(x',\mu,x'^2\zeta/x^2)\,, \qquad (\text{E.1})$$

$$\frac{\mathrm{d}}{\mathrm{d}\log\mu}\widehat{Z}_a(\mu,\zeta) = \gamma_{F,a}(\mu,\zeta)\,\widehat{Z}_a(\mu,\zeta)\,. \qquad (\text{E.2})$$

The decompositions into cusp and non-cusp terms read

$$^{RR'}P_{ab}(x,\mu,\zeta) = {}^{RR'}\widehat{P}_{ab}(x,\mu)\,,$$
$$-\frac{1}{4}\delta_{R\overline{R}'}\,\delta_{ab}\,\delta(1-x)\,{}^R\gamma_J(\mu)\,\log\frac{\zeta}{\mu^2}\,, \qquad (\text{E.3})$$

$$\gamma_{F,a}(\mu,\zeta) = \gamma_a(\mu) - \frac{1}{2}\,\gamma_{K,a}(\mu)\,\log\frac{\zeta}{\mu^2}\,. \qquad (\text{E.4})$$

In (E.1) and (E.2), we use the RGE derivatives in $D = 4 - 2\epsilon$ dimensions,

$$\frac{\mathrm{d}}{\mathrm{d}\log\mu} = \frac{\partial}{\partial\log\mu} + \left(\frac{\mathrm{d}a_s}{\mathrm{d}\log\mu} - 2\epsilon a_s\right)\frac{\partial}{\partial a_s}$$
$$= \frac{\partial}{\partial\log\mu} - \left(\sum_{n=1}^{\infty}\beta_{n-1}\,a_s^{n+1} + 2\epsilon a_s\right)\frac{\partial}{\partial a_s}\,, \qquad (\text{E.5})$$

where we used the β-function (A.5) to obtain the second expression. The renormalisation factors depend on μ implicitly through $a_s(\mu)$ and explicitly through the dimensionless ratio ζ/μ^2, such that the partial derivatives are

$$\frac{\partial}{\partial\log\mu}{}^{RR'}Z_{ab}(x,\mu,\zeta) = {}^R\Lambda(a_s)\,{}^{RR'}Z(x,\mu,\zeta)\,, \qquad (\text{E.6})$$

$$\frac{\partial}{\partial \log \mu} \widetilde{Z}_a(\mu, \zeta) = \Lambda_a(a_s) \, \widetilde{Z}_a(\mu, \zeta) \,, \tag{E.7}$$

where $^R\Lambda(a_s)$ is defined in (2.40). $\Lambda_a(a_s)$ has the equivalent role in the renormalisation of K_a. Their perturbative expansions read

$$^R\Lambda(\mu, \epsilon) = \sum_{n=1}^{\infty} a_s^n(\mu) \, ^R\Lambda^{(n)}(\epsilon) \,. \tag{E.8}$$

Anomalous dimensions. As introduced in (2.43) and (2.51), we expand all anomalous dimensions in the convention

$$\gamma = \sum_{n=1}^{\infty} a_s^n \, \gamma^{(n-1)} \,, \tag{E.9}$$

and equivalently for the DGLAP kernels,

$$^{RR'}P_{ab}(x, \mu, \zeta) = \sum_{n=1}^{\infty} a_s^n \, ^{RR'}P^{(n-1)}(x, \zeta/\mu^2) \,. \tag{E.10}$$

Perturbative coefficients up to NNLO of the TMD anomalous dimension can be found in appendix D.2 of [94]. The notation there differs slightly,

$$\gamma_a^{(n)} = -\frac{1}{2^{n+1}} \gamma_V^{a(n+1)} \Big|_{[94]} \,, \qquad \gamma_{K,a}^{(n)} = \frac{4}{2^n} C_{F,A} \, \Gamma^{(n+1)} \Big|_{[94]} \,. \tag{E.11}$$

The LO and NLO coefficients are

$$\gamma_q^{(0)} = 3 C_F \,, \qquad\qquad\qquad \gamma_g^{(0)} = \beta_0 \,, \tag{E.12}$$

$$\gamma_q^{(1)} = C_F^2 \left(\frac{3}{4} - \pi^2 + 12 \, \zeta_3 \right) + C_F C_A \left(\frac{961}{108} + \frac{11}{12} \pi^2 - 13 \, \zeta_3 \right)$$

$$- C_F n_f \left(\frac{65}{54} + \frac{1}{6} \pi^2 \right) \,, \tag{E.13}$$

$$\gamma_g^{(1)} = C_A^2 \left(\frac{346}{27} - \frac{11}{36} \pi^2 - \zeta_3 \right) + C_A n_f \left(-\frac{64}{27} + \frac{1}{18} \pi^2 \right) - C_F n_f \,, \tag{E.14}$$

and

$$\gamma_{K,q}^{(0)} = 4 C_F \,, \qquad\qquad\qquad \gamma_{K,g}^{(0)} = 4 C_A \,, \tag{E.15}$$

$$\gamma_{K,q}^{(1)} = C_F C_A \left(\frac{134}{9} - \frac{2}{3} \pi^2 \right) - \frac{20}{9} C_F n_f \,, \qquad \gamma_{K,g}^{(1)} = \frac{C_A}{C_F} \gamma_{K,q}^{(1)} \,. \tag{E.16}$$

The LO coefficients of $^R\gamma_J$ can be obtained from $\gamma_{K,g}$ and Casimir scaling [58]:

$$^8\gamma_J^{(0)} = 2 C_A \,, \qquad\qquad ^{10}\gamma_J^{(0)} = 12 \,, \qquad\qquad ^{27}\gamma_J^{(0)} = 16 \,, \tag{E.17}$$

where we set $N = 3$ for $R = 10, 27$.

Collinear renormalisation factor. For the sake of better readability, we will omit parton flavour indices and irrelevant arguments in the following calculation. We note that (E.1) contains a partial derivative of $\log \mu$ in the explicit form of the RGE derivative (E.5). Since μ appears inside $^{RR'}Z$ via ζ/μ^2, we can reexpress this derivative:

$$\frac{1}{2}\frac{\partial}{\partial \log \mu}\,^{RR'}Z(\zeta/\mu^2) = -\frac{\partial}{\partial \log \zeta}\,^{RR'}Z(\zeta/\mu^2) = -\,^{R}\Lambda(a_s)\,^{RR'}Z(x,\mu,\zeta)\,. \qquad (E.18)$$

Thus, we also need to express $^R\Lambda$ in terms of $^R\gamma_J$. As given in (2.41), $^R\Lambda$ itself obeys the RGE

$$\frac{\mathrm{d}}{\mathrm{d}\log\mu}\,^R\Lambda(\mu) = -\,^R\gamma_J(\mu)\,. \qquad (E.19)$$

Note that $^R\gamma_J$ is finite to all orders. Thus, all pole terms on the left-hand side need to vanish. After inserting the RGE derivative (E.5), and the perturbative expansions (E.8) and (E.9) we obtain

$$^R\Lambda^{(N,1)} = \frac{1}{2N}\,^R\gamma_J^{(N-1)}\,, \qquad (E.20)$$

and

$$^R\Lambda^{(N,m)} = -\frac{1}{2N}\sum_{n=1}^{N-1}(N-n)\beta_{n-1}\,^R\Lambda^{(N-n,m-1)} \text{ for } 1 < m \leq N\,. \qquad (E.21)$$

Note that here and in the following a sum $\sum_{n=1}^{N-1}\ldots$ only contributes for $N > 1$. Higher poles vanish,

$$^R\Lambda^{(N,m)} = 0 \quad \forall\, m > N\,, \qquad (E.22)$$

which can be shown recursively in the perturbative order.

After carrying out the RGE derivative (E.5), partially using the perturbative expansions (3.71) and (E.10), and rearranging the left- and right-hand side, the RGE (E.1) becomes

$$^{RR'}P(a_s) = \frac{1}{2}\frac{\partial}{\partial \log \mu}\,^{RR'}Z(a_s) - \frac{1}{2}\left(\sum_{m=1}^{\infty}\beta_{m-1}\,a_s^{m+1} + 2\epsilon a_s\right)\left(\sum_{n=1}^{\infty}n\,a_s^{n-1}\,^{RR'}Z^{(n)}\right)$$

$$- \sum_{R''}{}^{R\overline{R}''}P(a_s) \otimes \left(\sum_{n=1}^{\infty}a_s^n\,^{R''R'}Z^{(n)}\right)\,. \qquad (E.23)$$

It can be shown by recursion in the perturbative order that the DGLAP kernel $^{RR'}P$ is independent from ϵ. Ordering the right-hand side of (E.23) in ϵ we can isolate the finite term and obtain

$$^{RR'}P_{ab}^{(N-1)} = -N\,^{RR'}Z_{ab}^{(N,1)} \qquad (E.24)$$

after restoring parton labels. With the same argument the remaining sum of poles in ϵ

needs to vanish term by term. Using (E.18) for the partial $\log \mu$ derivative, we find

$$
\begin{aligned}
{}^{RR'}Z_{ab}^{(N,m)} = {} & -\frac{1}{N} \Bigg\{ \sum_{n=1}^{N-1} \bigg[\frac{1}{2}(N-n)\beta_{n-1} {}^{RR'}Z_{ab}^{(N-n,m-1)} \\
& + \sum_{c,R''} {}^{R\overline{R}''}P_{ac}^{(n-1)} \otimes {}^{R''R'}Z_{cb}^{(N-n,m-1)} \\
& + \frac{1}{2}\sum_{i=1}^{m-2} {}^{R}\Lambda^{(n,i)}\, {}^{RR'}Z_{ab}^{(N-n,m-i-1)} \bigg] \\
& + \frac{1}{2}\delta_{R\overline{R}'}\delta_{ab}\delta(1-x)\, {}^{RR'}\Lambda_{ab}^{(N,m-1)} \Bigg\} \\
& \forall\, N > 1 \text{ and for } 1 < m \le N\,.
\end{aligned}
\tag{E.25}
$$

From this formula, we can deduce that

$$
{}^{RR'}Z_{ab}^{(N,m)} = 0 \tag{E.26}
$$

for $m > 2N$ if $R \ne 1$. In the color singlet, where ${}^{1}\Lambda = 0$, the relation above already holds for $m > N$.

Evaluating these formulae at LO and NLO, now with explicit function arguments, yields

$$
{}^{RR'}Z_{ab}^{(1,1)}(x,\zeta/\mu^2) = -{}^{RR'}P_{ab}^{(0)}(x,\zeta/\mu^2)\,, \tag{E.27}
$$

$$
{}^{RR'}Z_{ab}^{(1,2)}(x) = -\frac{1}{4}\delta_{R\overline{R}'}\delta_{ab}\delta(1-x){}^{R}\gamma_{J}^{(0)} \tag{E.28}
$$

and

$$
{}^{RR'}Z_{ab}^{(2,1)}(x,\zeta/\mu^2) = -\frac{1}{2}\,{}^{RR'}P_{ab}^{(1)}(x,\zeta/\mu^2)\,, \tag{E.29}
$$

$$
\begin{aligned}
{}^{RR'}Z_{ab}^{(2,2)}(x,\zeta/\mu^2) = {} & \frac{1}{2}\Bigg\{ \sum_{c,R''} {}^{R\overline{R}''}P_{ac}^{(0)}(x',\zeta/\mu^2) \underset{x}{\otimes} {}^{R''R'}P_{cb}^{(0)}\big(x',x'^{2}\zeta/(x^2\mu)^2\big) \\
& + \frac{1}{2}\beta_0\,{}^{RR'}P_{ab}^{(0)}(x,\zeta/\mu^2) - \frac{1}{8}\delta_{R\overline{R}'}\,\delta_{ab}\delta(1-x){}^{R}\gamma_{J}^{(1)} \Bigg\} \\
= {} & \frac{1}{2}\sum_{c,R''} {}^{R\overline{R}''}\widehat{P}_{ac}^{(0)}(x') \underset{x}{\otimes} {}^{R''R'}\widehat{P}_{cb}^{(0)}(x') \\
& + \frac{1}{4}\bigg[\beta_0 - {}^{R}\gamma_{J}^{(0)}\Big(\log\frac{\zeta}{\mu^2} - \log x\Big)\bigg]\,{}^{RR'}\widehat{P}_{ab}^{(0)}(x) \\
& + \frac{1}{16}\delta_{R\overline{R}'}\,\delta_{ab}\,\delta(1-x) \\
& \quad\times \bigg[\frac{1}{2}\Big({}^{R}\gamma_{J}^{(0)}\log\frac{\zeta}{\mu^2}\Big)^{2} - \beta_0\,{}^{R}\gamma_{J}^{(0)}\log\frac{\zeta}{\mu^2} - {}^{R}\gamma_{J}^{(1)}\bigg]\,,
\end{aligned}
\tag{E.30}
$$

$$ {}^{RR'}Z_{ab}^{(2,3)}(x,\zeta/\mu^2) = \frac{1}{4}{}^{R}\gamma_J^{(0)}\left\{{}^{RR'}P_{ab}^{(0)}(x,\zeta/\mu^2) + \frac{3}{8}\delta_{R\overline{R}'}\,\delta_{ab}\,\delta(1-x)\,\beta_0\right\}, \qquad \text{(E.31)} $$

$$ {}^{RR'}Z_{ab}^{(2,4)}(x) = \frac{1}{32}\delta_{R\overline{R}'}\,\delta_{ab}\,\delta(1-x)\left({}^{R}\gamma_J^{(0)}\right)^2. \qquad \text{(E.32)} $$

We have used the decomposition (E.3) for the second expression in (E.30).

TMD renormalisation factor. The RGE analysis for $\widetilde{Z}_{ab}$ can be performed following the same steps as the previous one for ${}^{RR'}Z_{ab}$. The calculation even simplifies due to the ordinary multiplication in (E.2) instead of the convolution in (E.1). For an arbitrary perturbative order, we find

$$ \widehat{Z}_a^{(N,1)} = -\frac{1}{2N}\gamma_{F,a}^{(N-1)} \quad \forall N \geq 1\,, \qquad \text{(E.33)} $$

$$ \widehat{Z}_a^{(N,m)} = -\frac{1}{N}\left\{\sum_{n=1}^{N-1}\left[\frac{1}{2}(N-n)\,\beta_{n-1}\,\widehat{Z}_a^{(N-n,m-1)} + \frac{1}{2}\gamma_{F,a}^{(n-1)}\,\widehat{Z}_a^{(N-n,m-1)}\right.\right. $$
$$ \left.\left. + \frac{1}{2}\sum_{i=1}^{m-2}\Lambda_a^{(n,i)}\,\widehat{Z}_a^{(N-n,m-i-1)}\right] + \frac{1}{2}\Lambda_a^{(N,m-1)}\right\} $$
$$ \forall N > 1 \text{ and for } 1 < m \leq N\,, $$

$$ \widehat{Z}^{(N,m)} = 0 \ \forall \ m > 2N\,, \qquad \text{(E.34)} $$

where

$$ \Lambda_a^{(N,1)} = \frac{1}{2N}\,\gamma_{K,a}^{(N-1)} \qquad \text{(E.35)} $$

$$ \Lambda_a^{(N,m)} = \frac{1}{2N}\sum_{n=1}^{N-1}(N-n)\,\beta_{n-1}\,\Lambda_a^{(N-n,m-1)} \text{ for } 1 < m \leq N\,, $$

$$ \Lambda_a^{(N,m)} = 0 \ \forall m > N\,. \qquad \text{(E.36)} $$

The LO and NLO coefficients thus are

$$ \widehat{Z}_a^{(1,1)}(\zeta/\mu^2) = -\frac{1}{2}\gamma_{F,a}^{(0)}(\zeta/\mu^2) \qquad \text{(E.37)} $$

$$ \widehat{Z}_a^{(1,2)} = -\frac{1}{4}\gamma_{K,a}^{(0)} \qquad \text{(E.38)} $$

$$ \widehat{Z}_a^{(2,1)}(\zeta/\mu^2) = -\frac{1}{4}\gamma_{F,a}^{(1)}(\zeta/\mu^2) \qquad \text{(E.39)} $$

$$ \widehat{Z}_a^{(2,2)}(\zeta/\mu^2) = \frac{1}{8}\left\{\left(\gamma_{F,a}^{(0)}(\zeta/\mu^2)\right)^2 + \beta_0\,\gamma_{F,a}^{(0)}(\zeta/\mu^2) - \frac{1}{2}\gamma_{K,a}^{(1)}\right\} $$
$$ = \frac{1}{8}\left\{\frac{1}{4}\left(\gamma_{K,a}^{(0)}\right)^2\log^2\frac{\zeta}{\mu^2} - \left(\frac{1}{2}\beta_0 + \gamma_a^{(0)}\right)\gamma_{K,a}^{(0)}\log\frac{\zeta}{\mu^2}\right. $$
$$ \left. + \left(\gamma_a^{(0)}\right)^2 + \beta_0\,\gamma_a^{(0)} - \frac{1}{2}\gamma_{K,a}^{(1)}\right\} \qquad \text{(E.40)} $$

$$\widehat{Z}_a^{(2,3)}(\zeta/\mu^2) = \frac{1}{8}\gamma_{K,a}^{(0)}\left\{\gamma_{F,a}^{(0)}(\zeta/\mu^2)\right. \tag{E.41}$$

$$\widehat{Z}_a^{(2,4)} = \frac{1}{32}\left(\gamma_{K,a}^{(0)}\right)^2. \tag{E.42}$$

Appendix F

Convolution of two distributions

F.1 General overview

Both convolution products in the second line of eq. (3.85) contain plus- and δ-distributions. Thus, let us have closer look at the behaviour of these distributions when convoluted with each other. In general, a distribution D defines a functional F_D which maps a smooth test function $t(x)$, $x \in [0, 1]$, to a real number. Such a functional can be expressed in terms of an integral,

$$F_D[t] = \int \mathrm{d}x' D(x') \, t(x') \,. \tag{F.1}$$

Then F_D is uniquely defined by the prescription of how to evaluate this integral for a given distribution D and an arbitrary test function $t(x)$. The two distributions that occur in our context are the δ-distribution (at $x = 1$), which fulfils

$$\int \mathrm{d}x' \delta(1 - x') \, t(x)' = t(1) \,, \tag{F.2}$$

and the plus-distribution defined in (A.8). This distribution itself depends on a function $f(x)$, $x \in [0, 1]$, that diverges at $x = 1$.

In our application, the distributions are accompanied by arbitrary smooth functions

which we call $d(x)$ or $p(x)$. We find

$$d(x')\,\delta(1-x') \underset{x}{\otimes} t(x') = \int_x^1 \frac{\mathrm{d}x'}{x'}\,d(x')\,\delta(1-x')\,t\!\left(\tfrac{x}{x'}\right) = d(1)\,t(x)\,, \qquad \text{(F.3)}$$

$$p(x')\big[f(x')\big]_+ \underset{x}{\otimes} t(x') = \int_x^1 \frac{\mathrm{d}x'}{x'}\,p(x')\big[f(x')\big]_+\,t\!\left(\tfrac{x}{x'}\right)$$

$$= \int_x^1 \mathrm{d}x' \left(\frac{1}{x'}p(x')\,t\!\left(\tfrac{x}{x'}\right) - p(1)\,t(x)\right) f(x')$$

$$- p(1)\,t(x) \int_0^x \mathrm{d}x'\,f(x') \qquad \text{(F.4)}$$

for convoluted plus- and δ-distribution.

We are now interested in the case where two distributions D_1 and D_2 are convoluted to form a new distribution

$$D_{12}(x) = D_1(x') \underset{x}{\otimes} D_2(x') = \int_x^1 \frac{\mathrm{d}x'}{x'}\,D_1(x')\,D_2\!\left(\tfrac{x}{x'}\right). \qquad \text{(F.5)}$$

To derive a prescription for D_{12}, we convolute again with a test function,

$$D_{12}(x') \underset{x}{\otimes} t(x') = \int_x^1 \frac{\mathrm{d}x'}{x'} \int_{x'}^1 \frac{\mathrm{d}x''}{x''}\,D_1(x'')\,D_2\!\left(\tfrac{x}{x''}\right) t\!\left(\tfrac{x}{x'}\right)$$

$$= \int_x^1 \frac{\mathrm{d}x'}{x'}\,D_1(x') \int_{\frac{x}{x'}}^1 \frac{\mathrm{d}x''}{x''}\,D_2(x'')\,t\!\left(\tfrac{x}{x'x''}\right), \qquad \text{(F.6)}$$

where we substituted x/x'' in the second step and renamed the integration variables afterwards. We can thus describe the action of D_{12} by the action of its constituents D_1 and D_2, as the integral of D_2 and $t(x)$ produces again a test function to be convoluted with D_1. If not both of D_1 and D_2 are plus-distributions, this formula can be evaluated in a straightforward way:

$$d_1(x')\,\delta(1-x') \underset{x}{\otimes} d_2(x')\,\delta(1-x') = d_1(1)\,d_2(1)\,\delta(1-x)\,,$$

$$d(x')\,\delta(1-x') \underset{x}{\otimes} p(x')[f(x')]_+ = p(x')\,[f(x')]_+ \underset{x}{\otimes} d(x')\,\delta(1-x')$$

$$= d(1)\,p(x)\big[f(x)\big]_+\,. \qquad \text{(F.7)}$$

F.2   Convolution of two plus-distributions

For the convolution of two plus distributions, we find

$$
p_1(x')[f(x')]_+ \underset{x}{\otimes} p_2(x')[f(x')]_+
$$

$$
= p_1(1)p_2(1)[f(x')]_+ \underset{x}{\otimes} [f(x')]_+ + p_1(1)[f(x')]_+ \underset{x}{\otimes} \big(p_2(x') - p(1)\big)f(x')
$$

$$
+ \big(p_1(x') - p_1(1)\big)f(x') \underset{x}{\otimes} p_2(1)[f(x')]_+
$$

$$
+ \big(p_1(x') - p_1(1)\big)f(x') \underset{x}{\otimes} \big(p_2(x') - p_2(1)\big)f(x') \,, \tag{F.8}
$$

where we used

$$
p_i(x)[f(x)]_+ = p_i(1)[f(x)]_+ + \big(p_i(x) - p_i(1)\big)f(x) \,. \tag{F.9}
$$

Only the evaluation of the first term is non-trivial. In the context of section 3.2, we exclusively encounter the case

$$
f(x) = \frac{1}{1-x} \,. \tag{F.10}
$$

To make our lives simpler, we restrict ourselves to this choice. In the following, we will introduce in two methods two different representations of the plus-distribution to calculate its convolution with itself. The first calculation will be explained quite extensively, while the second one will be only sketched. In the end, we will present a short but strong cross check of the final result by calculating its Mellin transform.

First representation.   Without a test function, the plus distribution can be defined via

$$
[f(x)]_+ = \lim_{\epsilon \to 0} \left\{ \Theta(1 - \epsilon - x)\, f(x) - \delta(1 - x) \int\limits_0^{1-\epsilon} \mathrm{d}x'\, f(x') \right\}, \tag{F.11}
$$

where $\Theta(x)$ is the Heaviside distribution. We use a parameter $\epsilon > 0$ to regulate the divergences both in the subtraction term and the integral with the test function. The

convolution of two plus distributions thus becomes

$$[f(x')]_+ \underset{x}{\otimes} \Big([f(x'')]_+ \underset{x'}{\otimes} t(x'') \Big)$$

$$= \lim_{\epsilon_1 \to 0} \int_x^1 \frac{\mathrm{d}x'}{x'} [f(x')]_+ \left\{ \int_{\frac{x}{x'}}^{1-\epsilon_1} \frac{\mathrm{d}x''}{x''} f(x'') t\big(\tfrac{x}{x'x''}\big) - t\big(\tfrac{x}{x'}\big) \int_0^{1-\epsilon_1} \mathrm{d}x'' f(x'') \right\}$$

$$= \lim_{\epsilon_{1,2} \to 0} \left\{ \int_x^{1-\epsilon_2} \frac{\mathrm{d}x'}{x'} f(x') \int_{\frac{x}{x'}}^{1-\epsilon_1} \frac{\mathrm{d}x''}{x''} f(x'') \, t\big(\tfrac{x}{x'x''}\big) \right.$$

$$- \int_x^{1-\epsilon_2} \frac{\mathrm{d}x'}{x'} f(x') \, t\big(\tfrac{x}{x'}\big) \int_0^{1-\epsilon_1} \mathrm{d}x'' f(x'') - \int_0^{1-\epsilon_2} \mathrm{d}x' f(x') \int_x^{1-\epsilon_1} \frac{\mathrm{d}x''}{x''} f(x'') t\big(\tfrac{x}{x''}\big)$$

$$\left. + t(x) \int_0^{1-\epsilon_2} \mathrm{d}x' f(x') \int_0^{1-\epsilon_1} \mathrm{d}x'' f(x'') \right\}. \tag{F.12}$$

For reasons of convenience, we set $\epsilon_1 = \epsilon_2 = \epsilon$ for the rest of the calculation. When now substituting $x' = \tilde{x}/x''$, one needs to pay particular attention to the ϵ dependence of integration limits. We find

$$[f(x')]_+ \underset{x}{\otimes} \Big([f(x'')]_+ \underset{x'}{\otimes} t(x'') \Big)$$

$$= \lim_{\epsilon \to 0} \left\{ \int_x^{(1-\epsilon)^2} \frac{d\tilde{x}}{\tilde{x}} \int_{\frac{\tilde{x}}{1-\epsilon}}^{1-\epsilon} \frac{\mathrm{d}x''}{x''} f(x'') f\big(\tfrac{\tilde{x}}{x''}\big) t\big(\tfrac{x}{\tilde{x}}\big) \right.$$

$$\left. - 2 \int_x^{1-\epsilon} \frac{\mathrm{d}x'}{x'} f(x') \, t\big(\tfrac{x}{x'}\big) \int_0^{1-\epsilon} \mathrm{d}x'' f(x'') + t(x) \bigg(\int_0^{1-\epsilon} \mathrm{d}x' f(x') \bigg)^2 \right\}$$

$$= \lim_{\epsilon \to 0} \left\{ \int_x^{1-\epsilon} \frac{\mathrm{d}x'}{x'} \bigg(\int_{\frac{x'}{1-\epsilon}}^{1-\epsilon} \frac{\mathrm{d}x''}{x''} f(x'') f\big(\tfrac{x'}{x''}\big) - 2 f(x') \int_0^{1-\epsilon} \mathrm{d}x'' f(x'') \bigg) t\big(\tfrac{x}{x'}\big) \right.$$

$$\left. + t\big(\tfrac{x}{x_\epsilon}\big) \int_{1-\epsilon}^{(1-\epsilon)^2} \frac{\mathrm{d}x'}{x'} \int_{\frac{x'}{1-\epsilon}}^{1-\epsilon} \frac{\mathrm{d}x''}{x''} f(x'') f\big(\tfrac{x'}{x''}\big) + t(x) \bigg(\int_0^{1-\epsilon} \mathrm{d}x' f(x') \bigg)^2 \right\}, \tag{F.13}$$

where in the second step we separated the integral in the second line to combine it with the ones in the third line. Since the distance between both endpoints of the first x' integral in the last line is of order ϵ, it can be made sufficiently small for the smooth function $t\big(\tfrac{x}{x'}\big)$ to be monotonic. Therefore, we could use the mean value theorem for integrals and take t at some point x/x_ϵ, where $x_\epsilon \in \big[(1-\epsilon)^2, 1-\epsilon \big]$.

For the case relevant to us, $f(x) = 1/(1-x)$, the integrals in (F.13) evaluate to

$$\int\limits_{\frac{x'}{1-\epsilon}}^{1-\epsilon} \frac{\mathrm{d}x''}{x''} \frac{1}{(1-x'')\left(1-\frac{x'}{x''}\right)} - \frac{2}{1-x'} \int\limits_0^{1-\epsilon} \mathrm{d}x'' \frac{1}{1-x''} = \frac{2\ln(1-\epsilon-x') - \ln(x')}{1-x'}, \quad \text{(F.14)}$$

$$\int\limits_{1-\epsilon}^{(1-\epsilon)^2} \frac{\mathrm{d}x'}{x'} \int\limits_{\frac{x'}{1-\epsilon}}^{1-\epsilon} \frac{\mathrm{d}x''}{x''} \frac{1}{(1-x'')\left(1-\frac{x'}{x''}\right)} = \mathrm{Li}_2(\epsilon) + \frac{1}{2}\ln^2(1-\epsilon) + \frac{\pi^2}{6}, \quad \text{(F.15)}$$

$$\int\limits_0^{1-\epsilon} \mathrm{d}x' \frac{1}{1-x'} = -\ln(\epsilon), \quad \text{(F.16)}$$

in order of their appearance. $\mathrm{Li}_2(x)$ denotes the dilogarithm,

$$\mathrm{Li}_2(x) = -\int\limits_0^x \mathrm{d}z \frac{\log(1-z)}{z}. \quad \text{(F.17)}$$

The result in (F.14) still diverges at $x' = 1$. To deal with this singularity, we add and subtract

$$t(x) \int\limits_0^{1-\epsilon} \mathrm{d}x' \frac{2\ln(1-\epsilon-x')}{1-x'} = t(x)\left(2\mathrm{Li}_2(\epsilon) - \ln^2(\epsilon) - \frac{\pi^2}{3}\right) \quad \text{(F.18)}$$

such that we obtain an overall plus-distribution in eq. (F.13). Combining the results above, (F.13) becomes

$$\frac{1}{[1-x']_+} \underset{x}{\otimes} \left(\frac{1}{[1-x'']_+} \underset{x'}{\otimes} t(x'')\right)$$

$$= \lim_{\epsilon \to 0}\left\{\int\limits_x^{1-\epsilon} \frac{\mathrm{d}x'}{x'}\left(\frac{2\ln(1-\epsilon-x') - \ln(x')}{1-x'}\right)t\left(\frac{x}{x'}\right) - t(x)\int\limits_0^{1-\epsilon} \mathrm{d}x' \frac{2\ln(1-\epsilon-x')}{1-x'}\right.$$

$$\left. + t\left(\frac{x}{x_\epsilon}\right)\left(\mathrm{Li}_2(\epsilon) + \frac{1}{2}\ln^2(1-\epsilon) + \frac{\pi^2}{6}\right) + t(x)\left(2\mathrm{Li}_2(\epsilon) - \frac{\pi^2}{3}\right)\right\}. \quad \text{(F.19)}$$

In the limit $\epsilon \to 0$, the integration region $[(1-\epsilon)^2, 1-\epsilon]$ shrinks to a point, and therefore $x_\epsilon \to 1$. Hence,

$$\frac{1}{[1-x']_+} \underset{x}{\otimes} \frac{1}{[1-x']_+} = -\frac{\ln(x)}{1-x} + 2\left[\frac{\ln(1-x)}{1-x}\right]_+$$

$$+ \lim_{\epsilon \to 0}\left(3\mathrm{Li}_2(\epsilon) + \frac{1}{2}\ln^2(1-\epsilon) - \frac{\pi^2}{6}\right)\delta(1-x)$$

$$= 2\left[\frac{\ln(1-x)}{1-x}\right]_+ - \frac{\ln(x)}{1-x} - \frac{\pi^2}{6}\delta(1-x)\,, \tag{F.20}$$

which is the final result of our calculation. We implicitly used that

$$\lim_{\epsilon \to 0}\left\{\frac{\ln(1-\epsilon-x)}{1-x}\Theta(1-\epsilon-x) - \delta(1-x)\int\limits_0^{1-\epsilon} dx'\frac{\ln(1-\epsilon-x)}{1-x}\right\} = \left[\frac{\ln(1-x)}{1-x}\right]_+\,. \tag{F.21}$$

This can be proven by convoluting the difference of both sides of the equation with a test function, expanding it in a Taylor series around $\epsilon = 0$, integrating by parts and then showing that each individual term vanishes such that the difference corresponds to a zero in distribution space.

Second representation. Following eq. (3.17) of [91], one can define the plus-distribution as

$$\frac{1}{[1-x]_+} = \lim_{\eta \to 0}\left\{\frac{1-x}{(1-x)^2 + \eta^2} + \ln(\eta)\,\delta(1-x)\right\}\,. \tag{F.22}$$

This approach has the advantage of leaving the integral limits untouched. Hence, The Mellin convolution itself can be calculated in a straightforward way:

$$\frac{1}{[1-x']_+} \underset{x}{\otimes} \frac{1}{[1-x']_+} = \lim_{\eta \to 0}\left\{\int\limits_x^1 \frac{dx'}{x'}\frac{(1-x')\left(1-\frac{x}{x'}\right)}{\left((1-x')^2 + \eta^2\right)\left(\left(1-\frac{x}{x'}\right)^2 + \eta^2\right)}\right.$$
$$\left. + 2\frac{1-x}{(1-x)^2 + \eta^2}\ln(\eta) + \ln^2(\eta)\,\delta(1-x)\right\}\,, \tag{F.23}$$

where

$$\int\limits_x^1 \frac{dx'}{x'}\frac{(1-x')\left(1-\frac{x}{x'}\right)}{\left((1-x')^2 + \eta^2\right)\left(\left(1-\frac{x}{x'}\right)^2 + \eta^2\right)}$$
$$= \frac{\eta}{(1-x+\eta^2)^2 + 4\eta^2 x}\left\{\arctan\left(\frac{x-\eta^2-1}{\eta x}\right) + \arctan\left(\frac{x-1}{\eta}\right) + \arctan(\eta)\right\}$$
$$+ \frac{(1-x)^2 + \eta^2(1+x)}{(1-x+\eta^2)\left((1-x+\eta^2)^2 + 4\eta^2 x\right)}\left\{\ln\left((1-x)^2 + \eta^2\right) - \ln(x) - 2\ln(\eta)\right\}\,. \tag{F.24}$$

The limit $\eta \to 0$ then however is highly non-trivial and can be performed only in a convolution with a test function, as the result will consist of distributions again. Looking at the expressions (F.23) and (F.24), it becomes obvious that performing the integral with the test function is quite cumbersome due to the complicated integrands. Again, the mean value theorem is used to show that some parts of the integral vanish. In the end, we obtain the same result as in the last line of (F.20).

Cross-check via Mellin transform. The final result (F.20) can be checked by transforming to Mellin space via

$$\mathrm{MT}\{f(x)\} = \int\limits_0^1 \mathrm{d}x\, x^{N-1}\, f(x)\,. \tag{F.25}$$

This turns the Mellin convolution into a simple product. Making use of the identities given in the appendix of [134], we then find

$$\mathrm{MT}\left\{ 2\left[\frac{\log(1-x)}{1-x}\right]_+ - \frac{\log(x)}{1-x} - \frac{\pi^2}{6}\delta(1-x) \right\}$$

$$= 2\left(\frac{1}{2}\big(S_1(N-1)\big)^2 + \frac{1}{2}S_2(N-1) \right) - \big(S_2(N-1) - \zeta_2 \big) - \frac{\pi^2}{6}$$

$$= \big(S_1(N-1)\big)^2$$

$$= \mathrm{MT}\left\{ \left[\frac{1}{1-x}\right]_+ \right\}^2$$

$$= \mathrm{MT}\left\{ \left[\frac{1}{1-x'}\right]_+ \underset{x}{\otimes} \left[\frac{1}{1-x'}\right]_+ \right\}\,, \tag{F.26}$$

where

$$S_n(N) = \frac{(-1)^n}{(n-1)!} \int\limits_0^1 \mathrm{d}x\, \log^{n-1}(x)\, \frac{x^N - 1}{x - 1} \overset{N\in\mathbb{N}}{=} \sum_{i=1}^N \frac{1}{i^n}\,,\, n \in \mathbb{N}\,, \tag{F.27}$$

are harmonic sums and

$$\zeta_2 = \frac{\pi^2}{6} \tag{F.28}$$

is a functional value of the Rieman zeta function.

Appendix G

NLO DGLAP kernels:
x-dependent parts

For the sake of completeness, we give the LO expressions of DGLAP kernels for all colour representations in section G.1. Sections G.2 to G.4 contain the NLO contributions for all polarisations, whose limiting behaviour can be found in section G.5. Section G.6 provides the underlying tables for colour factors and graph-by-graph results.

G.1   LO terms

At LO, the x dependent parts of DGLAP kernels for different colour channels are proportional to each other. These expressions were already given in (3.13) to (3.16), the corresponding colour factors in (3.17) to (3.22). As mentioned in section 3.1.2, polarised kernels obey identical relations. It is thus sufficient to give the colour singlet kernels in all polarisations:

$$^{11}\widetilde{P}_{qq}^{V(0)}(x) = C_F\, p_{qq}(x)\,, \tag{G.1}$$

$$^{11}\widetilde{P}_{\Sigma^+ g}^{(0)}(x) = n_f\, p_{qg}(x)\,, \tag{G.2}$$

$$^{11}\widetilde{P}_{g\Sigma^+}^{(0)}(x) = C_F\, p_{gq}(x)\,, \tag{G.3}$$

$$^{11}\widetilde{P}_{gg}^{(0)}(x) = 2C_A\, p_{gg}(x)\,, \tag{G.4}$$

$$^{11}\widetilde{P}_{\Delta q\Delta q}^{V(0)}(x) = {}^{11}\widetilde{P}_{qq}^{V(0)}(x)\,, \tag{G.5}$$

$$^{11}\widetilde{P}_{\Delta\Sigma^+ \Delta g}^{(0)}(x) = n_f\, p_{\Delta q\Delta g}(x)\,, \tag{G.6}$$

$$^{11}\widetilde{P}_{\Delta g\Delta\Sigma^+}^{(0)}(x) = C_F\, p_{\Delta g\Delta q}(x)\,, \tag{G.7}$$

$$^{11}\widetilde{P}_{\Delta g\Delta g}^{(0)}(x) = 2C_A\, p_{\Delta g\Delta g}(x)\,, \tag{G.8}$$

$$^{11}\widetilde{P}_{\delta q\delta q}^{V(0)}(x) = C_F\, p_{\delta q\delta q}(x)\,, \tag{G.9}$$

where

$$p_{qq}(x) = \frac{1 + x^2}{[1-x]_+} \,, \tag{G.10}$$

$$p_{qg}(x) = x^2 + (1-x)^2 \,, \tag{G.11}$$

$$p_{gq}(x) = \frac{1 + (1-x)^2}{x} \,, \tag{G.12}$$

$$p_{gg}(x) = \frac{1}{[1-x]_+} + \frac{1}{x} + x(1-x) - 2 \,, \tag{G.13}$$

$$p_{\Delta q \Delta g}(x) = x^2 - (1-x)^2 = 2x - 1 \,, \tag{G.14}$$

$$p_{\Delta g \Delta q}(x) = \frac{1 - (1-x)^2}{x} = 2 - x \,, \tag{G.15}$$

$$p_{\Delta g \Delta g}(x) = \frac{1}{[1-x]_+} - 2x + 1 \,, \tag{G.16}$$

$$p_{\delta q \delta q}(x) = \frac{2x}{[1-x]_+} \,. \tag{G.17}$$

The plus-distribution is defined in (A.8).

The corresponding flavour matching coefficients at $\mathcal{O}(a_s)$, introduced in section 2.3.3, are based on the same kind of splitting graphs as the LO DGLAP kernels. Thus, as introduced in section 3.1.2, the x-dependent parts of the colour non-singlet kernels depend on the same colour factors $c_{ab}(RR')$, while the $\delta(1-x)$ part remains unchanged:

$$^{11}A_{Qg}^{(1)}(x, m_Q/\mu) = -\left(x^2 + (1-x)^2\right) \log \frac{m_Q^2}{\mu^2} \,, \tag{G.18}$$

$$^{11}A_{gg}^{(1)}(x, m_Q/\mu) = \frac{1}{3} \delta(1-x) \log \frac{m_Q^2}{\mu^2} \,, \tag{G.19}$$

$$^{RR'}A_{Qg}^{(1)}(x, m_Q/\mu) = c_{qg}(RR') \, ^{11}A_{Qg}^{(1)}(x, m_Q/\mu) \,, \tag{G.20}$$

$$^{RR'}A_{gg}^{(1)}(x, m_Q/\mu) = \, ^{11}A_{gg}^{(1)}(x, m_Q/\mu) \,, \tag{G.21}$$

where m_Q is the heavy quark mass and the colour singlet kernels are taken from [135].

G.2   Unpolarised kernels

In the following, we use

$$S_2(x) = \int_{\frac{x}{x+1}}^{\frac{1}{x+1}} \frac{dz}{z} \ln\left(\frac{1-z}{z}\right) = -2\,\mathrm{Li}_2(-x) + \frac{1}{2}\ln^2(x) - 2\ln(x)\ln(1+x) - \frac{\pi^2}{6} \,. \tag{G.22}$$

G.2.1 Quark sector

$$
^{11}\widetilde{P}_{qq}^{V(1)}(x) = \frac{C_F}{6}\Bigg\{ C_F\bigg[-3\,(1+x)\ln^2(x) - 12 p_{qq}(x)\ln(x)\ln(1-x)
$$
$$
-\Big(9 p_{qq}(x) + 21x + 9\Big)\ln(x) - 30\,(1-x)\bigg]
$$
$$
+ C_A\bigg[3 p_{qq}(x)\ln^2(x) + \Big(11 p_{qq}(x) + 6\,(1+x)\Big)\ln(x)
$$
$$
+ \Big(\frac{67}{3} - \pi^2\Big)p_{qq}(x) + 40(1-x)\bigg]
$$
$$
+ n_f\bigg[-2 p_{qq}(x)\ln(x) - \frac{10}{3}p_{qq}(x) - 4\,(1-x)\bigg]\Bigg\}, \tag{G.23}
$$

$$
^{88}\widetilde{P}_{qq}^{V(1)}(x) = c_{qq}(88)\Bigg\{ {}^{11}\widetilde{P}_{qq}^{V(1)}(x) - \frac{C_F C_A}{4}\bigg[\Big(2 p_{qq}(x) - (1+x)\Big)\ln^2(x)
$$
$$
+ (8 - 4x)\ln(x) + 6\,(1-x)\bigg]\Bigg\}, \tag{G.24}
$$

$$
^{11}\widetilde{P}_{q\bar{q}}^{V(1)}(x) = -C_F\,(C_A - 2C_F)\Bigg\{ S_2(x)\,p_{qq}(-x) + (1+x)\ln(x) + 2\,(1-x)\Bigg\}, \tag{G.25}
$$

$$
^{88}\widetilde{P}_{q\bar{q}}^{V(1)}(x) = c_{qq}(88)\,(N^2 + 1)\,{}^{11}\widetilde{P}_{q\bar{q}}^{V(1)}(x), \tag{G.26}
$$

$$
^{11}\widetilde{P}_{qq}^{S(1)}(x) = \frac{C_F}{2}\Bigg\{ -(1+x)\ln^2(x) + \Big(\frac{8}{3}x^2 + 5x + 1\Big)\ln(x) - \frac{56}{9}x^2 + 6x - 2 + \frac{20}{9x}\Bigg\}, \tag{G.27}
$$

$$
^{88}\widetilde{P}_{qq}^{S(1)}(x) = -c_{qq}(88)\,(N^2 - 2)\,{}^{11}\widetilde{P}_{qq}^{S(1)}(x), \tag{G.28}
$$

$$
^{11}\widetilde{P}_{q\bar{q}}^{S(1)}(x) = {}^{11}\widetilde{P}_{qq}^{S(1)}(x), \tag{G.29}
$$

$$
^{88}\widetilde{P}_{q\bar{q}}^{S(1)}(x) = 2 c_{qq}(88)\,{}^{11}\widetilde{P}_{q\bar{q}}^{S(1)}(x). \tag{G.30}
$$

G.2.2 Mixing channels

$$
^{11}\widetilde{P}^{(1)}_{\Sigma^+ g}(x) = C_F\, n_f \left\{ \frac{1}{2}(2x-1)\ln^2(x) + p_{qg}(x)\ln^2\!\left(\frac{x}{1-x}\right) + \left(2p_{qg}(x) + 2x - \frac{1}{2}\right)\ln(x) \right.
$$

$$
\left. + 2\Big(1 - p_{qg}(x)\Big)\ln(1-x) + \left(5 - \frac{\pi^2}{3}\right)p_{qg}(x) - \frac{9}{2}x + 2 \right\}
$$

$$
+ C_A\, n_f \left\{ -\left(\frac{1}{2}p_{qg}(x) + 4x + 1\right)\ln^2(x) - p_{qg}(x)\ln^2(1-x) \right.
$$

$$
+ \frac{1}{3}\Big(22 p_{qg}(x) + 68x - 19\Big)\ln(x) + 2\Big(p_{qg}(x) - 1\Big)\ln(1-x)
$$

$$
\left. + \left(\frac{\pi^2}{6} - \frac{109}{9}\right)p_{qg}(x) + S_2(x)\,p_{qg}(-x) + \frac{7}{9}x + \frac{91}{9} + \frac{20}{9x} \right\},
$$

$$\tag{G.31}$$

$$
^{8A}\widetilde{P}^{(1)}_{\Sigma^- g}(x) = c_{qg}(8A)\left\{ {}^{11}\widetilde{P}^{(1)}_{\Sigma^+ g}(x) + \frac{1}{2}C_A\, n_f \left[\left(-p_{qg}(x) + 3x + \frac{3}{2}\right)\ln^2(x) \right.\right.
$$

$$
- \frac{1}{3}\Big(22 p_{qg}(x) + 89x - 4\Big)\ln(x) + \frac{109}{9}p_{qg}(x)
$$

$$
\left.\left. - 2S_2(x)\,p_{qg}(-x) + \frac{83}{9}x - \frac{172}{9} - \frac{20}{9x} \right]\right\}, \quad \text{(G.32)}
$$

$$
^{8S}\widetilde{P}^{(1)}_{\Sigma^+ g}(x) = \frac{c_{qg}(8S)}{c_{qg}(8A)}\, {}^{8A}\widetilde{P}^{(1)}_{\Sigma^- g}(x) \tag{G.33}
$$

$$
^{11}\widetilde{P}^{(1)}_{g\Sigma^+}(x) = \frac{C_F}{18}\left\{ C_F\left[(9x-18)\ln^2(x) - 18 p_{gq}(x)\ln^2(1-x) + (63x+36)\ln(x) \right.\right.
$$

$$
\left. - \Big(54 p_{gq}(x) + 36x\Big)\ln(1-x) - 63x - 45 \right]
$$

$$
+ C_A\left[\Big(9 p_{gq}(x) + 18x + 72\Big)\ln^2(x) - 36 p_{gq}(x)\ln(x)\ln(1-x) \right.
$$

$$
+ 18 p_{gq}(x)\ln^2(1-x) - \Big(48x^2 + 90x + 216\Big)\ln(x)
$$

$$
+ \Big(66 p_{gq}(x) + 36x\Big)\ln(1-x) + \Big(9 - 3\pi^2\Big)p_{gq}(x)
$$

$$
\left. + 18 S_2(x)\,p_{gq}(-x) + 88x^2 + 65x + 56 \right]
$$

$$
\left. + n_f\left[-12 p_{gq}(x)\ln(1-x) - 12x - 20 p_{gq}(x)\right] \right\}, \tag{G.34}
$$

$$^{A8}\widetilde{P}_{g\Sigma-}^{(1)}(x) = c_{gq}(A8)\left\{ {}^{11}\widetilde{P}_{g\Sigma+}^{(1)}(x) + \frac{C_F C_A}{18}\left[-\left(9p_{gq}(x) + \frac{27}{2}x + 27\right)\ln^2(x)\right.\right.$$
$$+\left(24x^2 + 27x + 135\right)\ln(x) + 58p_{gq}(x)$$
$$\left.\left. - 18S_2(x)\,p_{gq}(-x) - 44x^2 - 58x + 44\right]\right\},$$
(G.35)

$$^{S8}\widetilde{P}_{g\Sigma+}^{(1)}(x) = \frac{c_{gq}(S8)}{c_{gq}(A8)}\,{}^{A8}\widetilde{P}_{g\Sigma-}^{(1)}(x)\,.$$
(G.36)

G.2.3 Gluon sector

Additional to the terms given in table G.10 we need to add the contributions from 4-gluon vertex graphs given in eq. (3.32). Note that the fraction $c_{gg}(SS)/c_{gg}(AA)$ is 1 according to eq. (3.20). We choose to make this 1 explicit such that the overall pattern is not broken.

$$^{11}\widetilde{P}_{gg}^{(1)}(x) = C_F n_f\left\{-(1+x)\ln^2(x) - (5x+3)\ln(x) + \frac{10}{3}x^2 + 4x - 8 + \frac{2}{3x}\right\}$$
$$+ C_A^2\left\{\left(p_{gg}(x) + 4(1+x)\right)\ln^2(x) - 4p_{gg}(x)\ln(x)\ln(1-x)\right.$$
$$- \frac{1}{3}\left(44x^2 - 11x + 25\right)\ln(x) + \frac{1}{3}\left(\frac{67}{3} - \pi^2\right)p_{gg}(x) + 2S_2(x)\,p_{gg}(-x)$$
$$\left.+ \frac{67}{9}x^2 + \frac{27}{2}(1-x) - \frac{67}{9x}\right\}$$
$$+ C_A n_f\left\{-\frac{2}{3}(1+x)\ln(x) - \frac{10}{9}p_{gg}(x) + \frac{13}{9}x^2 - x + 1 - \frac{13}{9x}\right\},$$
(G.37)

$$^{AA}\widetilde{P}_{gg}^{(1)}(x) = c_{gg}(AA)\left\{C_A^2\left[2(1+x)\ln^2(x) - 4p_{gg}(x)\ln(x)\ln(1-x)\right.\right.$$
$$- \frac{1}{3}\left(22x^2 - 14x + 4\right)\ln(x)$$
$$\left.+ \frac{1}{3}\left(\frac{67}{3} - \pi^2\right)p_{gg}(x) + 6(1-x)\right]$$
$$+ C_A n_f\left[-\frac{1}{2}(1+x)\ln^2(x) - \frac{1}{6}(19x+13)\ln(x) - \frac{10}{9}p_{gg}(x)\right.$$
$$\left.\left.+ \frac{28}{9}x^2 + x - 3 - \frac{10}{9x}\right]\right\},$$
(G.38)

$$^{SS}\widetilde{P}_{gg}^{(1)}(x) = \frac{c_{gg}(SS)}{c_{gg}(AA)} \, ^{AA}\widetilde{P}_{gg}^{(1)}(x)$$

$$+ 2c_{gg}(SS)(C_A - 2C_F)n_f \left\{ (1+x)\ln^2(x) + (5x+3)\ln(x) \right.$$

$$\left. - \frac{10}{3}x^2 - 4x + 8 - \frac{2}{3x} \right\}, \tag{G.39}$$

$$^{10\,\overline{10}}\widetilde{P}_{gg}^{(1)}(x) = 0\,, \tag{G.40}$$

$$^{27\,27}\widetilde{P}_{gg}^{(1)}(x) = c_{gg}(27\,27)\left\{ -\Big(15p_{gg}(x) + 12\,(1+x)\Big)\ln^2(x) - 36p_{gg}(x)\ln(x)\ln(1-x) \right.$$

$$+ \Big(44x^2 + 57x + 93\Big)\ln(x) + 3\Big(\frac{67}{3} - \pi^2\Big)p_{gg}(x)$$

$$- 30S_2(x)\,p_{gg}(-x) - \frac{335}{3}x^2 - \frac{117}{2}(1-x) + \frac{335}{3x}$$

$$\left. + n_f\left[-2\,(1+x)\ln(x) - \frac{10}{3}p_{gg}(x) + \frac{13}{3}x^2 + 3(1-x) - \frac{13}{3x} \right] \right\}. \tag{G.41}$$

G.3 Longitudinal kernels

G.3.1 Quark sector

As discussed in the context of eqs. (3.50) and (3.51), the canonical choice for the finite renormalisation constant is

$$^{1}\widetilde{Z}^{(1)}(x) = -4C_F(1-x) \tag{G.42}$$

and

$$^{8}\widetilde{Z}^{(1)}(x) = c_{qq}(88)\, ^{1}\widetilde{Z}^{(1)}(x)\,. \tag{G.43}$$

Remarkably, this leads to helicity conservation in both the colour singlet *and* octet:

$$^{11}\widetilde{P}_{\Delta q\Delta q}^{V(1)}(x) = \, ^{11}\widetilde{P}_{qq}^{V(1)}(x)\,, \tag{G.44}$$

$$^{88}\widetilde{P}_{\Delta q\Delta q}^{V(1)}(x) = \, ^{88}\widetilde{P}_{qq}^{V(1)}(x). \tag{G.45}$$

The remaining kernels are

$$^{11}\widetilde{P}_{\Delta q\Delta \bar{q}}^{V(1)}(x) = - \, ^{11}\widetilde{P}_{q\bar{q}}^{V(1)}(x)\,, \tag{G.46}$$

$$^{88}\widetilde{P}_{\Delta q\Delta \bar{q}}^{V(1)}(x) = - \, ^{88}\widetilde{P}_{q\bar{q}}^{V(1)}(x)\,, \tag{G.47}$$

$$^{11}\widetilde{P}_{\Delta q\Delta q}^{S(1)}(x) = \frac{C_F}{2}\left\{ -(1+x)\ln^2(x) + (3x-1)\ln(x) + 1 - x \right\}, \tag{G.48}$$

$$^{88}\widetilde{P}^{S(1)}_{\Delta q\Delta q}(x) = -c_{qq}(88)\,(N^2-2)\,^{11}\widetilde{P}^{S(1)}_{\Delta q\Delta q}(x)\,, \tag{G.49}$$

$$^{11}\widetilde{P}^{S(1)}_{\Delta q\Delta \bar{q}}(x) = ^{11}\widetilde{P}^{S(1)}_{\Delta q\Delta q}(x)\,, \tag{G.50}$$

$$^{88}\widetilde{P}^{S(1)}_{\Delta q\Delta \bar{q}}(x) = 2c_{qq}(88)\,^{11}\widetilde{P}^{S(1)}_{\Delta q\Delta \bar{q}}(x)\,. \tag{G.51}$$

In the colour singlet, one can deduce a relation for the flavour singlet part of $^{11}P_{\Delta q\Delta q}$ from the ABJ anomaly of the axial current [70, 136, 137],

$$\mathrm{MT}\big\{^{11}P^{S(n)}_{\Delta q\Delta q} + ^{11}P^{S(n)}_{\Delta q\Delta \bar{q}}\big\}\Big|_{N=1} = -2\,\mathrm{MT}\big\{^{11}P^{(n-1)}_{g\Sigma^+}\big\}\Big|_{N=1}\,, \tag{G.52}$$

where the Mellin transform is defined in (F.25). Using the simple structure of eqs. (G.49) to (G.51) and the absence of $\delta(1-x)$ terms inside flavour singlet kernels one obtains a similar relation for the NLO octet kernels:

$$\begin{aligned}
\mathrm{MT}\Big\{^{88}P^{S(1)}_{\Delta q\Delta q} + ^{88}P^{S(1)}_{\Delta q\Delta \bar{q}}\Big\}\Big|_{N=1} &= c_{qq}(88)\,\mathrm{MT}\Big\{-(N_c^2-2)\,^{11}P^{S(1)}_{\Delta q\Delta q} + 2\,^{11}P^{S(1)}_{\Delta q\Delta \bar{q}}\Big\}\Big|_{N=1} \\
&= \frac{N_c^2-4}{N_c^2-1}\,\mathrm{MT}\Big\{^{11}P^{S(1)}_{\Delta q\Delta q}\Big\}\Big|_{N=1} \\
&= -2c_{gq}^2(S8)\,\mathrm{MT}\Big\{^{11}P^{(0)}_{\Delta g\Delta\Sigma^+}\Big\}\Big|_{N=1} \\
&= -2c_{gq}(S8)\,\mathrm{MT}\Big\{^{S8}P^{(0)}_{\Delta g\Delta\Sigma^+}\Big\}\Big|_{N=1}\,, \tag{G.53}
\end{aligned}$$

where we used N_c as the number of colours to distinguish it from the variable of the Mellin transform. The explicit value of the first moment is

$$\mathrm{MT}\Big\{^{S8}P^{(0)}_{\Delta g\Delta\Sigma^+}\Big\}\Big|_{N=1} = c_{gq}(S8)\,\mathrm{MT}\Big\{^{11}P^{(0)}_{\Delta g\Delta\Sigma^+}\Big\}\Big|_{N=1} = \frac{3}{2}\,c_{gq}(S8)\,C_F\,. \tag{G.54}$$

G.3.2 Mixing channels

According to eq. (3.47), we need to add

$$\begin{aligned}
^{R}\widehat{Z}^{(1)}(x) \otimes {}^{RR'}\widetilde{P}^{(0)}_{\Delta q\Delta g}(x) &= c_{qg}(RR')\,c_{qq}(RR)\,C_F \\
&\quad \times \Big\{-4p_{\Delta q\Delta g}(x)\ln(x) - 8\ln(x) + 12(x-1)\Big\}. \tag{G.55}
\end{aligned}$$

to the $\overline{\text{MS}}$ kernel in the (qg) channel. It is understood that $c_{ab}(11) = 1$. This yields

$$
^{11}\widetilde{P}^{(1)}_{\Delta\Sigma^+ \Delta g}(x) = C_F n_f \left\{ \frac{1}{2} p_{\Delta q \Delta g}(x) \ln^2(x) - 2 p_{\Delta q \Delta g}(x) \ln(x) \ln(1-x) + p_{\Delta q \Delta g}(x) \ln^2(1-x) \right.
$$

$$
\left. - \frac{9}{2} \ln(x) + 4(1-x) \ln(1-x) - \frac{\pi^2}{3} p_{\Delta q \Delta g}(x) + \frac{27}{2} x - 11 \right\}
$$

$$
+ C_A n_f \left\{ -\frac{3}{2}(2x+1) \ln^2(x) - p_{\Delta q \Delta g}(x) \ln^2(1-x) \right.
$$

$$
+ (8x+1) \ln(x) - 4(1-x) \ln(1-x)
$$

$$
\left. + \frac{\pi^2}{6} p_{\Delta q \Delta g}(x) - S_2(x) \, p_{\Delta q \Delta g}(-x) - 11x + 12 \right\}, \tag{G.56}
$$

$$
^{8A}\widetilde{P}^{(1)}_{\Delta\Sigma^- \Delta g}(x) = c_{qg}(8A) \left\{ ^{11}\widetilde{P}^{(1)}_{\Delta\Sigma^+ \Delta g}(x) \right.
$$

$$
+ C_A n_f \left[\frac{1}{4} \left(p_{\Delta q \Delta g}(x) + 6 \right) \ln^2(x) - \frac{1}{4} \left(7 p_{\Delta q \Delta g}(x) + 11 \right) \ln(x) \right.
$$

$$
\left. \left. + S_2(x) \, p_{\Delta q \Delta g}(-x) - \frac{9}{2}(1-x) \right] \right\}, \tag{G.57}
$$

$$
^{8S}\widetilde{P}^{(1)}_{\Delta\Sigma^+ \Delta g}(x) = \frac{c_{qg}(8S)}{c_{qg}(8A)} \, ^{8A}\widetilde{P}^{(1)}_{\Delta\Sigma^- \Delta g}(x). \tag{G.58}
$$

The shift of $^{RR'}\widetilde{P}^{(1)}_{\Delta g \Delta q}(x)$, eq. (3.49), can be calculated in the same way as it was done for $^{RR'}\widetilde{P}^{(1)}_{\Delta q \Delta g}(x)$:

$$
-^{RR'}P^{(0)}_{\Delta g \Delta q}(x) \otimes ^{R'}\widehat{Z}^{(1)}(x) = c_{gq}(RR')c_{qq}(R'R')C_F^2
$$

$$
\times \left\{ 4 p_{\Delta g \Delta q}(x) \ln(x) - 16 \ln(x) + 12(x-1) \right\}. \tag{G.59}
$$

The final results are

$$
^{11}\widetilde{P}^{(1)}_{\Delta g \Delta\Sigma^+}(x) = \frac{C_F}{18} \left\{ C_F \left[9 p_{\Delta g \Delta q}(x) \ln^2(x) - 18 p_{\Delta g \Delta q}(x) \ln^2(1-x) + 9(x-4) \ln(x) \right. \right.
$$

$$
\left. - 18(x+2) \ln(1-x) + 72x - 153 \right]
$$

$$
+ C_A \left[27(x+2) \ln^2(x) - 36 p_{\Delta g \Delta q}(x) \ln(x) \ln(1-x) \right.
$$

$$
+ 18 p_{\Delta g \Delta q}(x) \ln^2(1-x) + (72 - 234x) \ln(x)
$$

$$+ 6\left(x + 10\right)\ln(1 - x) - 3\pi^2 p_{\Delta g \Delta q}(x)$$

$$- 18 S_2(x)\, p_{\Delta g \Delta q}(-x) + 70x + 82\Bigg]$$

$$+ n_f \left[-12 p_{\Delta g \Delta q}(x) \ln(1 - x) - 4x - 16 \right] \Bigg\}, \tag{G.60}$$

$$^{A8}\widetilde{P}^{(1)}_{\Delta g \Delta \Sigma^-}(x) = c_{gq}(A8) \Bigg\{ {}^{11}\widetilde{P}^{(1)}_{\Delta g \Delta \Sigma^+}(x) + \frac{C_F C_A}{4}\Big[-(x + 10)\ln^2(x) + 10\left(2x + 1\right)\ln(x)$$

$$+ 4 S_2(x)\, p_{\Delta g \Delta q}(-x) + 30(1 - x)\Big]\Bigg\}, \tag{G.61}$$

$$^{S8}\widetilde{P}^{(1)}_{\Delta g \Delta \Sigma^+}(x) = \frac{c_{gq}(S8)}{c_{gq}(A8)}\, {}^{A8}\widetilde{P}^{(1)}_{\Delta g \Delta \Sigma^-}(x). \tag{G.62}$$

G.3.3 Gluon sector

Adding the contributions from 4-gluon vertex graphs, eq. (3.42), to the terms given in table G.15 we get (as in the unpolarised case, notice that $c_{gg}(SS)/c_{gg}(AA) = 1$)

$$^{11}\widetilde{P}^{(1)}_{\Delta g \Delta g}(x) = C_F n_f \left\{ -(1 + x)\ln^2(x) + (x - 5)\ln(x) - 5(1 - x) \right\}$$

$$+ C_A^2 \left\{ \Big(p_{\Delta g \Delta g}(x) + 4(1 + x)\Big)\ln^2(x) - 4 p_{\Delta g \Delta g}(x)\ln(x)\ln(1 - x) \right.$$

$$+ \frac{1}{3}(29 - 67x)\ln(x) + \frac{1}{3}\Big(\frac{67}{3} - \pi^2\Big) p_{\Delta g \Delta g}(x)$$

$$\left. - 2 S_2(x)\, p_{\Delta g \Delta g}(-x) - \frac{19}{2}(1 - x) \right\}$$

$$+ C_A n_f \left\{ -\frac{2}{3}(1 + x)\ln(x) - \frac{10}{9} p_{\Delta g \Delta g}(x) - 2(1 - x) \right\}, \tag{G.63}$$

$$^{AA}\widetilde{P}^{(1)}_{\Delta g \Delta g}(x) = c_{gg}(AA) \Bigg\{ C_A^2 \Big[2(1 + x)\ln^2(x) - 4 p_{\Delta g \Delta g}(x)\ln(x)\ln(1 - x)$$

$$+ \frac{1}{3}(32 - 40x)\ln(x) + \frac{1}{3}\Big(\frac{67}{3} - \pi^2\Big) p_{\Delta g \Delta g}(x)\Big]$$

$$+ C_A n_f \Big[-\frac{1}{2}(1 + x)\ln^2(x) - \frac{1}{6}(x + 19)\ln(x)$$

$$- \frac{10}{9} p_{\Delta g \Delta g}(x) - \frac{9}{2}(1 - x)\Big]\Bigg\}, \tag{G.64}$$

$$^{SS}\widetilde{P}^{(1)}_{\Delta g \Delta g}(x) = \frac{c_{gg}(SS)}{c_{gg}(AA)}\,^{AA}\widetilde{P}^{(1)}_{\Delta g \Delta g}(x)$$

$$+ 2c_{gg}(SS)\,(C_A - 2C_F)\,n_f \bigg\{ (1+x)\ln^2(x) + (5-x)\ln(x)$$

$$+ 5(1-x) \bigg\}, \tag{G.65}$$

$$^{10\,\overline{10}}\widetilde{P}^{(1)}_{\Delta g \Delta g}(x) = 0\,, \tag{G.66}$$

$$^{27\,27}\widetilde{P}^{(1)}_{\Delta g \Delta g}(x) = c_{gg}(27\,27)\bigg\{ -\Big(15 p_{\Delta g \Delta g}(x) + 12\,(1+x)\Big)\ln^2(x)$$

$$- 36 p_{\Delta g \Delta g}(x)\ln(x)\ln(1-x)$$

$$+ (15x + 111)\ln(x) + 3\Big(\frac{67}{3} - \pi^2\Big) p_{\Delta g \Delta g}(x)$$

$$+ 30 S_2(x)\, p_{\Delta g \Delta g}(-x) + \frac{285}{2}(1-x)$$

$$+ n_f \bigg[-2(1+x)\ln(x) - \frac{10}{3} p_{\Delta g \Delta g}(x) - 6\,(1-x) \bigg] \bigg\}\,. \tag{G.67}$$

G.4 Transversity kernels

$$^{11}\widetilde{P}^{V(1)}_{\delta q \delta q}(x) = C_F \bigg\{ C_F \bigg[-\Big(2\ln(x)\ln(1-x) + \frac{3}{2}\ln(x) \Big) p_{\delta q \delta q}(x) + 1 - x \bigg]$$

$$+ \frac{1}{2} C_A \bigg[\Big(\ln^2(x) + \frac{11}{3}\ln(x) \Big) p_{\delta q \delta q}(x) + \frac{1}{3}\Big(\frac{67}{3} - \pi^2 \Big) p_{\delta q \delta q}(x) - (1-x) \bigg]$$

$$- \frac{1}{9} n_f \Big(3\ln(x) + 5 \Big) p_{\delta q \delta q}(x) \bigg\}, \tag{G.68}$$

$$^{88}\widetilde{P}^{V(1)}_{\delta q \delta q}(x) = c_{qq}(88)\bigg\{ ^{11}\widetilde{P}^{V(1)}_{\delta q \delta q}(x) - \frac{1}{2} C_F C_A \Big[\ln^2(x)\, p_{\delta q \delta q}(x) + 1 - x \Big] \bigg\}, \tag{G.69}$$

$$^{11}\widetilde{P}^{V(1)}_{\delta q \delta \bar{q}}(x) = -\frac{1}{2} C_F (C_A - 2C_F)\bigg\{ 2 S_2(x)\, p_{\delta q \delta q}(-x) - (1-x) \bigg\}, \tag{G.70}$$

$$^{88}\widetilde{P}^{V(1)}_{\delta q \delta \bar{q}}(x) = c_{qq}(88)\,(N^2 + 1)\,^{11}\widetilde{P}^{V(1)}_{\delta q \delta \bar{q}}(x)\,. \tag{G.71}$$

G.5 Small and large x limits

In this section, we omit x arguments throughout.

$x \to 1$ We find

$$^{88}\widetilde{P}_{qq}^{V(1)} \approx c_{qq}(88) \, ^{11}\widetilde{P}_{qq}^{V(1)} \,, \tag{G.72}$$

$$^{8A}\widetilde{P}_{\Sigma^- g}^{(1)} \approx c_{qg}(8A) \, ^{11}\widetilde{P}_{\Sigma^+ g}^{(1)} \,, \qquad\qquad ^{A8}\widetilde{P}_{g\Sigma^-}^{(1)} \approx c_{gq}(A8) \, ^{11}\widetilde{P}_{g\Sigma^+}^{(1)} \,, \tag{G.73}$$

$$^{8S}\widetilde{P}_{\Sigma^+ g}^{(1)} \approx c_{qg}(8S) \, ^{11}\widetilde{P}_{\Sigma^+ g}^{(1)} \,, \qquad\qquad ^{S8}\widetilde{P}_{g\Sigma^+}^{(1)} \approx c_{gq}(S8) \, ^{11}\widetilde{P}_{g\Sigma^+}^{(1)} \,, \tag{G.74}$$

$$^{RR}\widetilde{P}_{gg}^{(1)} \approx c_{gg}(RR) \, ^{11}\widetilde{P}_{gg}^{(1)} \,, \tag{G.75}$$

for all polarisations. The proportionality factors $c_{ab}(RR')$ are the same as in the LO relations (3.13) to (3.16). The colour singlet limits are

$$^{11}\widetilde{P}_{qq}^{V(1)} \approx {}^{11}\widetilde{P}_{\Delta q\Delta q}^{V(1)} \approx {}^{11}\widetilde{P}_{\delta q\delta q}^{V(1)} \approx \frac{1}{9} C_F \Big(C_A \big(67 - 3\pi^2\big) - 10 n_f \Big) \frac{1}{[1-x]_+} \,, \tag{G.76}$$

$$^{11}\widetilde{P}_{gg}^{(1)} \approx {}^{11}\widetilde{P}_{\Delta g\Delta g}^{(1)} \approx \frac{C_A}{C_F} \, ^{11}\widetilde{P}_{qq}^{V(1)} \,, \tag{G.77}$$

$$^{11}\widetilde{P}_{\Sigma^+ g}^{(1)} \approx {}^{11}\widetilde{P}_{\Delta\Sigma^+\Delta g}^{(1)} \approx -(C_A - C_F) n_f \ln^2(1-x) \,, \tag{G.78}$$

$$^{11}\widetilde{P}_{g\Sigma^+}^{(1)} \approx {}^{11}\widetilde{P}_{\Delta g\Delta\Sigma^+}^{(1)} \approx C_F(C_A - C_F) \ln^2(1-x) \,. \tag{G.79}$$

The remaining channels vanish in this limit,

$$^{RR}\widetilde{P}_{q\bar{q}}^{V(1)} \,, \; ^{RR}\widetilde{P}_{qq}^{S(1)} \,, \; ^{RR}\widetilde{P}_{q\bar{q}}^{S(1)} \,, \; ^{RR}\widetilde{P}_{\Delta q\Delta\bar{q}}^{V(1)} \,, \; ^{RR}\widetilde{P}_{\Delta q\Delta q}^{S(1)} \,, \; ^{RR}\widetilde{P}_{\Delta q\Delta\bar{q}}^{S(1)} \,, \; ^{RR}\widetilde{P}_{\delta q\delta\bar{q}}^{V(1)} \underset{x\to 1}{\longrightarrow} 0 \tag{G.80}$$

for $R = 1, 8$.

Let us take a little excursion on the difference between unpolarised and longitudinal kernels,

$$^{RR'}\delta_{ab}^{(1)}(x) = {}^{RR'}P_{ab}^{(i)}(x) - {}^{RR'}P_{\Delta a\Delta b}^{(i)}(x) \,, \quad a, b = \Sigma^+, g \,, \tag{G.81}$$

which for $RR' = 11$ corresponds to the physical probability for a helicity flip. For $x \to 1$, it is argued in [70] that $^{11}\delta_{ab}^{(i)}$ should be suppressed in a "physical" scheme by a factor of $(1-x)^2$ compared to the sum of both kernels, which behaves like $\mathcal{O}\big((1-x)^{-1}\big)$ for $\Sigma^+\Sigma^+$ and gg, and $\mathcal{O}(1)$ otherwise. At LO, $i = 0$, this is indeed fulfilled for every kernel. For $i = 1$, the authors find

$$^{11}\delta_{\Sigma^+\Sigma^+}^{(1)}(x), {}^{11}\delta_{gg}^{(1)}(x) \sim \mathcal{O}(1-x) \,, \tag{G.82}$$

$$^{11}\delta_{\Sigma^+ g}^{(1)}(x) \sim \mathcal{O}\big((1-x)^2\big) \,, \tag{G.83}$$

but

$$^{11}\delta_{g\Sigma^+}^{(1)}(x) \sim \dots \times \ln(1-x) + \dots \times (1-x) + \mathcal{O}\big((1-x)^2\big) \,. \tag{G.84}$$

In the colour non-singlet case, both $^{88}\delta_{\Sigma^+\Sigma^+}^{(1)}(x)$ and $^{R\overline{R}}\delta_{gg}^{(1)}(x)$ exhibit the same behaviour for $x \to 1$ as the respective colour singlet differences. The mixed channels receive additional contributions:

$$^{8S}\delta_{\Sigma^+ g}^{(1)}(x) = c_{qg}(8S) \left({}^{11}\delta_{\Sigma^+ g}^{(1)}(x) + \mathcal{O}(1-x) \right) \,, \tag{G.85}$$

139

$$^{8A}\delta^{(1)}_{\Sigma^- g}(x) = \frac{c_{qg}(8A)}{c_{qg}(8S)} \, ^{8S}\delta^{(1)}_{\Sigma^+ g}(x) \,, \tag{G.86}$$

$$^{S8}\delta^{(1)}_{g\Sigma+}(x) = c_{gq}(S8) \left(^{11}\delta^{(1)}_{g\Sigma+}(x) + \mathcal{O}(1-x) \right) \,, \tag{G.87}$$

$$^{A8}\delta^{(1)}_{g\Sigma-}(x) = \frac{c_{gq}(A8)}{c_{gq}(S8)} \, ^{S8}\delta^{(1)}_{g\Sigma-}(x) \,. \tag{G.88}$$

The proposed way in [70] to get rid of the unwanted terms in (G.84) is to change the lower left entry of the renormalisation factor matrix in (D.16) from 0 to $a_s {}^{11}P^{(0)}_{g\Sigma+}(x)$. Extending this approach to arbitrary colour representations would however not yield the desired results due to the additional $\mathcal{O}(1-x)$ terms.

$\boldsymbol{x \to 0}$ The limits for unpolarised kernels are

$$^{11}\widetilde{P}^{V(1)}_{qq} \approx \frac{1}{2} C_F (C_A - C_F) \ln^2(x) \,, \tag{G.89}$$

$$\frac{^{88}\widetilde{P}^{V(1)}_{qq}}{c_{qq}(88)} \approx \frac{1}{4} C_F (C_A - 2C_F) \ln^2(x) \,, \tag{G.90}$$

$$^{11}\widetilde{P}^{V(1)}_{q\bar{q}} \approx -\frac{1}{2} C_F (C_A - 2C_F) \ln^2(x) \,, \tag{G.91}$$

$$^{11}\widetilde{P}^{S(1)}_{qq} = {}^{11}\widetilde{P}^{S(1)}_{q\bar{q}} \approx \frac{10}{9} C_F \frac{1}{x} \tag{G.92}$$

in the quark sector. The colour octet kernels $^{88}\widetilde{P}^{V(1)}_{q\bar{q}}$, $^{88}\widetilde{P}^{S(1)}_{qq}$, and $^{88}\widetilde{P}^{S(1)}_{q\bar{q}}$ are proportional to their colour singlet counterparts, see equations (G.26), (G.28), and (G.30). The remaining limits are

$$^{11}\widetilde{P}^{(1)}_{\Sigma^+ g} \approx \frac{20}{9} C_A n_f \frac{1}{x} \,, \tag{G.93}$$

$$\frac{^{8A}\widetilde{P}^{(1)}_{\Sigma^- g}}{c_{qg}(8A)} = \frac{^{8S}\widetilde{P}^{(1)}_{\Sigma^+ g}}{c_{qg}(8S)} \approx \frac{10}{9} C_A n_f \frac{1}{x} \,, \tag{G.94}$$

$$^{11}\widetilde{P}^{(1)}_{g\Sigma+} \approx \frac{1}{9} C_F (9C_A - 20n_f) \frac{1}{x} \,, \tag{G.95}$$

$$\frac{^{A8}\widetilde{P}^{(1)}_{g\Sigma-}}{c_{gq}(A8)} = \frac{^{S8}\widetilde{P}^{(1)}_{g\Sigma+}}{c_{gq}(S8)} \approx \frac{1}{9} C_F \left(C_A \left(67 - 3\pi^2 \right) - 20n_f \right) \frac{1}{x} \,, \tag{G.96}$$

$$^{11}\widetilde{P}^{(1)}_{gg} \approx \frac{1}{9} \left[6C_F n_f - 23C_A n_f \right] \frac{1}{x} \,, \tag{G.97}$$

$$\frac{^{AA}\widetilde{P}^{(1)}_{gg}}{c_{gg}(AA)} \approx \frac{1}{9} \left[C_A^2 \left(67 - 3\pi^2 \right) - 20C_A n_f \right] \frac{1}{x} \,, \tag{G.98}$$

$$\frac{^{SS}\widetilde{P}^{(1)}_{gg}}{c_{gg}(SS)} \approx \frac{1}{9} \left[C_A^2 \left(67 - 3\pi^2 \right) + 24C_F n_f - 32C_A n_f \right] \frac{1}{x} \,, \tag{G.99}$$

$$\frac{^{27\,27}\widetilde{P}^{(1)}_{gg}}{c_{gg}(27\,27)} \approx \frac{1}{3}\left[8\left(67 - 3\pi^2\right) - 23n_f\right]\frac{1}{x}\,. \tag{G.100}$$

For the longitudinal polarisation, the behaviour of all valence kernels can be deduced from the ones for unpolarised quarks, see (G.44) to (G.47)). In addition, $^{88}\widetilde{P}^{S(1)}_{\Delta q\Delta q}$ and $^{88}\widetilde{P}^{S(1)}_{\Delta q\Delta\bar{q}}$ are related to their colour singlet counterparts, which are given below with the other limits:

$$^{11}\widetilde{P}^{S(1)}_{\Delta q\Delta q} = {}^{11}\widetilde{P}^{S(1)}_{\Delta q\Delta\bar{q}} \approx -\frac{1}{2}C_F\ln^2(x)\,, \tag{G.101}$$

$$^{11}\widetilde{P}^{(1)}_{\Delta\Sigma^+\Delta g} \approx -\frac{1}{2}\left(C_F + 2C_A\right)n_f\ln^2(x)\,, \tag{G.102}$$

$$\frac{^{8A}\widetilde{P}^{(1)}_{\Delta\Sigma^-\Delta g}}{c_{qg}(8A)} = \frac{^{8S}\widetilde{P}^{(1)}_{\Delta\Sigma^+\Delta g}}{c_{qg}(8S)} \approx -\frac{1}{4}\left(2C_F + C_A\right)n_f\ln^2(x)\,, \tag{G.103}$$

$$^{11}\widetilde{P}^{(1)}_{\Delta g\Delta\Sigma^+} \approx C_F(C_F + 2C_A)\ln^2(x)\,, \tag{G.104}$$

$$\frac{^{A8}\widetilde{P}^{(1)}_{\Delta g\Delta\Sigma^-}}{c_{gq}(A8)} = \frac{^{S8}\widetilde{P}^{(1)}_{\Delta g\Delta\Sigma^+}}{c_{gq}(S8)} \approx \frac{1}{2}C_F(2C_F + C_A)\ln^2(x)\,, \tag{G.105}$$

$$^{11}\widetilde{P}^{(1)}_{\Delta g\Delta g} \approx \left(4C_A^2 - C_F n_f\right)\ln^2(x)\,, \tag{G.106}$$

$$\frac{^{AA}\widetilde{P}^{(1)}_{\Delta g\Delta g}}{c_{gg}(AA)} \approx \frac{1}{2}\left(4C_A^2 - C_A n_f\right)\ln^2(x)\,, \tag{G.107}$$

$$\frac{^{SS}\widetilde{P}^{(1)}_{\Delta g\Delta g}}{c_{gg}(SS)} \approx \frac{1}{2}\left(4C_A^2 - 8C_F n_f + 3C_A n_f\right)\ln^2(x)\,, \tag{G.108}$$

$$\frac{^{27\,27}\widetilde{P}^{(1)}_{\Delta g\Delta g}}{c_{gg}(27\,27)} \approx -12\ln^2(x)\,. \tag{G.109}$$

The kernels for transverse polarisation exhibit a finite behaviour for $x \to 0$,

$$^{11}\widetilde{P}^{V(1)}_{\delta q\delta q} \approx -\frac{1}{2}C_F(C_A - 2C_F)\,, \tag{G.110}$$

$$\frac{^{88}\widetilde{P}^{V(1)}_{\delta q\delta q}}{c_{qq}(88)} \approx -C_F(C_A - C_F)\,, \tag{G.111}$$

$$^{11}\widetilde{P}^{V(1)}_{\delta q\delta\bar{q}} \approx \frac{1}{2}C_F(C_A - 2C_F)\,. \tag{G.112}$$

$^{88}\widetilde{P}^{V(1)}_{\delta q\delta\bar{q}}$ can be obtained from $^{11}\widetilde{P}^{V(1)}_{\delta q\delta\bar{q}}$, see equation (G.71).

G.6 Colour factors and graph-by-graph results

In the following, we first give the colour factors for every real graph in all possible representations, assuming the definitions of colour projectors given in appendix B.1. The labelling convention for the NLO splitting graph topologies is adopted from [105] and can be found in figure 3.2. After that, we list the x-terms for all channels and graphs. They can be extracted from the references given in the respective tables, with some additional factors of 2, $1/2$ and -1 that were absorbed into the x-dependent terms there. Furthermore, some combinations of colour factors were only given for a linear combination of two graphs. These systems of linear equations can be solved in a straight-forward way such that the tables below contain the entangled results for every graph.

For ${}^{R\overline{R}}\widetilde{P}_{gg}^{(1)}$ and ${}^{R\overline{R}}\widetilde{P}_{\Delta g \Delta g}^{(1)}$ we set $N = 3$ in the column of $R\overline{R} = 27\,27$.

The longitudinal x-terms are given in the HVBM scheme before the finite scheme change described in section 3.1.5.

The divergent integrals I_0 and I_1 are defined in (3.9). They depend on the δ-regulator introduced in section 3.1.1. It is associated with divergencies that appear in the gluon propagator and are unique to the axial gauge. The sum of all diagrams is required to be independent of these divergent terms. As we have seen in the appendices G.2, G.3, and G.4, all kernels indeed fulfil this requirement in every colour representation.

RR	11	88
global factor	1	1
$^{RR}\widetilde{P}_{qq}^{V(1)}$		
graph (b)	$-\frac{N^2-1}{4N^2}$	$\frac{N^2+1}{4N^2}$
graph (c)	$-\frac{N^2-1}{4N^2}$	$\frac{1}{4N^2}$
graph (d)	$-\frac{N^2-1}{4}$	$\frac{1}{4}$
graph (e)	$\frac{(N^2-1)^2}{4N^2}$	$-\frac{N^2-1}{4N^2}$
graph (f)	$\frac{N^2-1}{4N}n_f$	$-\frac{1}{4N}n_f$
graph (g)	$\frac{N^2-1}{2}$	$-\frac{1}{2}$
graph (h)	$\frac{(N^2-1)^2}{4N^2}$	$\frac{1}{4N^2}$
$^{RR'}\widetilde{P}_{qq}^{S(1)}$		
graph (h)	$\frac{N^2-1}{4N}$	$\frac{N^2-2}{4N}$
$^{RR'}\widetilde{P}_{q\bar{q}}^{V(1)}$		
graph (b)	$-\frac{N^2-1}{4N^2}$	$\frac{N^2+1}{4N^2}$
$^{RR'}\widetilde{P}_{q\bar{q}}^{S(1)}$		
graph (h)	$\frac{N^2-1}{4N}$	$-\frac{1}{2N}$

Table G.1: NLO colour factors of the pure quark sector for all R.

RR'	11	$8A$	$8S$
global factor	1	$c_{qg}(8A)$	$c_{qg}(8S)$
graph (b)	$-\frac{N}{4}$	0	0
graph (c)	$\frac{N}{4}$	$\frac{N}{4}$	$\frac{N}{4}$
graph (d)	$-\frac{1}{4N}$	$-\frac{1}{4N}$	$-\frac{1}{4N}$
graph (e)	$\frac{N^2-1}{4N}$	$\frac{N^2-1}{4N}$	$\frac{N^2-1}{4N}$
graph (f)	$\frac{N^2-1}{4N}$	$\frac{N^2-1}{4N}$	$\frac{N^2-1}{4N}$
graph (h)	$\frac{N}{2}$	$\frac{N}{4}$	$\frac{N}{4}$
graph (i)	$\frac{N^2-1}{4N}$	$-\frac{1}{4N}$	$-\frac{1}{4N}$

Table G.2: NLO colour factors of $^{RR'}\widetilde{P}_{qg}^{(1)}$ for all RR'.

RR'	11	$A8$	$S8$
global factor	1	$c_{gq}(A8)$	$c_{gq}(S8)$
graph (b)	$-\frac{N^2-1}{4}$	0	0
graph (c)	$-\frac{N^2-1}{4N^2}$	$-\frac{N^2-1}{4N^2}$	$-\frac{N^2-1}{4N^2}$
graph (d)	$\frac{N^2-1}{4}$	$\frac{N^2-1}{4}$	$\frac{N^2-1}{4}$
graph (e$_\mathrm{q}$)	$\frac{N^2-1}{4N}n_f$	$\frac{N^2-1}{4N}n_f$	$\frac{N^2-1}{4N}n_f$
graph (e$_\mathrm{g}$)	$\frac{N^2-1}{2}$	$\frac{N^2-1}{2}$	$\frac{N^2-1}{2}$
graph (f)	$\frac{(N^2-1)^2}{4N^2}$	$\frac{(N^2-1)^2}{4N^2}$	$\frac{(N^2-1)^2}{4N^2}$
graph (h)	$\frac{N^2-1}{2}$	$\frac{N^2-1}{4}$	$\frac{N^2-1}{4}$
graph (i)	$\frac{(N^2-1)^2}{4N^2}$	$-\frac{N^2-1}{4N^2}$	$-\frac{N^2-1}{4N^2}$

Table G.3: NLO colour factors of $^{RR'}\widetilde{P}_{gq}^{(1)}$ for all RR'.

$R\overline{R}$	11	AA	SS	$27\,27$
global factor	1	1	1	1
graph (b_q)	$-\frac{1}{2N}n_f$	0	$-\frac{1}{N}n_f$	$\frac{1}{2}n_f$
graph (b_g)	$\frac{N^2}{2}$	0	0	$\frac{5}{2}$
graph (c)	$\frac{N^2}{2}$	$\frac{1}{4}N^2$	$\frac{1}{4}N^2$	$-\frac{3}{2}$
graph (d)	$\frac{N}{2}n_f$	$\frac{1}{4}Nn_f$	$\frac{1}{4}Nn_f$	$-\frac{1}{2}n_f$
graph (e_q)	$\frac{N}{2}n_f$	$\frac{1}{4}Nn_f$	$\frac{1}{4}Nn_f$	$-\frac{1}{2}n_f$
graph (e_g)	N^2	$\frac{1}{2}N^2$	$\frac{1}{2}N^2$	-3
graph (f)	N^2	$\frac{1}{2}N^2$	$\frac{1}{2}N^2$	-3
graph (g)	$\frac{N}{2}n_f$	$\frac{1}{4}Nn_f$	$\frac{1}{4}Nn_f$	$-\frac{1}{2}n_f$
graph (h)	N^2	$\frac{1}{4}N^2$	$\frac{1}{4}N^2$	1
graph (i)	$\frac{N^2-1}{2N}n_f$	$\frac{1}{4}Nn_f$	$\frac{N^2-4}{4N}n_f$	0

Table G.4: NLO colour factors of $^{RR'}\widetilde{P}_{gg}^{(1)}$ for all $R\overline{R}$. All contributions for $RR' = AS$, SA, 10 and $\overline{10}$ vanish and are thus not shown.

Terms	Graphs						
	(b)	(c)	(d)	(e)	(f)	(g)	(h)
$p_{qq}(x)\ln^2(x)$	-1	1	-1	-2			2
$p_{qq}(x)\ln^2(1-x)$			-2			-1	
$p_{qq}(x)\ln(x)\ln(1-x)$		2	-6	-4		-2	
$p_{qq}(x)I_0\big(\ln(1-x)+\ln(x)\big)$		4	-8	-4		-2	
$p_{qq}(x)\ln(x)$		$-3/2$	$3/2$		$-2/3$	$11/6$	
$p_{qq}(x)\ln(1-x)$	4	-3	-5	3		-2	-4
$p_{qq}(x)\pi^2/3$		2	-3	-2		-1	
$p_{qq}(x)I_0$	4		-8			-2	-4
$p_{qq}(x)I_1$		-4	8	4		2	
$p_{qq}(x)$		-7	11	7	$-10/9$	$103/18$	
$(x+1)\ln^2(x)$							$-1/2$
$(x+1)\ln(x)$	2	$-7/2$	$-1/2$				-1
$(1-x)\ln(x)$		2	-2	-4			3
$(1-x)\ln(1-x)$			-4			-2	
$(1-x)I_0$		4	-8	-4		-2	
$1-x$		-11	1	3	$-4/3$	$5/3$	3

Table G.5: Results for $^{RR}\widetilde{P}_{qq}^{V(1)}$. Adapted from [10], table I.

Terms	(h)
$x\ln^2(x)$	-1
$\ln^2(x)$	-1
$x^2\ln(x)$	$8/3$
$x\ln(x)$	5
$\ln(x)$	1
x^2	$-56/9$
x	6
1	-2
$1/x$	$20/9$

Table G.6: Results for $^{RR}\widetilde{P}_{qq}^{S(1)}$ and $^{RR}\widetilde{P}_{q\bar{q}}^{S(1)}$. Adapted from [105], eq. (57).

Terms	(b)
$p_{qq}(-x)S_2(x)$	2
$(x+1)\ln(x)$	2
$1-x$	4

Table G.7: Results for $^{RR}\widetilde{P}_{q\bar{q}}^{V(1)}$. Adapted from [10], eq. (4.51).

Terms	Graphs						
	(b)	(c)	(d)	(e)	(f)	(h)	(i)
$p_{qg}(x)\ln^2(x)$	2	2	2	-4			4
$p_{qg}(x)\ln^2(1-x)$		2	2		-2	-2	2
$p_{qg}(x)\ln(x)\ln(1-x)$		12	4	-8	-4	-4	4
$p_{qg}(x)I_0\Big(\ln(1-x)+\ln(x)\Big)$		16	8	-8	-4	-4	4
$p_{qg}(x)\ln(x)$	-6	-4	-4	8	3	$35/3$	-3
$p_{qg}(x)\ln(1-x)$	-8	-2	-2	6			-8
$p_{qg}(x)\text{Li}_2(1-x)$		8	-8			-8	8
$p_{qg}(x)\pi^2/3$		4	6	-4	-2	2	-2
$p_{qg}(-x)S_2$	-4						
$p_{qg}(x)I_0$	-8	-8		8			-8
$p_{qg}(x)I_1$		-16	-8	8	4	4	-4
$p_{qg}(x)$	26	-22	-14	8	7	$-65/9$	9
$x\ln^2(x)$						-8	2
$\ln^2(x)$						-2	-1
$x\ln(x)$	-40	20				$46/3$	4
$\ln(x)$	-2	-6	2	-8		$-29/3$	5
$\ln(1-x)$		4	4		-4	-4	4
I_0		16	8	-8	-4	-4	4
x	8	10	2		1	$14/9$	-12
1	-34	-4	-8	6	3	$11/9$	3
$1/x$						$40/9$	

Table G.8: Results for $^{RR'}\widetilde{P}_{qg}^{(1)}(x)$. Adapted from [105], table 2.

Terms	Graphs							
	(b)	(c)	(d)	(e_q)	(e_g)	(f)	(h)	(i)
$p_{gq}(x)\ln^2(x)$	1		2		-2		2	
$p_{gq}(x)\ln^2(1-x)$		1	1			-1	1	-1
$p_{gq}(x)\ln(x)\ln(1-x)$		4	4		-4	-2	2	-2
$p_{gq}(x)I_0\big(\ln(1-x)+\ln(x)\big)$		4	8		-4	-2	2	-2
$p_{gq}(x)\ln(x)$	3	-3	-3			$3/2$	$3/2$	$3/2$
$p_{gq}(x)\ln(1-x)$	-4	1	1	$-4/3$	$11/3$	-2	-2	-2
$p_{gq}(x)\mathrm{Li}_2(1-x)$		4	-4				4	-4
$p_{gq}(x)\pi^2/3$			5		-2	-1	-1	1
$p_{gq}(-x)S_2$	-2							
$p_{gq}(x)I_0$	-4	4	4			-2	-2	-2
$p_{gq}(x)I_1$		-4	-8		4	2	-2	2
$p_{gq}(x)$	13	-10	-14	$-20/9$	$67/9$	5	$14/9$	5
$x\ln^2(x)$							1	$1/2$
$\ln^2(x)$							4	-1
$x^2\ln(x)$							$-8/3$	
$x\ln(x)$	1	1	9		-4		$-9/2$	$5/2$
$\ln(x)$	20		-10				3	2
$x\ln(1-x)$		2	2			-2	2	-2
xI_0		4	8		-4	-2	2	-2
x^2							$44/9$	
x	-17	-4	-2	$-4/3$	$11/3$	$3/2$	$-86/9$	-1
1	4	1	5			$1/2$	$28/9$	-4

Table G.9: Results for $^{RR'}\widetilde{P}_{gq}^{(1)}(x)$. Adapted from [105], table 3.

Terms	Graphs									
	(b_q)	(b_g)	(c)	(d)	(e_q)	(e_g)	(f)	(g)	(h)	(i)
$p_{gg}(x)\ln^2(x)$		-2	4			-4			4	
$p_{gg}(x)\ln^2(1-x)$			4				-2			
$p_{gg}(x)\ln(x)\ln(1-x)$			16			-8	-4			
$p_{gg}(x)I_0\big(\ln(1-x)+\ln(x)\big)$			24			-8	-4			
$p_{gg}(x)\ln(x)$			$-22/3$	$4/3$			$11/3$	$-4/3$		
$p_{gg}(x)\ln(1-x)$		8	$4/3$	$8/3$	$-8/3$	$22/3$	-4		-8	
$p_{gg}(x)\pi^2/3$			10			-4	-2			
$p_{gg}(-x)S_2(x)$		4								
$p_{gg}(x)I_0$		8	16				-4		-8	
$p_{gg}(x)I_1$			-24			8	4			
$p_{gg}(x)$			$-340/9$	$40/9$	$-40/9$	$134/9$	$103/9$	$-20/9$		
$x\ln^2(x)$									4	-1
$\ln^2(x)$									4	-1
$x^2\ln(x)$	$4/3$	$-22/3$	$-22/3$	$4/3$					$-22/3$	$-4/3$
$x\ln(x)$	4	$-34/2$	$-23/3$	$8/3$					16	-9
$\ln(x)$	4	$-34/2$	$-23/3$	$8/3$					4	-7
$\ln(x)/x$	$4/3$	$-22/3$	$-22/3$	$4/3$					$22/3$	$-4/3$
x^2	$-38/9$	$272/9$	$44/3$	$-8/3$			$1/3$	$4/3$	$-46/3$	$68/9$
x	2	$-105/4$	$-50/3$	$5/3$			$-5/12$	$-5/3$	$19/2$	2
1	-2	$105/4$	$50/3$	$-5/3$			$5/12$	$5/3$	$-19/2$	-6
$1/x$	$38/9$	$-272/9$	$-44/3$	$8/3$			$-1/3$	$-4/3$	$46/3$	$-32/9$

Table G.10: Results for $^{RR'}\widetilde{P}_{gg}^{(1)}(x)$. Adapted from [105], table 4.

Terms	Graphs						
	(b)	(c)	(d)	(e)	(f)	(g)	(h)
$(1-x)\ln(x)$		-8	8	16			-8
$(1-x)\ln(1-x)$			16			8	
$(1-x)I_0$		-16	32	16		8	
$1-x$		12	-12	-12	$8/3$	$-22/3$	

Table G.11: Results for ${}^{RR}\widetilde{P}^{V(1)}_{\Delta q\Delta q,\overline{\mathrm{MS}}} - {}^{RR}\widetilde{P}^{V(1)}_{qq}$. Adapted from [106], table 1.

Terms	Graphs						
	(b)	(c)	(d)	(e)	(f)	(h)	(i)
$p_{\Delta q\Delta g}(x)\ln^2(x)$	2	2	2	-4		-2	3
$p_{\Delta q\Delta g}(x)\ln^2(1-x)$		2	2		-2	-2	2
$p_{\Delta q\Delta g}(x)\ln(x)\ln(1-x)$		12	4	-8	-4	-4	4
$p_{\Delta q\Delta g}(x)I_0\Big(\ln(1-x)+\ln(x)\Big)$		16	8	-8	-4	-4	4
$p_{\Delta q\Delta g}(x)\ln(x)$	-10	-6	-4	8	3	4	1
$p_{\Delta q\Delta g}(x)\ln(1-x)$	-8	-2	-2	6			-8
$p_{\Delta q\Delta g}(x)\mathrm{Li}_2(1-x)$		8	-8			-8	8
$p_{\Delta q\Delta g}(x)\pi^2/3$		4	6	-4	-2	2	-2
$p_{\Delta q\Delta g}(-x)S_2(x)$	4						
$p_{\Delta q\Delta g}(x)I_0$	-8	-8		8			-8
$p_{\Delta q\Delta g}(x)I_1$		-16	-8	8	4	4	-4
$p_{\Delta q\Delta g}(x)$		-16	-20	14	11		
$\ln^2(x)$						-6	
$\ln(x)$	-22	12	6	-8		-4	9
$\ln(1-x)$		4	4		-4	-4	4
I_0		16	8	-8	-4	-4	4
$1-x$	-44	-2	-10	12	7		-2

Table G.12: Results for ${}^{RR'}\widetilde{P}^{(1)}_{\Delta q\Delta g,\overline{\mathrm{MS}}}(x)$. Adapted from [106], table 2.

Terms	(h)
$(1+x)\ln^2(x)$	-1
$(1-3x)\ln(x)$	-1
$1-x$	1

Table G.13: Results for ${}^{RR}\widetilde{P}^{S(1)}_{\Delta q \Delta q}$ and ${}^{RR}\widetilde{P}^{S(1)}_{\Delta q \Delta \bar{q}}$. Adapted from [106], eq. (45).

Terms	Graphs							
	(b)	(c)	(d)	(e_q)	(e_g)	(f)	(h)	(i)
$p_{\Delta g \Delta q}(x)\ln^2(x)$	1		2		-2			1/2
$p_{\Delta g \Delta q}(x)\ln^2(1-x)$		1	1			-1	1	-1
$p_{\Delta g \Delta q}(x)\ln(x)\ln(1-x)$		4	4		-4	-2	2	-2
$p_{\Delta g \Delta q}(x)I_0\big(\ln(1-x)+\ln(x)\big)$		4	8		-4	-2	2	-2
$p_{\Delta g \Delta q}(x)\ln(x)$	-6	-2	-6		8	3/2	4	-4
$p_{\Delta g \Delta q}(x)\ln(1-x)$	-4	-3	-3	$-4/3$	11/3	2	-6	2
$p_{\Delta g \Delta q}(x)\mathrm{Li}_2(1-x)$		4	-4				4	-4
$p_{\Delta g \Delta q}(x)\pi^2/3$			5		-2	-1	-1	1
$p_{\Delta g \Delta q}(-x)S_2(x)$	2							
$p_{\Delta g \Delta q}(x)I_0$	-4	-4	-12		8	2	-6	2
$p_{\Delta g \Delta q}(x)I_1$		-4	-8		4	2	-2	2
$p_{\Delta g \Delta q}(x)$		-10	-8	$-20/9$	67/9	11/2		
$\ln^2(x)$							6	
$\ln(x)$	22	-2			-8		-4	17
$\ln(1-x)$		4	4			-4	4	-4
I_0		8	16		-8	-4	4	-4
$1-x$	22	5	1	8/3	$-22/3$	$-7/2$	8	11

Table G.14: Results for ${}^{RR'}\widetilde{P}^{(1)}_{\Delta g \Delta q,\overline{\mathrm{MS}}}(x)$. Adapted from [106], table 3.

Terms	Graphs									
	(b_q)	(b_g)	(c)	(d)	(e_q)	(e_g)	(f)	(g)	(h)	(i)
$p_{\Delta g \Delta g}(x)\ln^2(x)$		-2	4			-4			4	
$p_{\Delta g \Delta g}(x)\ln^2(1-x)$			4				-2			
$p_{\Delta g \Delta g}(x)\ln(x)\ln(1-x)$			16			-8	-4			
$p_{\Delta g \Delta g}(x)I_0\big(\ln(1-x)+\ln(x)\big)$			24			-8	-4			
$p_{\Delta g \Delta g}(x)\ln(x)$			$-22/3$	$4/3$			$11/3$	$-4/3$		
$p_{\Delta g \Delta g}(x)\ln(1-x)$		8	$4/3$	$8/3$	$-8/3$	$22/3$	-4		-8	
$p_{\Delta g \Delta g}(x)\pi^2/3$			10			-4	-2			
$p_{\Delta g \Delta g}(-x)S_2(x)$		-4								
$p_{\Delta g \Delta g}(x)I_0$		8	16				-4		-8	
$p_{\Delta g \Delta g}(x)I_1$			-24			8	4			
$p_{\Delta g \Delta g}(x)$			$-340/9$	$40/9$	$-40/9$	$134/9$	$103/9$	$-20/9$		
$(1+x)\ln^2(x)$									4	-1
$(1+x)\ln(x)$	4	-21	$-41/3$	$8/3$					8	-6
$(1-x)\ln(x)$			-16			16			8	-3
$(1-x)\ln(1-x)$			-16				8			
$(1-x)I_0$			-48			16	8			
$1-x$	8	$-233/4$	$14/3$	$-5/3$	$16/3$	$-44/3$	$-95/12$	$1/3$	32	-13

Table G.15: Results for ${}^{RR'}\widetilde{P}^{(1)}_{\Delta g \Delta g}(x)$. Adapted from [106], table 4.

Terms	Graphs						
	(b)	(c)	(d)	(e)	(f)	(g)	(h)
$p_{\delta q\delta q}(x)\ln^2(x)$	-1	1	-1	-2			2
$p_{\delta q\delta q}(x)\ln^2(1-x)$			-2			-1	
$p_{\delta q\delta q}(x)\ln(x)\ln(1-x)$		2	-6	-4		-2	
$p_{\delta q\delta q}(x)\ln(x)$		$-3/2$	$3/2$		$-2/3$	$11/6$	
$p_{\delta q\delta q}(x)\ln(1-x)$	4	-3	-5	3		-2	-4
$p_{\delta q\delta q}(x)\pi^2/3$		2	-3	-2		-1	
$p_{\delta q\delta q}(x)I_0\Big(\ln(1-x)+\ln(x)\Big)$		4	-8	-4		-2	
$p_{\delta q\delta q}(x)I_1$		-4	8	4		2	
$p_{\delta q\delta q}(x)I_0$	4		-8			-2	-4
$p_{\delta q\delta q}(x)$		-7	11	7	$-10/9$	$103/18$	
$1-x$	1						

Table G.16: Results for $^{RR}\widetilde{P}^{V(1)}_{\delta q\delta q}$. Based on unpublished notes of W. Vogelsang connected to [107].

Appendix H

Additional luminosity plots

In this appendix, we present a selection of luminosities for several flavour combinations. These plots complete the $(g, g), (g, g)$ luminosities shown in section 4.3.4, figures 4.15 to 4.17.
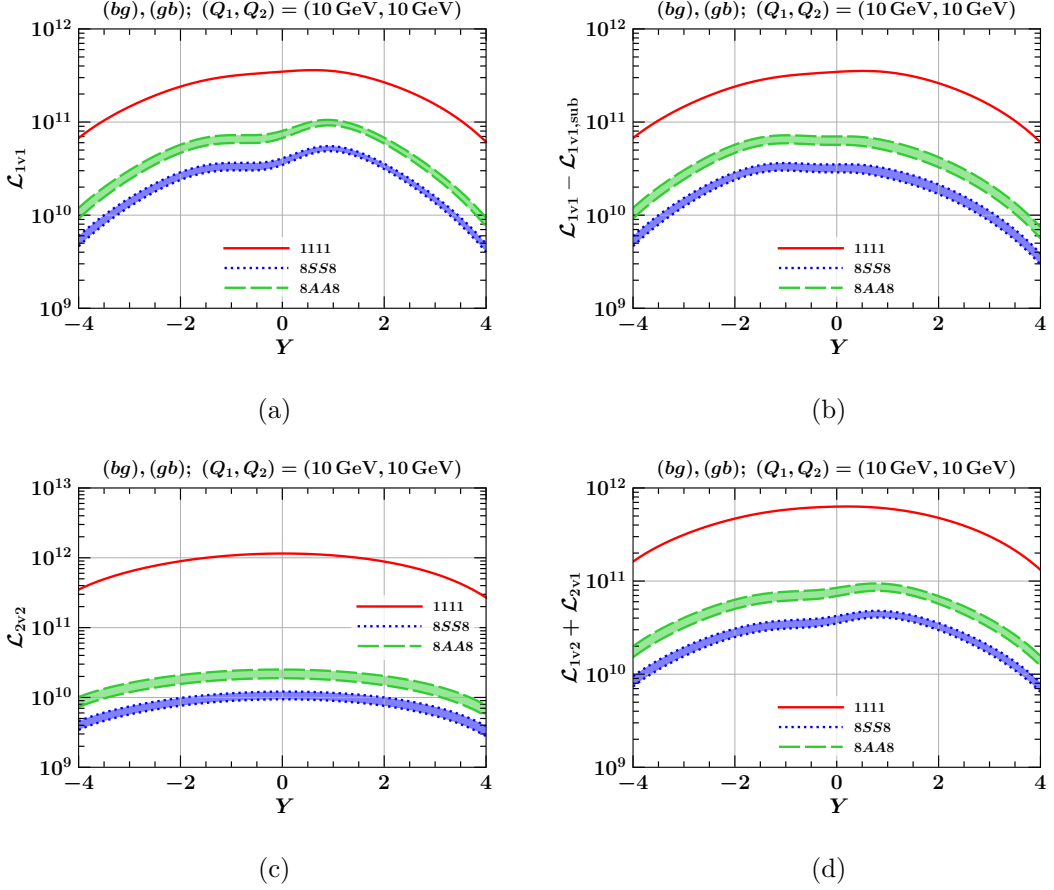
Figure H.1: Luminosities for $(bg), (gb)$ at $(Q_1, Q_2) = (10\,\text{GeV}, 10\,\text{GeV})$ in all colour representations. The bands span the area between minimum and maximum of luminosities calculated with the five ansätze for $^R\Delta J$ given in eqs. (4.48) to (4.52).
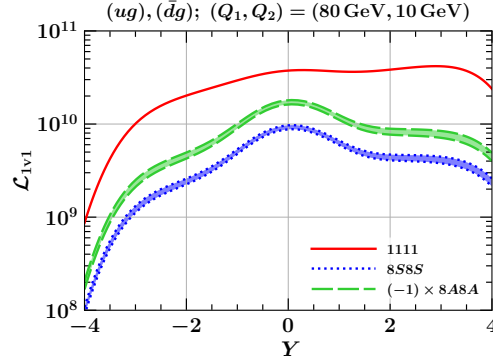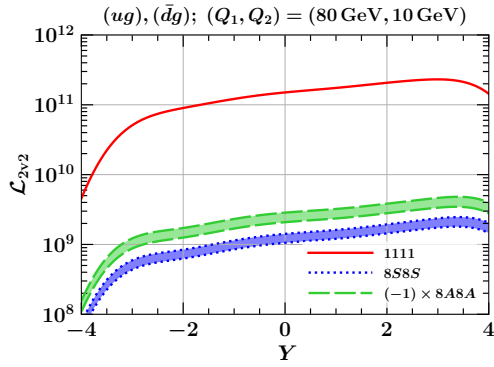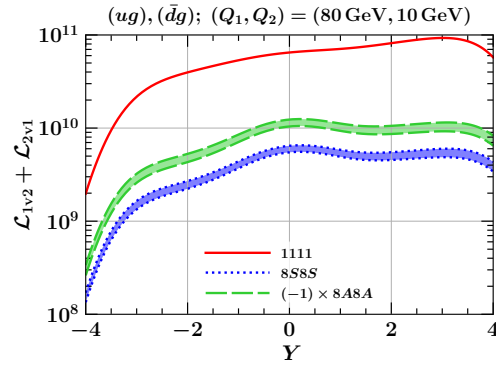
Figure H.2: Luminosities for $(ug), (\bar{d}g)$ at $(Q_1, Q_2) = (80\,\text{GeV}, 10\,\text{GeV})$ in all colour representations. The bands span the area between minimum and maximum of luminosities calculated with the five ansätze for $^R\Delta J$ given in eqs. (4.48) to (4.52).

(a)

(b)

(c)
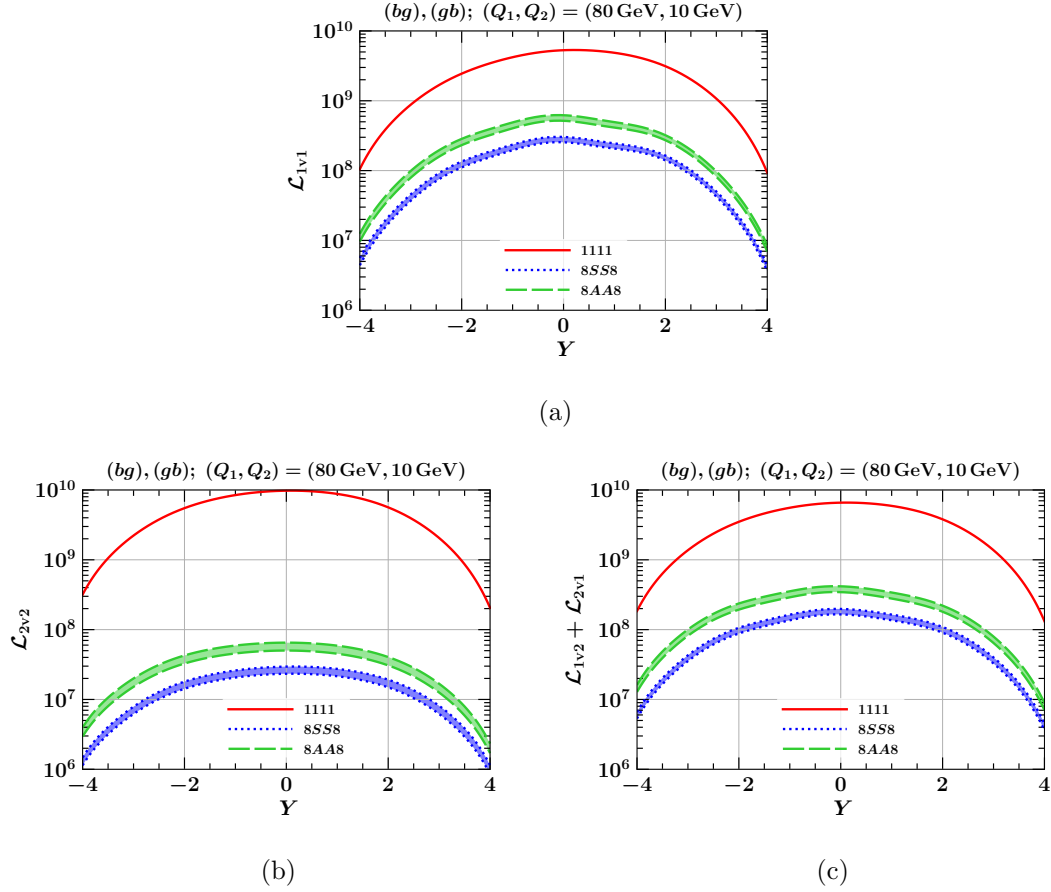
Figure H.3: Luminosities for $(bg), (gb)$ at $(Q_1, Q_2) = (80\,\text{GeV}, 10\,\text{GeV})$ in all colour representations. The bands span the area between minimum and maximum of luminosities calculated with the five ansätze for $^R\Delta J$ given in eqs. (4.48) to (4.52).
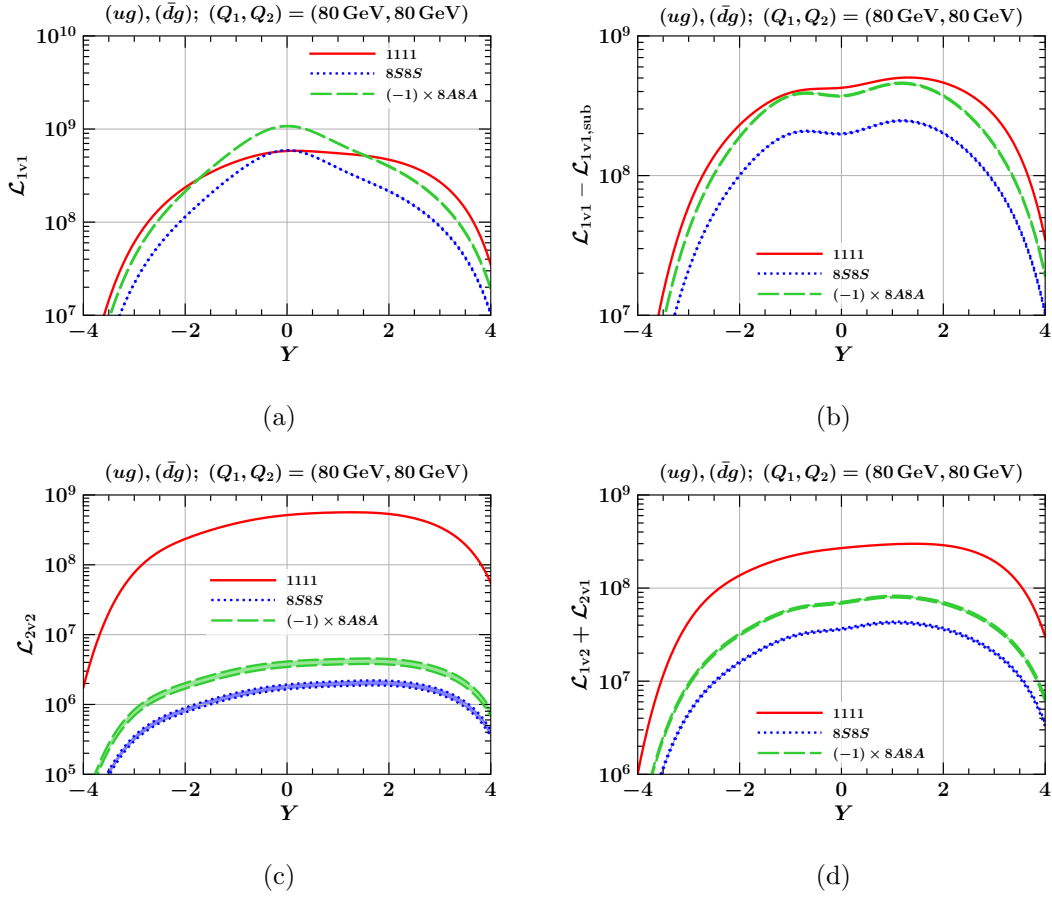
Figure H.4: Luminosities for $(ug), (\bar{d}g)$ at $(Q_1, Q_2) = (80\,\mathrm{GeV}, 80\,\mathrm{GeV})$ in all colour representations. The bands span the area between minimum and maximum of luminosities calculated with the five ansätze for $^R\Delta J$ given in eqs. (4.48) to (4.52).
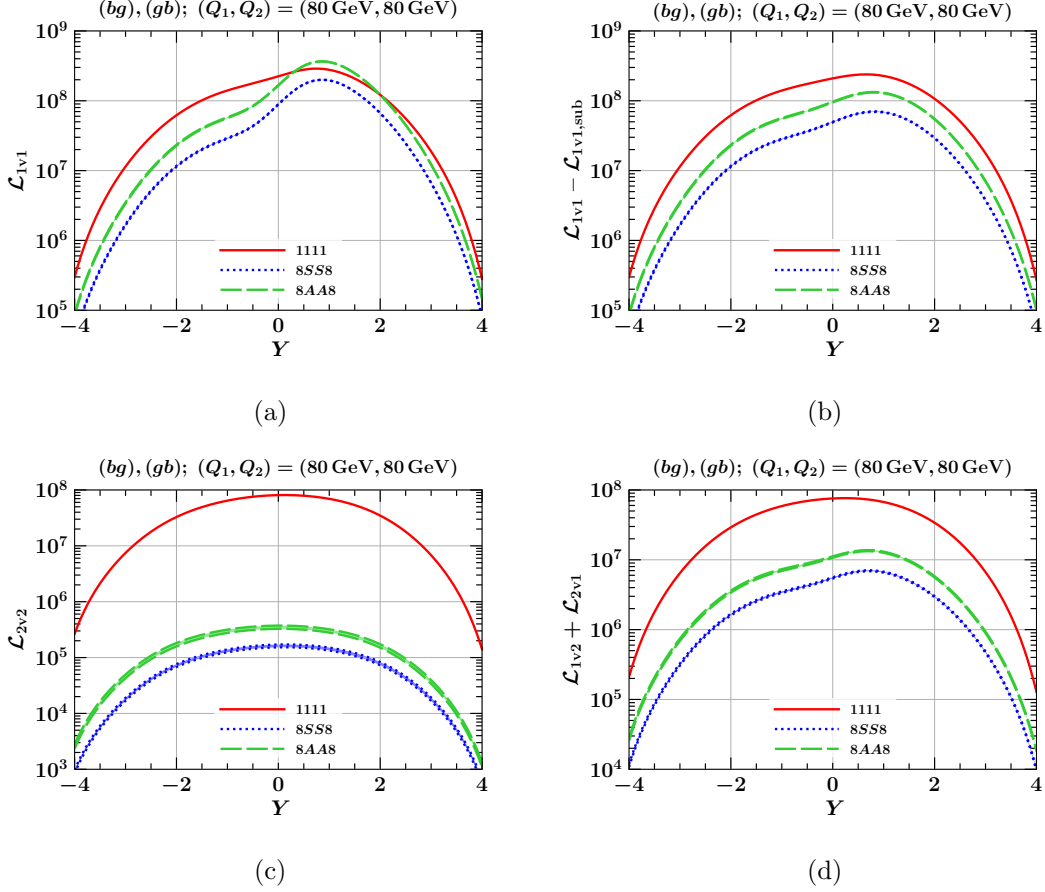
Figure H.5: Luminosities for $(bg), (gb)$ at $(Q_1, Q_2) = (80 \, \text{GeV}, 80 \, \text{GeV})$ in all colour representations. The bands span the area between minimum and maximum of luminosities calculated with the five ansätze for $^R\Delta J$ given in eqs. (4.48) to (4.52).
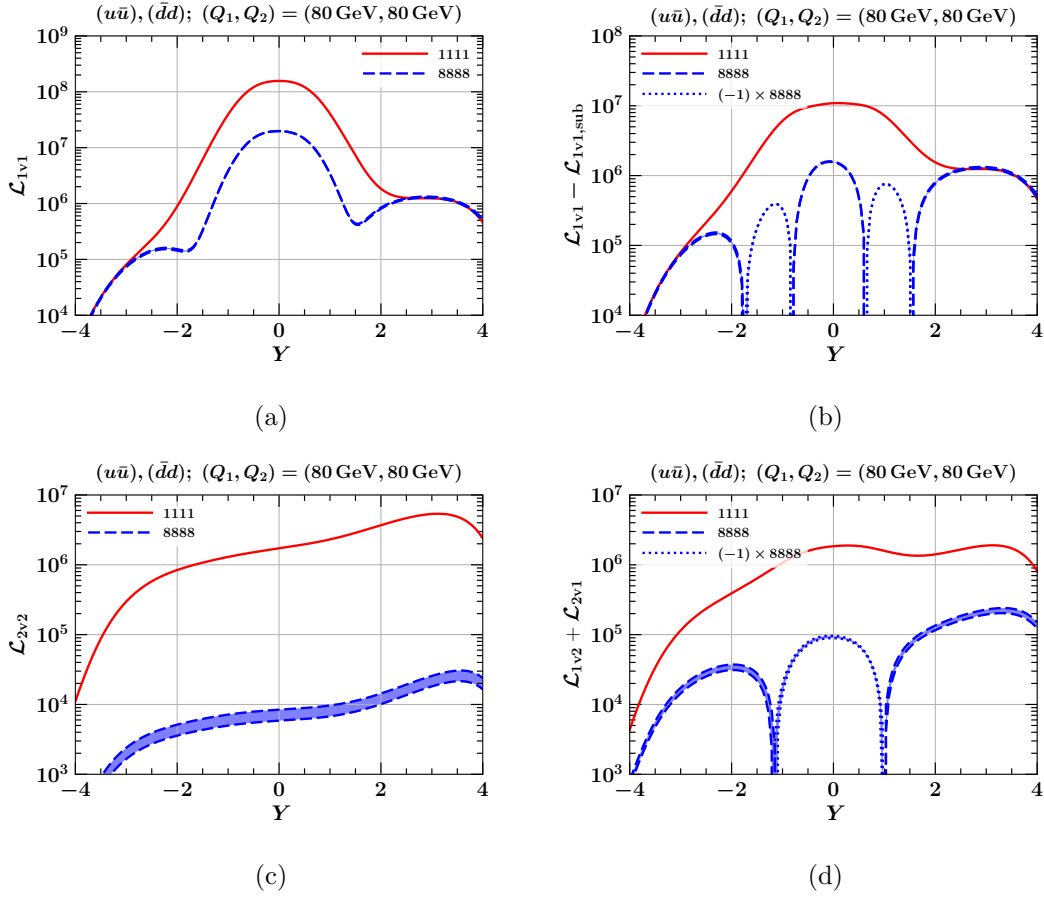
Figure H.6: Luminosities for $(u\bar{u})$, $(\bar{d}d)$ at $(Q_1, Q_2) = (80\,\mathrm{GeV}, 80\,\mathrm{GeV})$ in all colour representations. The bands span the area between minimum and maximum of luminosities calculated with the five ansätze for ${}^R\Delta J$ given in eqs. (4.48) to (4.52).
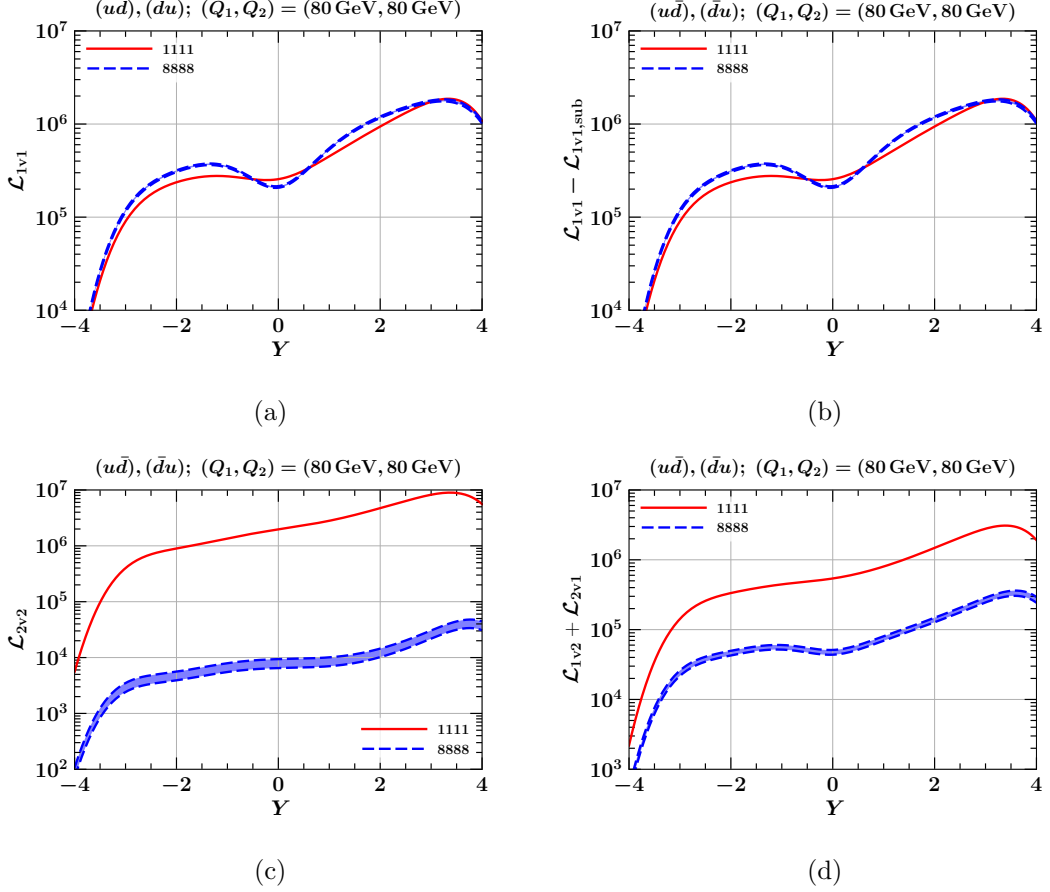
Figure H.7: Luminosities for $(u\bar{d}), (\bar{d}u)$ at $(Q_1, Q_2) = (80\,\text{GeV}, 80\,\text{GeV})$ in all colour representations. The bands span the area between minimum and maximum of luminosities calculated with the five ansätze for $^R\Delta J$ given in eqs. (4.48) to (4.52).
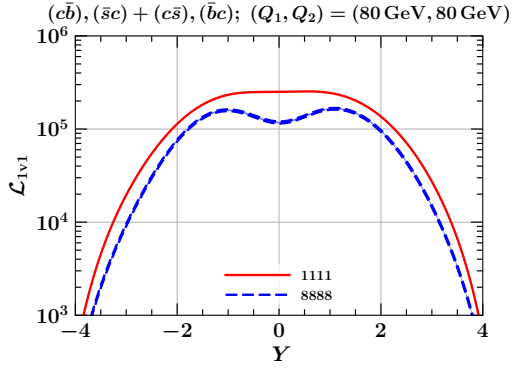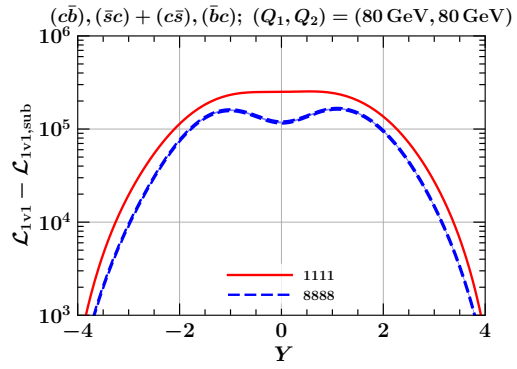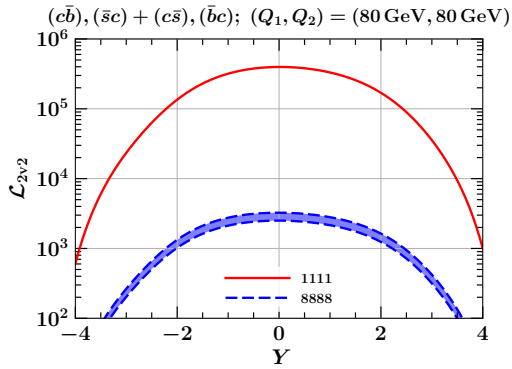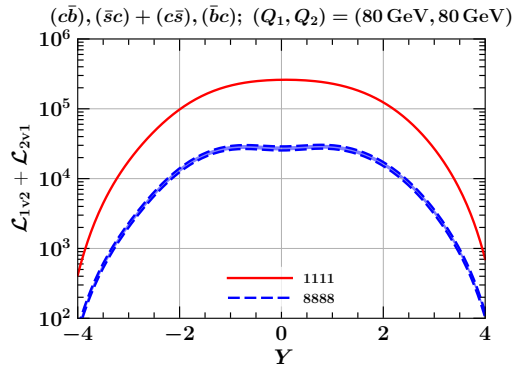
Figure H.8: Luminosities for $(c\bar{b}), (\bar{s}c) + (c\bar{s}), (\bar{b}c)$ at $(Q_1, Q_2) = (80\,\text{GeV}, 80\,\text{GeV})$ in all colour representations. The bands span the area between minimum and maximum of luminosities calculated with the five ansätze for $^R\Delta J$ given in eqs. (4.48) to (4.52).

Bibliography

[1] M. Diehl, F. Fabry and A. Vladimirov, *Two-loop evolution kernels for colour dependent double parton distributions*, *JHEP* **2023** (2023) 67 [`2212.11843`].

[2] M. Diehl, F. Fabry and P. Ploessl, *Evolution of colour correlated double parton distributions: a quantitative study*, `2310.16432`.

[3] ATLAS collaboration, *Observation of a new particle in the search for the Standard Model Higgs boson with the ATLAS detector at the LHC*, *Phys. Lett. B* **716** (2012) 1 [`1207.7214`].

[4] CMS collaboration, *Observation of a New Boson at a Mass of 125 GeV with the CMS Experiment at the LHC*, *Phys. Lett. B* **716** (2012) 30 [`1207.7235`].

[5] Muon g-2 collaboration, *Measurement of the Positive Muon Anomalous Magnetic Moment to 0.46 ppm*, *Phys. Rev. Lett.* **126** (2021) 141801 [`2104.03281`].

[6] Muon g-2 collaboration, *Measurement of the Positive Muon Anomalous Magnetic Moment to 0.20 ppm*, `2308.06230`.

[7] J.C. Collins, D.E. Soper and G.F. Sterman, *Factorization for Short Distance Hadron - Hadron Scattering*, *Nucl. Phys. B* **261** (1985) 104.

[8] J.C. Collins, D.E. Soper and G.F. Sterman, *Soft Gluons and Factorization*, *Nucl. Phys. B* **308** (1988) 833.

[9] R. Ellis, H. Georgi, M. Machacek, H. Politzer and G.G. Ross, *Perturbation theory and the parton model in QCD*, *Nuclear Physics B* **152** (1979) 285.

[10] G. Curci, W. Furmanski and R. Petronzio, *Evolution of Parton Densities Beyond Leading Order: The Nonsinglet Case*, *Nucl. Phys. B* **175** (1980) 27.

[11] H. David Politzer, *Power corrections at short distances*, *Nuclear Physics B* **172** (1980) 349.

[12] N. Paver and D. Treleani, *Multiquark scattering and large-pT jet production in hadronic collisions*, *Il Nuovo Cimento A (1965-1970)* **70** (1982) 215.

[13] M. Mekhfi, *Correlations in Color and Spin in Multiparton Processes*, *Phys. Rev. D* **32** (1985) 2380.

[14] M. Mekhfi, *Multiparton processes: An application to the double Drell-Yan mechanism*, *Phys. Rev. D* **32** (1985) 2371.

[15] T. Sjöstrand and M. Van Zijl, *Multiple parton-parton interactions in an impact parameter picture*, *Physics Letters B* **188** (1987) 149.

[16] B. Blok, Y. Dokshitzer, L. Frankfurt and M. Strikman, *The Four jet production at LHC and Tevatron in QCD*, *Phys. Rev. D* **83** (2011) 071501 [1009.2714].

[17] J.R. Gaunt and W.J. Stirling, *Double Parton Scattering Singularity in One-Loop Integrals*, *JHEP* **06** (2011) 048 [1103.1888].

[18] M.G. Ryskin and A.M. Snigirev, *A Fresh look at double parton scattering*, *Phys. Rev. D* **83** (2011) 114047 [1103.3495].

[19] A.V. Manohar and W.J. Waalewijn, *A QCD Analysis of Double Parton Scattering: Color Correlations, Interference Effects and Evolution*, *Phys. Rev. D* **85** (2012) 114009 [1202.3794].

[20] A.V. Manohar and W.J. Waalewijn, *What is Double Parton Scattering?*, *Phys. Lett. B* **713** (2012) 196 [1202.5034].

[21] M.G. Ryskin and A.M. Snigirev, *Double parton scattering in double logarithm approximation of perturbative QCD*, *Phys. Rev. D* **86** (2012) 014018 [1203.2330].

[22] J.R. Gaunt, *Single Perturbative Splitting Diagrams in Double Parton Scattering*, *JHEP* **01** (2013) 042 [1207.0480].

[23] T. Kasemets and M. Diehl, *Angular correlations in the double Drell-Yan process*, *JHEP* **01** (2013) 121 [1210.5434].

[24] B. Blok, Y. Dokshitzer, L. Frankfurt and M. Strikman, *Perturbative QCD correlations in multi-parton collisions*, *Eur. Phys. J. C* **74** (2014) 2926 [1306.3763].

[25] J.R. Gaunt and W.J. Stirling, *Double Parton Distributions Incorporating Perturbative QCD Evolution and Momentum and Quark Number Sum Rules*, *JHEP* **03** (2010) 005 [0910.4347].

[26] M. Diehl, D. Ostermeier and A. Schäfer, *Elements of a theory for multiparton interactions in QCD*, *JHEP* **03** (2012) 089 [1111.0910].

[27] T. Kasemets and P.J. Mulders, *Constraining double parton correlations and interferences*, *Phys. Rev. D* **91** (2015) 014015 [1411.0726].

[28] A. Vladimirov, *Soft factors for double parton scattering at NNLO*, *JHEP* **12** (2016) 038 [1608.04920].

[29] B. Blok, Y. Dokshitser, L. Frankfurt and M. Strikman, *pQCD physics of multiparton interactions*, *Eur. Phys. J. C* **72** (2012) 1963 [1106.5533].

[30] D. Treleani and G. Calucci, *About Double Parton Scattering at Short Relative Transverse Distances*, 1808.02337.

[31] B. Cabouat, J.R. Gaunt and K. Ostrolenk, *A Monte-Carlo Simulation of Double Parton Scattering*, *JHEP* **11** (2019) 061 [1906.04669].

[32] B. Cabouat and J.R. Gaunt, *Combining single and double parton scatterings in a parton shower*, *JHEP* **10** (2020) 012 [2008.01442].

[33] O. Fedkevych and A. Kulesza, *Double parton scattering in four-jet production in proton-proton collisions at the LHC*, *Phys. Rev. D* **104** (2021) 054021 [2008.08347].

[34] D0 Collaboration collaboration, *Study of double parton interactions in* diphoton + dijet *events in $p\overline{p}$ collisions at $\sqrt{s} = 1.96$ TeV*, *Phys. Rev. D* **93** (2016) 052008.

[35] ATLAS collaboration, *Measurement of hard double-parton interactions in $W(\to l\nu)+$ 2 jet events at $\sqrt{s}=7$ TeV with the ATLAS detector*, *New J. Phys.* **15** (2013) 033038 [1301.6872].

[36] CMS collaboration, *Study of Double Parton Scattering Using W + 2-Jet Events in Proton-Proton Collisions at $\sqrt{s} = 7$ TeV*, *JHEP* **03** (2014) 032 [1312.5729].

[37] CDF Collaboration collaboration, *Double parton scattering in $\overline{p}p$ collisions at $\sqrt{s} = 1.8$TeV*, *Phys. Rev. D* **56** (1997) 3811.

[38] Axial Field Spectrometer collaboration, *Double Parton Scattering in pp Collisions at $\sqrt{s} = 63$ GeV*, *Z. Phys. C* **34** (1987) 163.

[39] CDF collaboration, *Study of four jet events and evidence for double parton interactions in $p\overline{p}$ collisions at $\sqrt{s} = 1.8$ TeV*, *Phys. Rev. D* **47** (1993) 4857.

[40] CDF collaboration, *Double parton scattering in $\overline{p}p$ collisions at $\sqrt{s} = 1.8$TeV*, *Phys. Rev. D* **56** (1997) 3811.

[41] CMS collaboration, *Measurement of double-parton scattering in inclusive production of four jets with low transverse momentum in proton-proton collisions at $\sqrt{s} = 13$ TeV*, *JHEP* **01** (2022) 177 [2109.13822].

[42] CMS collaboration, *Study of Z boson plus jets events using variables sensitive to double-parton scattering in pp collisions at 13 TeV*, *JHEP* **10** (2021) 176 [2105.14511].

[43] ATLAS collaboration, *Observation and measurements of the production of prompt and non-prompt J/ψ mesons in association with a Z boson in pp collisions at $\sqrt{s} = 8$ TeV with the ATLAS detector*, *Eur. Phys. J. C* **75** (2015) 229 [1412.6428].

[44] D0 collaboration, *Observation and Studies of Double J/ψ Production at the Tevatron*, *Phys. Rev. D* **90** (2014) 111101 [1406.2380].

[45] D0 collaboration, *Evidence for simultaneous production of J/ψ and Υ mesons*, *Phys. Rev. Lett.* **116** (2016) 082002 [1511.02428].

[46] LHCв collaboration, *Measurement of the J/ψ pair production cross-section in pp collisions at $\sqrt{s} = 13$ TeV*, *JHEP* **06** (2017) 047 [1612.07451].

[47] CMS collaboration, *Observation of triple J/ψ meson production in proton-proton collisions*, *Nature Phys.* **19** (2023) 338 [2111.05370].

[48] LHCв collaboration, *Observation of double charm production involving open charm in pp collisions at $\sqrt{s} = 7$ TeV*, *JHEP* **06** (2012) 141 [1205.0975].

[49] LHCв collaboration, *Production of associated Y and open charm hadrons in pp collisions at $\sqrt{s} = 7$ and 8 TeV via double parton scattering*, *JHEP* **07** (2016) 052 [1510.05949].

[50] ATLAS collaboration, *Study of the hard double-parton scattering contribution to inclusive four-lepton production in pp collisions at $\sqrt{s} = 8$ TeV with the ATLAS detector*, *Phys. Lett. B* **790** (2019) 595 [1811.11094].

[51] CMS collaboration, *Constraints on the double-parton scattering cross section from same-sign W boson pair production in proton-proton collisions at $\sqrt{s} = 8$ TeV*, *JHEP* **02** (2018) 032 [1712.02280].

[52] CMS collaboration, *Observation of same-sign WW production from double parton scattering in proton-proton collisions at $\sqrt{s} = 13$ TeV*, 2206.02681.

[53] CMS collaboration, *Event generator tunes obtained from underlying event and multiparton scattering measurements*, *Eur. Phys. J. C* **76** (2016) 155 [1512.00815].

[54] CMS collaboration, *Search for physics beyond the standard model in events with jets and two same-sign or at least three charged leptons in proton-proton collisions at $\sqrt{s} = 13$ TeV*, *Eur. Phys. J. C* **80** (2020) 752 [2001.10086].

[55] A. Del Fabbro and D. Treleani, *A Double parton scattering background to Higgs boson production at the LHC*, *Phys. Rev. D* **61** (2000) 077502 [hep-ph/9911358].

[56] P. Bartalini and J.R. Gaunt, *Multiple Parton Interactions at the LHC*, World Scientific (2018), 10.1142/10646, [https://www.worldscientific.com/doi/pdf/10.1142/10646].

[57] M. Diehl, J.R. Gaunt and K. Schönwald, *Double hard scattering without double counting*, *JHEP* **06** (2017) 083 [`1702.06486`].

[58] M.G.A. Buffing, M. Diehl and T. Kasemets, *Transverse momentum in double parton scattering: factorisation, evolution and matching*, *JHEP* **01** (2018) 044 [`1708.03528`].

[59] M. Diehl, J.R. Gaunt, P. Plößl and A. Schaäfer, *Cancellation of Glauber Gluon Exchange in the Double Drell-Yan Process*, *JHEP* **01** (2016) 076 [`1510.08696`].

[60] M. Diehl and R. Nagar, *Factorisation of soft gluons in multiparton scattering*, *JHEP* **04** (2019) 124 [`1812.09509`].

[61] M. Jaarsma, R. Rahn and W.J. Waalewijn, *Towards Double Parton Distributions from First Principles using Large Momentum Effective Theory*, `2305.09716`.

[62] J.-H. Zhang, *Double Parton Distributions from Euclidean Lattice*, `2304.12481`.

[63] G.S. Bali, M. Diehl, B. Gläßle, A. Schäfer and C. Zimmermann, *Double parton distributions in the nucleon from lattice QCD*, *JHEP* **09** (2021) 106 [`2106.03451`].

[64] B. Blok and J. Mehl, *Perturbative Color Correlations in Double Parton Scattering*, `2210.13282`.

[65] V.N. Gribov and L.N. Lipatov, *Deep inelastic e p scattering in perturbation theory*, *Sov. J. Nucl. Phys.* **15** (1972) 438.

[66] G. Altarelli and G. Parisi, *Asymptotic Freedom in Parton Language*, *Nucl. Phys. B* **126** (1977) 298.

[67] Y.L. Dokshitzer, *Calculation of the Structure Functions for Deep Inelastic Scattering and $e^+ e^-$ Annihilation by Perturbation Theory in Quantum Chromodynamics.*, *Sov. Phys. JETP* **46** (1977) 641.

[68] A. Vogt, S. Moch and J.A.M. Vermaseren, *The Three-loop splitting functions in QCD: The Singlet case*, *Nucl. Phys. B* **691** (2004) 129 [`hep-ph/0404111`].

[69] S. Moch, J.A.M. Vermaseren and A. Vogt, *The Three loop splitting functions in QCD: The Nonsinglet case*, *Nucl. Phys. B* **688** (2004) 101 [`hep-ph/0403192`].

[70] S. Moch, J.A.M. Vermaseren and A. Vogt, *The Three-Loop Splitting Functions in QCD: The Helicity-Dependent Case*, *Nucl. Phys. B* **889** (2014) 351 [`1409.5131`].

[71] G. Falcioni, F. Herzog, S. Moch and A. Vogt, *Four-loop splitting functions in QCD – The quark-quark case*, *Phys. Lett. B* **842** (2023) 137944 [`2302.07593`].

[72] S. Moch, B. Ruijl, T. Ueda, J.A.M. Vermaseren and A. Vogt, *Low moments of the four-loop splitting functions in QCD*, *Phys. Lett. B* **825** (2022) 136853 [`2111.15561`].

[73] J. Blümlein, P. Marquard, C. Schneider and K. Schönwald, *The three-loop unpolarized and polarized non-singlet anomalous dimensions from off shell operator matrix elements*, *Nucl. Phys. B* **971** (2021) 115542 [2107.06267].

[74] J. Blümlein, P. Marquard, C. Schneider and K. Schönwald, *The three-loop anomalous dimensions from off-shell operator matrix elements*, *PoS* **LL2022** (2022) 048 [2207.07943].

[75] B. Blok, R. Segev and M. Strikman, *Hot spot model of nucleon and double parton scattering*, *Eur. Phys. J. C* **83** (2023) 415 [2212.08848].

[76] M. Diehl, R. Nagar and F.J. Tackmann, *ChiliPDF: Chebyshev interpolation for parton distributions*, *Eur. Phys. J. C* **82** (2022) 257 [2112.09703].

[77] D. Binosi and L. Theußl, *A graphical user interface for drawing Feynman diagrams*, *Computer Physics Communications* **161** (2004) .

[78] J.D. Hunter, *Matplotlib: A 2D Graphics Environment*, *Computing in Science & Engineering* **9** (2007) 90.

[79] B. Ruijl, T. Ueda and J. Vermaseren, *FORM version 4.2*, 1707.06453.

[80] M. Sjödahl, *ColorMath - A package for color summed calculations in SU(Nc)*, *Eur. Phys. J. C* **73** (2013) 2310 [1211.2099].

[81] M. Diehl and A. Schafer, *Theoretical considerations on multiparton interactions in QCD*, *Phys. Lett. B* **698** (2011) 389 [1102.3081].

[82] M. Diehl and J.R. Gaunt, *Double Parton Scattering - Theory Overview*, *Adv. Ser. Direct. High Energy Phys.* **29** (2018) 7 [1710.04408].

[83] A. Kulesza and W.J. Stirling, *Like sign W boson production at the LHC as a probe of double parton scattering*, *Phys. Lett. B* **475** (2000) 168 [hep-ph/9912232].

[84] J.R. Gaunt, C.-H. Kom, A. Kulesza and W.J. Stirling, *Same-sign W pair production as a probe of double parton scattering at the LHC*, *Eur. Phys. J. C* **69** (2010) 53 [1003.3953].

[85] J.C. Collins, *Foundations of Perturbative QCD*, Cambridge University Press, Cambridge (2011).

[86] G.F. Sterman, *Mass Divergences in Annihilation Processes. 1. Origin and Nature of Divergences in Cut Vacuum Polarization Diagrams*, *Phys. Rev. D* **17** (1978) 2773.

[87] S.B. Libby and G.F. Sterman, *Mass Divergences in Two Particle Inelastic Scattering*, *Phys. Rev. D* **18** (1978) 4737.

[88] G. Grammer, Jr. and D.R. Yennie, *Improved treatment for the infrared divergence problem in quantum electrodynamics*, *Phys. Rev. D* **8** (1973) 4332.

[89] M. Diehl, J.R. Gaunt, P. Pichini and P. Plößl, *Double parton distributions out of bounds in colour space*, *Eur. Phys. J. C* **81** (2021) 1033 [`2109.14304`].

[90] M. Diehl, J.R. Gaunt, P. Plößl and A. Schäfer, *Two-loop splitting in double parton distributions*, *SciPost Phys.* **7** (2019) 017 [`1702.06486`].

[91] M. Diehl, J.R. Gaunt and P. Plößl, *Two-loop splitting in double parton distributions: the colour non-singlet case*, *JHEP* (2021) [`2105.08425`].

[92] M. Diehl, R. Nagar and P. Plößl, *Quark mass effects in double parton distributions*, `2212.07736`.

[93] M.G. Echevarria, A. Idilbi and I. Scimemi, *Factorization Theorem For Drell-Yan At Low q_T And Transverse Momentum Distributions On-The-Light-Cone*, *JHEP* **07** (2012) 002 [`1111.4996`].

[94] M.G. Echevarria, I. Scimemi and A. Vladimirov, *Unpolarized Transverse Momentum Dependent Parton Distribution and Fragmentation Functions at next-to-next-to-leading order*, *JHEP* **09** (2016) 004 [`1604.07869`].

[95] J.C. Collins and T.C. Rogers, *Equality of Two Definitions for Transverse Momentum Dependent Parton Distribution Functions*, *Phys. Rev. D* **87** (2013) 034018 [`1210.2100`].

[96] M. Diehl, P. Plößl and A. Schäfer, *Proof of sum rules for double parton distributions in QCD*, *The European Physical Journal C* **79** (2019) [`1811.00289`].

[97] M. Diehl, R. Nagar, P. Ploessl and F.J. Tackmann, *Evolution and interpolation of double parton distributions using Chebyshev grids*, `2305.04845`.

[98] M. Buza, Y. Matiounine, J. Smith and W.L. van Neerven, *Charm electroproduction viewed in the variable flavor number scheme versus fixed order perturbation theory*, *Eur. Phys. J. C* **1** (1998) 301 [`hep-ph/9612398`].

[99] J. Blümlein, A. De Freitas, C. Schneider and K. Schönwald, *The Variable Flavor Number Scheme at Next-to-Leading Order*, *Phys. Lett. B* **782** (2018) 362 [`1804.03129`].

[100] T. Appelquist and J. Carazzone, *Infrared Singularities and Massive Fields*, *Phys. Rev. D* **11** (1975) 2856.

[101] M.G. Echevarria, I. Scimemi and A. Vladimirov, *Universal transverse momentum dependent soft function at NNLO*, *Phys. Rev. D* **93** (2016) 054004 [`1511.05590`].

[102] M.G. Echevarria, I. Scimemi and A. Vladimirov, *Transverse momentum dependent fragmentation function at next-to–next-to–leading order*, *Physical Review D* **93** (2016) [1509.06392].

[103] J.C. Collins, D.E. Soper and G. Sterman, *Factorization of Hard Processes in QCD*, hep-ph/0409313.

[104] J. Collins, T.C. Rogers and N. Sato, *Positivity and renormalization of parton densities*, *Phys. Rev. D* **105** (2022) 076010 [2111.01170].

[105] R.K. Ellis and W. Vogelsang, *The Evolution of parton distributions beyond leading order: The Singlet case*, hep-ph/9602356.

[106] W. Vogelsang, *The Spin dependent two loop splitting functions*, *Nucl. Phys. B* **475** (1996) 47 [hep-ph/9603366].

[107] W. Vogelsang, *Next-to-leading order evolution of transversity distributions and Soffer's inequality*, *Physical Review D* **57** (1998) 1886.

[108] G. 't Hooft and M. Veltman, *Regularization and renormalization of gauge fields*, *Nuclear Physics B* **44** (1972) 189.

[109] P. Breitenlohner and D. Maison, *Dimensional Renormalization and the Action Principle*, *Commun. Math. Phys.* **52** (1977) 11.

[110] J. Kodaira, S. Matsuda, K. Sasaki and T. Uematsu, *QCD higher order effects in spin-dependent deep inelastic electroproduction*, *Nuclear Physics B* **159** (1979) 99.

[111] D. Gutierrez-Reyes, I. Scimemi and A. Vladimirov, *Transverse momentum dependent transversely polarized distributions at next-to-next-to-leading-order*, *JHEP* **07** (2018) 172 [1805.07243].

[112] L.N. Trefethen, *Approximation Theory and Approximation Practice*, Society for Industrial and Applied Mathematics (2012).

[113] A. Buckley, J. Ferrando, S. Lloyd, K. Nordström, B. Page, M. Rüfenacht et al., *LHAPDF6: parton density access in the LHC precision era*, *The European Physical Journal C* **75** (2015) .

[114] C. Runge, *Über empirische Funktionen und die Interpolation zwischen äquidistanten Ordinaten*, *Z. Math. Phys.* **46** (1901) 224.

[115] J. Dormand and P. Prince, *A family of embedded Runge-Kutta formulae*, *Journal of Computational and Applied Mathematics* **6** (1980) 19.

[116] P. Prince and J. Dormand, *High order embedded Runge-Kutta formulae*, *Journal of Computational and Applied Mathematics* **7** (1981) 67.

[117] M.A. Ebert, *Analytic results for Sudakov form factors in QCD*, *JHEP* **02** (2022) 136 [2110.11360].

[118] M. Diehl, J.R. Gaunt, D.M. Lang, P. Plößl and A. Schäfer, *Sum rule improved double parton distributions in position space*, *Eur. Phys. J. C* **80** (2020) 468 [2001.10428].

[119] M. Diehl, J.R. Gaunt and P. Ploessl, *Two-loop splitting in double parton distributions: the colour non-singlet case*, *JHEP* **08** (2021) 040 [2105.08425].

[120] M. Diehl, J.R. Gaunt, P. Plößl and A. Schäfer, *Two-loop splitting in double parton distributions*, *SciPost Phys.* **7** (2019) 017 [1902.08019].

[121] I. Scimemi and A. Vladimirov, *Non-perturbative structure of semi-inclusive deep-inelastic and Drell-Yan scattering at small transverse momentum*, *JHEP* **06** (2020) 137 [1912.06532].

[122] F. Hautmann, I. Scimemi and A. Vladimirov, *Non-perturbative contributions to vector-boson transverse momentum spectra in hadronic collisions*, *Phys. Lett. B* **806** (2020) 135478 [2002.12810].

[123] MAP (MULTI-DIMENSIONAL ANALYSES OF PARTONIC DISTRIBUTIONS) collaboration, *Unpolarized transverse momentum distributions from a global fit of Drell-Yan and semi-inclusive deep-inelastic scattering data*, *JHEP* **10** (2022) 127 [2206.07598].

[124] V. Moos, I. Scimemi, A. Vladimirov and P. Zurita, *Extraction of unpolarized transverse momentum distributions from fit of Drell-Yan data at N^4LL*, 2305.07473.

[125] M. Schlemmer, A. Vladimirov, C. Zimmermann, M. Engelhardt and A. Schäfer, *Determination of the Collins-Soper Kernel from Lattice QCD*, *JHEP* **08** (2021) 004 [2103.16991].

[126] H.-T. Shu, M. Schlemmer, T. Sizmann, A. Vladimirov, L. Walter, M. Engelhardt et al., *Universality of the Collins-Soper kernel in lattice calculations*, 2302.06502.

[127] A. Avkhadiev, P. Shanahan, M. Wagman and Y. Zhao, *Collins-Soper kernel from lattice QCD at the physical pion mass*, 2307.12359.

[128] R. Abbate, M. Fickinger, A.H. Hoang, V. Mateu and I.W. Stewart, *Thrust at N^3LL with Power Corrections and a Precision Global Fit for $\alpha_s(mZ)$*, *Phys. Rev. D* **83** (2011) 074021 [1006.3080].

[129] C.F. Berger, C. Marcantonini, I.W. Stewart, F.J. Tackmann and W.J. Waalewijn, *Higgs Production with a Central Jet Veto at NNLL+NNLO*, *JHEP* **04** (2011) 092 [1012.4480].

[130] S. Bailey, T. Cridge, L.A. Harland-Lang, A.D. Martin and R.S. Thorne, *Parton distributions from LHC, HERA, Tevatron and fixed target data: MSHT20 PDFs*, *Eur. Phys. J. C* **81** (2021) 341 [`2012.04684`].

[131] I.W. Stewart, F.J. Tackmann, J.R. Walsh and S. Zuberi, *Jet p_T resummation in Higgs production at $NNLL' + NNLO$*, *Phys. Rev. D* **89** (2014) 054001 [`1307.1808`].

[132] Y.L. Dokshitzer and G. Marchesini, *Soft gluons at large angles in hadron collisions*, *JHEP* **01** (2006) 007 [`hep-ph/0509078`].

[133] C.D. Palmer and M.E. Carrington, *A General Expression for Symmetry Factors of Feynman Diagrams*, *Canadian Journal of Physics* (2001) [`0108088`].

[134] Blümlein, Johannes and Kurth, Stefan, *Harmonic sums and Mellin transforms up to two loop order*, *Phys. Rev. D* **60** (1999) 014018 [`hep-ph/9810241`].

[135] A. Behring, I. Bierenbaum, J. Blümlein, A. De Freitas, S. Klein and F. Wißbrock, *The logarithmic contributions to the $O(\alpha_s^3)$ asymptotic massive Wilson coefficients and operator matrix elements in deeply inelastic scattering*, *Eur. Phys. J. C* **74** (2014) 3033 [`1403.6356`].

[136] S.L. Adler, *Axial vector vertex in spinor electrodynamics*, *Phys. Rev.* **177** (1969) 2426.

[137] J.S. Bell and R. Jackiw, *A PCAC puzzle: $\pi^0 \to \gamma\gamma$ in the σ model*, *Nuovo Cim. A* **60** (1969) 47.

Acknowledgements

First of all, I want to thank *Markus*, for giving me the opportunity to work on such an intriguing topic, for always being willing to spare time to discuss new problems or offer help with existing ones, for countless discussion at the (virtual) blackboard, and for providing new perspectives when I needed them;
Sven for agreeing to co-supervise my thesis;
Alexey for working with me on the calculation of two-loop matrix elements;
and *Peter*, for all the helpful advice and discussions about double parton scattering.

My thanks go to *DESY* for creating an inspiring and unique environment for writing a PhD thesis;
the *third floor of building 1b* for its wonderful working atmosphere, especially in the famous coffee table discussions;
and *Georgios*, *Oskar*, and *Rebecca*, as they made working in our office a lot nicer.

I am grateful to *my parents* and *my brother* for their constant support.

Finally, I want to thank *Marieke* for being the best companion in life one could wish for.

Eidesstattliche Versicherung

Hiermit versichere ich an Eides statt, die vorliegende Dissertationsschrift selbst verfasst und keine anderen als die angegebenen Hilfsmittel und Quellen benutzt zu haben.
Die eingereichte schriftliche Fassung entspricht der auf dem elektronischen Speichermedium.
Die Dissertation wurde in der vorgelegten oder einer ähnlichen Form nicht schon einmal in einem früheren Promotionsverfahren angenommen oder als ungenügend beurteilt.

Hamburg, den 04.09.2023

Florian Fabry